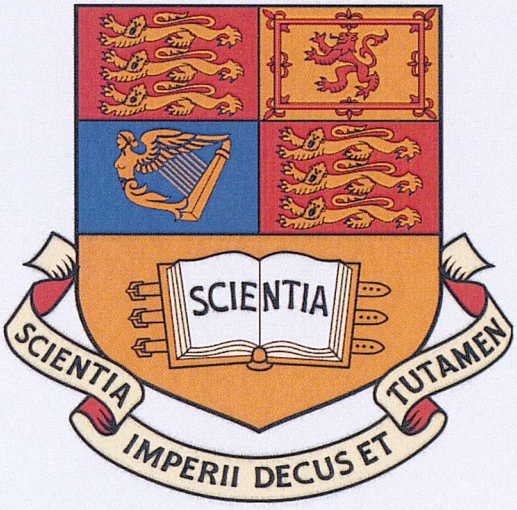
University of London



Imperial College London
The Blackett Laboratory
Photonics Group

Modelocking the bounce geometry laser

Dominic Farrell

Thesis submitted in partial fulfilment of the
requirements for the degree of
Doctor of Philosophy
of the
University of London

September 2009

For Mum and Dad

Acknowledgements

First of all a huge amount of thanks should go to my supervisor Prof. Mike "Damlad" Damzen for giving me the opportunity to work in his lab, and for the advice, guidance, encouragement and rudeness, more often than not above and beyond the call of duty.

Special thanks also to the right-hand man, Ara! "Aralad" Minassian for the wealth of day-to-day assistance in the lab, learning me the ropes when I was a fresh-faced newbie, LaTeX help, and always being wonderfully, blindly optimistic about what the next experiment should be.

Thanks to the guys in the Optics Workshop for making bits and pieces guided only by my scribbles on the back of napkins, and for the glorious feasts that are the Optics Christmas parties.

Thanks to the principle mixers, Gez and Boycie. To Gez especially for keeping everything in perspective, and helping me to fully appreciate the greatness of the Twyman-Green. And to Boycie for making sure the lab stayed safe and porn-free.

To the Old Skool of Tim "two times prize-winning" Jackson, Mike "punch in the stomach " Bye, Dr Dave "The North!" Sinden and Captain Alan "Bamfool" Bamford, for all the good times in those formative early years. To the Nu Skool of Pete, Simon and Andy for taking up the lab traditions with gusto to preserve them for the next generation. And Gabsla, for proof-reading, support, funtimes and continuously turning the rude up to full-bore-and-a-half.

Huge amounts of love to Dan, Jo and Hugh, for being just bonkers and geeky enough to make me feel relatively normal, most of the time. It wouldn't have been the same without you and the good times are only just beginning.

And finally to my parents, whom I never thank enough, and whom I could never thank anywhere near enough. I did it!

Abstract

This thesis investigates the possibility of generating a picosecond modelocked laser source using a laser configuration known as the bounce geometry. The bounce geometry is capable of producing efficient, high power, high spatial quality outputs in both CW and Q-switched regimes and these qualities would also be desirable in a modelocked source.

A basic TEM_{00} bounce geometry oscillator is constructed and then modified by the addition of an intracavity relay-imaging system. A Semiconductor Saturable Absorber Mirror (SESAM) is added as one of the cavity mirrors and this results in the formation of a modelocked pulse train consisting of 30 ps pulses with an average output power of 16.7 W at a repetition rate of 77 MHz. This is used as the oscillator in a master oscillator power amplifier (MOPA) configuration to produce a modelocked pulse train with an average power of 60 W. The oscillator is then improved to produce a train of 12 ps pulses with an average power of 6.1 W

The initial SESAM is then replaced with similar devices based on Quantum Dots (QDs). Quantum Dots offer a number of advantages as modelocking devices and a batch of QD-SESAMS based on a novel design grown by another research group are tested. Initial tests produce 200 ps pulses and these results are used to inform the design of a second set of devices. These result in the production of 84 ps pulses, and the pulse duration is seen to vary in accordance with the modulation depth of the devices. This is the first demonstration of modelocking with this type of SESAM structure.

A different mechanism for the production of modelocking is then investigated. Non-linear mirror (NLM) modelocking involves the use of an intracavity non-linear crystal to create second harmonic and difference frequency generation. Correct phasing of these two processes results in an element with a non-linear reflectivity, and modelocking can be realised. Two different non-linear crystals are utilised; one results in the highest power ever demonstrated with this technique, the second produces the shortest pulses ever demonstrated.

Contents

Acknowledgements 3

Abstract 4

Contents 5

List of figures 10

Publications 14

1 Introduction 15

1.1 Introduction 15

1.2 Diode-pumped solid-state lasers 16

1.2.1 Pumping of solid-state media 18

1.2.1.1 Flashlamps and arc lamps 18

1.2.1.2 Laser diodes 19

1.2.2 Diode pumping geometries 20

1.2.3 The bounce geometry 23

1.3 Pulsed laser sources 24

1.4 Q-switching 26

1.4.1 Theory 27

1.4.2 Implementation 28

1.4.2.1 Electro-optic Q-switching 28

1.4.2.2 Acousto-optic Q-switching 29

1.4.2.3 Passive saturable absorber Q-switching 30

1.5 Modelocking 31
1.6 Motivation of thesis 33
1.7 Thesis outline 34

2 Modelocked laser sources **37**
2.1 Introduction 37
2.2 Frequency domain description 38
2.3 Time domain description 43
2.4 Methods for modelocking 45
2.4.1 Active Modelocking 46
2.4.2 Passive modelocking 50
2.4.2.1 Fast Saturable absorber modelocking 50
2.4.2.2 Slow saturable absorber modelocking 52
2.4.2.3 Kerr lens modelocking 54
2.4.2.4 Non-linear mirror (Stankov) modelocking 56
2.4.2.5 Additive pulse modelocking 57
2.5 Pulse measurement 59
2.5.1 Autocorrelation 60
2.5.2 Spinning mirror autocorrelator 62
2.6 Conclusions 64

3 The Bounce Geometry Amplifier **66**
3.1 Introduction 66
3.2 Thermo-optic effects in solid state media 67
3.2.1 Quantum defect heating 67
3.2.2 Auger upconversion 69
3.2.3 Cross relaxation 70
3.2.4 Excited state absorption 70
3.2.5 How optical properties are affected by thermal loading . . . 72
3.3 The bounce geometry amplifier 74
3.3.1 Crystal geometry 77
3.3.2 Crystal cooling 78
3.3.3 Diode pumping geometry 78

3.3.4 Bounce angle 79
3.3.4.1 Refraction through a crystal with angled end faces 79
3.3.4.2 Crystal with 5° end faces 80
3.3.4.3 Crystal with 14° end faces 81
3.4 Bounce geometry laser oscillators 82
3.4.1 Multimode bounce laser oscillator 82
3.4.2 Cavity stability and the effect of an intra-cavity lens 86
3.4.3 TEM_{00} asymmetric bounce laser oscillator 92
3.5 Conclusions 94

4 A SESAM modelocked bounce geometry laser oscillator 97
4.1 Introduction 97
4.2 Action of a saturable absorber 98
4.2.1 Fast and slow saturable absorbers 102
4.2.2 The Q-switching instability 105
4.3 Semiconductor Saturable Absorber Mirrors (SESAMs) 108
4.3.1 SESAM device structure 109
4.3.2 Action as a saturable absorber 110
4.4 Cavity design considerations for extension to modelocking 112
4.4.1 Varying the pulse energy, E_p 113
4.4.2 Varying the saturation energy of the absorber, E_{SA} 114
4.4.3 Varying the modulation depth of the absorber, ΔR 115
4.5 Evolution of the fundamental laser cavity to a CW ML laser oscillator 116
4.5.1 Compact cavity with no magnification 117
4.5.1.1 Forcing the second stability zone 119
4.5.2 Extended cavity with m=1 120
4.5.2.1 Single spherical mirror 120
4.5.2.2 Dual spherical mirrors 121
4.5.3 Extended cavity with m=1/2 127
4.5.3.1 Improving the spatial quality 128
4.5.3.2 Balancing the Q-switching inequality 130
4.6 Power scaling the modelocked system 132

4.6.1 Master Oscillator - Power Amplifier 133
4.7 Conclusions 135

5 Quantum dot SESAM devices **138**
5.1 Introduction 138
5.2 Quantum dots 139
5.2.1 Quantum dots vs Quantum wells 140
5.2.2 Growth of quantum dots 143
5.2.2.1 Rapid Thermal Annealing 145
5.3 Investigation of QDSAM devices 147
5.4 QDSAMs with higher modulation depths 152
5.4.1 Chemical etching 153
5.5 Investigation of high modulation depth QDSAM devices 154
5.6 Conclusions 158

6 Non-linear mirror modelocking **160**
6.1 Introduction 160
6.2 Non-linear optics and the $\chi^{(2)}$ susceptibility 161
6.2.1 Second harmonic generation 162
6.2.2 Difference frequency generation 165
6.3 Phase matching considerations 166
6.3.1 Type I phase-matching 167
6.3.2 Type II phase-matching 169
6.3.3 Non-critical phase matching 170
6.3.4 Non-linear media 171
6.4 The Non-linear mirror (NLM) modelocking technique 172
6.5 A NLM modelocked bounce geometry laser oscillator 176
6.5.1 NLM with type II phase matched KTP 178
6.5.1.1 Dispersion problems with KTP 180
6.5.2 NLM with type I phase matched BiBO 181
6.6 Conclusions 183

7 Conclusions **185**

7.1 Introduction 185

7.2 Thesis summary 186

7.3 Future work 190

7.4 Conclusions 192

References **195**

List of Figures

1.1 Emission from a diode bar with fast-axis collimation. 20
1.2 A basic end-pumped laser scheme 21
1.3 A basic side-pumped laser scheme. 22
1.4 Simple schematic of the bounce geometry amplifier 23
1.5 Two photon excitation microscopy colour image 25
1.6 Picosecond micromachining image 26
1.7 Cavity dynamics of Q-switching 27
1.8 Typical arrangement for EO Q-switching 29
1.9 Typical arrangement for AO Q-switching 30
1.10 Amplitude modulation leads to injection locking of cavity modes . . 32

2.1 Uniform mode amplitude distribution in a modelocked laser. 38
2.2 Pulse formation from superposition of cavity modes 39
2.3 Gaussian mode amplitude distribution in a modelocked laser 41
2.4 Cavity shutter positions for harmonic modelocking 44
2.5 Time domain picture of active modelocking 47
2.6 Steady state situation for fast saturable absorber modelocking . . . 51
2.7 Steady state situation for slow saturable absorber modelocking . . . 53
2.8 Implementation of Kerr lens modelocking 55
2.9 Implementation of non-linear mirror modelocking 56
2.10 The self-phase modulation effect 58
2.11 Background free autocorrelation 60
2.12 Duty cycle of the spinning mirror autocorrelator 63

3.1 Simple schematic of a four level laser system 68
3.2 Auger upconversion between two ions with four-level systems 69
3.3 Cross relaxation between two ions with four-level systems 71
3.4 Excited state absorption between two ions with four-level systems . 71
3.5 Stress induced birefringence and refracive index ellipsoids 73
3.6 Schematic of the bounce amplifier geometry 75
3.7 Laser crystal geometry in the bounce amplifier 77
3.8 Diode pumping geometry 79
3.9 Refraction of a beam through a general crystal 80
3.10 Refraction through a crystal with end faces angled at 14° 81
3.11 Symmetric bounce geometry laser cavity 83
3.12 Power curve for compact symmetric cavity 85
3.13 Cavity stability zones with an intracavity lens 89
3.14 Intracavity mode shapes at the edge of stability zones 90
3.15 Intracavity spot sizes with an intracavity lens 91
3.16 Asymmetric bounce geometry laser 92
3.17 Power curve for an asymmetric cavity 93

4.1 Schematic cavity used to calculate transmission operators 98
4.2 Saturable absorber response for a slow absorber 103
4.3 CW and Q-switched modelocking 106
4.4 Typical construction of an anti-resonant SESAM device 110
4.5 Density of states for bulk GaAs and a multiple quantum well system 111
4.6 Bi-temporal form of the absorber recovery time 112
4.7 A basic asymmetric bounce cavity with SESAM 118
4.8 Asymmetric SESAM cavity with HCL 119
4.9 An extended SESAM bounce cavity with magnification 1 120
4.10 Dual mirror extended SESAM cavity 122
4.11 Modelocked pulse train and spatial quality 122
4.12 Comparison of a modelocked and a CW cavity 123
4.13 Higher order transverse modes in a cavity 124
4.14 Imaged mode on the SESAM 125

4.15 Extended SESAM cavity with $m = 1/2$ 127
4.16 Manual autocorrelation trace for the $m = 1/2$ cavity 128
4.17 Bounce geometry MOPA implementation 134
4.18 Output power from the MOPA as a function of amplifier pump power 135

5.1 Low temperature photoluminescence of quantum dots 142
5.2 Stimulated absorption coefficients for quantum dots 142
5.3 Atomic force microscope image of a quantum dot layer 144
5.4 Schematic view of a strain coupled quantum dot bilayer system . . 145
5.5 Ground state emission energy for a quantum dot sample 147
5.6 The full width at half maximum of the ground state quantum dot transition 148
5.7 Refractive index profile and electric field structure for the QDSAM 148
5.8 Base cavity for the QDSAM investigation 149
5.9 Autocorrelation of pulses from the low modulation depth QDSAM . 151
5.10 TEM and reflectivity spectrum of the QDSAM 151
5.11 Refractive index and electric field in the multi-layer quantum dot sample 152
5.12 Measured reflectivity of the QDSAM for a range of etch durations . 154
5.13 Modulation depth and saturation fluence of QDSAM devices 155
5.14 Autocorrelation of the QDSAM pulse 156
5.15 Minimum pulse duration from QDSAMs of varying modulation depth 157

6.1 Second harmonic growth in a non-linear crystal 164
6.2 Photon picture of second harmonic generation 165
6.3 Second harmonic generation in a birefringent crystal 166
6.4 Example refractive index curves for a negative uniaxial crystal . . . 167
6.5 Polarisation states for type I phase matching 167
6.6 Refractive index ellipsoids for type I phase-matching 168
6.7 Polarisation states for type II phase matching 169
6.8 Beam walk-off in critical phase matching 170
6.9 Basic operation of a non-linear mirror 173
6.10 A non-linear mirror modelocked bounce geometry laser cavity . . . 176

6.11 Output beam parameters for the NLM KTP modelocked system . . 179
6.12 Output beam parameters for the NLM BiBO modelocked system . . 182

Publications

1. D.J. Farrell and M.J. Damzen, "Passively modelocked Nd:YVO_4 laser in a bounce amplifier geometry," (Paper **TuD7**, *EPS-QEOD Europhoton Conference on Solid-State and Fiber Coherent Light Sources*, 2006, Pisa, Italy)

2. D.J. Farrell and M.J. Damzen, "High power scaling of a passively modelocked laser oscillator in a bounce geometry," Opt. Exp., **8**, 4781 (2007)

3. M.P. Lumb, E.M. Clarke, D.J. Farrell, M.J. Damzen and R. Murray, "Tailoring Quantum Dot Saturable Absorber Mirrors for Ultrashort Pulse Generation", Mater. Res. Soc. Symp. Proc., **1076**, K0904 (2008)

4. M.P. Lumb, D.J. Farrell, E.M. Clarke, M.J. Damzen and R. Murray, "Post-growth tailoring of quantum-dot saturable absorber mirrors by chemical etching," Appl. Phys. B, **94**, 393 (2009)

5. G. Thomas, D.J. Farrell, A. Bauerle and M.J. Damzen, "Non-linear mirror modelocking of a bounce amplifier laser," (Paper **CA8.4Wed** *Conference on Lasers and Electro-Optics Europe* (E-CLEO), 2009, Munich, Germany.

In all of the work presented in these publications, the majority of the laser development was driven and performed by the author of this thesis. For items 3 and 4, the design and manufacture of the quantum-dot devices was carried out by Lumb and Clarke.

Chapter 1

Introduction

1.1 Introduction

Since the first demonstration by Theodore Maiman of optical lasing action in ruby in 1960 [1], the laser has become one of the most prevalent tools in science, technology and industry, with a vast array of applications across a huge variety of fields. Enormous research has taken place during its development, taking in gas, liquid and solid laser media, and innumerable materials. The advancement of materials science has led to lasers based on solid materials becoming one of the two dominant classes, alongside the semiconductor lasers used in communications and electronic devices. Many different output formats are possible, and nanosecond, picosecond and femtosecond pulses at varying power levels are now widely used across all science and industry.

This thesis addresses the production of ultra-short laser pulses in a diode-pumped solid-state laser. Therefore in order to place the results and achievements presented in this thesis in context, this chapter will give a brief overview of the importance of both solid-state lasers and pulsed sources. This will include a brief outline of the developmental history of the solid-state laser, alongside common pumping mechanisms and the two broad categories of laser amplifier configurations. The bounce geometry will be introduced as a special case of one of these

categories, and the basis of all the work in this thesis. The importance of pulsed sources will be discussed and the two methods of pulse production described, thus leading into an explanation of the motivation for the work presented here.

1.2 Diode-pumped solid-state lasers

Solid-state lasers are so-called because they typically consist of a dielectric host material, in crystalline or glass form, that is doped with a certain percentage of an active ion or 'impurity'. The host crystal provides the overall thermo-mechanical and thermo-optical properties of the laser and the dopant ion the optical and spectroscopic properties. Host crystals are usually oxides, such as Al_2O_3 (also known as sapphire), or fluorides such as $YLiF_4$ (abbreviated to YLF), although oxides are generally harder with better mechanical and thermo-mechanical properties. Suitable combinations of oxides can be formed to produce synthetic garnets, and yttrium aluminium garnet, $Y_3Al_5O_{12}$ (abbreviated to YAG), has been the solid-state material of choice for many years. Vanadate materials such as YVO_4 and $GdVO_4$ are oxides which are becoming increasingly popular as a replacement for YAG, as they result in improved optical and spectroscopic qualities, despite generally poorer thermo-mechanical properties.

The most common active ions used in these host crystals are generally transition elements, in particular rare earth or transition metal ions. The Al^{3+} site can accommodate transition metal ions, while the Y^{3+} can be used for rare earth ions which are too large to fit into the Al^{3+} site. Compared to crystals, many glasses are easier and cheaper to fabricate in large dimensions and the amplification bandwidth also tends to be larger due to the amorphous nature of the glass, leading to large inhomogenous broadening. The disadvantage of glass hosts is that the thermal conductivity is much lower, leading to poorer thermo-mechanical and thermo-optical properties and the emission cross-sections also tend to be lower, increasing the threshold pump power.

Solid-state lasers are currently the dominant class of lasers for research, industrial, medical and military applications. This can be traced through the historical development of the ruby laser. The output of the first ruby lasers consisted of a

series of irregular spikes over the period of the pump pulse. The first continuous wave (CW) laser was a helium-neon gas laser developed by Javan in 1961 [2], but a year later, CW action in ruby was demonstrated [3]. In 1961, the technique of Q-switching was proposed, a method to concentrate all the output energy of a laser into a single short pulse [4], and the first demonstration was performed in 1962 [5]. After this, there was considerable research into Q-switching of ruby [6, 7] and it was found that a Q-switched ruby laser was ideal for range-finding by measuring the time of flight of a laser pulse reflected from a target. This was the one of the first commercial and military applications of a solid-state laser.

After about ten years of extensive research, the ruby laser was replaced by the neodymium-doped YAG laser (written as Nd:YAG), as system efficiency increased by a factor of about ten. CW lasing in Nd:YAG was first demonstrated in 1964 [8] and the first diode-pumped Nd:YAG laser was demonstrated in 1968 [9]. After the first demonstration of laser action of neodymium in a barium crown glass in 1961 [10], the potential of Nd:glass lasers were realised in delivering pulses of multi-kJ energy in nanosecond pulses. The idea of heating matter to thermo-nuclear temperatures using the incredibly high energy densities available from pulses of this kind, opened up huge world-wide experiments in laser fusion research and high energy plasma physics. The Nd:glass lasers were the only type of laser that could produce the extremely high pulse energies required for this research.

Continuously pumped, repetitively Q-switched Nd:YAG lasers with high peak power output were the first solid-state lasers to find application in the commercial mass-production market, mainly in the semiconductor industry. Up to this point, solid-state lasers could generate very high peak powers but average power or CW outputs were limited to a few tens of watts. By the end of the 1960s, CW Nd:YAG laser systems with multi-hundred watt output powers had been demonstrated. The dominance of the solid-state laser was established in the late 1970s and into the 1980s, as a number of tunable solid-state materials were developed, namely alexandrite, titanium-doped sapphire and chromium-doped fluoride. Lasers utilising these solid-state materials replaced the less efficient and toxic dye lasers which had been the systems of choice for tunable and short pulse operation for over a decade or so.

The flexibility and widespread use of solid state lasers is summarised in four main reasons: (a) the size and shape of the laser medium can be chosen to achieve a particular performance, (b) various laser media can be selected with different gain, energy storage and wavelength properties, (c) output energy and power can be scaled with additional amplifiers, and (d) a large number of passive and active components are available to shape the spectral, temporal and spatial profile of the output beam.

1.2.1 Pumping of solid-state media

Pump sources for solid-state gain medium should ideally supply the maximum possible energy in the spectral region which excites fluorescence in the laser medium, and produce minimal emissions outside of the useful absorption bands. There are generally three different classes of pump sources in use today for solid-state lasers: flashlamps, arc lamps and laser diodes.

1.2.1.1 Flashlamps and arc lamps

Flashlamps used for pulsed laser pumping are long arc devices designed so that the plasma completely fills the tube. A flashlamp consists of a linear quartz tube, two electrodes which are sealed into the envelope and a gas fill. Xenon has the highest overall conversion efficiency for a flashlamp gas, i.e. for a given electrical input power, xenon generates the highest optical output power, and so is used in most cases. However the emission lines from krypton are much better suited to the absorption bands of Nd:YAG. Typically, the radiation efficiency (the ratio of optical output power to electrical input power) of a flashlamp is ~40-60 % but since the output consists of a large continuum component and several discrete line components, the actual useful pumping efficiency to the absorption bands in the active medium is much lower, perhaps a few percent.

The design of arc lamps for CW laser pumping is similar to linear flashlamps. Arc lamps are typically filled with an inert gas and their optical output has many lines in the near-infrared. Similar to flashlamps, krypton and xenon are the most common gas fills, although krypton has a higher conversion efficiency. Krypton is

also used for pumping Nd:YAG due to the strong absorption of the spectral lines occurring at 760 nm and 811 nm, while the xenon lines do not coincide with many of the pump bands.

1.2.1.2 Laser diodes

The performance of diode lasers has steadily increased, as new laser structures and new material growth and processing have been developed, so that now they are by far the most common form of pump source. The first diodes capable of CW operation at room temperature were produced in the 1970s, and as the technology in the manufacture of diode lasers became more sophisticated, devices with longer lifetimes, lower threshold currents and higher output powers were developed. The main advantage of diode pumping compared to flashlamp pumping is that the spectral output of the diode can be closely controlled to match the absorption of the solid-state medium. This leads to a large increase in system efficiency and a consequent reduction of the thermal load in the solid-state material [11]. In fact, the radiation efficiency of a diode laser is ~35-50 % and so is similar to a flashlamp, but since a large fraction of the radiation can be tuned to match a material's absorption band, the overall system efficiency is much higher.

As well as the large increase in system efficiency, diode-pumped solid-state lasers are generally more reliable and compact compared to flashlamp-pumped systems. Diode pumping has allowed much greater flexibility in the design of solid-state lasers, mainly due to the fact that the diode emission can be re-shaped and adapted to suit the form of the laser cavity, or vice versa. Today, a number of new laser materials, such as Nd:YVO_4 [12], Yb:YAG [13, 14] and Tm:YAG [15, 16] have only reached prominence due to pumping with diode lasers.

For high power, multi-watt pumping applications, a number of separate semiconductor emitters are used in a linear array to form a diode bar. A typical diode bar can consist of 10 to 50 separate emitters, each of width 100-200 μm. The overall dimensions of the bar depend on the number of emitters and the emitter separation, but for a typical spacing between emitters of ~500 μm, an array may have a width ~10 mm and a height ~100 μm. Due to the dimensions of the emitter, the diode emits radiation in a cone of light with a fast and slow axis di-

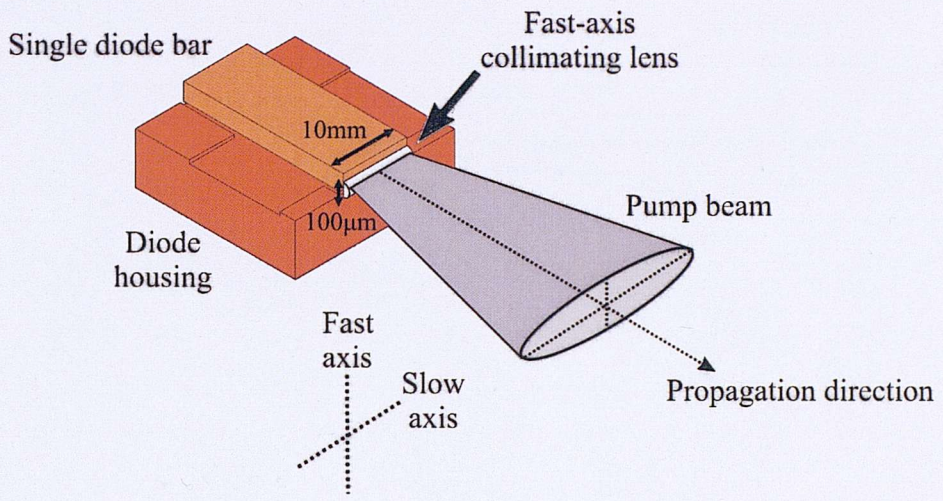


Fig 1.1. *Emission from a diode bar with fast-axis collimation.*

vergence. The diode bars used in this thesis as pumping sources for crystals have fast-axis collimating lenses to aid collection of radiation and emit a cone of light as shown in Fig 1.1. In the experiments, the diode radiation was focused further with an additional cylindrical lens to form a line focus on to the laser crystal.

In experiments in this thesis, single diode bars were used with output powers up to 40 W. The most important spectral properties of a laser diode array when used for pumping solid-state lasers are the centre wavelength, spectral bandwidth, polarisation and the wavelength shift with temperature. Diodes used in experiments emitted at 808 nm (with a bandwidth typically 1.5-3 nm) to match the absorption profile of the Nd:YVO_4 used. The diode radiation was polarised parallel to the crystallographic c-axis of the crystals, enabling access to the high absorption coefficient of approximately 30 cm^{-1} for 1.1 at. % Nd:YVO_4. To remove excess heat caused by the electrical current and ensure that the emission wavelength of the diodes was maintained at 808 nm, the diodes were mounted on a copper heatsink connected to a temperature controlled flow of water.

1.2.2 Diode pumping geometries

There are several pumping configurations for diode-pumped solid-state lasers, falling under the main categories of end-pumped and side-pumped schemes. In the end-pumped configuration, the radiation from a diode laser is focused to a

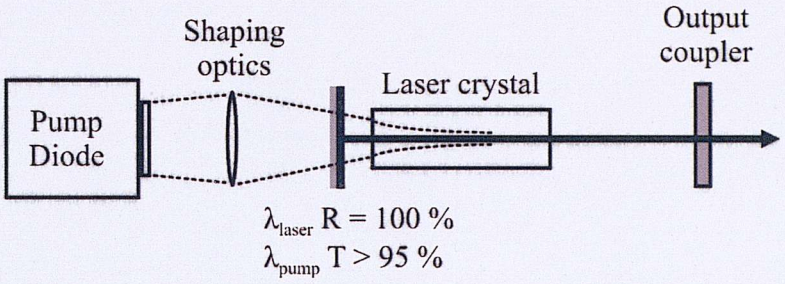


Fig 1.2. *A basic end-pumped laser scheme. The pump and laser radiation are colinear, with the back mirror having a high reflectivity for the laser wavelength and a high transmission for the pump radiation.*

small spot on the end of a laser rod. With a suitable choice of focusing optics, the diode pump radiation can be adjusted to coincide with the diameter of the TEM_{00} resonator mode. A simple end-pumped design is shown in Fig 1.2. The back mirror is highly reflecting for the laser wavelength, λ_{laser} (R = 100 %), and has a high transmission for the pump wavelength, λ_{pump} (T > 95 %). Using this longitudinal pumping scheme, efficient coupling is possible between the pump volume and the TEM_{00} mode volume, as the laser mode passes through the entirety of the inversion region. A variation of the end-pumped system is to use a gain medium with an end face that is anti-reflection coated for the pump wavelength and highly reflective for the laser wavelength, thus reducing complexity by eliminating the need for a separate back mirror.

The side-pumped scheme describes a pumping process which is orthogonal to the direction of laser radiation, shown in Fig 1.3. The first diode-pumped solid-state laser, in fact, used a side-pumping geometry [9]. In general, the side-pumped pumping scheme is simpler as there is no need for optics which must simultaneously transmit the pump radiation and reflect the laser radiation. However, the side-pumped configuration can lead to non-uniformity of gain and difficulty of overlap with the symmetry of the TEM_{00} mode. There are several variations on the side-pumped scheme to reduce this asymmetry, which usually involve the use of many diode arrays pumping from opposite sides of the crystal to create a uniform pumped region [17–19].

The end-pump design has generally been shown to provide the best conversion

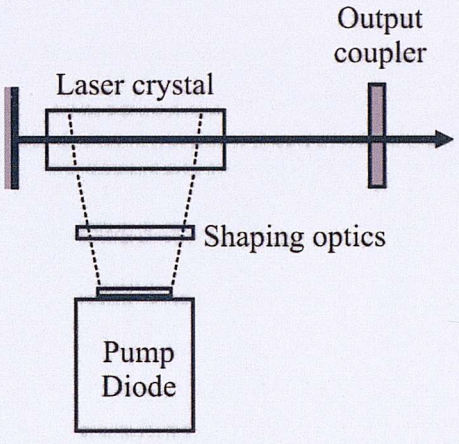


Fig 1.3. *A basic side-pumped laser scheme where the pump and laser radiation are orthogonal. The back mirror just has a high reflectivity for the laser wavelength.*

efficiency and high quality TEM_{00} operation for low and medium power lasers [20–22]. In end-pumped lasers there is difficulty in diode re-shaping and coupling to the TEM_{00} laser mode and so complex and expensive coupling optics are sometimes required with careful alignment. Higher powers are hard to achieve for end pumping due to strong thermal effects and possible crystal fracture as the pumped region is relatively small. However there is current research interest in thin-disk lasers which pump and cool a large surface area to minimise thermal effects and deliver large amounts of pump radiation [23, 24]. For the highest power laser outputs, multi-diode bar designs are commonly used in the side-pump configuration [17–19], as relatively larger volumes of the crystal may be pumped, and the addition of many pump diodes is easier to implement than in the end-pumped case. A major source of inefficiency in side-pumped schemes results from the fact that the absorbed pump radiation is concentrated near the surface of the crystal, whereas the laser mode is located in the interior. To overcome this disadvantage whilst still maintaining the positive aspects of side-pumped schemes, an amplifier configuration known as the bounce geometry was realised.

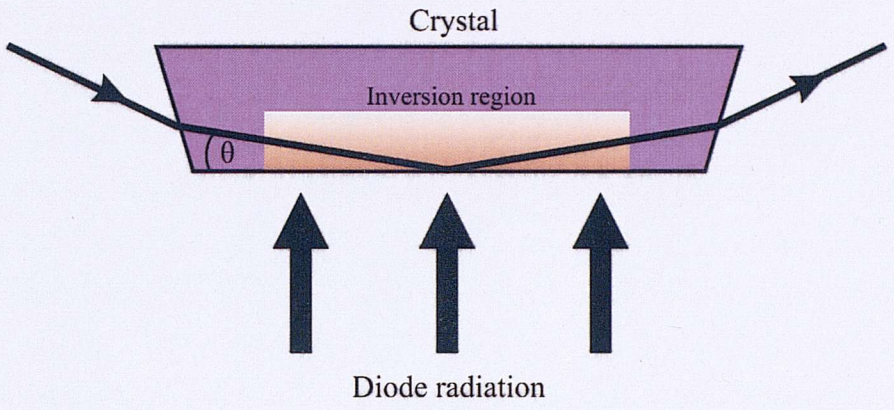


Fig 1.4. *A simple schematic of the bounce geometry amplifier showing the total internal reflection the laser mode takes off the internal pump face.*

1.2.3 The bounce geometry

First proposed by Bernard and Alcock in 1991 [25] the bounce geometry is a side-pumped laser amplifier scheme which aims to reduce the effects of gain asymmetry and thermal loading by having the laser mode take a total internal reflection (bounce) off the internal pump face (Fig 1.4). This has the multiple effects of allowing the laser mode to overlap with a very large proportion of the absorbed pump power near the surface, and performing considerable averaging of any spatial non-uniformities that may arise in the laser crystal from e.g. thermal effects and gain asymmetry. This means that high power, high efficiency, TEM_{00} operation is possible while still being able to make use of the side-pumping scheme advantages of easy power scaling and thermal management.

The bounce geometry has been used to great effect in a number of laser systems. Ultra-high efficiency has been demonstrated [26], as well as high power multi-mode and TEM_{00} operation [27]. This is linked to the very high small-signal gains that have been measured [28]. High power, high repetition rate Q-switched sources have been produced [29], as well as a number of adaptive implementations [30, 31]. The bounce geometry is a very versatile laser amplifier configuration and forms the basis of all the experimental work presented in this thesis.

1.3 Pulsed laser sources

Many laser systems begin life as CW sources and there are many applications for CW systems at various power levels and over a range of wavelengths. Pulsed laser sources now, form an indispensable part of a vast array of modern scientific tools and industrial applications, ranging from spectroscopy and biological imaging, to remote sensing and micromachining. The great benefits of pulses are the high peak powers (many kW) and the very short pulse durations that are attainable (nanosecond and below), which cannot be obtained from a CW signal.

In scientific applications such as time-resolved spectroscopy, laser pulses can be used to probe carrier dynamics in semiconductor materials [32]. In photochemistry studies [33], pulses initiate and analyse chemical reactions, and the demand for ultra-short pulses arises because of the need for very high temporal-resolution due to the timescale of the investigated processes being on the order of picoseconds or less. In multiphoton microscopy, a significant area of research in the field of bio-imaging, the non-linear fluorescence based technique relies on multiphoton excitation. The simplest case is that of two-photon excitation (TPE) [34], in which the simultaneous interaction of two photons with a molecule produces the equivalent excitation as one photon with twice the energy. The fluorescence of this molecule occurs at a higher photon energy and can therefore be easily distinguished and detected. To create an image, a pulsed laser is focused and scanned across a sample and the TPE fluorescence detected. Ultrashort pulses are required to achieve high peak powers, which improve the rate of fluorescence, whereas low average powers minimise damage to the sample, allowing high-resolution, three dimensional images of biological materials to be produced. Pulsed sources are also extensively used in research in plasma physics [36, 37] where the intense electric fields are used to create and explore new physical regimes, and the ultra-short pulse durations enable very high temporal resolution. There is a great deal of research activity concerning the interaction of ultra-short, high intensity laser pulses with plasmas, as well as plasma spectroscopy and even charged particle acceleration by generation of plasma waves. In particular, interactions between plasmas and short pulse lasers ($\sim$1 fs) have produced world records in electron

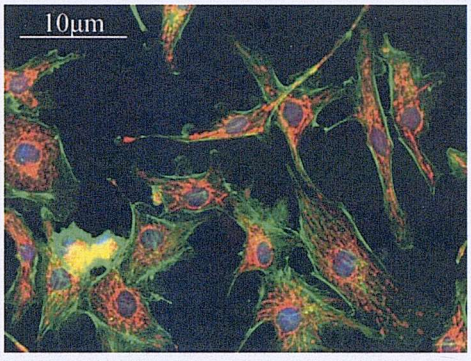


Fig 1.5. *Two-photon excitation microscopy false-colour image of cells [35].*

acceleration, harmonic generation and self-generated magnetic fields.

In industry, light detection and ranging (LIDAR) is a remote sensing technology that measures properties of scattered light to find range and/or other information of a distant target. This is similar to the concept of radar except that with LIDAR much shorter wavelengths, typically in the ultraviolet, visible, or near infrared are used so that it is possible to image a feature or object on a much smaller scale. LIDAR is highly sensitive to aerosols and cloud particles and has applications in atmospheric research, meteorology, archaeology, geology and mapping. The technique requires short pulses (typically nanoseconds) to achieve a high resolution and high pulse repetition rates to allow for fast data acquisition. Particle image velocimetry (PIV) is a technique to monitor the flow of liquids, and again, short pulses and fast repetition rates are required to illuminate the flow under observation and take a rapid series of very short exposure pictures.

The largest category of application for pulsed laser sources can be covered under the term 'micromachining'. This covers such techniques as laser marking, engraving, mask repair, stencil cutting, hole drilling and many more. Pulsed laser sources with nanosecond pulse durations and kW peak powers are used to heat, melt, and then vaporise material from small, localised regions of interest. The short timescale of the laser pulse allows for low dissipation of heat into the rest of the material, resulting in a precise, clean feature. Picosecond and femtosecond pulses take this a step further and largely negate residual heating effects by directly ablating material from a surface, although heating can still take place for high

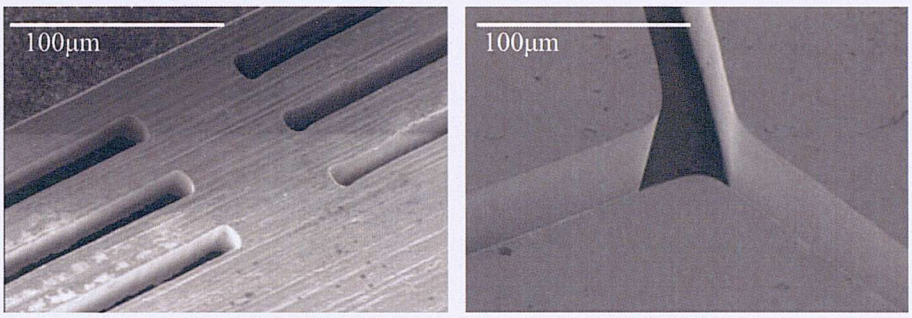


Fig 1.6. *An example of the micromachining possible with short pulse lasers. A picosecond laser generated these 15 μm wide slots in a 20 μm thick silver sheet (left) and 35 μm wide slots in a 100 μm metal sheet (right)[38].*

repetition rate pulse trains. This, coupled with high quality spatial beam profiles gives the cleanest features possible, leaving the surface unaffected apart from the intended mark.

There are thus two quite distinct regimes for pulsed laser operation, each of which requires a different method for pulse production. Many applications require the use of nanosecond pulses and these are provided by a technique known as Q-switching. The picosecond and femtosecond pulses require the use of a more advanced technique known as modelocking and generally, the complexity of the laser systems increases as the pulse duration falls. In order to draw a distinction between the two regimes, the basic mechanisms of Q-switching and modelocking will now be outlined in brief.

1.4 Q-switching

Q-switching is a widely used laser technique where the laser pumping process is allowed to build up a much larger population inversion than normal, while keeping the cavity from oscillating by removing the cavity feedback or massively increasing the cavity losses. After this large inversion has accumulated, the cavity feedback is restored using some rapid modulation. The cavity 'Q' value is switched from a low to a high value. This results in a short, intense pulse which dumps all the accumulated inversion into a single burst, typically a few tens of nanoseconds long.

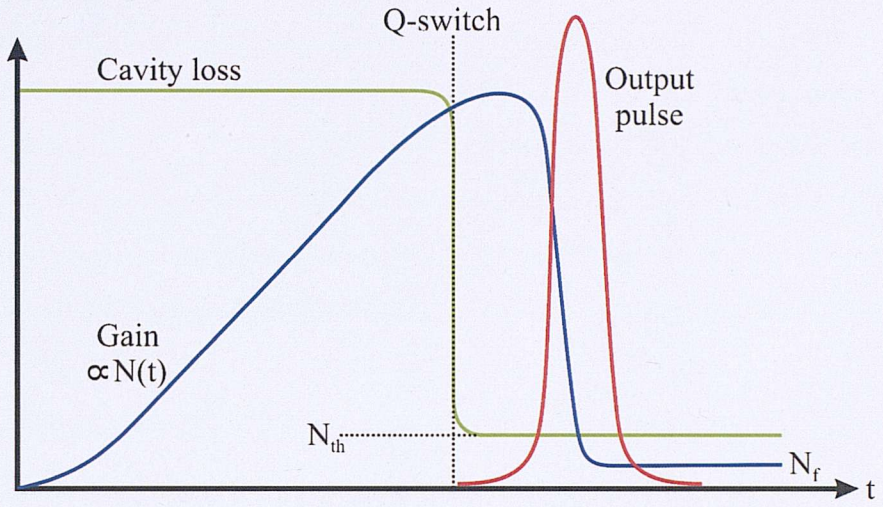


Fig 1.7. *The cavity dynamics of Q-switching. The inversion (and hence gain) in the system builds up to far above normal threshold while the Q-switch is closed and the cavity loss is high. When the Q-switch takes place, the large gain present results in a the formation of a giant pulse.*

1.4.1 Theory

The fundamental dynamics of Q-switching are shown in Fig 1.7. The cavity loss is initially set at some artificially high value (low 'Q'-value) while the inversion, and hence the gain and energy stored, are pumped up to a value much larger than would normally be present in the oscillating laser. This essentially involves blocking one of the cavity mirrors so that the pump process can build up a larger than normal inversion over some period of time.

When this large inversion has accumulated, the cavity loss is suddenly lowered to a much more normal value, the cavity 'Q'-value is switched. This results in a round trip gain that is much larger than the cavity loss, and far greater than normal. The initial spontaneous emission in the cavity then immediately starts to build up at an unusually rapid rate. This develops into a rapidly rising and intense burst, or "giant pulse", of laser oscillation. This giant pulse rapidly becomes sufficiently powerful that it begins to saturate and deplete the population inversion in a very short space of time. The oscillation signal in fact quickly drives the inversion down well below the new cavity loss level, after which the pulse dies out as fast as it grew.

The oscillation build-up interval, and particularly the output pulse duration, are generally much shorter than the pumping time during which the population inversion was created. The energy stored during this long pumping time is thus dumped during a very short pulse duration. The peak power in the Q-switched pulse can be several orders of magnitude more intense than the CW oscillation that would be created in the same laser using the same pumping rate.

1.4.2 Implementation

There are currently three main mechanisms for achieving the required Q-switching: electro-optic modulation; acousto-optic modulation; and use of a passive saturable absorber.

1.4.2.1 Electro-optic Q-switching

An electro-optic modulator in general consists of an electro-optic crystal which becomes birefringent under application of a high voltage, plus one or more polarising elements inside the cavity. One common form consists of a Pockels crystal which has a voltage applied to it to turn it into a quarter-wave plate. Radiation circulating once around the laser cavity thus has its polarisation rotated by 90° about the cavity axis, so that the circulating radiation can be coupled out by the polarising element after one round trip. Switching the cavity to the low loss condition is then achieved by suddenly turning the voltage off. Alternatively, a fixed quarter-wave plate can create the high loss condition with no voltage applied, and the Pockels cell can be switched on to cancel this birefringence. A typical implementation is shown in Fig 1.8.

Electro-optic Q-switching provides the fastest form of Q-switching (switching times $\leq$10 ns) with precise timing, good stability and repeatability, and a large hold-off ratio (i.e. large insertion loss). This approach however requires both an expensive electro-optic crystal, and a very fast-rising high voltage pulse source (several kV in a few tens of nanoseconds). Nanosecond rise-time pulses at this voltage level are hard to obtain and can produce electrical interference in nearby electrical equipment. Additionally, this method requires the use of several elements

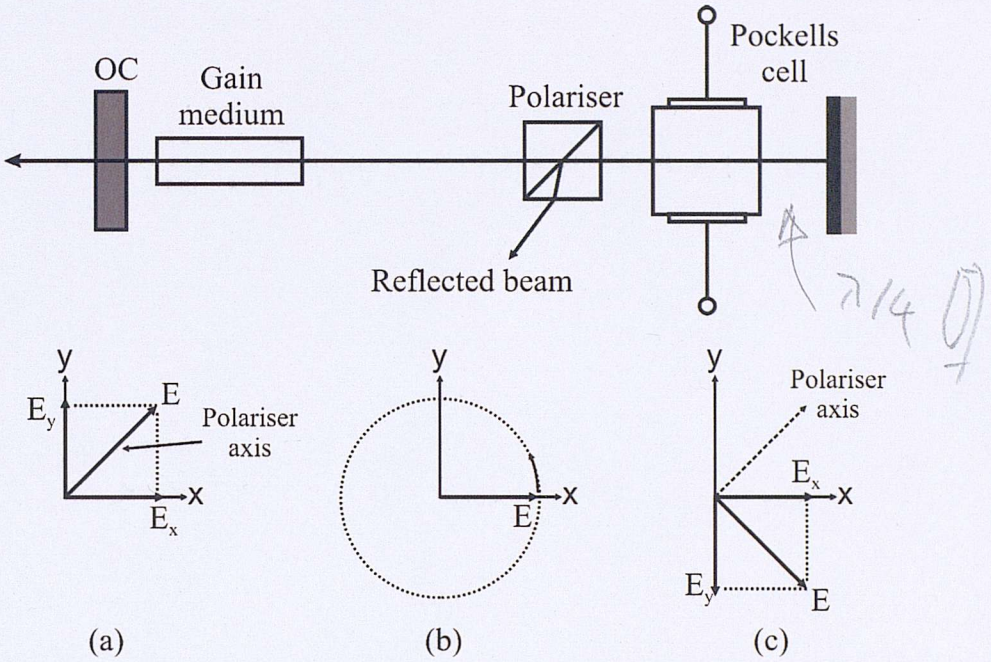


Fig 1.8. *Typical arrangement for electro-optic Q-switching using a polariser and a Pockels cell switching between $\lambda/4$ and 0 rotation. The electric field relative to the Pockels cell axis, before (a), after one pass (b) and after the second pass (c) through the cell.*

inside the laser cavity which may be both optically lossy and susceptible to damage at the high intensities inside the Q-switched cavity.

1.4.2.2 Acousto-optic Q-switching

An acousto-optic modulator consists of a block of transparent optical material in which an ultrasonic wave is launched by a piezoelectric transducer bonded to one side of the block and driven by an RF oscillator (Fig 1.9). The side of the block opposite to the transducer is cut at an angle and has an absorber for the acoustic wave placed on its surface. This suppresses the back reflection of the acoustic wave so that only a traveling acoustic wave is present. The strain induced by the ultrasonic wave results in local changes to the material refractive index, which thus acts as a phase grating with a period equal to the acoustic wavelength. Its effect is to diffract a fraction of the incident beam from the incident direction. Thus, if an acousto-optic element is inserted into a laser cavity, an additional

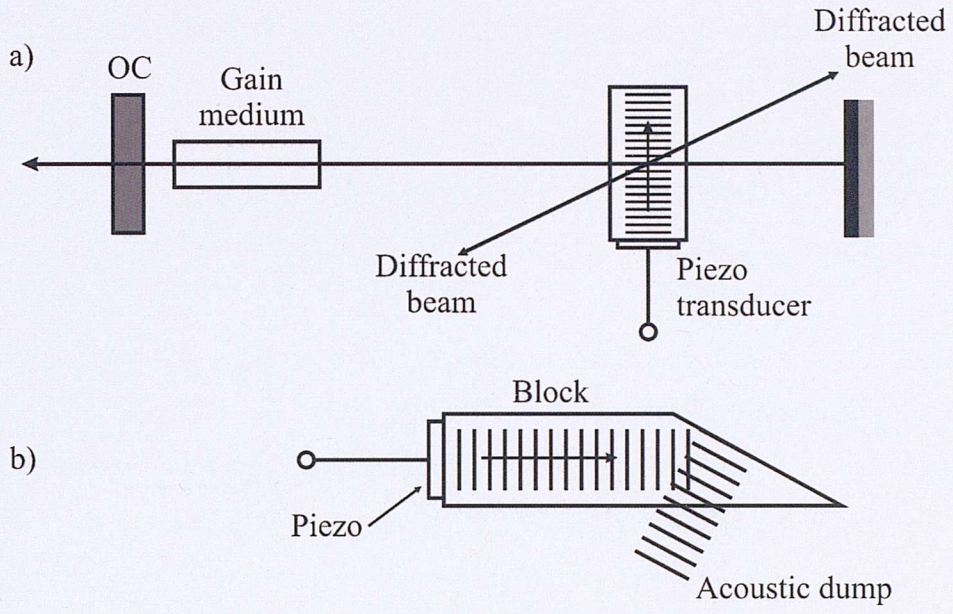


Fig 1.9. *Typical arrangement for acousto-optic Q-switching (a) using an RF driven piezo transducer bonded onto an optical block (b).*

loss is introduced while the driving voltage is applied to the transducer. If the driving voltage is high enough, this additional loss is sufficient to hold off the laser oscillation. The laser is then returned to its high-Q state by switching off the transducer voltage.

Acousto-optic modulators have the advantage of low optical insertion losses, and for repetitive Q-switching they can be readily driven at high repetition rates (tens-hundreds kHz). The loss induced by the modulator is rather limited however and the Q-switching time is quite long (principally established by the time taken for the acoustic wave to traverse the beam profile). These modulators are therefore primarily used for Q-switching of low gain, CW pumped lasers.

1.4.2.3 Passive saturable absorber Q-switching

Passive Q-switching uses some form of easily saturable absorbing medium inside the cavity. Laser inversion is built up by the pumping process until the gain inside the cavity exceeds the absorption of the medium and laser oscillation occurs. If the absorption of the medium is high, then the corresponding value of the population inversion required is also very high. When the laser intensity equals the saturation

intensity, the absorber begins to bleach and the growth rate of the laser intensity is increased. This in turn results in a more rapid bleaching of the absorber. If the saturation intensity is comparatively small, the inversion left in the laser medium is essentially the same as the very large inversion present before the bleaching of the absorber. The laser thus has a gain in excess of the losses, and a giant pulse is produced.

Passive Q-switching is generally simple, convenient, requires a minimum of extra optical elements inside the cavity, and requires no external driving electronics. It is however subject to some shot-to-shot amplitude fluctuations and timing jitter so any external apparatus must be synchronised to it, rather than vice versa with the active cases. The saturable absorbers were typically organic dyes in solution and so were subject to chemical and photochemical degradation in use. This is now far less of a problem with the advent of solid state semiconductor saturable absorbers and this type of Q-switching is very popular. Passive Q-switching also enables shorter pulses to be obtained, with pulse durations <1 ns possible, compared to typically 10's nanoseconds for active Q-switching.

1.5 Modelocking

Modelocking is another mechanism by which short laser pulses may be achieved. It differs from Q-switching in that the pulses formed are much shorter than the cavity round trip time, and pulse formation, rather than being controlled by large scale dynamical changes in the laser gain medium, is instead controlled by manipulation of the fundamental longitudinal cavity modes. Modelocking involves very many of these longitudinal modes, and the term itself arises because the pulse formation mechanism is to achieve a fixed phase relation between all of the oscillating modes i.e. to 'lock' the phases of the modes together.

A sinusoidal amplitude modulation is applied to the cavity at a frequency Ω_m which creates sidebands in the frequency domain at $\omega_0 \pm \Omega_m$ (Fig 1.10). If Ω_m is set correctly, to correspond with the longitudinal mode spacing of the laser cavity, c/2L where L is the length of the cavity, then these sidebands will injection lock adjacent modes and cause them to oscillate at the same frequency. These then

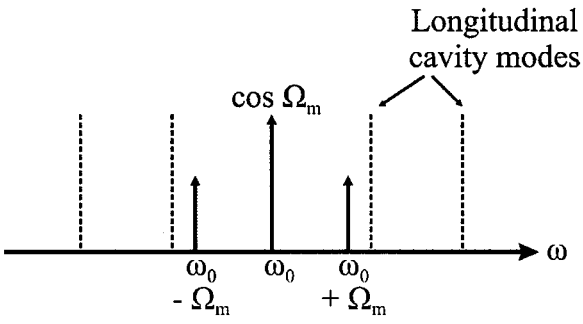


Fig 1.10. *Amplitude modulation at Ω_m creates sidebands at $\pm\Omega_m$ which coincide with the cavity mode spacing if Ω_m is chosen correctly.*

injection lock their adjacent modes and so on, until there are many thousands of modes oscillating together in phase. From Fourier analysis, the superposition of many sinusoidal waves oscillating in phase at different, evenly spaced frequencies, results in the formation of a narrow pulse whose width is inversely proportional to the total frequency bandwidth of the component sinusoids (bandwidth theorem : $\Delta\tau \sim 1/\Delta\nu$).

In modelocking schemes, the frequency bandwidth of the component sinusoids (the fundamental cavity modes which can experience gain inside the laser cavity), is usually comparable to the gain bandwidth of the laser gain medium, and for solid state systems this is typically in the range 100 GHz - 800 THz depending on the laser material used. Using the simple bandwidth theorem, this results in a potential range of pulse durations of 10 ps - 1.25 fs. In fact, pulse durations as short as 5 fs have been achieved from solid state laser systems [39]. These are several orders of magnitude shorter than can be achieved with Q-switching techniques, which potentially offers peak powers several orders of magnitude higher. In practice, this is often tempered by the fact that many modelocked systems have far higher repetition rates and so the energy per pulse is usually smaller resulting in comparable peak powers, but the much higher repetition rates can be advantageous in some applications.

There are many methods by which modelocking can be achieved in practice and several of these will be covered in detail in later chapters. In general though, modern modelocked systems rely on a passive modulation to achieve the phase-locking condition. This means that it is the propagation of a pulse inside the cavity

which helps to maintain the phase-locking, as opposed to an externally modulated electric signal as in many Q-switched systems. This results in the pulse repetition rate being very closely related to the length of the laser cavity and essentially fixed for any particular cavity design. This in contrast to externally modulated Q-switching where the repetition rate can be varied over a large range by changing the modulating signal.

Picosecond pulse sources can be relatively simple systems, comparable in complexity to many Q-switched lasers and offering similar levels of performance in terms of output power and efficiency. This complexity increases rapidly however once the pulse duration falls into the femtosecond regime. Here, the pulse durations are so short that the frequency spectrum of the signal is very large and dispersion effects in the cavity become significant. These dispersion effects can severely limit the pulse durations attainable and steps have to be taken to compensate for this, greatly increasing the design complexity of the system. With this increase in complexity comes a decrease in overall efficiency and average power output. Despite this, there are many applications that require the use of femtosecond pulses.

1.6 Motivation of thesis

As discussed above, both Q-switched nanosecond and modelocked pico- and femtosecond pulse sources are used widely in science and industry depending on the specific application. However, there is currently great interest in the development of high power picosecond sources for micromachining applications due to the mechanism by which the material is processed. As previously mentioned, when using nanosecond pulses, the machining process involves heating, melting and then vaporisation of the surface in question. Unavoidably, this can lead to undesired thermal side-effects like burr, recrystallization and micro-cracks, the consequences of which often only become apparent later in the product life.

At the other end of the scale, laser pulses in the femtosecond regime require more complex lasers that deliver less average power at a higher price, but with limited improvement in micromachining quality. The higher peak power of fem-

tosecond pulses can also complicate the beam-delivery system and is susceptible to unwanted non-linear effects.

Picosecond laser pulses offer a solid compromise where higher average power and repetition rates allow for a good balance between high throughput and improved reliability, at a fraction of the cost of competing technologies. Specifically, the machining mechanism that occurs for picosecond pulses is superior to that which occurs for nanosecond pulses. Rather than heating and vaporisation, the surface structures are formed by ablation which removes a thin layer or small volume of material and leaves no residual heat to contaminate the surface. There are currently many applications requiring this kind of processing and picosecond laser sources are being implemented across all kinds of manufacturing disciplines, including the semiconductor, photovoltaics and display industries. They are also being used to produce micro moulds on demand, precise apertures and electrode structures, microstructured surfaces for the printing industry, embossed rolls and medical implants.

Given this huge area of potential application and the demonstrated ability of the bounce geometry to produce efficient, high quality, high power sources in a Q-switched regime, it is the aim of this thesis to examine the feasibility of using the bounce geometry to produce a multi-watt picosecond laser source. There are a number of possible routes to achieving this goal and so the investigation will consider several of these with a view to determine which, if any, is the best way of realising a modelocked source whilst retaining the key advantages of the bounce geometry. In the long term, a pulsed output of 100 W, or even higher, may be the goal, and while this performance will not be reported in this thesis, the potential of the bounce geometry to achieve this, and suitable methods of doing so, will need to be considered.

1.7 Thesis outline

Chapter 2 continues the thesis by giving a detailed account of modelocking. It describes the concept behind the production of short pulses and gives two complementary pictures of how the process arises, in the frequency domain and in

the time domain. It then describes how modelocking can be achieved in practice, drawing a distinction between the two main categorisations of active and passive modelocking. Some of the most common passive modelocking mechanisms are outlined in brief, including the methods of Semiconductor Saturable Absorber Mirror (SESAM) and Non-linear Mirror (NLM) which form the basis of later experimental chapters.

Chapter 3 is dedicated to the bounce geometry laser amplifier. The origins of thermo-optic effects in solid state media are explained, before a detailed account is given of the functional principles and the pumping, cooling and crystal geometries of the bounce amplifier. An experimental bounce laser is presented that has a 57% optical-optical conversion efficiency in a 23 W beam, but with a multi-mode spatial output. The cavity stability theory of Magni is then introduced to explain how an experimental bounce laser with TEM_{00} output is realised.

Chapter 4 looks at the extension of a simple bounce laser to one which produces a modelocked output by use of a SESAM device. Starting with a detailed description of how the SESAM modelocking mechanism works, the evolution of the laser cavity is discussed in terms of the available design parameters. This culminates in the description of a modelocked bounce geometry laser oscillator which produces a 81 MHz train of 12 ps pulses and an average output power of 6.6 W. A master oscillator power amplifier system is demonstrated which uses a bounce geometry module as its amplifier stage to amplify a modelocked bounce oscillator to the 60 W power level [40, 41].

Chapter 5 investigates the use of quantum dot SESAM devices to produce a modelocked output. The first part of the chapter introduces quantum dots and what they are; what the advantages of using them are; how they are grown; and how their properties can be altered post-growth to tailor their operation for specific laser systems. Two different sets of quantum dot devices are then tested in a bounce laser. A minimum pulse duration of 84 ps is achieved and it is shown that the pulse duration varies with the reflectivity of the SESAM structure [42, 43].

Chapter 6 investigates the use of the NLM modelocking mechanism. A brief introduction to some important non-linear optics starts the chapter, before this is used to explain the principle of operation of the NLM. A modelocked source is

then constructed using this technique and two different non-linear crystals. The first produces the highest output power of 11.3 W ever seen from this technique. Changing the non-linear crystal to eliminate the dispersion problems found with the first, results in a second cavity that produces the shortest ever pulses from this technique of 6 ps [44].

Chapter 7 is the final chapter and presents a summary of the main results and conclusions in this thesis. In addition, possibilities and suggestions for future work to build on the main achievements presented in this thesis are discussed.

Chapter 2

Modelocked laser sources

2.1 Introduction

This chapter will now expand on the brief introduction to modelocked sources and look in slightly more detail at the methods of modelocking. It will first describe how the modelocking arises from a frequency domain perspective by considering the addition of many longitudinal modes inside the cavity. Then it will look at the equivalent time domain description which considers the action of a fast shutter inside the laser cavity, which is often more instructive when describing the function of real-life modelocking systems. Following this, active and passive modelocking are identified as the two main categories by which the cavity modulation may be obtained, using an external signal, or some non-linear process affected by the passage of a laser pulse. Some of the theoretical detail of pulse formation in active systems is covered and the three main types of active modelocking are looked at: frequency modulation; amplitude modulation; and synchronous pumping. The distinction is then made with passive modelocking, and four main implementations are discussed: additive pulse modelocking; Kerr lens modelocking; non-linear mirror modelocking; and saturable-absorber modelocking, leaving a more detailed analysis of passive modelocking pulse formation for a later chapter. The chapter finishes with an outline of the ultra-short pulse duration measurement technique

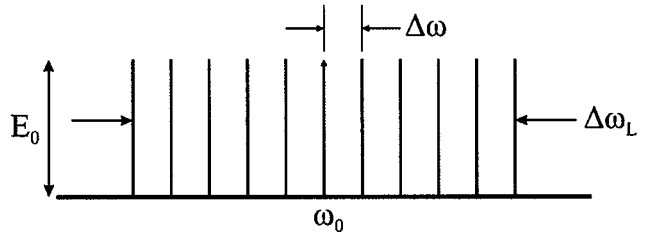


Fig 2.1. *Uniform mode amplitude distribution in a modelocked laser.*

of autocorrelation, together with a 'spinning mirror' design that was implemented in this thesis.

2.2 Frequency domain description

Looking first in the frequency domain, consider the case of $2n+1$ longitudinal modes oscillating with the same amplitude E_0 (Fig 2.1), and assume that there is a fixed phase relation between modes, according to:

$$\phi_l - \phi_{l-1} = \Delta\phi \tag{2.1}$$

where ϕ is a constant. The total electric field of the EM wave at any point can thus be written as:

$$E(t) = \sum_{l=-n}^{+n} E_0 \exp\{i[(\omega_0 + l\Delta\omega)t + l\Delta\phi]\} \tag{2.2}$$

where ω_0 is the central frequency of the spectrum considered and $\Delta\omega$ is the mode frequency spacing, which in a standing wave laser cavity is given by $\Delta\omega = 2\pi c/2L$ where L is the optical length of the cavity. This can then be expressed in terms of a carrier wave modulated by some envelope function, so that the total electric field can be expressed as:

$$E(t) = A(t)\exp(i\omega_0 t) \tag{2.3}$$

where,

$$A(t) = \sum_{l=-n}^{+n} E_l \exp[il(\Delta\omega t + \phi)] \tag{2.4}$$

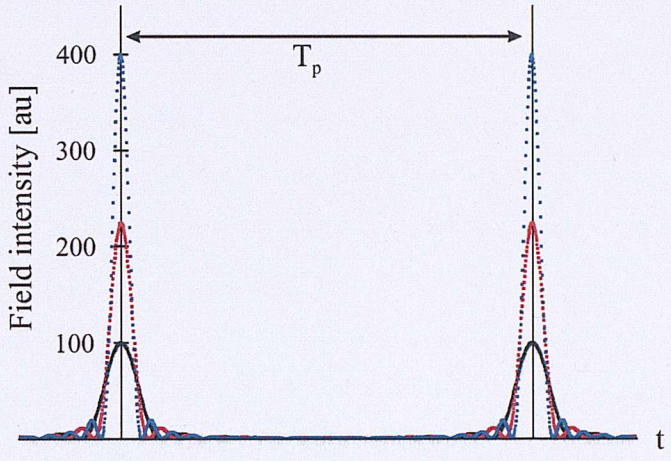


Fig 2.2. *A plot of Eqn(2.6) for different numbers of total cavity modes. Black - 10 oscillating modes; Red - 15 oscillating modes; Blue - 20 oscillating modes. The pulse duration decreases, and the peak intensity increases as the number of modes increases, but the pulse spacing remains constant.*

$A(t)$ now describes the amplitude of the electric field, and thus the form of the pulses created in the cavity. To look at the time behaviour of $A(t)$ we perform a simple rescaling of the time paramter so that $\Delta\omega t' = \Delta\omega t + \phi$ so that $A(t)$ may be re-written as:

$$A(t') = \sum_{l=-n}^{+n} E_0 \exp il(\Delta\omega t') \tag{2.5}$$

This sum can be identified as a geometric progression with a ratio of $\exp i(\Delta\omega t')$ which can be summed over $2n+1$ terms to give:

$$A(t') = E_0 \frac{\sin[(2n+1)\Delta\omega t'/2]}{\sin(\Delta\omega t'/2)} \tag{2.6}$$

The physical significance of Eqn(2.6) can be seen in Fig 2.2 which shows a plot of $A^2(t')$ (proportional to the intensity of the EM field), for three cases with different numbers of total oscillating cavity modes. Even with these small numbers of modes a well defined train of pulses is produced and it is clearly seen that the pulse duration decreases as the number of modes increases, and that the peak intensity of the pulse increases as the square of the number of modes. The pulse separation remains constant for all numbers of modes. The oscillating modes are

seen to interfere due to the phase relation Eqn(2.1) such that the resultant is a train of evenly spaced, intense pulses. Making the approximation $\sin\alpha \simeq \alpha$, for small values of α, to maintain a rational fraction in Eqn(2.6) at $t' = 0$, it can be seen that the peak intensity of the pulse train $A^2 = (2n+1)^2 E_0^2$. So for a modelocked laser source, where modes oscillate in phase, the peak intensity is proportional to the *square* of the total number of oscillating modes, $(2n+1)$. For a non-modelocked laser with random phases between modes, the average intensity is simply the sum of the intensities of all the modes, and is thus proportional to the number of oscillating modes. The ratio of the intensities in the two cases is then the same as the total number of modes, $(2n+1)$, which in solid state lasers can be $10^2 - 10^4$. The modelocking process is therefore seen to not only produce a pulsed output, but also high peak intensities, and as will be seen shortly, very short pulse durations.

The next pulse occurs when the denominator in Eqn(2.6) again goes to zero, which happens at a time such that $(\Delta\omega t'/2) = \pi$, which gives the result that successive pulses are separated by a time:

$$T_p = \frac{2\pi}{\Delta\omega} = \frac{1}{\Delta\nu} \tag{2.7}$$

where $\Delta\nu = c/2L$ is the frequency spacing between two adjacent cavity modes. A simple approximation for the pulse duration, τ_p (FWHM), can be obtained by considering when the field amplitude function $A^2(t')$ first equals zero for $t' > 0$. As it can be seen from Fig 2.2, this position is approximately equal to the FWHM of the pulse. This happens when the numerator in Eqn(2.6) goes to zero, which occurs at a time t'_0 such that:

$$\frac{(2n+1)\Delta\omega t'_0}{2} = \pi \tag{2.8}$$

$$\Rightarrow \tau_p \cong \frac{2\pi}{(2n+1)\Delta\omega} = \frac{1}{\Delta\nu_L} \tag{2.9}$$

where $\Delta\nu_L$ is the total bandwidth of the oscillating modes. This then demonstrates that for many solid state lasers, where the total oscillating bandwidth is typically hundreds of GHz, it is possible to obtain pulses which are less than 10 ps in duration; much shorter than the cavity round trip time, and much shorter than from

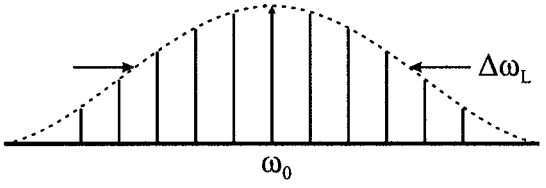


Fig 2.3. *Gaussian mode amplitude distribution in a modelocked laser over a bandwidth (FWHM) $\Delta\omega_L$*

Q-switched systems. In fact, there are some laser materials, notably Ti:Sapphire and Cr:LiSAF, that have such large gain bandwidths (up to ~100 THz) due to homogeneous broadening in the crystal host material, that it is possible to produce pulses with durations well into the femtosecond regime [45–48]. For pulses this short, the situation is far more complicated than will be considered here as the effects of dispersion within the laser cavity begin to play a very important role in pulse formation and propagation. Careful control and compensation of dispersion, including terms up to fourth order, is required so that pulses with such a large spectral bandwidth are not broadened significantly on passage through the amplifier, and full advantage can be taken of the available gain bandwidth. Using these sophisticated dispersion control and compensation mechanisms, the shortest reported pulse duration produced from a solid state laser is 2.8 fs, achieved using a Ti:Sapphire laser [39].

For all the experimental work discussed in this thesis, the bandwidth of the laser gain medium is ~300 GHz, which puts a lower limit on the possible pulse duration of ~3 ps and under normal circumstances the passage through the amplifier of a pulse this short would result in a spreading of <5 fs. The effects of dispersion are thus negligible in the work presented and so no further detail is given on the role of cavity dispersion in modelocked laser systems.

This simple frequency domain treatment has also only considered the unrealistic scenario of many, equal-amplitude spectral modes. In reality, the oscillating modes will be components of the gain bandwidth of the laser medium, and this is usually taken to have a Gaussian form. This more realistic form causes a slight change in the relationship between the spectral bandwidth of the pulse and its duration. Assuming a Gaussian amplitude envelope of the frequency components

as pictured in Fig 2.3 with a FWHM of $\Delta\omega_L$, the amplitude E_l of the lth mode can be written as:

$$E_l^2 = E_0^2 \exp[-(\frac{2l\Delta\omega}{\Delta\omega_L})^2 \ln 2] \tag{2.10}$$

If a fixed phase relation as in Eqn(2.1) is then assumed, $E(t)$ can be expressed as in Eqn(2.3), where the field amplitude $A(t')$, in the time reference t' as before, is given similarly by:

$$A(t') = \sum_{l=-n}^{n} E_l \exp i(l\Delta\omega t') \tag{2.11}$$

Approximating this sum as an integral, the field amplitude $A(t')$ is actually proportional to the Fourier transform of the spectral amplitude E_l, from where it is possible to show that the intensity of the resulting pulse, $A^2(t')$ is a Gaussian function of time.

$$A^2(t') \propto \exp[-(2t/\tau_p)^2 \ln 2] \tag{2.12}$$

where τ_p, the FWHM of the pulse intensity, is given by:

$$\tau_p = \frac{2\ln 2}{\pi\Delta\nu_L} = \frac{0.441}{\Delta\nu_L} \tag{2.13}$$

This is now a more exact version of Eqn(2.9) for a pulse with a Gaussian spectral lineshape of width $\Delta\nu_L$, and represents the minimum possible pulse duration if the phase relation Eqn(2.1) holds true. In general, if Eqn(2.1) is true for the full bandwidth of the system, then the pulse shape, given by the field amplitude $A(t)$, is simply the Fourier transform of the spectral amplitude (which need not be Gaussian, but could equally be e.g. Lorentzian), and the pulse is said to be *transform-limited*. Of course, this relation is only true for the linear phase relationship in Eqn(2.1), which need not be true in general, and a different phasing condition can lead to a far from transform-limited pulse. As a very brief example, if, instead of the condition in Eqn(2.1), which can also be written as $\phi_l = l\phi$, the phasing condition is:

$$\phi_l = l\psi_1 + l^2\psi_2 \tag{2.14}$$

where ψ_1 and ψ_2 are simply constants, it can be shown that the pulse amplitude is still of a Gaussian form, but the spectral bandwidth and pulse duration are now related by:

$$\Delta\nu_L \propto \frac{0.441}{\tau_p}[1 + (\psi_2\tau_p^2)^2]^{1/2} \tag{2.15}$$

Thus, for values of ψ_2 such that $\psi_2\tau_p^2 \gg 1$ the product $\Delta\tau_p\Delta\nu_L$ can be much greater than 1 and the pulse far from transform-limited.

2.3 Time domain description

The modelocking process is now considered from the *time-domain* perspective by referring back to Eqn(2.7), the equation for the pulse separation, T_p. From the sum of many in-phase modes, this was shown to be $1/\Delta\nu$, where the frequency separation of the cavity modes $\Delta\nu = c/2L$. Thus, $T_p = 2L/c$, which is simply the round trip time of a cavity of length L, and the spatial extent of a pulse within the cavity is $c\tau_p$, which for a 10 ps pulse is 3 mm, much shorter than a typical cavity length of ~1 m. The oscillating behaviour in this case can then be considered to be a single ultra-short pulse which propagates back and forth inside the laser cavity, thus producing an output consisting of a train of pulses separated by the cavity round trip time.

The modelocking condition can now be seen to be achieved by placing a fast shutter at one end of the cavity, timed to open at the arrival of the pulse on each trip, and remain open only for the duration of the pulse. Consider a non-modelocked cavity whose oscillating modes do not have any fixed phase relationship between themselves, the longitudinal spatial amplitude profile of the cavity electric field will be a periodic, noisy function. If the shutter were then to open to coincide with the arrival of a particularly intense noise spike, remain open only for the duration of the spike, and then be timed such that subsequent shutter openings are at the round trip time of the cavity, $T = 2L/c$, the noise would be attenuated and only the intense pulse would be able to transit the cavity and experience gain. This gives rise to the modelocking condition, and is the situation illustrated in Fig 2.4a, known as *fundamental modelocking*. This term implies that

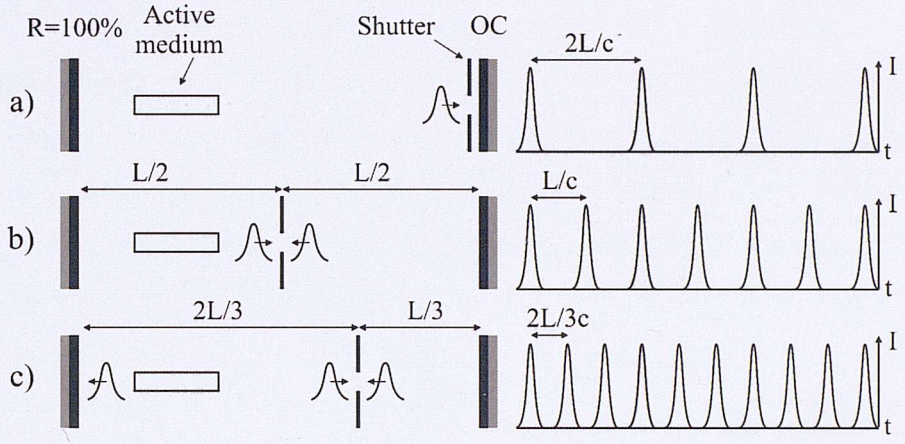


Fig 2.4. *Cavity shutter positions for (a)fundamental, (b)second, and (c) third harmonic modelocking, showing the resultant pulse trains and their spacing.*

there are other kinds of modelocking, and this is indeed the case. Considering a similar situation to the one just discussed, but with the shutter placed at the halfway point of the cavity and opened with a period $T = L/c$, two ultra-short pulses can traverse the cavity and the situation in Fig 2.4b is reached. Here, the two pulses are separated such that they cross each other at the position of the shutter, when it is open. Similarly, if the shutter is placed a distance $L/3$ from one of the end mirrors, and opened with period $T = 2L/3c$, the situation in Fig 2.4c arises, and three ultra-short pulses propagate inside the cavity such that two of them always cross at the shutter position, when the shutter is open. In these two cases, it can be seen that the repetition rate of the output train of pulses is $2\Delta\nu$ and $3\Delta\nu$ respectively, where $\Delta\nu$ is the repetition rate of the fundamental cavity. For this reason, the situations in Fig 2.4(b-c) are referred to as *harmonic modelocking*. Since the phase relation Eqn(2.1) was shown to result in the situation shown in Fig 2.4a, the cases in Fig 2.4(b-c) must correspond to a different phase locking condition, so for instance, second order harmonic modelocking, as in Fig 2.4b, is given by the condition $\phi_{l+1} - \phi_l = \phi_l - \phi_{l-1} + \pi$.

In brief conclusion then, it has just been shown that by engineering a situation where very many longitudinal modes in a laser cavity can be made to oscillate in phase, such that the relationship between their phases is of the form $\phi_l = l\phi$, then

the resultant field takes the form of a train of pulses with a high peak intensity and short duration, which is then the basis for the process known as *modelocking*. It was shown that the peak intensity of the pulses was proportional to the square of the number of oscillating modes, which is much higher than for an equivalent number of modes with random phases, and that the duration of the pulses was inversely proportional to the total bandwidth of the modes, which results in the potential for picosecond pulses to be produced from many solid state lasers with hundreds of GHz bandwidth (and even femtosecond pulses in certain special media). It was then shown, in a more general sense, that when the stated phase relationship holds, the intensity profile of the pulses is the Fourier transform of the spectral amplitude profile, which results in Gaussian shaped pulses for a typical Gaussian laser spectral bandwidth. Under this condition, it was shown finally that the minimum achievable (transform-limited), pulse duration, τ_p, from a spectrum of width $\Delta\nu_L$ was $0.441/\Delta\nu_L$.

The equivalent description in the time domain was then considered at and it was seen how the modelocking condition is achieved by having a fast shutter at one end of the cavity that is timed to open with a period equal to the round trip time of the cavity. It was also shown that this approach allows an easy understanding of so called *harmonic modelocking*, where the pulse repetition rate is an integer multiple of the fundamental cavity repetition rate, controlled by suitable positioning and timing of the shutter within the cavity.

2.4 Methods for modelocking

Like Q-switching, modelocking methods can be divided into two categories depending on the source of the cavity modulation: 1) Active modelocking, where the modulation of the modelocking element is driven by an external signal; 2) Passive modelocking, where self-amplitude modulation is induced in the modelocking element by the action of a propagating pulse on some non-linear optical property of a suitable material, typically a saturable absorption or non-linear refractive index change.

2.4.1 Active Modelocking

Within the category of active modelocking, there are two main types: 1) Modelocking induced by an amplitude modulation (AM modelocking); 2) Modelocking induced by a phase modulation (FM modelocking). There is a third method known as synchronous pumping, but this is not widely used as it typically requires the use of a modelocked source as a pump and is generally only useful for dye lasers, so will not be discussed further here.

To describe AM modelocking, consider the action of a modulator in the cavity that introduces a time-varying loss at a frequency Ω_m, and with a modulation depth of δ, so that the electric field of each of the cavity modes, $E_l(t)$, will experience an amplitude modulation and be given by:

$$E_l(t) = E_0\{1 - \frac{\delta}{2}[1 - \cos(\Omega_m t)]\}\cos(\omega_l t + \phi_l) \tag{2.16}$$

where ω_l is the mode frequency, and ϕ_l is its phase. This gives an electric field whose amplitude is modulated between E_0 and $E_0(1-\delta)$. The term containing the product of the two cosines, $(E_0\delta/2)\cos\Omega_m t \times \cos(\omega_l t + \phi_l)$ may be re-written as:

$$(\frac{E_0\delta}{4}) \times \{\cos[(\omega_l + \Omega_m)t + \phi_l] + \cos[(\omega_l - \Omega_m)t + \phi_l]\} \tag{2.17}$$

which shows that $E_l(t)$ contains two terms oscillating at $\omega_l \pm \Omega_m$. If Ω_m is now selected such that it is equal to the longitudinal cavity mode spacing, these sidebands of E_l will contribute to the field equations for E_{l-1} and E_{l+1}. This results in each cavity mode being coupled to its two adjacent modes, thus acquiring the phase of these modes. In this manner, it is possible to propagate a fixed phase relation between many oscillating modes so that a condition such as that in Eqn(2.1) can be achieved, and modelocking can occur.

The details of AM modelocking are more easily understood in the time domain, as illustrated in Fig 2.5. Here it is seen that if the modulation frequency of the cavity losses, Ω_m, is matched to the cavity round trip time, the steady state condition results in pulses passing through the modulator when it is at its minimum-loss value. If a pulse is assumed to pass through the modulator at this minimum value, it will return to the modulator when it is again at its minimum

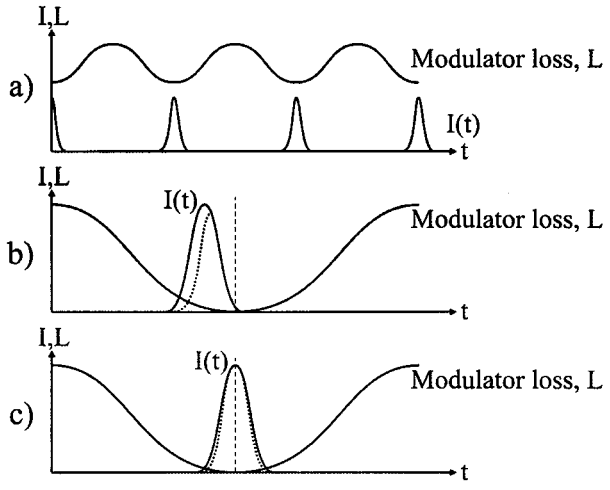


Fig 2.5. *Time domain picture of active modelocking illustrating how the minimum modulator loss coincides with the arrival of the pulse (a). The dotted lines represent the attenuated pulse after passage through the modulator. For slightly incorrect timing (b), the pulse is effectively shifted towards the minimum loss. The steady state situation (c) shortens the pulse on each passage.*

loss. If however, a pulse arrives at the modulator slightly before its minimum value, then as Fig 2.5b shows, the leading edge of the pulse will be attenuated more than the rest of the pulse, and the shape of the peak will be as indicated by the dashed line. This effectively retards the pulse and so the next time it arrives at the modulator it will be closer to the time of lowest loss, and the steady state situation is gradually approached. In the steady state situation, Fig 2.5c shows that the pulse is effectively shortened on each pass through the modulator due the greater attenuation of the leading and trailing edges of the pulse by the time varying loss, compared to the peak. If this were the only process occurring, the pulse duration would thus eventually go to zero upon many passes through the modulator. This is prevented from happening by the finite bandwidth of the laser gain medium so that as the pulse shortens and its spectrum thus widens, the wings of the pulse spectrum are no longer amplified and a fundamental limit is placed on the pulse duration by limitation of the pulse bandwidth.

This finite bandwidth limitation however, affects the steady-state pulse duration quite differently in homogeneous and inhomogeneously line broadened media.

In a laser medium with an homogeneously broadened linewidth, the oscillating bandwidth $\Delta\nu_L$ tends to be the same as the gain bandwidth $\Delta\nu_0$ of the medium. In this case, all the necessary modes are already oscillating, and in the frequency domain, the purpose of the modulator is to lock all the modes in phase. Under the synchronisation condition $\Omega_m = \Delta\omega$ the phase-locking condition (Eqn(2.1)) develops and the resultant pulse duration is as in Eqn(2.13), $\tau_p \simeq \frac{0.441}{\Delta\nu_0}$. If this laser is non-modelocked, short-noise pulses that have this duration will already be present in the random noise signal in the cavity, and the purpose of the modulator in the time-domain is to ensure that only a single pulse can survive in the cavity. The modulator does not perform any appreciable pulse shortening.

In the case of an homogeneously broadened line however, spatial hole burning tends to confine the oscillating bandwidth to a small region around the central frequency ν_0, thus limiting the pulse duration. In this case, noise-pulses in the non-modelocked cavity can have a duration significantly longer than $1/\Delta\nu_0$, and the action of the modulator as in Fig 2.5 can have a significant pulse-shortening effect, broadening the pulse spectrum. In this case, it can be shown that the pulse duration is given by:

$$\tau_p \simeq \frac{0.45}{(\nu_m \Delta\nu_0)^{1/2}} \tag{2.18}$$

where ν_m is the modulator frequency ($= \Omega_m/2\pi$). Thus, for an actively mode-locked, homogeneously broadened laser, the minimum pulse duration is severely limited by the modulation frequency, which in turn is limited by the length of the cavity, and so in general $\tau_{p,hom} \gg \tau_{p,inhom}$.

FM modelocking is considered in a very similar way, but instead of introducing a time-varying loss, the modulator introduces a sinusoidally varying refractive index change. This imparts a time-varying phase shift on the cavity modes, $\phi = (2\pi L_m/\lambda) \times n \sin \Omega_m t$, where L_m is the length of the modulator. This then introduces sidebands on the electric field as before and modes can be locked together. To get a better physical understanding of how a phase or frequency modulation can lead to effectively a strong amplitude modulation, consider that, in effect, the refractive index variation is equivalent to varying the length of the cavity by e.g. translating one of the end mirrors. If a propagating pulse were to strike the mirror during its range of motion, it would experience a Doppler shift, which, if

the frequency of the mirror oscillation was matched to the round trip time of the cavity, it would continue to see on each arrival at the mirror. Thus, after many round trips in the cavity, the pulse's wavelength would be shifted out of the gain region of the laser, and the pulse would decay out of existence. If however, the pulse were to strike the mirror at one of the extremes of its motion, i.e. when the mirror is stationary, it would not pick up this Doppler shift, but would instead pick up a small quadratic phase shift, or frequency chirp, which would tend to broaden its spectrum slightly. Steady state FM modelocking then represents the condition whereby the chirp picked up from the modulator (spectral broadening) is just cancelled by the propagation of the chirped pulse through the gain medium (spectral narrowing).

For generally high-gain lasers, AM modelocking is commonly achieved by use of an electro-optic Pockels cell. The configuration used is identical to that used in Q-switching (§1.4.2.1) where a linear polariser and Pockels cell are used in combination to rotate the polarisation of the beam on a double pass through the cell so that the reflected light may be coupled out of the cavity. In this case though, the voltage applied to the Pockels cell is sinusoidally modulated from zero to some fraction of the $\lambda/4$ voltage, to provide the necessary sinusoidally varying loss from the combined action of the elements. For generally low-gain lasers, acousto-optic modulators are more commonly used as they typically have lower insertion losses than a Pockels cell. These are configured differently to the ones used for Q-switching, with the face opposite the piezoelectric driver being cut parallel to the one being driven so that the sound wave is reflected directly back. For a suitable crystal width, this then results in an acoustic standing wave pattern being set up, and since this is sinusoidally modulated in time, the same is true for the diffraction losses. FM modelocking also uses a sinusoidally driven Pockels cell, but in this case it is orientated such that one of the axes of birefringence, n_x say, is parallel to the polariser axis. Then, rather than rotating the polarisation of the beam, the cell action introduces a sinusoidally varying phase shift, $\phi = (2\pi L_m/\lambda)n_x \sin \Omega_m t$, and modelocking action as described above can occur.

2.4.2 Passive modelocking

The limits of active modelocking are related to the speed of the external signal modulator. In passive modelocking the cavity modulation is derived from the passage of the pulse itself and so much shorter pulses can be obtained. There are five implementations of passive modelocking that will be considered here: 1) *Fast saturable absorber* modelocking, which uses the saturation properties of an absorber medium with a very short upper state lifetime; 2) *Slow saturable absorber* modelocking, which exploits the dynamic gain saturation of the laser medium together with a saturable absorber; 3) *Kerr lens* modelocking, which uses the intensity dependent refractive index, and resultant self-focusing effect, of a suitable non-linear medium; 4)*Non-linear mirror* modelocking, which uses sum- and difference-frequency generation in a non-linear optical material to create an effective saturable absorber; 5) *Additive pulse* modelocking, which uses the self-phase modulation induced in a non-linear element in a secondary cavity coupled to the main cavity.

2.4.2.1 Fast Saturable absorber modelocking

A saturable absorber is a material that under low intensity illumination exhibits an absorption at the illumination wavelength, but under high intensity illumination becomes saturated, and displays a much reduced, possibly zero, loss. Fast saturable absorber modelocking uses an absorber with a low saturation intensity and a relaxation time (the time taken to recover from it's completely saturated state to its completely unsaturated state) shorter than the duration of the modelocked pulses. To a first order approximation, this type of absorber can be considered as a simple two level system, and in order to have a low value of saturation intensity together with a short lifetime, must have a relatively high absorption cross-section ($I_s = h\nu/2\sigma\tau$). Early systems modelocked in this fashion thus typically used organic dyes as the saturable absorber as they have the high cross-sections required ($\sim 10^{-16}\text{cm}^2$). As deposition techniques have developed though, these have been very much superceded by semiconductor, quantum well based, devices.

The use of semiconductor saturable absorber devices to passively modelock

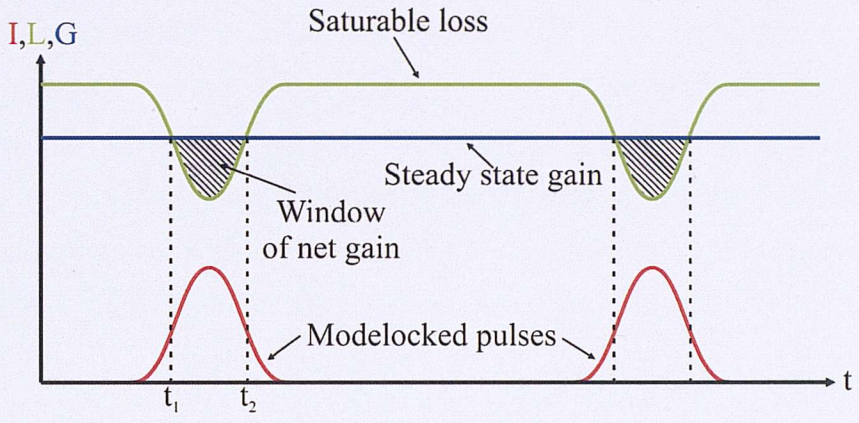


Fig 2.6. *Steady state situation for fast saturable absorber modelocking, with a net gain window established between $t_1 < t < t_2$ when the saturable loss drops below the level of the steady state gain.*

a solid-state laser system is one of the main experimental focuses of this thesis, and so the discussion here will be restricted to a qualitative treatment of the modelocking mechanism, leaving a more detailed treatment for a later chapter.

Considering a modelocked pulse propagating in a cavity containing a saturable absorber, before the arrival of the pulse the unsaturated loss is considered to be greater than the saturated gain of the cavity. As the pulse passes through the absorber its low intensity leading edge will experience the unsaturated loss of the absorber. As the intensity of the pulse rises however, the absorber will begin to saturate and the loss experienced will become smaller until at some point (t_1), the saturated gain is equal to the saturable loss. The pulse then sees a net gain for $t > t_1$ as the absorber continues to be saturated by the intense region of the pulse. As the pulse continues through the absorber and the instantaneous intensity decreases in its trailing edge, the absorber begins to recover so that at some time t_2 the saturable loss is again equal to the saturated gain. For $t > t_2$ the trailing edge of the pulse again experiences a loss, and a net gain window in the region $t_1 < t < t_2$ is formed. This dynamic is summarised in Fig 2.6 where it is then easy to see that the saturable absorber effectively acts as a shutter in the cavity, allowing only the pulse to propagate without loss, and attenuating any low intensity signal in the cavity. This then leads to modelocking as described in 2.3.

As was seen when considering AM modelocking, this net gain window has the

effect of shortening the pulse on each passage through the absorber, and again a steady state is achieved by the balance between this pulse shortening and the broadening due to the finite gain bandwidth. The situation in Fig 2.6 is also only applicable to gain media with lifetimes much longer than the duration of the pulse (~hundreds microseconds), so that the gain does not vary during passage of the pulse, and the saturated gain value is determined by the average intracavity laser intensity.

2.4.2.2 Slow saturable absorber modelocking

Many passively modelocked laser systems use this fast saturable absorber mechanism, but it is also possible, under special circumstances, to use a slow saturable absorber. In this case, the following conditions must be met: 1) The recovery time of both the absorber and gain medium must be comparable to the cavity round trip time; 2) The saturation fluence of both the gain medium and absorber must be such that both can be saturated by the intracavity fluence; 3) The saturation fluence of the gain medium must be comparable, yet slightly larger, than that of the absorber.

In order to meet these criteria then, suitable gain media must have a short upper state lifetime comparable to the round trip time of a realistic cavity (~few nanoseconds), and a high emission cross-section ($\sim 10^{-16}\text{cm}^2$). As such, the most suitable materials are dyes and semiconductors [49–54], with crystalline solid state materials having long lifetimes (~hundreds of microseconds) that discount dynamic gain saturation. Dyes are also typically used as saturable absorbers in these systems as they have the short lifetimes and high cross sections required.

The physical phenomena leading to modelocking in this situation are slightly different to that of the fast case, and are illustrated with the help of Fig 2.7. Before the modelocked pulse arrives, the gain is assumed to be smaller than the losses so that the leading edge of the pulse suffers a net loss. Then, if the accumulated pulse fluence is sufficiently large, saturation of the absorber can occur and at some point during the leading edge of the pulse (t_1) the absorber loss equals the laser gain and the pulse sees a net gain for $t > t_1$. Now, if the saturation fluence of the gain medium has a suitable value (typically $2\times$ higher than the

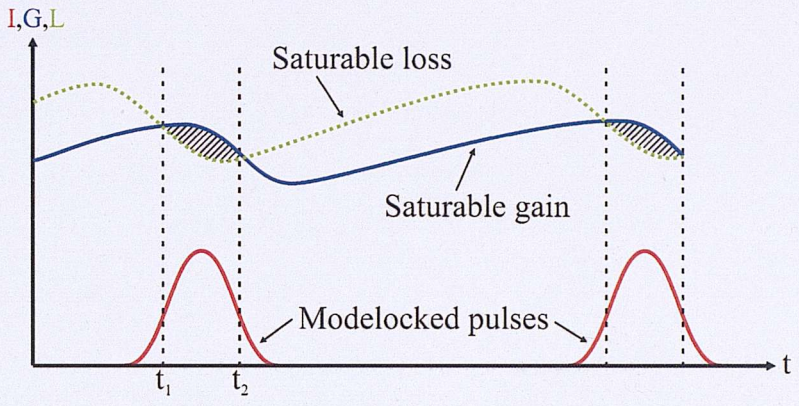


Fig 2.7. *Steady state situation for slow saturable absorber modelocking, with a net gain window established between $t_1 < t < t_2$ when the saturable loss drops below the level of the saturable gain.*

absorber), gain saturation can occur so that the net gain begins to reduce, and at some time t_2 during the trailing edge of the pulse, laser gain equals absorber loss. Beyond t_2 the pulse again sees a net loss, and so a time window of net gain has been established between t_1 and t_2, and the pulse is shortened on each round trip, with a steady state condition again established by the balance between this shortening mechanism and the broadening arising from the finite gain bandwidth. The evolution towards this state is again described by an initial noise spike in the unlocked cavity gradually producing this window of net gain at the expense of the lower intensity noise signal.

Fig 2.7 also illustrates the point that inbetween consecutive pulses, the saturable loss must recover to its unsaturated value, while the gain medium must also recover, but to a level that leaves the gain smaller than the loss. Thus, the absorber recovery time must be shorter than the round trip time, whilst the lifetime of the gain medium must be somewhat longer.

Although the balance of these conditions can be delicate, once achieved, the fact that the gain medium is typically a dye with a very large gain bandwidth (tens THz) means that pulses with durations as short as 10's femtoseconds can be produced with this technique.

2.4.2.3 Kerr lens modelocking

At sufficiently high intensities, the refractive index of a material can be noticeably modified by the field intensity, so that in general, $n = n(I)$. To a first order approximation then, the refractive index can be written as:

$$n = n_0 + n_2 I \tag{2.19}$$

where the intensity dependent refractive index term has a coefficient n_2 that is a positive constant depending on material ($n_2 \simeq 3.45 \times 10^{-16}$ cm^2/W for sapphire). This phenomenon is called the *optical Kerr effect* and is generally due to the high electric fields deforming atomic or molecular orbitals, or reorientating elongated molecules (for gases or liquids), resulting in hyperpolarization of the medium. For a solid, only deformation of the ion's electron cloud can occur and so the response time of the Kerr effect is on the scale of the rotation period of the outermost electrons, which is extremely fast and of the order of a few attoseconds.

Now, considering a beam propagating through this Kerr medium, in general it will have a non-uniform transverse intensity profile (e.g. Gaussian), so that the intensity at the centre of the beam will be higher than at the wings. This will result in a non-linear refractive index change $\Delta n = n_2 I$, that is large at the beam centre, but goes to zero in the wings. For a beam with a Gaussian transverse intensity profile $I = I_p \exp[-2(r/w)^2]$, where I_p is the peak intensity, r is the radial coordinate from the centre of the beam, and w is defined as the radius of the beam. The non-linear phase shift picked up by the beam as it propagates through a length l of the medium is then:

$$\delta\phi = \frac{2\pi\Delta n l}{\lambda} \tag{2.20}$$

$$= \left(\frac{2\pi n_2 I_p l}{\lambda}\right) \exp[-2\left(\frac{r}{w}\right)^2] \tag{2.21}$$

$$\simeq \left(\frac{2\pi n_2 I_p l}{\lambda}\right) \times [1 - 2\left(\frac{r}{w}\right)^2] \tag{2.22}$$

and so to a first order approximation, $\delta\phi$ is parabolic in (r/w), which is equivalent to saying that a spherical lens is induced in the medium by the Kerr effect. Under sufficiently high field conditions, when the beam power reaches a critical value

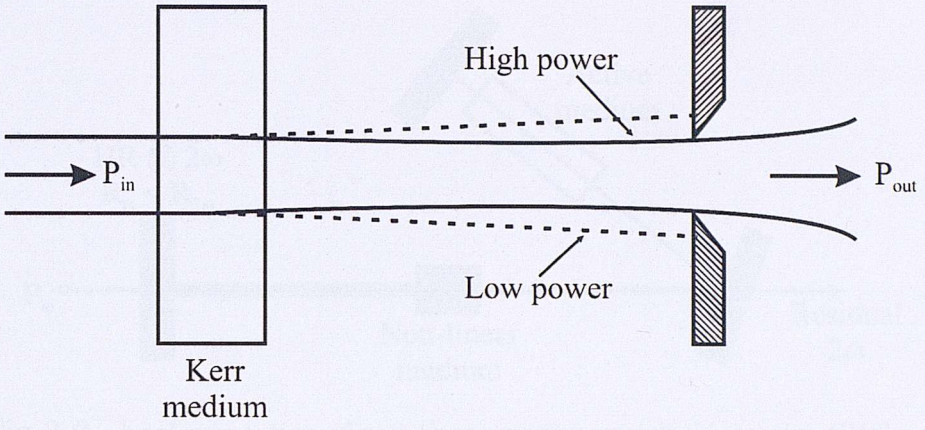


Fig 2.8. *Implementation of Kerr lens modelocking by using self-focusing in a Kerr medium and a hard aperture.*

the propagating beam may be focused by this induced lens. This phenomenon is known as *self-focusing* and can be used to produce a non-linear loss element which displays an intensity dependent loss.

One realisation of this technique, hard aperture Kerr lens modelocking (KLM), is shown in Fig 2.8. The intracavity beam is focused down into a Kerr material and a small aperture is placed beyond this. The low intensity leading and trailing edges of the beam will not induce any significant Kerr effect and will be attenuated by the aperture, introducing a loss to the cavity. By contrast, the high intensity region of the beam will focus more strongly, and suitable positioning of the Kerr medium and aperture will result in a reduced loss for this part of the beam. With this discrimination between low and high intensity regions of the pulse, modelocking can be realised by analogy with the fast saturable absorber case (Fig 2.6) where the intensity dependent loss is now introduced by the attenuation of the aperture. It is also possible to implement KLM using a 'soft-aperture' where the self-focusing is used to produce a better overlap of the laser mode with the gain region. The more strongly focused regions of the beam thus experience a higher level of gain, and the discrimination between low and high intensity regions of the pulse is achieved in this way. With suitable control of cavity dispersion, this technique has been successfully implemented in a number of ultrabroadband gain media ($\Delta\nu_L \approx 100$ THz) to produce pulses as short as 2.8 fs [39, 55–61].

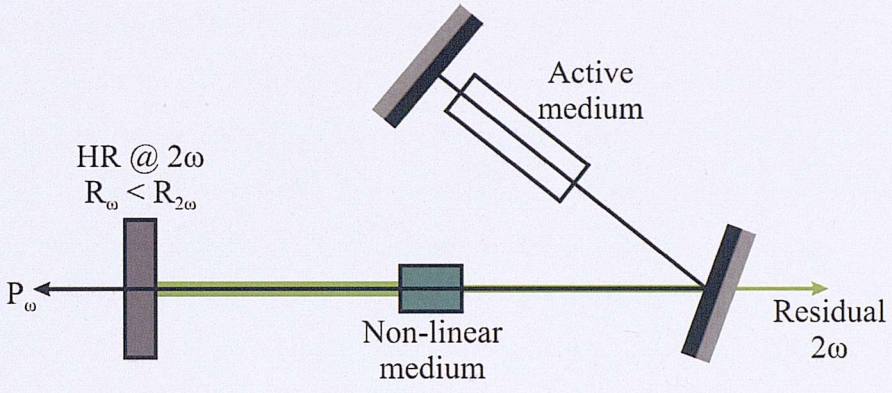


Fig 2.9. *Implementation of non-linear mirror modelocking using SHG and DFG in a non-linear medium together with a dichroic mirror.*

2.4.2.4 Non-linear mirror (Stankov) modelocking

Another mechanism that utilises the non-linear optical properties of a material was proposed by Stankov [62] and although it gained initial interest [63–66] it has rather fallen out of fashion with the advent of semiconductor saturable absorber devices. It is another technique that forms a main focus of this thesis, so again the discussion here is restricted to qualitative description a more detailed treatment left for a later chapter.

The technique is based on the combination of second harmonic conversion in a suitable non-linear medium combined with a dichroic mirror that has differential reflectivity between the fundamental and second harmonic frequencies, to produce a system that has an intensity dependent loss. This intensity dependent loss is then again analogous to the action of the fast saturable absorber and can lead to modelocking as previously described.

The system is best described with use of Fig 2.9. A non-linear medium with a $\chi^{(2)}$ susceptibility is introduced into the laser cavity and optimised for second harmonic generation (SHG) so that the propagating radiation is a combination of fundamental and second harmonic frequencies. A dichroic mirror is used at one end of the cavity that has a very high reflectivity for the second harmonic frequency ($R_{2\omega}$), but only a partial reflectivity for the fundamental (R_ω). This mirror then serves as the output coupling for the fundamental radiation. The second harmonic is reflected back into the cavity and to the non-linear medium, where, under the

correct conditions, it can be mixed with the fundamental radiation through the process of difference frequency generation (DFG) and be converted back to the fundamental wavelength. The initial SHG is a non-linear, intensity dependent process, so it can be seen that the passage of a short intense pulse through this system can easily result in an intensity dependent loss.

Initially, the low intensity leading edge of the pulse is too weak to produce much SHG and so it sees the low partial reflectivity of the dichroic mirror at the fundamental frequency and is strongly coupled out of the cavity. As the pulse intensity rises, the amount of SHG will rise and the second harmonic radiation will see the high reflectivity of the dichroic mirror. If this reflected radiation can then be efficiently converted back into fundamental radiation, the intense regions of the pulse will have experienced a smaller overall loss than the lower intensity regions because a higher proportion of the pulse that exited the non-linear medium has been retained in the cavity. The combination of SHG in the non-linear medium and dichroic mirror can thus be combined to produce a non-linear, intensity dependent loss to the cavity. The combination could also equally be considered as producing a non-linear reflectivity from the SHG-differential reflectivity-DFG system, and so this mechanism is referred to as *Non-linear Mirror modelocking* (NLM).

As with the Kerr effect, the SHG process is effectively instantaneous and so pulse duration-limiting effects from a finite recovery time are not an issue. The process is also robust under the high intensities used and so does not suffer from damage or deterioration as the fragile semiconductor devices can. Conversely, optimisation of the system relies on very accurate and sensitive phase matching and so the long term stability of the system can be a problem.

2.4.2.5 Additive pulse modelocking

The final technique to look at briefly is Additive Pulse Modelocking (APM) which also utilises the non-linear optical Kerr effect, this time induced in a secondary cavity that is coupled to the main cavity.

As well as the self-focusing effect described earlier, the Kerr non-linearity (Eqn 2.19) can also lead to a phenomenon called Self-Phase Modulation (SPM) whereby the instantaneous frequency of the carrier wave acquires a varying shift across the

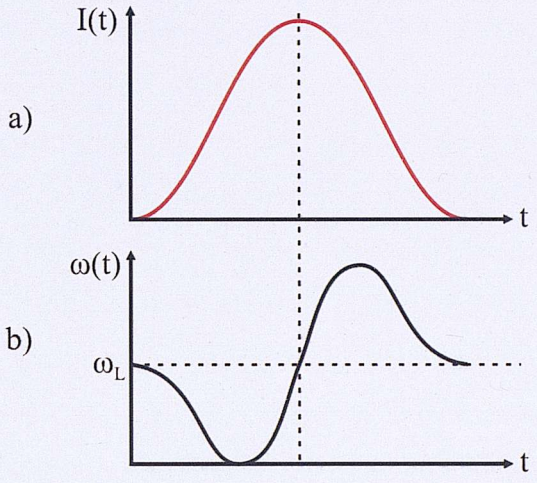


Fig 2.10. *The self-phase modulation effect. A Gaussian pulse (a) with frequency ω_L propagating through a non-linear medium can pick up a frequency chirp (b) that is negative in the leading edge of the pulse and positive in the trailing edge.*

duration of the pulse. If the refractive index of the non-linear medium can be written $n = n_0 + n_2 I$, then if $I = I(t)$, the refractive index is also a function of time and varies throughout the passage of the pulse with the same temporal form. The non-linear phase shift picked up by the pulse on passage through a length l of this index is:

$$\delta\phi(t) = -\frac{2\pi l}{\lambda} n(t)$$

and we can relate this phase shift to the instantaneous frequency shift of the pulse ($\delta\omega$) by:

$$\delta\omega(t) = \frac{\mathrm{d}(\delta\phi)}{\mathrm{d}t} \tag{2.23}$$

$$= -\frac{2\pi l}{\lambda}\frac{\mathrm{d}n(t)}{\mathrm{d}t} \tag{2.24}$$

For a pulse with a Gaussian temporal format, the resulting frequency shift (or chirp) is shown in Fig 2.10 and is seen to be negative in the leading edge of the pulse, zero at the peak, and positive in the trailing edge of the pulse, while the envelope of the pulse remains unchanged.

In order to convert this process into a modelocking mechanism, a small portion of a master cavity is coupled into another secondary cavity of equivalent length which contains a non-linear optical element that displays a Kerr non-linearity.

Typically, this cavity is constructed from optical fibre as the high intensities found in the small cores result in a high effective non-linearity. For propagation of a short Gaussian pulse through this fibre, the leading and trailing edges of the pulse will pick up a phase shift, with the central, more intense region of the pulse experiencing a much smaller or zero shift. After propagation through the fibre, the chirped pulse and the un-chirped pulse in the master cavity are recombined at the coupling mirror and interfere. If the amount of chirp is correct, the wings of the pulse interfere destructively, whilst the central, intense region is reinforced by constructive interference. This then creates a system which displays an effective non-linear, intensity dependent loss, and modelocking can occur as described previously.

Although this method garnered some initial interest [67–70], it is not as popular anymore, as the need to stabilise the two cavity lengths to within, typically, a fraction of a wavelength of one another means that it is difficult to produce devices for use in industry.

2.5 Pulse measurement

In order to measure an event in time, another event which occurs on a comparable or shorter time scale is required. At the shortest time scales, this becomes a problem because there are no shorter events that can lead to an accurate measurement. Electronic equipment relies on the motion and subsequent counting of electrons, and even with modern technology it is not possible to resolve events on a time scale much less than a nanosecond. This poses a problem when one wishes to measure a pulse of light that could be as short as femtoseconds and it was realised early on in the development of short pulse systems that a new way of measuring and quantifying these extremely short events would be required. Once pulses reach the picosecond regime, the only thing that exists on a comparable time scale is the pulse itself and so the technique of autocorrelation was developed where the pulse is compared to itself in order to realise a measurement.

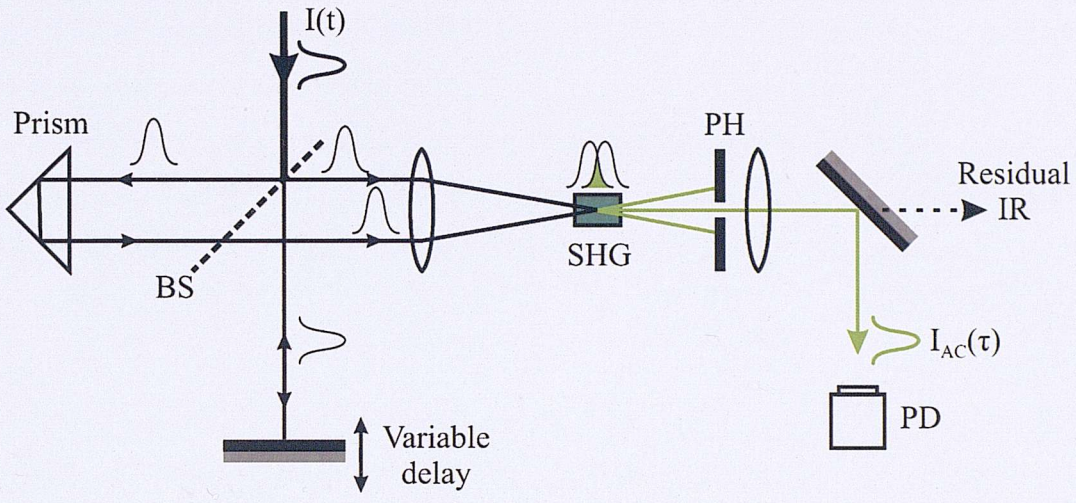


Fig 2.11. *Background free autocorrelation. PH - pinhole; BS - beamsplitter; PD - photodiode.*

2.5.1 Autocorrelation

The technique of autocorrelation is simple and elegant. The pulse is first taken and split into two copies by use of a beamsplitter. The two beams then follow different paths of similar length with one path introducing a variable delay. The pulses are then brought back together such that they overlap both in time and space, one of the beams has travelled further than the other and so there is a delay between the arrival of the pulses at a given point. The variable delay of one of the beam paths allows the amount of overlap between the beams to be varied continuously. If the two beams are recombined by focusing into a non-linear medium, the overlap region between the beams results in sum-frequency generation, and if the delay between the beams is varied so that one pulse sweeps completely over the other, the temporal shape of this generated harmonic signal can be used to infer the width of the pulse.

One implementation of this technique is shown in Fig 2.11. This design is known as a background free autocorrelation because while the frequency conversion due to the beam overlap occurs along the optical axis of the system, the two recombining beams are directed off axis and so it can be arranged by use of a pupil that the residual frequency conversion from each beam individually does not contribute to the detected signal. In this case however, the frequency conversion

for the main signal is not as efficient as it could be because each beam is slightly detuned from ideal phase matching.

The photodetector used has a long response time (1MΩ coupling) and so averages the detected signal over a long time T. The autocorrelator intensity signal is then given in terms of the delay τ and the pulse's intensity distribution $I(t)$ by:

$$I_{AC}(\tau) \propto \frac{1}{T}\int_{-\infty}^{\infty} I(t+\tau)I(t)\,\mathrm{d}t \tag{2.25}$$

In order to be able to extract a pulse width from this signal, an assumption needs to be made about the form of the pulse's intensity distribution. Assuming for now that this is given by a sech^2 distribution of the form

$$I(t) = I_0\,\mathrm{sech}^2\,(t/t_s)$$

then the normalised intensity autocorrelation function is given by:

$$I_{AC}(\tau) = \frac{\int_{-\infty}^{\infty}\mathrm{sech}^2\,(t/t_s)\,\mathrm{sech}^2\,(t/t_s-\tau)\,\mathrm{d}t}{\int_{-\infty}^{\infty}\{\mathrm{sech}^2\,(t/t_s)\}^2\,\mathrm{d}t} \tag{2.26}$$

$$= 12e^{2\tau}\frac{e^{2\tau}\tau - e^{2\tau} + \tau + 1}{e^{6\tau} - 1 - 3e^{4\tau} + 3e^{2\tau}} \tag{2.27}$$

of which the FWHM is $\Delta\tau_{FWHM} = 2.720$. Note that τ is dimensionless and normalised to t_s, so that the corresponding delay is $\Delta t_{AC,FWHM} = 2.720t_s$. At the same time, the sech^2 function with parameter t/t_s has a FWHM $\Delta t_{pulse,FWHM} = 1.763t_s$, and therefore the FWHM of the actual pulse can be calculated from the autocorrelation by:

$$\Delta t_{pulse,FWHM} = \frac{1}{1.543}\Delta t_{AC,FWHM} \tag{2.28}$$

The factor $1/1.543$ is known as the deconvolution factor for sech^2 pulses. Assuming a different fundamental pulse shape will result in a different deconvolution factor, Gaussian pulses for example result in a factor of $\sqrt{2}$. This then allows for the possibility of some uncertainty in the duration of the deconvolved pulse as it is extremely difficult to know its true form. The deconvolution factor of 1.543 is used throughout this thesis.

2.5.2 Spinning mirror autocorrelator

One potential problem when measuring picosecond pulses is the issue of how to continuously vary the path length in one arm of the autocorrelator to give a real time assessment of the pulse duration. It is of course possible to take a series of discrete measurements by manual translation of one of the mirrors on a micrometer stage, and build up an autocorrelation trace this way, but this is time consuming and requires separate data analysis and manipulation before a value for τ_p can be reached. During optimisation of the cavity, a better solution is to have the arm length continuously scanning through its range so that changes to the pulse duration can be seen in real time as adjustments are made. For pulses in the femtosecond regime, this is relatively simple as the spatial extent of, say, a 50 fs pulse, is only $\sim$15 μm and the path length variation can be introduced by use of a piezoelectric transducer which can be moved very rapidly. For pulses of 50 ps duration, the spatial extent of the pulse is $\sim$1.5 cm, and given that it is not always known what the pulse duration will be and that there may be some difficulty matching the arm lengths exactly, it could well be desirable to have a path length difference of several centimetres. This is outside the range of piezo transducers, and so some kind of mechanical solution would be required. The challenge is then to produce some mechanism that can scan rapidly (scan time $\sim$1 s) through its range of motion, but also do this smoothly so as not to introduce any deviation to the sensitive alignment of the autocorrelator.

There have been various methods implemented in the past for picosecond autocorrelators and after considering several options it was decided that the most cost effective and simplest to implement would be the spinning mirror design first demonstrated by Yasa and Amer [71]. It consists simply of a pair of parallel mirrors, mounted on opposite ends of a platform that is rotating at a constant angular frequency, such that light striking one of the mirrors will be reflected to the other and emerge parallel to the initial path. During the period of rotation, there will only be a short time where light is reflected between the mirrors. For a large part of the cycle the light will be reflected so that it misses the second mirror; during this short time however, as the mirror rotates the light will be incident across a

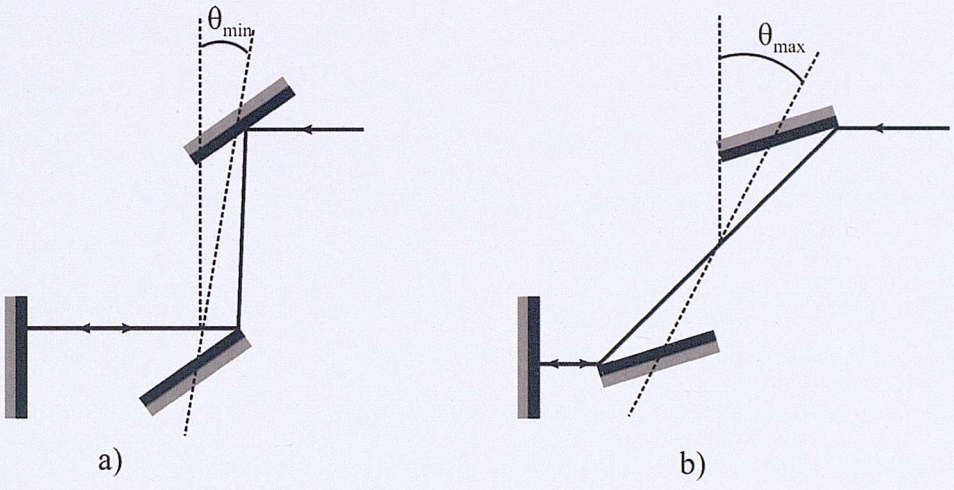


Fig 2.12. *The two extremes of the duty cycle of the spinning mirror autocorrelator design. Retro-reflection of the beam path occurs between θ_{min} and θ_{max} and during this period the path length is smoothly varying.*

range of angles and positions so that the path followed through the system will vary with the rotation angle. This continuous variation in path is seen to correspond to a continuous variation in path length so that if the spinning platform is positioned between the beamsplitter and the retro-reflecting mirror in one of the beam arms, a variable delay is introduced that can be scanned at the rotation rate of the platform.

The construction is best shown in Fig 2.12, the two pictures depicting the path when the beam is at the beginning and end of its duty cycle. It can be shown [72], that within various approximations, the total delay attainable with this technique is predominantly proportional to the diameter of the mirrors used, with minor adjustment available if the distance between, and the angle of the mirrors (relative to the axis that joins their centres) are varied. In order to keep the instrument as compact as possible, and so that the situation does not arise where large, heavy optics need to mounted on a rotating platform, standard 2.54cm (1") optics were used which enable a total delay time of ~100 ps to be achieved. This gives a suitably large window in which to capture the pulses, which are hoped to be in the region of 10's picoseconds long, and to give some margin for error in matching the path lengths during alignment.

The distance between the centres of the mirrors was set to be 10 cm as effective

operation relies on the mirror separation being greater than the mirror diameter, and a distance much larger than this would have resulted in excessive load on the driving motor. The mirror angle is defined relative to the axis joining the centres of the mirrors, and this was set at 45° as the maximum in path length difference occurs around this point.

In operation, it is necessary to initially calibrate the autocorrelator so that the width in time of the signal from the photodetector can be related to a real pulse delay time. In order to do this one first has to achieve an autocorrelation trace with the spinning mirrors, with the peak of the trace visible in the scan. Then the length of the delay arm is changed by a known amount by translating the mirror in this arm. This will cause the peak in the scan to shift, and by measuring the size of this shift and equating it to the time delay that has been introduced by translating the mirror, calibration of the scale is possible, and the real width of the autocorrelation can be measured.

2.6 Conclusions

This chapter has covered in detail the basic theory explaining modelocking and introduced the major mechanisms for producing modelocked sources. It began by considering the frequency domain picture of modelocking where the effect of a coherent superposition of many longitudinal cavity modes with some fixed phase relation between them is calculated. This relatively simple picture was shown to lead to the production of a train of short, intense pulses that are separated in time by $\frac{2L}{c}$, where L is the length of the cavity. It was also seen that the pulse duration reduced as the bandwidth of the oscillating modes increased, while the peak intensity increased as the square of the number of oscillating modes. With many solid-state laser systems having bandwidths of hundreds of GHz, this opens up the possibility for producing pulses of picosecond duration with extremely high peak intensities if all of the cavity modes can be made to oscillate in phase.

As a complement to the frequency domain description, the description of modelocking in the time domain is then seen to correspond to the action of a fast shutter inside the cavity. If the opening and closing of the shutter can initially be

timed so that only a particularly intense noise spike is allowed to pass, this spike will be amplified at the expense of all the other lower intensity noise. The steady state situation is then one in which there is only a single pulse propagating inside the cavity, a fraction of which is coupled out after every round trip interval, $\frac{2L}{c}$. The time domain description was also used to illustrate how integer multiples of the pulse repetition rate could be achieved by suitable positioning of the shutter within the cavity.

The question was then how this cavity modulation required for modelocking action (fixed phase relation or shutter timing) could be achieved in practice. This introduced the two main categories of modelocking : active and passive. Active modelocking where an external signal is used to drive the modulation, and passive modelocking where the action of the propagating pulse on some non-linear optical property of a suitable material affects the modulation. The amplitude modulation of a particular frequency component was shown to lead to the production of sidebands in its spectrum, also with the same amplitude modulation. For the correctly chosen frequency of modulation, these sidebands correspond to the adjacent frequency modes of the cavity, which are therefore also subject to the amplitude modulation. This process repeats so that the amplitude modulation propagates through the frequency modes, resulting in all modes oscillating in phase, as required for modelocking.

Passive modelocking was then identified as the most prevalent category due to its general ease of implementation and ability to generate shorter pulses then active modelocking. Four common types of passive modelocking - saturable absorber, Kerr lens, additive pulse and non-linear mirror modelocking - were then introduced, and a simple outline of their implementations was described. The saturable absorber and non-linear mirror techniques were covered more qualitatively as these form the basis for the experimental sections of this thesis.

The chapter finished with an explanation of how ultra-short pulses can be measured using an autocorrelator, and a description of the spinning mirror design for measuring picosecond pulses that was constructed for use in this thesis was briefly outlined.

Chapter 3

The Bounce Geometry Amplifier

3.1 Introduction

One of the main problems in the generation of high average power solid state laser sources with high beam quality is the effect of the thermal loading of the laser crystal on its optical properties. Thermal lensing and aberration, stress induced birefringence, and mechanical strain on the crystal all result from this loading and lead to a degradation in performance of the solid state laser source. The bounce amplifier has been designed to try to mitigate these effects and so this chapter provides a detailed description of the operation of a bounce geometry laser. Before this is discussed, the origins of the thermal loading and how it results in optical degradation will be briefly outlined. This is followed by a complete description of the bounce amplifier including the general operating principle, the crystal geometry, cooling geometry and diode pumping geometry used. Two experimental variants of the bounce amplifier are then demonstrated, a compact form which gives an efficient, high power, spatially multi-mode output, and an asymmetric form that produces a TEM_{00} output. This is interspersed with a simple explanation of the cavity stability theory of Magni which helps to explain the operation of laser cavities with intracavity lenses. As will be seen, the thermal loading in the laser crystal can lead to the production of an effective lens and so the theory helps

to explain the performance of the bounce cavities, and instructs the construction of the TEM_{00} cavity.

3.2 Thermo-optic effects in solid state media

Within a solid state laser medium under optical pumping conditions, not all of the incident pump radiation will be converted into useful optical output from the laser. There are several processes that cause the conversion of this radiation into heating in the crystal, and subsequently several effects this can have on its optical behaviour. This section will briefly describe four processes that contribute to this heating: quantum defect heating; Auger upconversion; cross relaxation and excited state absorption. Then go on to discuss the effect these have on the optical properties of the crystal, and hence the performance of the laser itself.

3.2.1 Quantum defect heating

The main contributor to heat dissipation in the laser crystal is the so-called quantum defect which arises due to the difference in energy between the pump radiation and the laser radiation, and results in direct thermalisation in the solid state medium. To explain this effect in more detail the fundamental production of laser radiation in a four-level laser system needs to be understood and a schematic of this system is shown in Fig 3.1.

Initially, all atoms are in the ground state, level 0, and excitation by pump photons of frequency ν_p populates level 3, the pump band. In general, the pump band is made up of a relatively broad continuum of energy levels so that optical pumping can be achieved over a similarly broad spectral range. This was particularly useful for improving the efficiency in flash lamp pumped schemes where the lamps emitted over a very broad spectral range.

From the pump band, the majority of the excited atoms decay into the upper laser level, level 2, by non-radiative transitions on a timescale t_{32}^{nr}. These non-radiative transitions excite phonons in the host material which are subsequently absorbed directly into the crystal lattice, increasing its kinetic energy, and hence

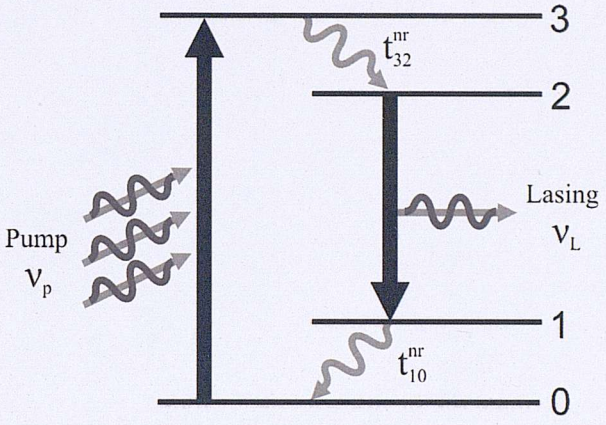


Fig 3.1. *Simple schematic of a four level laser system. Pumping from level 0 at ν_p populates level 3. Lasing at ν_L occurs between level 2 and level 1. t^{nr} represents non-radiative transitions between levels.*

temperature. Above threshold there is then a population inversion between levels 2 and 1, and lasing occurs at a frequency ν_L. Atoms in level 1 can then undergo further fast non-radiative transitions back to the ground state of the system, on a timescale t_{10}^{nr}, generating further heating by the same processes as that between 3 and 2.

The total heat energy dissipated in the crystal per photon absorbed can thus be seen to be the difference between the energy of the pump radiation, and the energy of the laser radiation. $\Delta E = h(\nu_p - \nu_L)$. The heating effect in the crystal is therefore reduced if the energy difference between pumping and lasing transitions is reduced, but always increases with increasing pump power. A method has been shown of reducing the quantum defect heating effect by directly pumping into the pump band, creating a quasi-four level system. Typically in neodymium (Nd) systems, the upper lasing level (2) is a doublet, and the upper of these is populated by the pumping process, from where fast non-radiative transitions fill the upper lasing level 2 as before. There is then a very small energy difference between levels 3 and 2 and the energy dissipated as heat through the non-radiative transitions has been almost eliminated. There will still be energy deposited in the crystal from the transition between levels 1 and 0, with consequential thermal effects.

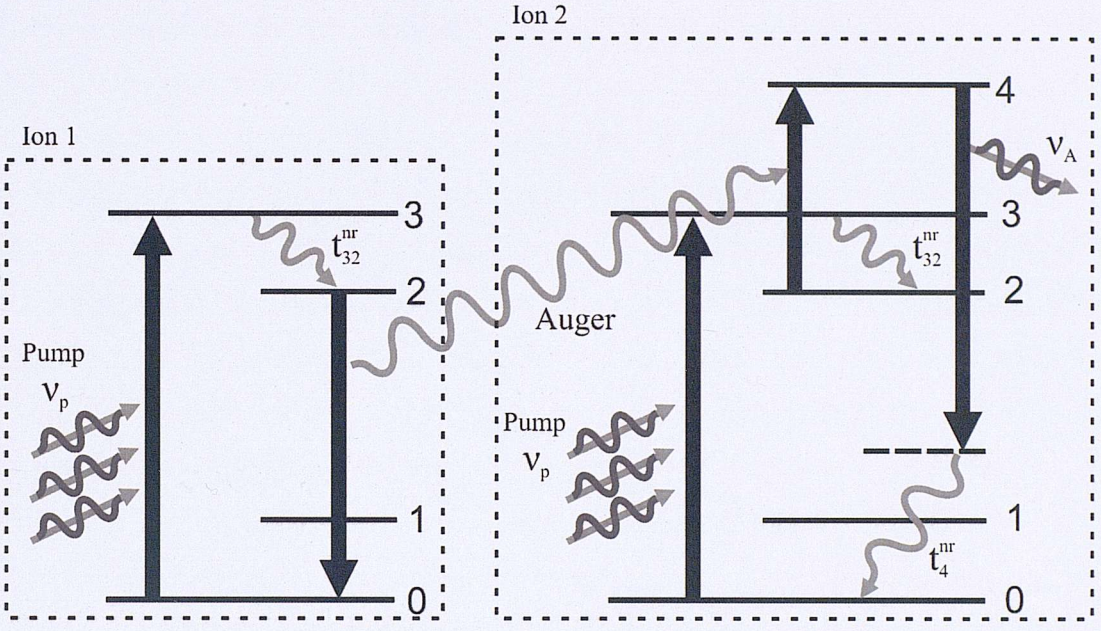


Fig 3.2. *Auger upconversion between two ions with four-level systems. Decay of Ion 1 from level 2 causes further excitation of Ion 2 to level 4. Ion 2 then decays radiatively from here at a frequency ν_A. ν_p is the pump frequency, t^{nr} non-radiative transitions.*

3.2.2 Auger upconversion

A second effect that leads to heating in the crystal is Auger, or energy transfer, upconversion. Illustrated in Fig 3.2, Auger upconversion is a result of energy transfer between two excited ions. The energy emitted when one ion decays from level 2 excites another ion, also in level 2, to a further higher energy level 4. This second ion then decays from level 4 via a combination of radiative and non-radiative processes. Radiative decay from level 4 can be seen as fluorescence in the laser material at higher frequencies than the diode pump radiation, hence the term *upconversion*. The non-radiative transitions cause further heating of the crystal and the amount of energy deposited in this way can be greater than in the quantum defect heating. The combined energy of the radiative and non-radiative processes will remain constant, but the ratio of the two, and hence the extent of the heating effect, will depend on the allowed decay processes within the energy level structure. As the upconversion process involves interactions of pairs of excited state ions, the rate of the process is dependent on the square

of the population density of level 2. Hence, at low diode pumping levels (small population inversions) this effect is not expected to be significant compared to quantum defect heating. At high pumping rates though, with higher population inversions, the probability of upconversion increases significantly and it contributes more to the heating process. Inside the laser cavity however, a high extraction efficiency will deplete the population inversion and hence reduce the likelihood of the upconversion process, minimising the heating effect. This does mean that the amount of heat deposited in the crystal can vary significantly between lasing and non-lasing situations.

The energy transfer process just described was radiative, however it is also possible for the energy transfer to occur by non-radiative processes e.g. dipole-dipole interactions, over short ranges. This case requires a high concentration of ions to become significant, but since the ion doping concentrations of typical laser crystals are of the order of a few percent, the radiative transfer is the dominant mechanism.

3.2.3 Cross relaxation

A further effect contributing to heating of the medium is additional non-radiative transitions resulting from cross relaxation between an excited ion and a neighbouring ground state ion. Illustrated in Fig 3.3 the decay energy of one ion from level 2 to an excited sub level causes the ground state ion to be excited to another sub level, from which both ions decay non-radiatively to their ground state. This can result in all of the energy from the upper laser level 2 being deposited as heat in the laser crystal.

3.2.4 Excited state absorption

Excited state absorption is similar to Auger upconversion in that it involves excitation from level 2 to a higher lying level 4, but in this case the transition is restricted to a single ion. Illustrated in Fig 3.4, an ion in level 2 can absorb either pump or laser radiation and be excited to level 4. From here, in a similar way to the previous effects, the ion can then decay by a combination of radiative and

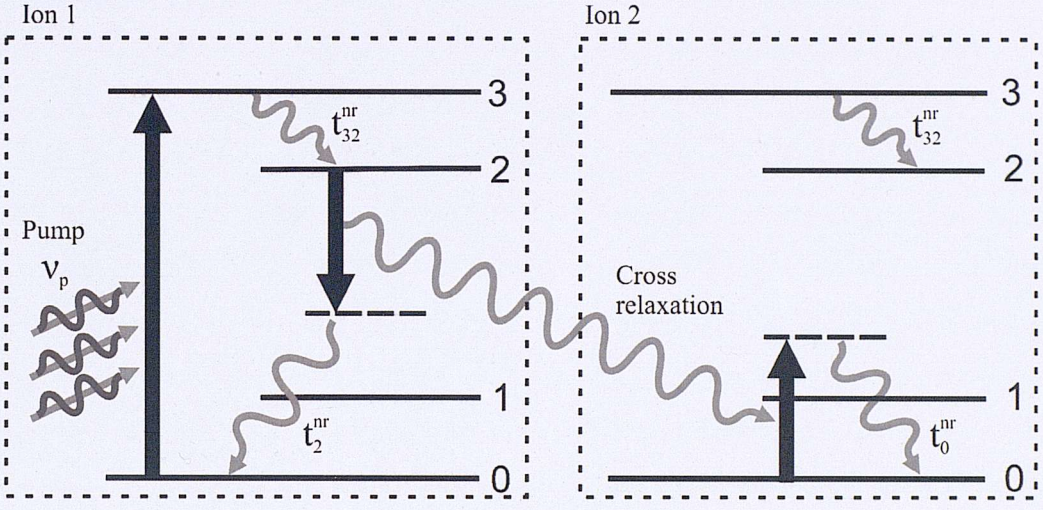


Fig 3.3. *Cross relaxation between two ions with four-level systems. Decay of Ion 1 from level 2 to a sub-level causes excitation of Ion 2 from ground state to a further sub-level. Both ions can then decay non-radiatively from their respective sub-levels.*

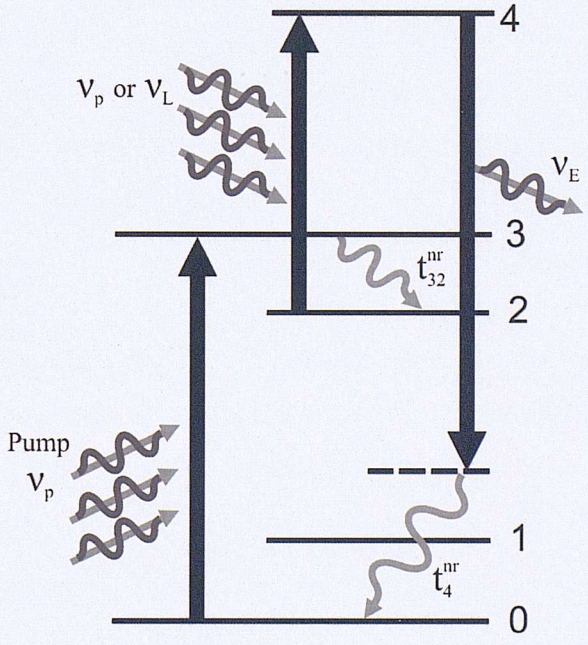


Fig 3.4. *Excited state absorption. An ion in level 2 can be excited to a higher lying level 4 by absorption of either pump or laser radiation. Decay to the ground state can then occur by both radiative and non-radiative processes.*

non-radiative processes back to the ground state. The radiative transitions can again be visible as fluorescence, and the non-radiative transitions will contribute to the thermal loading on the crystal.

Auger upconversion and cross relaxation both result from an interaction between neighbouring ions, and as such the probability of these processes depends on the ion density in the medium, which for laser media corresponds to the doping density of the crystal. For typical bulk laser crystals, this is relatively low (1-2 at.%) and so the ions are far apart and the Auger and cross relaxation processes are weak. In this case, the quantum defect and excited state absorption are the main contributors to the material heating. For cases where the doping density and population inversion are high, the Auger and cross relaxation terms become more significant, and could come to dominate.

3.2.5 How optical properties are affected by thermal loading

The temperature gradients set up in the medium as a result of heating can have a number of consequences including: thermal lensing; thermal aberrations; material stress and distortion; stress induced birefringence and potential material damage if the heating is too severe. Ultimately, if mechanical stress becomes too high, the material will fracture and this limits the maximum average output power of a solid state laser.

The origin of thermal lensing is due to the temperature dependence of a material's refractive index, n. A spatial distribution in temperature T will result in a corresponding distribution in n, which can result in a thermal lens. The two main material properties for determining the strength of a thermal lens within a solid state medium are thermal conductivity κ and thermo-optic coefficient dn/dT. Most of the work into thermal lensing effects in solid state lasers has considered the cylindrically symmetric rod geometry with lamp pumping or diode end pumping. For the case of a medium with end pumping, the dioptric power K of the lens is given by [73]:

$$K = \frac{1}{f} = \frac{dn/dT}{\kappa} \frac{\xi P_p}{\pi w_p^2} \text{ m}^{-1} \tag{3.1}$$

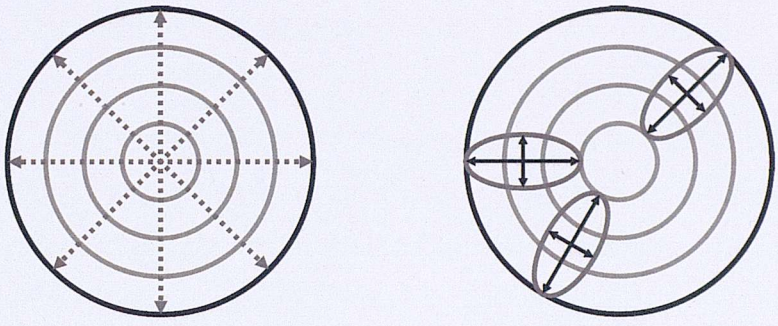


Fig 3.5. *Radial and tangential stress contours due to thermal expansion in a crystal rod (a). The principal birefringent axes align parallel or perpendicular to these contours at all points (b), leading to depolarisation of incident radiation.*

where ξ is the fractional heat load, P_p is the absorbed pump power and w_p is the $1/e^2$ Gaussian radius of the pump beam. Thermal lensing can have a serious effect on lasing stability within a laser cavity due to changes in mode sizes with pump power. The effect of a thermal lens in a bounce geometry laser oscillator will be discussed in more detail later in this chapter. As well as thermal lensing, localised thermal variations within a medium can lead to non-uniformity in the refractive index which can aberrate an optical beam under amplification, severely degrading the output quality.

Material stress and distortion due to the thermal expansion coefficient α_T of the material is also a problem when solid state media are optically pumped. The main consequence is stress-induced birefringence and depolarisation of incident radiation due to the change in refractive index via the photoelastic effect. This effect is explained for the simple case of pumping in a rod geometry. In the rod, thermal expansion in the material will occur, leading to induced stresses. The stresses are the result of the materials elastic properties resisting the expansion, giving contours of radial and tangential stress as shown in Fig 3.5(a).

The stresses on the material cause a change in the refractive index via the photoelastic effect, similar to the thermo-optic effect, and deform the refractive index ellipsoids, as shown in Fig 3.5(b). The ellipsoids represent the fast and slow axes for the birefringence at each particular point. For any point within

the medium, the birefringence ellipsoid will be orientated such that the principal axis will be either perpendicular or parallel to the stress contours from Fig 3.5(a). The resultant birefringence from multiple ellipsoids will combine, to give to a depolarising effect for any incident radiation. For naturally birefringent materials, the depolarisation effect is small as the additional stress-induced birefringence will only be a small perturbation from the natural state.

As well as the depolarisation effect, the expansion of the material will also result in bulging at the boundaries to varying degrees. This will add to the thermal lensing effect as the faces of the laser medium will act as lenses due to the material deformation. In cases of very high pump power, the thermal expansion within a laser medium may lead to critically-high strain at the surface of the medium, resulting in catastrophic damage and fracture. The fracture limit constrains the maximum average power output of a solid state laser.

3.3 The bounce geometry amplifier

All solid state amplifier systems will suffer from these thermo-optic effects to varying degrees, and to a large extent the performance requirements of the system will influence its design. Typical features that would need to be considered during the design of a solid state amplifier include the material to be used as the amplifying medium; the size and shape of the gain region within the medium; how pump radiation is delivered and shaped to match the cavity mode; how the cavity mode might need to be shaped to better match the gain region; and how to remove and control the heating in the amplifier.

End-pumped rod systems have been shown to produce some of the highest optical conversion efficiencies together with high quality TEM_{00} operation because of the ability to match very closely the gain region and the fundamental cavity mode shape [74–76]. They are generally restricted to low to medium power levels because of severe thermal lensing issues arising due to the high intensities (and hence thermal load) at the pump face, and complicated diode shaping and delivery systems mean the practical difficulties of power scaling are significant.

Side-pumped laser systems distribute the pump radiation over a larger volume

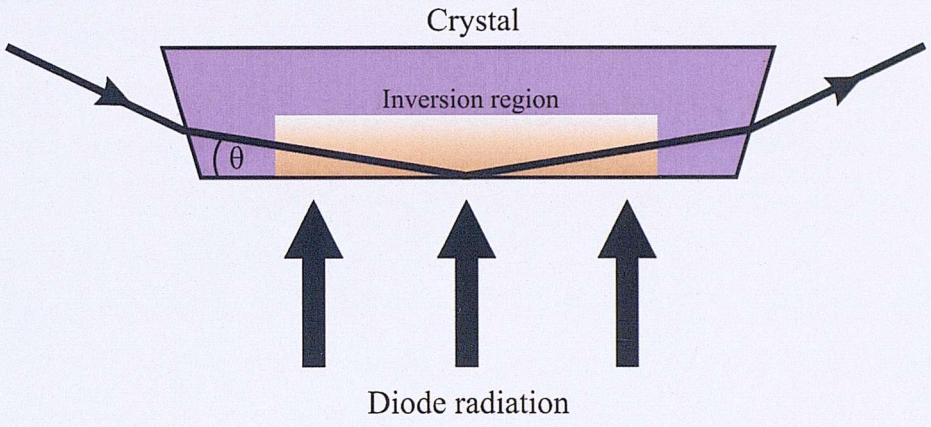


Fig 3.6. *Schematic of the bounce amplifier geometry where an incident beam experiences a total internal reflection at an angle θ in a region of high inversion near the crystal pump face.*

in an effort to control the thermal effects and so be able to deliver more pump power to the amplifier [77, 78]. This is generally at the cost of beam quality and conversion efficiency though because of the poorer spatial matching between the pump region and the cavity mode. Methods have been demonstrated whereby side-pumping from multiple angles simultaneously creates a more uniform gain region [17–19], and although this reduces the overall efficiency of the system and increases its complexity, it does make the systems more suitable for high power scaling.

The bounce geometry amplifier used throughout this thesis was first proposed by Bernard and Alcock [25] and is a variant on the side-pumping mechanism that aims to improve the symmetrical overlap between the gain region and cavity mode, thus improving the conversion efficiency and attainable beam quality. A schematic of the amplifier crystal is shown in Fig 3.6. It is referred to as the bounce amplifier because the design and construction causes a propagating laser beam to experience a total internal reflection with a small angle at the centre of the pump face of the amplifier crystal, as illustrated in Fig 3.6. By using a highly absorbing medium as the basis for the amplifier, the pump radiation creates a region of high inversion density in a very shallow depth just beneath the pump face of the crystal. The path followed by the laser mode then enables it to pass through virtually all of the high inversion region, thus experiencing a high gain. This is the key unique

feature of the bounce geometry. By use of line-focused diode pumping and a crystal with a high absorption coefficient at the pump wavelength, extremely high single pass small signal gains of $\sim 10^4 - 10^5$ have been demonstrated [28]. The gain is highest for lower bounce angles, and the working range of angles for the amplifier is typically $2° < \theta < 12°$.

As well as enabling very high extraction efficiencies to be obtained, the bounce action serves another extremely useful purpose. Whereas many side-pumped amplifier schemes suffer from asymmetrical amplification of the laser mode due to the gain region/cavity mode mismatch, the bounce path results in significant spatial averaging of any non-uniformities. Providing the position of the bounce is located centrally on the inversion region, over the whole path through the crystal each side of the beam will experience an equivalent amount of gain. This means symmetrical amplification of the mode can be achieved even though the inversion region decays exponentially from the face of the crystal. This is exactly the case with any thermal aberrations too. The bounce geometry suffers from adverse thermal effects just like any other solid-state amplifier, but this spatial averaging means that the cumulative effect of any aberrations is relatively uniform over the entire transverse profile of the beam. This spatial averaging, together with the very high gains achievable has meant that ultra-high efficiency lasers with excellent beam quality have been demonstrated using a bounce geometry amplifier [26, 79, 80]. The principles have also been applied to take advantage of the power scaling potential of this side-pumped bounce geometry and high power operation with excellent beam quality has been demonstrated in a number of configurations, including CW [27], adaptive [30, 31, 81] and Q-switched laser systems [29, 82, 83]. The intention of the work described in this thesis was to take advantage of the described properties of the bounce amplifier to produce a high power, modelocked, picosecond laser source.

Several practical ideas contribute to the successful implementation of the bounce amplifier in a laser system, and now that the advantages have been discussed, four specific considerations will be covered: the crystal geometry; the crystal cooling; the diode pumping; and the bounce angle.

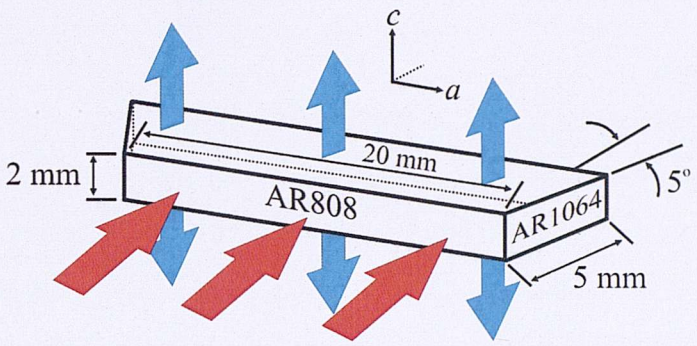


Fig 3.7. *Laser crystal geometry showing crystal dimensions and crystallographic axes, top and bottom cooling faces with the direction of heat removal (blue arrows), angled end faces with anti-reflection coatings at 1064 nm (AR1064) and the direction of pumping (red arrows). The diode pumping face is anti-reflection coated at 808 nm (AR808).*

3.3.1 Crystal geometry

The Nd:YVO_4 crystals used in the experiments throughout this thesis were a-cut slabs, such that the crystal cut is perpendicular to the crystallographic c-axis, with dimensions 20 × 5 × 2 mm, as illustrated in Fig 3.7. The end faces were angled off normal to prevent parasitic self-lasing within the high gain amplifier and in addition were anti-reflection (AR) coated for the lasing wavelength 1064nm to further limit parasitic oscillations. The slab was diode-pumped at 808 nm on the 20 × 2 mm front face, which was AR coated for this wavelength to reduce loss of pump power due to reflections. Dopant concentrations for Nd:YVO_4 are commercially available in the 0.25 - 3 at.% neodymium doping range, and experimentally 1.1 at.% is typically used, although some work in this thesis was also carried out with 0.7 at.% doping.

In experimental work in this thesis, two different variations of crystal geometry were used. The crystals had the same dimensions but one had end faces angled at 5°, the other at 14°. All details of the crystal cooling and diode pumping that are to follow are identical for both crystal configurations. After this, an analysis of the bounce angle for a general crystal with an arbitrary end face angle will be discussed.

3.3.2 Crystal cooling

The top and bottom 20 × 5 mm faces were conduction cooled to remove the heat generated by diode pumping. This conduction was by copper heat sinks with a good thermal contact between the crystal and metal surfaces maintained by a thin intermediate indium foil. The copper heat sink was connected to a constant flow and constant temperature water supply, with the blue arrows in Fig 3.7 indicating the heat flow from the crystal to the cooling mounts. The heat transfer in this geometry is thus predominantly in the vertical direction and so it is expected that thermally induced lensing within the Nd:YVO_4 will be strong in this direction due to the large temperature gradient between the centre of the crystal and the top and bottom cooling plates.

3.3.3 Diode pumping geometry

The crystals may be pumped by a single diode bar, multiple diode bars in combination, or a diode stack. Using multiple diode bars adds a small degree of extra complexity to an otherwise simple alignment, and diode stacks, while good for high power amplifiers, can result in slightly poorer beam qualities due the inherent structure in the pump radiation and hence gain region. The work in this thesis is carried out solely using single diode bars.

The diode bars had fast axis collimation and were focused onto the laser crystal using a vertical cylindrical lens, VCL_D. This formed a vertical line focus on the face of the crystal whose dimension depended on the focal length of the VCL used. For a typical VCL_D focal length of 12.7 mm, the line focus has a dimension in the vertical of ~100 μm. The emission from the diode bars was polarised parallel to the c-axis of the crystals used, which means the high absorption coefficient in that axis of ~30 cm^{-1} is accessed. This results in strong absorption of the pump power and a gain region which extends below the pump face of the crystal by ~330 μm. A schematic of the pump geometry is shown in Fig 3.8.

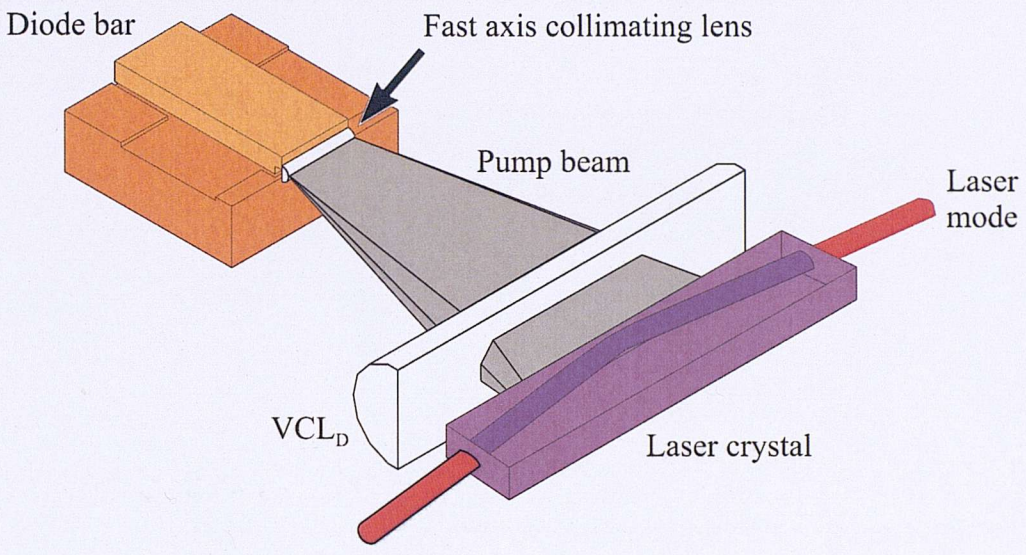


Fig 3.8. *Diode pumping geometry showing the bounce off the pump face of the crystal and the diode focusing lens, VCL_D.*

3.3.4 Bounce angle

In the bounce geometry amplifier, the bounce angle employed is shallow, and the typical working range is $2° < \theta < 12°$, essentially limited by the depth of the gain region and the physical size of the crystal. Experimental studies performed prior to the work in this thesis have shown that a bounce angle of 7° is optimal for achieving the best combination of high efficiency and high spatial quality. The next section describes refraction through a crystal with end faces angled at a general angle θ_c. Refraction in crystals with faces angled at 5° and 14° is described, together with the motivation for a 14° crystal.

3.3.4.1 Refraction through a crystal with angled end faces

For a beam incident through a crystal, refraction takes place at the crystal end faces, as shown schematically in Fig 3.9. A beam is incident at an angle of θ_{ext} with respect to the crystal's front face and is refracted at a bounce angle θ, also with respect to the crystal's front face. On leaving the crystal, the refraction is symmetric and the beam leaves at the angle θ_{ext}. Applying Snell's law to the beam

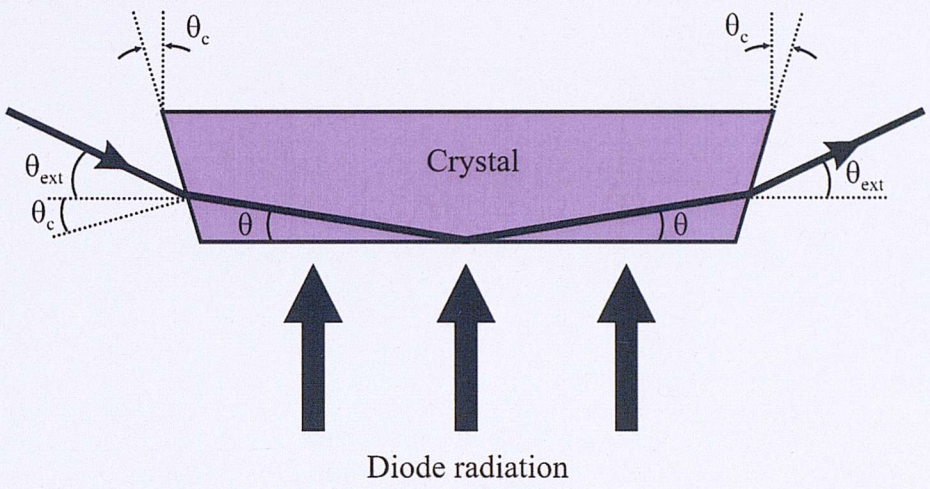


Fig 3.9. *Refraction of a beam through a general crystal with end faces angled at θ_c.*

entering from the left hand side of the crystal gives:

$$n_{air} \sin(\theta_{ext} + \theta_c) = n_{cry} \sin(\theta + \theta_c) \tag{3.2}$$

where n_{air} and n_{cry} are the refractive indices of air and the crystal respectively, and θ_c is the angle of the end face with respect to the normal of the crystals front face, as illustrated. This equation can now be used to calculate refraction angles for the two crystal cuts used in this thesis.

3.3.4.2 Crystal with 5° end faces

The general case of a crystal with end faces angled at θ_c is now modified to one of the specific crystal cuts used in this work where $\theta_c = 5°$. Taking a crystal of Nd:YVO_4 like that used in the experimental work, for the analysis, and using the refractive index $n_{cry} = 2.16$, together with the refractive index of air as $n_{air} = 1$, equation (3.2) gives:

$$1 \times \sin(\theta_{ext} + 5°) = 2.16 \times \sin(\theta + 5°) \tag{3.3}$$

In order to reproduce the optimum bounce angle of $\theta = 7°$, the external angle relative to the pump face at which the input beam should be incident can be calculated from (3.3) by substituting $\theta = 7°$ and solving for θ_{ext}. This is calculated

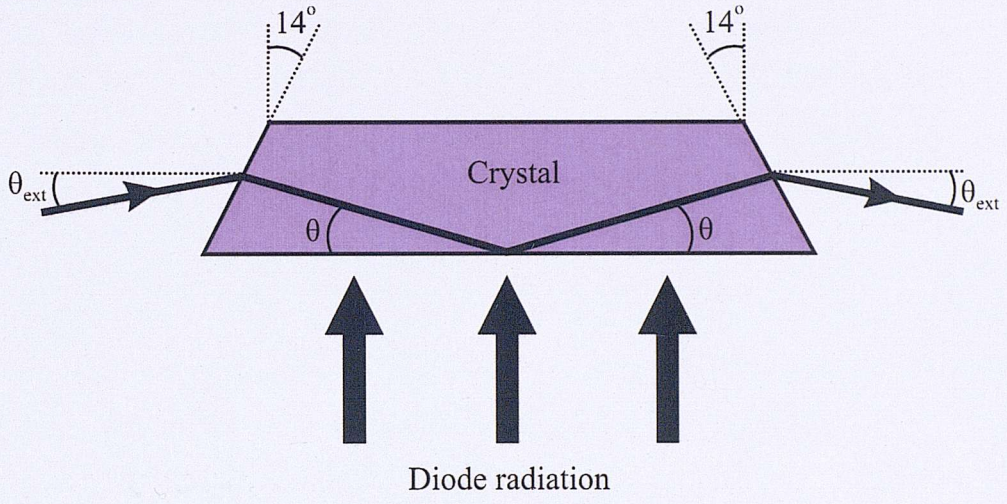


Fig 3.10. *Refraction through a crystal with end faces angled at 14°*

to be $\theta_{ext} = 21.7°$. As the angles involved are small, the small angle approximation, $\sin(\theta) \approx \theta$, can be used, and taking $n_{cry} = 2.2$, (3.3) can be rewritten as:

$$\theta_{ext} + 5° = 2.2 \times (\theta + 5°) \tag{3.4}$$

so that an approximate expression for the internal bounce angle can be given by:

$$\theta \approx \frac{\theta_{ext} + 5}{2.2} - 5 \tag{3.5}$$

Using this equation, an internal bounce angle of $\theta = 7°$ is achieved by an external angle of $\theta_{ext} = 21.4°$ relative to the pump face, which is almost identical to that calculated from the exact equation (3.3). This $\sim 20°$ external angle can be tricky and awkward to arrange experimentally, and may well be inconvenient when more than one bounce amplifier module is required. As a result, a different geometry was designed with end faces cut at 14°.

3.3.4.3 Crystal with 14° end faces

For a crystal with 14° end faces, the cut is in the opposite direction to the 5° crystal and an incident beam experiences refraction in this crystal as illustrated in Fig 3.10. Applying Snell's Law as before with $\theta_{ext} = 14°$ and again using a crystal of Nd:YVO_4 with $n_{cry} = 2.16$ gives:

$$\sin(\theta_{ext} + 14°) = 2.16 \times \sin(14° - \theta) \tag{3.6}$$

For an internal bounce angle of $\theta = 7°$, the required external angle can be calculated to be $\theta_{ext} = 1.3°$ with respect to the front face of the crystal. For the small angle approximation used before, the internal bounce angle can then be approximated as:

$$\theta \approx \frac{\theta_{ext} + 14}{2.2} - 14 \tag{3.7}$$

Which also gives a value of $\theta_{ext} = 1.2°$, and shows that, to a good approximation, a beam incident parallel to the front face of the crystal will exit without angular deviation, having followed a path internally with a bounce angle of 7°. Experimentally this "linear" amplifier arrangement is a simpler way to ensure that the optimal bounce angle of 7° is achieved, and is also advantageous if two or more bounce amplifier modules are to be used in series in a power amplification scheme.

3.4 Bounce geometry laser oscillators

Having now covered the fundamental design and operating principles of the bounce geometry amplifier module, the implementation as an amplifier in a laser oscillator, to take advantage of the high gain and spatial averaging effects to produce high efficiency, high power, high spatial quality laser sources can now be considered. The simplest case of a multimode laser oscillator is explained first and then the effect of an intra-cavity lens is covered so as to be able to take account of the thermal lensing effects that will occur in the amplifier. This will then help to explain how the multimode cavity can be modified to become a high power oscillator operating on a high quality, TEM_{00} spatial mode.

3.4.1 Multimode bounce laser oscillator

The simplest case of a laser oscillator based on the bounce geometry amplifier with a crystal with 14° cut end faces, is the cavity shown in Fig 3.11. The cavity consists of a highly reflecting plane back mirror M1 (reflectivity R = 100 % at the lasing wavelength 1064 nm) and a partially reflecting plane output coupler OC ($R_{oc} < 100$ % at 1064 nm). The back mirror is placed a distance L1 from the centre of the crystal, and the output coupler a distance L2. In this first specific

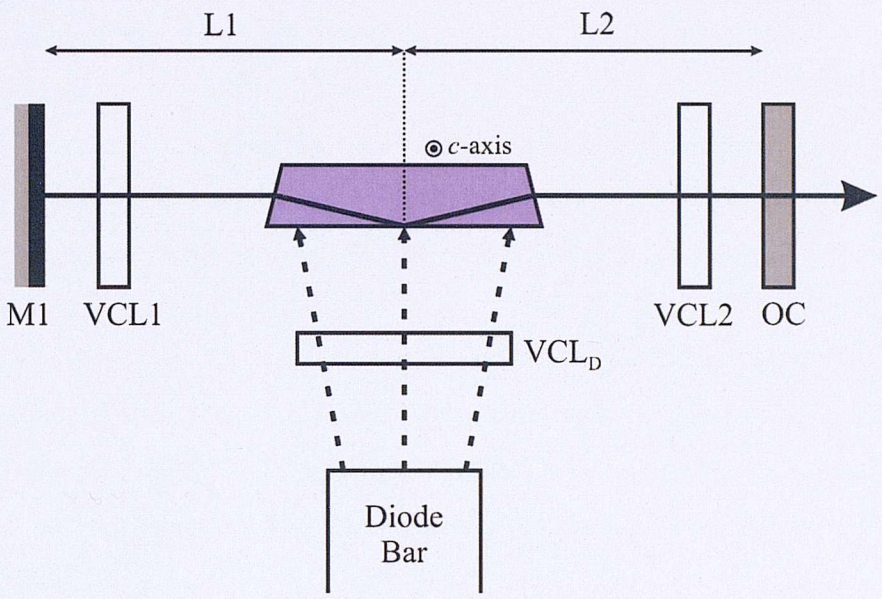


Fig 3.11. *An experimental, symmetrical bounce laser oscillator. The cavity is formed by a 100 % reflecting plane back mirror M1, and a partially reflecting plane output coupler, OC. The arm lengths L1 and L2 are in this case equal. Mode-matching of the cavity mode in the vertical dimension is done by cylindrical lenses VCL1 and VCL2 positioned at their focal length (f = 50 mm) from the centre of the crystal. The diode radiation is brought to a line focus by VCL_D.*

instance L1 = L2.

The crystal can be pumped by single diode, a combination of diodes, or a diode stack depending on the available power of individual diodes and the requirements of the system. For all the work carried out in this thesis, the laser oscillator was pumped by a single nLight diode bar rated to produce a maximum optical output power of 40 W at the pump wavelength of 808 nm. The emitter bar was 1 cm in length and consisted of 64 100 μm sized emitters separated by 150 μm. The room temperature emission spectrum was $\sim$2 nm wide and generally centred on a wavelength slightly larger than the 808 nm required. This was shifted by controlling the temperature of the diode heatsink to match the maximum absorption of the crystal. The emitters had a slow axis divergence of $\sim$10° and a fast axis divergence of $\sim$36° which was collimated by a microlens mounted on the emitters at manufacture. This collimated pump radiation was brought to a line focus on

the front face of the amplifier crystal by use of a plano-convex vertical cylindrical lens, VCL_D, of focal length 12.5 mm.

Inside the cavity, two further plano-convex VCLs (VCL1 and VCL2) with focal lengths f = 50 mm were positioned at roughly their focal length from the centre of the crystal, so that the size of the fundamental cavity mode in the vertical dimension was matched to the small size of the line-focused pump radiation in that same dimension. This contributes to a very good spatial overlap between the cavity mode and the gain region, thus helping to achieve a high power, high efficiency system. Additionally, VCL1 and VCL2 were orientated with their plane faces closest to the crystal to minimise the negative effects of spherical aberration in the system.

This initial system is known as a symmetric bounce oscillator because the back mirror and output coupler arm lengths (L1 and L2) are set equal. The minimum dimensions of the cavity are limited by the position of VCL1 and VCL2 and are to some extent dependent on the specific system requirements, but are typically in the range 60 mm < L1,L2 < 100 mm. For this type of short cavity, the fundamental mode is small in both horizontal and vertical dimensions and so due to the asymmetric gain volume the beam has near single mode spatial quality in the vertical (M^2 ~1) where the mode shape and gain region are well matched, but is multimode in the horizontal where the un-extracted gain region is large enough that higher order spatial modes can experience enough gain to reach lasing threshold. For this reason, the symmetric bounce oscillator is also known as a multimode bounce oscillator.

This simple type of cavity has now been well studied and previous investigations have determined that the optimum reflectivity for the output coupler in this high gain laser oscillator is typically R_{oc} = 30 %. Using this, previous work has also demonstrated multimode bounce laser oscillators with very high efficiencies (optical - optical ~ 60 %; slope ~ 70 %) and high output powers (>50 W). In a preliminary study for this thesis, a multimode bounce oscillator was constructed and the resultant power curve together with the spatial mode profile of the laser beam is shown in Fig 3.12. For the multimode case, the important performance parameters are output power, optical-optical conversion efficiency, and to a lesser

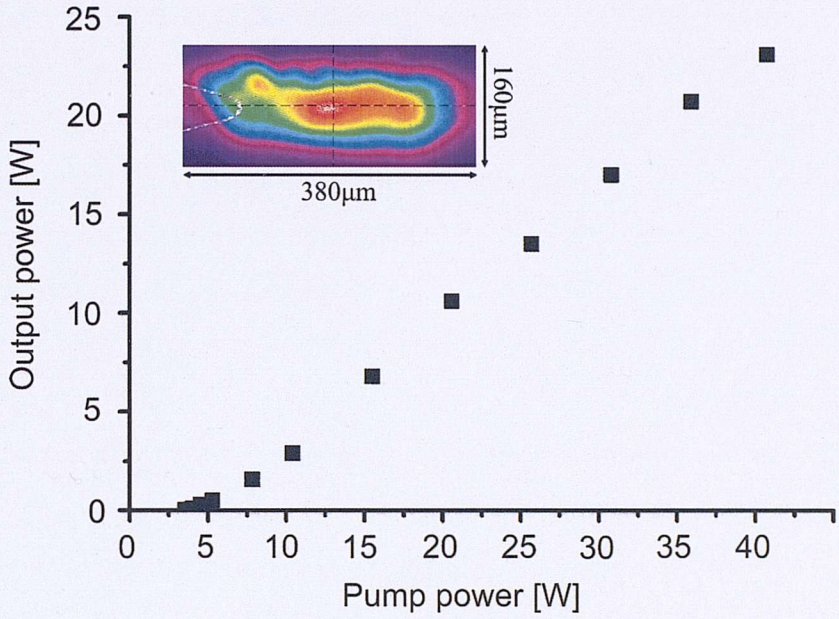


Fig 3.12. *Power curve and transverse beam profile at maximum pump power (inset) for a compact, symmetric, bounce geometry laser oscillator. Maximum output power is 23 W at 40 W pump power, with a 68% slope efficiency.*

extent, slope efficiency. As can be seen from the power curve, the output power of 23 W from 40 W of pump power represents an overall conversion efficiency of 57 % which is very good for this basic arrangement. The best reported in this geometery is $\sim$ 68 % [26] and the discrepency here is attributed to a number of factors. Predominantly the spectral quality of the pump diode, where very narrow band emission is desirable to maximise the population in the upper laser level, but also partly a poorer thermal contact which increases the strength of the thermal lens and affects the cavity mode and gain region overlap. The overall efficiency can never be greater than 74 % due to the quantum defect, and so achieving 57 % clearly illustrates the potential of the bounce amplifier. Another point to note regarding this system is the very linear nature of the power curve. There is no apparent saturation of the amplifier at the higher pump powers, indicating that, if the pump power was available, much more output power could be obtained from this simple system at a comparable efficiency. The downside of this simple configuration is that the beam quality is relatively poor; this is unavoidable in this

particular geometry and so the mulitmode bounce oscillator is particularly suited to high power applications where good beam quality is not critical.

These multimode cavities are relatively simple to align and produce high power, high efficiency operation from a very compact resonator. In many cases this could represent acceptable operating specifications. However, the ideal operating regime for laser oscillators is the production of a high efficiency TEM_{00} beam, with the possibility of high power operation if required. With a slight modification to the multimode cavity design, a bounce geometry oscillator can be configured for this high efficiency, high power operation in a TEM_{00} mode. To achieve this, the cavity in Fig 3.11 is changed so that L2 > L1, thus producing an asymmetric cavity. Previous studies have shown that the optimum dimensions have L2 $\sim$ 300 mm and L1 $\sim$ 80 mm, and adjustment of these for a given pump power can optimise beam quality and output power. To understand why this asymmetric configuration produces TEM_{00} operation, and to gain an understanding of the operating stability of the cavity under varying pump powers, and hence varying thermal lens strength, it is necessary to look in a little more detail at the effect an intra cavity thermal lens has on the spatial modes of the cavity.

3.4.2 Cavity stability and the effect of an intra-cavity lens

Knowledge of the cavity mode shape and its size, both in the gain region and on the output coupler, is a useful way of monitoring the performance of the oscillator, and an understanding of how they change with varying pump power will help when trying to design improvements to the cavity. For fixed cavity dimensions, an intra-cavity lens will define the shape and size of allowed modes within the cavity and so varying the strength of the lens can cause significant changes to the form of the cavity mode. The refractive index gradients created in the laser crystal due to thermal loading act as a lens of this form. Therefore, as the strength of the thermal lens increases with the pump power, due to the increased thermal load, the cavity mode size and shape can change significantly and the performance of the system will vary.

It was shown previously (Eqn(3.1)) that the strength of the thermal lens can

be given by:

$$K = \frac{1}{f} = \frac{dn/dT}{\kappa} \frac{\xi P_p}{\pi w_p^2} \text{ m}^{-1}$$

where ξ is the fractional heat load, P_p is the absorbed pump power and w_p is the $1/e^2$ Gaussian radius of the pump beam. This is the case for an end pumped, cylindrical rod geometry with circular symmetry, as most of the work into thermal lensing in solid-state media has considered. However, for the side pumped bounce geometry considered here, there is no cylindrical symmetry, the refractive index gradients are different in the horizontal and vertical directions and so the magnitude of the thermal lensing in the two directions will also be different.

In the vertical direction (normal to the plane of the bounce), the thermal lens is expected to be strong because the small size of the pump region will give a large temperature gradient between this area of highest thermal loading and the cold heatsink. However, the mode size in the vertical is small due to the focusing of the vertical cylindrical lenses incorporated into the cavity, and so is limited by diffraction. The lensing in the horizontal direction (in the plane of the bounce) is weaker, but the beam size is relatively much larger than in the vertical and so the lensing effect becomes more significant. In a previous study, the astigmatism of the cavity has been characterised as the ratio between the dioptric powers in the vertical and horizontal directions, and was found to be approximately 20 [84]. Despite this, the effect of the thermal lens on the mode in the horizontal direction within a bounce cavity will be the most significant contributor to the stability and performance of the system.

A model for finding mode sizes and describing the mode shape inside a cavity containing a thermal lens was first developed by Magni in 1986 [85]. He considered a solid state laser containing an amplifier rod which when pumped, acted as a thermal lens whose dioptric power increased with pump power. This was modeled as a thin lens positioned at the centre of the amplifier rod, a distance L_1 from a back mirror, and L_2 from the output coupler. The cavity length is then:

$$L = L_1 + L_2 \tag{3.8}$$

And the effective length of the cavity is defined as:

$$L' = L_1 + L_2 - \frac{L_1 L_2}{f} \tag{3.9}$$

The g-parameters g_1 and g_2 used in resonator stability analysis are then given by:

$$\begin{aligned} g_1 &= 1 - \frac{L_2}{f} - \frac{L'}{R_1} \\ g_2 &= 1 - \frac{L_1}{f} - \frac{L'}{R_2} \end{aligned} \tag{3.10}$$

where R_1 and R_2 are the radii of curvature of the two end mirrors. For a plane-plane cavity such as is used in the bounce, $R_1 = R_2 = \infty$, and these simplify to:

$$\begin{aligned} g_1 &= 1 - \frac{L_2}{f} \\ g_2 &= 1 - \frac{L_1}{f} \end{aligned} \tag{3.11}$$

Resonator stability is given by the condition $0 < g_1 g_2 < 1$ and a plot of g_2 as a function of g_1 is shown in Fig 3.13 to help understand the stability of the bounce cavity. The axes correspond to $g_1 g_2 = 0$, the hyperbolae to $g_1 g_2 = 1$ and the two areas indicated Zone I and Zone II correspond to stable regions of operation of the laser cavity. Starting at the point 1 and following the line indicated corresponds to moving along a line of increasing thermal lens power within a fixed cavity. This shows that for a general, asymmetric cavity, there are two stable regions of operation separated by an unstable region and these are defined by the strength of the thermal lens at four specific points. The equation of this straight line may be written as:

$$g_2 = \frac{L_1}{L_2} g_1 + (1 - \frac{L_1}{L_2}) \tag{3.12}$$

so the gradient of the line is defined by the ratio L_1/L_2, or the degree of asymmetry in the cavity. Thus, for the symmetric cavity, the line has a gradient of unity and passes through the origin of the stability plot, as indicated by the dotted line in Fig 3.13. This results in the symmetric cavity having a large single stability region up to high pump powers. It can then also be seen from Fig 3.13 that as the degree of asymmetry increases and the gradient of the line changes, the region of unstable operation becomes larger.

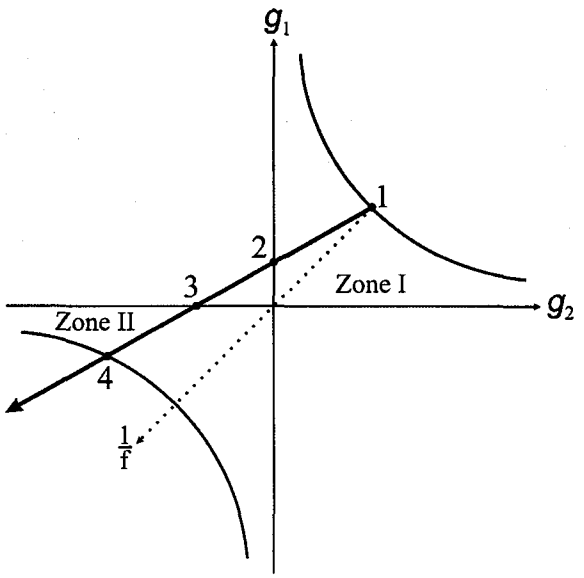


Fig 3.13. *A plot of the cavity stability parameters g_1 and g_2 showing the cavity stability zones for an intracavity lens with focal length* f. *Zone I and Zone II are regions of stable cavity operation. Points 1-4 mark specific mode shapes inside the cavity. The hyperbolae represent $g_1 g_2 = 1$.*

For the general, asymmetric case, the edges of the stability zones correspond to particular mode shapes determined by the power of the thermal lens, these points are shown schematically in Fig 3.14. For the case of no diode-pumping, there is no thermal lens ($1/f = 0$) so $g_1 = g_2 = 1$ and the cavity mode is as pictured in Fig 3.14.1. The cavity is then stable under further pumping, until point 2 is reached, at which point the power of the thermal lens is $1/f = 1/L_2$ and is strong enough to form a waist at the mirror in the long arm of the cavity, Fig 3.14.2. The cavity is then unstable until point 3, when the pumping has produced a thermal lens with power $1/f = 1/L_1$, and the mode forms a waist at the mirror in the short arm of the cavity, Fig 3.14.3. The cavity is then stable until point 4 where the thermal lens is strong enough to form a waist on both mirrors, Fig 3.14.4, and has a power $1/f = 1/L_1 + 1/L_2$.

To understand why the asymmetric case then leads to TEM_{00} operation, consider how the power of the thermal lens affects the size of the mode in the gain region. Magni shows that the spot size on the thin lens being considered as the

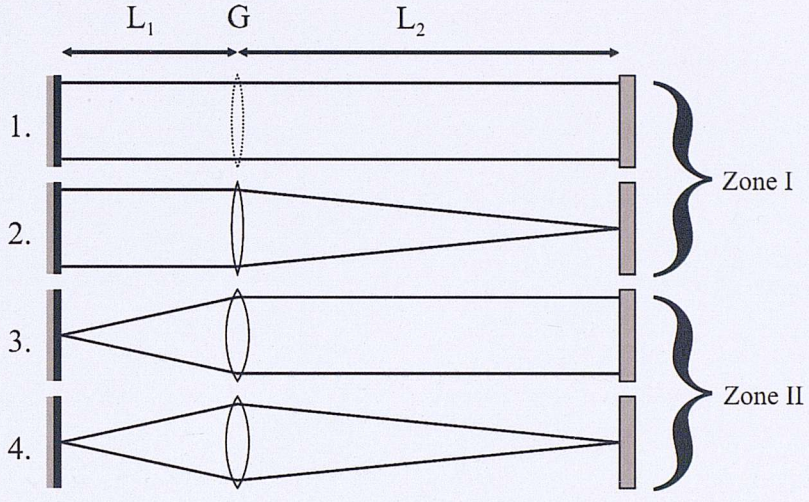


Fig 3.14. *Thermally-induced lensing effect on beam propagation through the cavity. Points 1-4 illustrate the mode shape at the edges of the stability regions marked in Fig 3.13 for specific values of the thermal lens power. G marks the position of the gain medium (and hence thermal lens). L_1 and L_2 are the cavity arm lengths.*

gain region, can be expressed as [85]:

$$w_g^2 = \frac{\lambda}{\pi} \frac{2KL_1L_2 + L_1 + L_2}{[(1 - g_1g_2)g_1g_2]^1/2}, \qquad K = \frac{1}{f} \tag{3.13}$$

Fig 3.15 shows a plot of w_g against $1/f$ for an asymmetric cavity, where the two stability regions can be clearly seen. The cavity is stable while the mode size in the gain remains a finite size, and so as the spot size asymptotically tends to infinity the cavity becomes unstable. These unstable points can be seen to coincide with the thermal lens powers of $1/f = 0$, $1/L_2$, $1/L_1$, $1/L_1 + 1/L_2$, as in the cavity mode shape discussion above. For high efficiency TEM_{00} operation, the cavity mode size in the gain region has to match closely the size of the gain region itself, therefore the minimum spot size w_{g0} should be close to x_g, the approximate size of the gain region as seen by the mode in the bounce geometry. Magni also shows that the minimum spot size in the gain region can be shown to be given by:

$$w_{g0}^2 = \frac{2\lambda}{\pi} \frac{1}{\Delta\frac{1}{f}} \tag{3.14}$$

where $\Delta(1/f)$ is the width of the stability region as indicated in Fig 3.15 and is equal to $1/L_2$. Therefore, $w_{g0} \propto \sqrt{L_2}$ and as the length of the longer cavity arm

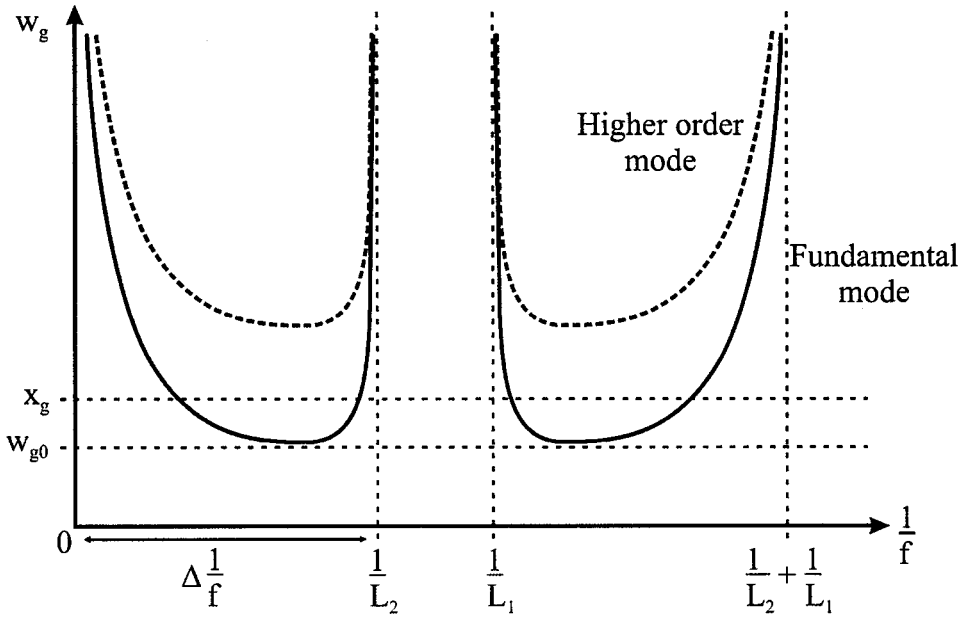


Fig 3.15. *Stability curves for an asymmetric cavity where w_g is the spot size in the gain region that has size x_g. The higher order modes have much larger spot sizes and so suffer larger diffractive losses.*

is increased, the plot in Fig 3.15 shifts upwards and the minimum spot size of the cavity mode can be matched better with the gain region size.

Equally important for TEM_{00} operation are the stability curves for higher order spatial modes of the cavity. These are shown on Fig 3.15 and have the same form as for the fundamental mode but with much larger spot sizes. This is significant for the operation of a TEM_{00} cavity. By operating the laser close to the beginning of one of the stability zones, it can be seen that while the fundamental mode may be smaller than the gain region, the higher order modes of the cavity are subject to far higher diffractive losses and are thus suppressed, even if there is a large amount of un-extracted gain. Thus, by suitable choice of cavity arm lengths, it is possible to configure a cavity such that for a certain region of pump powers (and hence thermal lens power) the only cavity mode that is stable is the TEM_{00}, and this is also well matched to the gain region for high efficiency operation. This has been achieved in a previous study where ultra-high efficiency operation (>68%) was obtained in a TEM_{00} beam with high power [26].

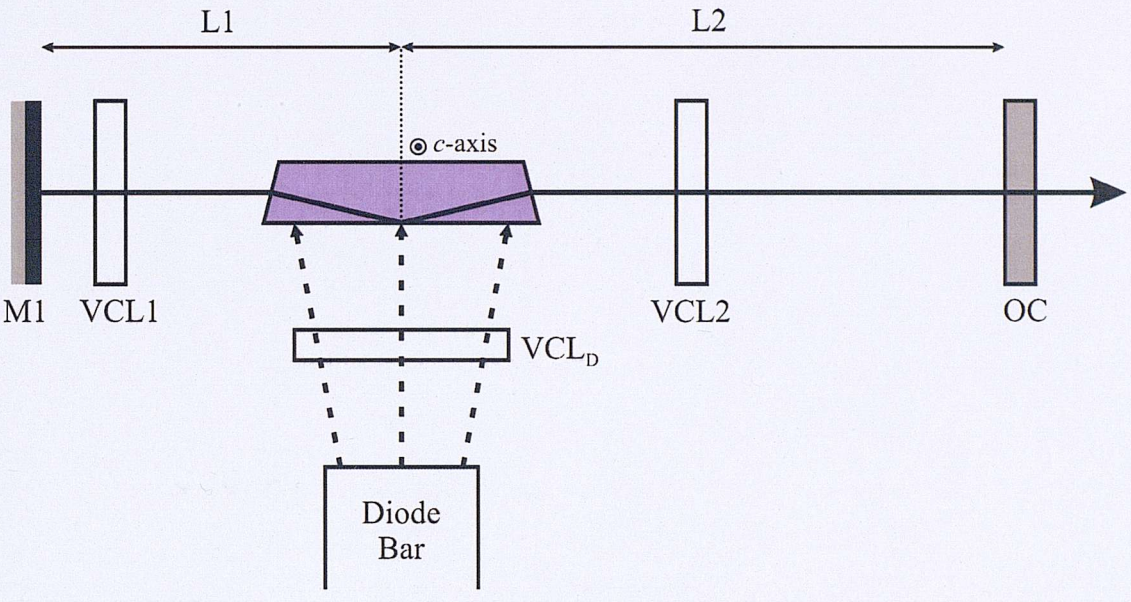


Fig 3.16. *An experimental, asymmetric bounce laser oscillator. The cavity is formed by a 100% reflecting plane back mirror M1, and a partially reflecting plane output coupler, OC. Mode-matching of the cavity mode in the vertical dimension is again done by cylindrical lenses VCL1 and VCL2. The diode radiation is brought to a line focus by VCL_D.*

3.4.3 TEM_{00} asymmetric bounce laser oscillator

The multimode bounce oscillator has been shown to be capable of producing high power, high efficiency laser beams, but is unable to produce the high spatial qualities that are demanded of many applications due to the fact that the fundamental cavity mode size in the plane of the bounce is much smaller than the high gain region, and so higher order spatial modes may oscillate. TEM_{00} operation can be achieved by making the cavity arm lengths asymmetric which generates a better matching between the gain and spatial mode, and also prohibits higher order spatial modes from oscillating and degrading the beam quality. In a preliminary study to this thesis, one such asymmetric cavity was constructed, and is shown in Fig 3.16. The cavity is very similar to the multimode oscillator in Fig 3.11 in that it consists of a 1.1 at.% neodymium doped Nd:YVO_4 crystal with end faces cut at 14°, pumped by a single diode bar rated to produce a maximum optical output power of 40 W at the pump wavelength of 808 nm, with the pump radia-

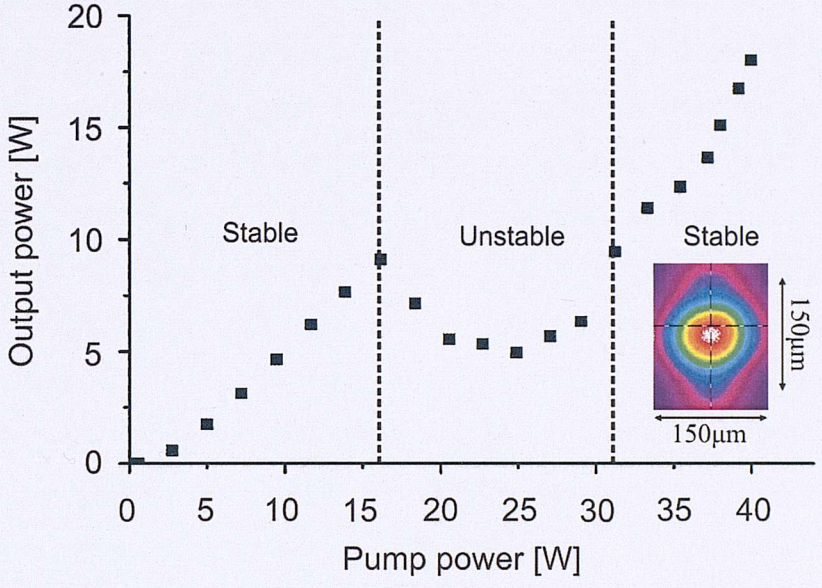


Fig 3.17. *Power curve for the asymmetric cavity, clearly showing the two stable regions of operation. Inset shows the output beam quality in the second stability region.*

tion brought to a line focus on the front face of the amplifier crystal by use of a plano-convex vertical cylindrical lens, VCL_D with focal length 12.5 mm. Inside the cavity, two further plano-convex VCLs (VCL1 and VCL2) with focal lengths f = 50 mm were positioned at their focal length from the centre of the crystal so that the size of the fundamental cavity mode in the vertical dimension was matched to the small size of the line-focused pump radiation in that same dimension. The cavity was once again formed by a highly reflecting plane back mirror M1 (reflectivity R = 100% at the lasing wavelength 1064 nm) and a partially reflecting plane output coupler, OC (R_{oc} = 30% at 1064 nm). The back mirror was placed a distance L1 from the centre of the crystal, and the output coupler a distance L2. For this asymmetric, TEM_{00} case, L1 = 80 mm and L2 = 300 mm was chosen.

The power curve for this cavity is shown in Fig 3.17 and is distinct from the multimode case in Fig 3.12 in that there are several different regions of operation clearly visible. From threshold, there is an initial increase in output power to a first peak. This corresponds to the first region of stability in Fig 3.13, between points 1 and 2. The power then drops significantly, despite the increased pumping, before starting to increase again, which corresponds to the unstable region in Fig

3.13 between points 2 and 3. The steady increase in power is then the second region of stability in Fig 3.13, between points 3 and 4. It is seen that this cavity does not become unstable again and this is due to the thermal lens being too weak to be able to form a waist at both cavity mirrors. It is also worth noting that the slope efficiency of the laser is very different in the two stable regions. Indeed, in the second stability zone it seems that the slope efficiency is over or approaching 100 %, whereas the quantum defect limit would suggest that the maximum attainable slope efficiency should be ~74 %. The large slope efficiency near the start of the second stabilty zone is in fact due to the rapidly improving overlap between the cavity mode and the gain region caused by the strong thermal lens. If the pump power could be increased further, the slope efficiency would reduce to a level similar to that seen in the first stability zone.

Good beam quality is achieved throughout both stability zones, and the highest quality TEM_{00} operation is achieved at the start of the second stability zone, an example of the beam profile is also shown in Fig 3.17. The maximum output power from this cavity was 18.1 W, achieved with a pump power of 40 W. This is lower than the multimode case due to the reduced spatial overlap between the TEM_{00} cavity mode and the gain region, although the overall efficiency of 45 % is still excellent for this type of cavity.

3.5 Conclusions

This chapter has introduced the bounce geometry laser and how its unique features enable it to produce high power outputs with very high spatial quality. Initially, the thermo-optic effects in solid state media had to be considered and so the mechanisms of quantum defect heating, Auger upconversion, cross relaxation and excited state absorption, by which heat is deposited in the laser crystal, were detailed. This heating leads to refractive index gradients in the crystal which effectively act as a lens in the cavity, whose strength varies with the applied pump power, affecting the cavity stability. The heating also leads to expansion of the crystal which generates strain in the crystal lattice and results in stress induced birefringence which distorts the polarisation state of the laser beam. The

gain of the laser medium is polarisation dependent and so the beam experiences non-uniform gain across it's transverse profile, degrading it's quality. These two effects are both more pronounced at high pump powers and can casue significant performance limitations in high average-power solid state systems.

The concept of the bounce geometry is then introduced as a means of combating the thermal lens and gain non-uniformities present at high pump powers. The basic idea behind the bounce is shown to be that by taking a total internal reflection off the pump face of the laser crystal, the very high inversion region close to the surface can be accessed, and the bounce path enables significant averaging of both the gain non-uniformity and the thermally induced lens aberrations. The passage through the high inversion region at the pump face also means that the bounce geometry exhibits very high gain and optical-optical conversion efficiencies. The methods of cooling by which the excess heat is efficiently removed from the crystal is briefly detailed, together with the diode pumping geometry and the explicit geometric form of the laser crystals used in this thesis.

Having covered the general operating principles of the bounce geometry, two specific experimental cavities are discussed. The first of these was a simple, compact, symmetric cavity which produces a spatially multi-mode output of 23 W when pumped with a 40 W diode, giving an overall optical-optical conversion efficiency of 57 % with a slope efficency of ~68 %. Before being able to describe the construction of a TEM_{00} cavity, the cavity stability theory of Magni is discussed. This describes the effect of an intracavity lens on the cavity mode shape and so is useful in describing the effect of the thermally induced lens. The theory shows that two distinct regions of stable laser operation should occur, depending on the position of the intracavity lens relative to the cavity mirrors. A second bounce geometry cavity is then detailed which has the laser crystal positioned asymmetrically within the laser cavity. This is shown to produce a maximum output power of 18.1 W in a TEM_{00} beam, with two distinct regions of stable operation visible in the total operating range.

In the context of this thesis, these two experimental cavities serve as a demonstration of the ease with which the bounce geometry can be used to produce a high power, TEM_{00} output. It is anticipated that obtaining stable modelocked

performance will be sensitive to the attainable beam quality and so a robust, high-power, high-beam quality cavity will be required. Th asymmetric bounce cavity provides this and so will be used as the starting point when it comes to designing a modelocked cavity.

Chapter 4

A SESAM modelocked bounce geometry laser oscillator

4.1 Introduction

With the function of the bounce geometry and the basic mechanisms of pulsed behaviour now understood, this chapter can move on to describe the main experimental work of the thesis. The aim of the work undertaken was to examine the feasibility of producing a high power, efficient, picosecond laser source based on the bounce geometry amplifier. In order to do this, one of the modelocking mechanisms described in Chapter 2 needed to be chosen. Saturable absorber modelocking was the mechanism employed initially as it is generally the simplest to implement. The saturable absorber to be used will be a semiconductor saturable absorber mirror (SESAM) which is an integrated device based on a small number of semiconductor quantum wells grown on top of a Bragg mirror. This was chosen mostly for its simplicity and availability, with commercial devices being readily available with a range of operating parameters. The use of SESAMs for short pulse production in solid-state laser media is now widespread [86–95] and so the principles of operation are now well understood and the manufacturing processes are of a high quality.

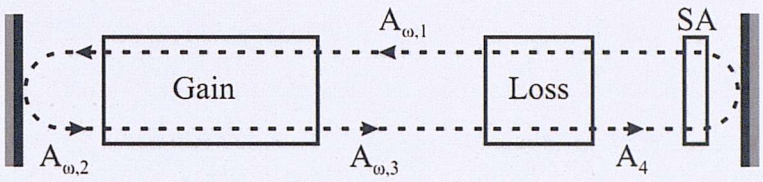


Fig 4.1. *Schematic cavity used to calculate transmission operators for the gain, loss, and saturable absorber (SA) elements*

The chapter begins by covering in more detail the saturable absorber modelocking mechanism introduced briefly in Chapter 2. This is followed by a description of the form and function of the SESAM devices to be used in this experimental work. There is then a discussion of the design considerations that will be important when building the modelocked cavity and the variables that will be available to modify the performance. The experimental laser cavities are then introduced as a development process of cavity modification, leading to the description of a picosecond modelocked bounce geometry laser oscillator with a 12 ps pulse duration, and 6.1 W of average power at a repetition rate of 81 MHz. The chapter is concluded with a brief discussion on power scaling, and an experimental implementation of a Master Oscillator Power Amplifier system is demonstrated as a means of achieving high power modelocked operation. This results in a 30 ps pulse train with average power 60 W at a repetition rate of 77 MHz, through use of a bounce geometry amplifier that gives a 50 % extraction efficiency.

4.2 Action of a saturable absorber

Having looked briefly in an earlier chapter at the qualitative action of a saturable absorber in a cavity, the action of a fast saturable absorber is now considered in more detail. This theory was developed mainly by Haus, with some early work done by Siegman and Kuizaga [96–98], although here the treatment by Svelto [99] will be outlined.

Consider a schematic laser cavity such as the one shown in Fig 4.1 where the two cavity mirrors enclose a gain element, a non-saturable loss element, and a saturable loss element. The analysis proceeds by constructing transmission opera-

tors that describe the effect of each element on the pulse, for each of the elements in turn. These transmission operators are then combined together with the requirement for replication of the pulse on one round trip in the cavity, to produce solutions that give the shape of the pulse.

The first step is to construct a transmission operator for the gain element. This is done by considering the effect of a single pass through the amplifier on the spectral amplitude of the pulse, A_ω. If $A_{\omega,1}$ is the amplitude before the amplifier, and $A_{\omega,2}$ is the amplitude after, then t_g, such that $A_{\omega,2} = t_g A_{\omega,1}$ is given by:

$$t_g = \frac{A_{\omega,2}}{A_{\omega,1}} = \exp\left\{\frac{-i\omega nl}{c}\right\} \times \exp\left\{\frac{g_0/2}{1+\frac{2i(\omega-\omega_0)}{\Delta\omega}}\right\} \tag{4.1}$$

where n is the refractive index of the gain medium of length l, ω_0 is the central laser frequency, and $\Delta\omega$ is the FWHM of the laser line. The first term corresponds to a phase delay on passage through the ampifier and the second term describes the effect of the gain, such that the power gain of the amplifier is given by:

$$G(\omega) = |t_g|^2 = \exp\{g_0(\omega)\} \tag{4.2}$$

so that the frequency dependent gain, $g_0(\omega)$, is the expected Lorentzian lineshape for a homogeneous line.

$$g_0(\omega) = \frac{g_0}{1+\left\{\frac{2(\omega-\omega_0)}{\Delta\omega}\right\}^2} \tag{4.3}$$

If it is assumed that the spectral width of the pulse is somewhat narrower than $\Delta\omega$ then the argument of the second exponent in Eqn(4.1) can be expanded as a power series in $(\omega - \omega_0)$, so that to second order:

$$t_g = \exp\left\{-i\left(\frac{\omega nl}{c} + \frac{g_0(\omega-\omega_0)}{\Delta\omega}\right)\right\} \times \exp\left\{\frac{g_0}{2}\left[1-\left(\frac{2(\omega-\omega_0)}{\Delta\omega}\right)^2\right]\right\} \tag{4.4}$$

The imaginary terms in the first exponent of Eqn(4.4) correspond to a phase delay acquired by the beam on passage through the amplifier. This corresponds to a time delay of the pulse, which is given by:

$$\Delta\tau = \frac{\mathrm{d}\phi}{\mathrm{d}\omega} = \frac{nl}{c} + \frac{g_0}{\Delta\omega} \tag{4.5}$$

Thus the delay is not simply nl/c but has an additional term contributed by the gain line which could be significant in certain applications. For example in

active modelocking schemes it needs to be accounted for so that the period of the modulator can be matched to the round trip time of the cavity.

The pulse amplitude is generally considered in a suitable local time parameter, and since the current interest is only the effect of the amplifier on this pulse amplitude, the phase term will be ignored from now on so that the single pass transmission operator is:

$$t_g = \exp\left\{\frac{g_0}{2}\left[1-\left(\frac{2(\omega-\omega_0)}{\Delta\omega}\right)^2\right]\right\} \tag{4.6}$$

Any loss introduced by the end mirror will also be ignored as this will be accounted for in the overall cavity loss. The modified pulse then passes through the amplifier again, experiencing another factor of t_g so that the spectral amplitude after a double pass though the amplifier, $A_{\omega,3}$, is given by:

$$A_{\omega,3} = t_g^2 A_{\omega,1} = A_{\omega,1}\exp\left\{g_0\left[1-\left(\frac{2(\omega-\omega_0)}{\Delta\omega}\right)^2\right]\right\} \tag{4.7}$$

Assuming that $g_0 \ll 1$ (this is not necessariy valid all the time, but makes the analysis simple), the exponent can be expanded to give:

$$A_{\omega,3} = A_{\omega,1}\left\{1+g_0\left[1-\left(\frac{2(\omega-\omega_0)}{\Delta\omega}\right)^2\right]\right\} \tag{4.8}$$

This now describes the effect a double pass through the amplifier has on a pulse's spectral amplitude. To proceed further, one needs to know the effect of the transmission in the time domain. To do this, use is made of the property of a Fourier transform which says that for a Fourier transform pair, $A(\omega) \rightleftharpoons A(t)$:

$$FT\left[\frac{\mathrm{d}^n A(t)}{\mathrm{d}t^n}\right] = \{i(\omega-\omega_0)\}^n A(\omega) \tag{4.9}$$

Applying this to Eqn(4.8):

$$A_3(t) = \left\{1+g_0\left[1+\left(\frac{2}{\Delta\omega}\right)^2\frac{\mathrm{d}^2}{\mathrm{d}t^2}\right]\right\}A_1(t) \tag{4.10}$$

Where $A_1(t)$ and $A_3(t)$ are the pulse amplitudes entering, and leaving the amplifier after one round trip. This then demonstrates that the effect of the amplifier on the pulses's amplitude after one round trip can be described by a round trip operator:

$$\hat{T_g} = \left\{1+g_0\left[1+\left(\frac{2}{\Delta\omega}\right)^2\frac{\mathrm{d}^2}{\mathrm{d}t^2}\right]\right\} \tag{4.11}$$

Next, the effect of cavity losses arising from partial mirror reflectivities and any other internal losses, not including the saturable absorber, are considered. These are all combined into a single loss parameter represented by the "loss" element in Fig 4.1. If $A_3(t)$ is the pulse amplitude entering the loss element, and $A_4(t)$ the pulse amplitude after transmission, then:

$$A_4(t) = [\exp(-\gamma_c/2)]A_3(t) \tag{4.12}$$

so that the ratio of the respective intensities, $I_4/I_3 = (A_4/A_3)^2$, shows the expected value exp(-γ_c). The transmission factor for the round trip is then given by $\exp(-\gamma_c)$. This can be expanded to give a transmission operator for the non-saturable round trip cavity losses of:

$$\hat{T}_l = 1 - \gamma_c \tag{4.13}$$

Finally, the action of the saturable absorber is taken account of. This is initially written in the same form as Eqn(4.12)

$$t_{sa} = \exp\{-\frac{\gamma_{sa}}{2}\} \tag{4.14}$$

where γ_{sa} is the single pass loss of the absorber, and is assumed to be of the form:

$$\gamma_{sa} = \frac{\gamma'}{1 + \frac{I}{I_s}} \tag{4.15}$$

where γ' is the unsaturated loss of the absorber, $I = I(t)$ is the pulse intensity, and I_s is the saturation intensity of the absorber. The double pass transmission through the absorber is then $t_{sa}^2 = \exp(-\gamma_a)$. Under the assumptions that $\gamma' \ll 1$ and $(I/I_s) \ll 1$ (again, these assumptions are not necessarily always valid, but make the analysis simple) the approximations:

$$t_{sa}^2 \simeq 1 - \gamma_{sa} \simeq 1 - \gamma' \left\{1 - \frac{I}{I_s}\right\} \tag{4.16}$$

are valid, and by introducing $|A|^2$ as the beam intensity, the transmission operator for a double pass of the saturable absorber can be written as:

$$\hat{T_{sa}} = 1 - \gamma' + \gamma' \frac{|A|^2}{I_s} \tag{4.17}$$

Now that a full set of transmission operators for the elements in the cavity have been obtained, self-consistency of the propagating pulse requires that in the steady state:

$$\hat{T}_g \hat{T}_l \hat{T}_{sa} A(t) = A(t) \tag{4.18}$$

and so combining Eqns(4.11),(4.13),(4.17) with the assumption that $(g_0, \gamma_c, \gamma') \ll 1$ results in:

$$\left\{ g_0 \left[1 + \left(\frac{2}{\Delta\omega} \right)^2 \frac{\mathrm{d}^2}{\mathrm{d}t^2} \right] - \gamma_c - \gamma' + \gamma' \frac{|A|^2}{I_s} \right\} A(t) = 0 \tag{4.19}$$

Which has solutions:

$$A(t) = A_0 \,\mathrm{sech}(\frac{t}{\tau}) \tag{4.20}$$

where

$$\tau = \left(\frac{2g_0}{\gamma'} \right)^{\frac{1}{2}} \left(\frac{2}{\Delta\omega} \right) \left(\frac{I_s}{|A_0|^2} \right)^{\frac{1}{2}} \tag{4.21}$$

and with g_0 being such that:

$$\gamma_c + \gamma' - g_o = \frac{4g_0}{\Delta\omega^2 \tau^2} \tag{4.22}$$

It is therefore seen from Eqn(4.20) that the intensity profile, $A^2(t)$, of steady state pulses in any cavity containing a saturable absorber is a sech^2 form. It can also be seen from Eqn(4.22) that $g_0 < \gamma_c + \gamma'$. This demonstrates that while the absorber is unsaturated, the saturated gain of the cavity is lower than the total unsaturated cavity losses and so the laser has a net loss. During the passage of the pulse through the absorber, the total cavity losses are reduced so that a time window of net gain exists only during passage of the pulse.

4.2.1 Fast and slow saturable absorbers

Up to this point, when considering the action of a fast saturable absorber on a cavity, it has been implicitly assumed that an ideal fast absorber whose absorption parameter reacts instantaneously to the intensity of the prevailing pulse is being considered. This resulted in the formation of a net gain window, which was opened and closed by the leading and trailing edges of the pulse. This window was open for a time comparable to that of the pulse duration, resulting in pulse shortening

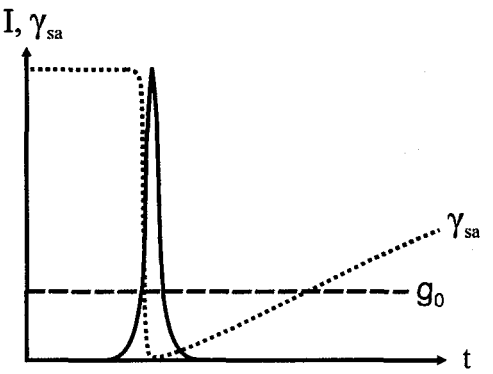


Fig 4.2. *Saturable absorber response for a slow absorber showing a long period of net gain in the tail of the pulse. (Adapted from [100])*

on each pass through the absorber. In practice this is not the case however, as the processes leading to the saturation effect occur on a finite timescale. Typically, saturable absorbers can react effectively instantaneously to the intensity of the pulse in the leading edge, but once saturated, they require a relaxation time to decay to their unsaturated state so that subsequent pulses can saturate the absorber again.

These relaxation times are typically 10's - 100's picoseconds (even nanoseconds for some organic dyes) and so it is quite easy to imagine a situation in a solid state laser system, where the pulse duration is significantly shorter than the relaxation time of the saturable absorber which is supposed to be affecting it. We are not however, in a situation where the gain changes during passage of the pulse; the gain in solid state medium will saturate with the average intracavity intensity. The qualitative treatment described in §2.3.2 for a 'slow' saturable absorber therefore does not apply in this case. What is true, is that a situation arises where using an absorber with a relaxation time much larger than the duration of the pulses it is generating, results in a net gain window which can be open for a significant length of time after the pulse has passed (see Fig 4.2).

Initially it seems as though this situation should not be possible. Pulses with durations much shorter than the relaxation time would not be stabilised by the absorber, because the long net gain window behind the pulse would amplify it's trailing edge, or noise inside the cavity. This was assumed to be the case for a long time and so it was surprising when numerical modelling [101] showed that

pulses with durations much shorter than the relaxation time of the absorber could be sustained. In fact, these models showed that a guideline for the minimum achievable pulse duration with this type of 'slow' absorber was only ~10 % longer than for an ideal fast absorber.

Two main things were found to contribute to this [100, 101]. Firstly, the losses due to the filtering action of the gain decrease quadratically with the pulse duration, Eqn(4.22), this means that the gain clamps to a lower value for the slightly longer pulse and so the net gain window is open for a shorter time in the tail (Fig 4.2). Secondly, the action of the absorber on the leading edge of the pulse effectively delays the pulse, shifting the peak backwards so that any noise can be absorbed before it has time to grow. From this consideration it is possible to obtain a guideline for the minimum pulse duration that can be supported stably by an absorber with a given recovery time [101].

The net gain immediately after passage of the pulse can be approximated as γ'/S where S is the saturation parameter of the absorber, defined as the ratio of the pulse fluence to the absorber saturation fluence, F_p/F_{sat}. The absorber recovery follows an exponential that can be approximated to a linear decay immediately after the pulse peak (see Fig 4.2) with a slope $-\gamma'/\tau_a$, where τ_a is the recovery time of the absorber. This allows us to define a time over which there is a net gain behind the pulse, measured from the peak of the pulse, this is $\frac{\gamma'/S}{\gamma'/\tau_a} = \tau_a/S$.

Numerical simulations have shown that the temporal shift of the pulse per round trip was:

$$\Delta t \approx 0.12 \times \gamma' \times \tau_p \tag{4.23}$$

for sech^2 pulses of duration τ_p, and was only weakly dependent on S. Considering a small amount of noise at a time τ_a/S behind the peak of the pulse, it experiences a linearly rising gain as the pulse is slowly shifted backwards, and the total gain experienced by the noise before it completely merges with the pulse can be calculated as:

$$g_{tot} \approx \frac{9}{2S^2}\frac{\tau_a}{\tau_p} \tag{4.24}$$

Setting the condition that this gain should be small enough so that the noise does not acquire energy comparable to the pulse energy allows an estimation of the

minimum pulse duration attainable. It is known that 60dB is enough to amplify quantum fluctuations to significant levels so if this is the maximum gain allowed, $g_{tot} < \ln 10^6 \approx 14$. Together with a saturation parameter of 5, this results in the simple stability condition that $\tau_p \gtrsim 0.013\tau_a$, which says that an absorber can stably modelock a pulse with a duration up to 80 times shorter than its own recovery time.

This condition is quite flexible though and depends on the saturation parameter chosen, as well as the accepted level of gain for the noise. However, because of the typically logarithmic nature of gain statements, a large change here does not strongly alter the limit. For larger saturation parameters, the net gain after the pulse is smaller, and the time window of net gain is shorter. This is only slightly offset by a smaller temporal shift of the pulse (Eqn(4.23)) and so even shorter pulses can be supported if the saturation is stronger. The criterion does not depend on the modulation depth of the absorber however, because a doubling of the modulation depth would give twice the net gain after the pulse, but also twice the temporal shift, so that the time for amplification is reduced by half and the total gain remains the same.

What has just been shown then, is that within the type of modelocking described in §2.4.2.1 as 'fast saturable absorber', there is a further distinction between cases with an ideally fast absorber, and one with a recovery time significantly longer than the pulse duration obtained. This type of 'slow absorber' modelocking is different from that described in §2.4.2.2 however because it does not make use of dynamic gain saturation. It requires a slightly different treatment than the ideal fast case to explain how the absorber can stabilise the pulse production when there is a net gain window of significant duration in the tail of the pulse. It was thus demonstrated, with a few simple assumptions, that a saturable absorber can produce stable pulses with durations significantly shorter than its recovery time.

4.2.2 The Q-switching instability

The discussion so far has been based around achieving CW modelocking (CWML), that is, a continuous train of pulses of equal duration and peak amplitude. How-

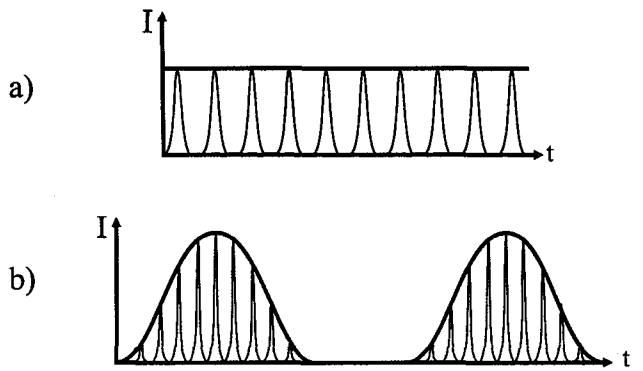


Fig 4.3. *The two different regimes of modelocking. Constant peak height CW (a), peak height modulated by a giant pulse Q-switched envelope (b).*

ever, because the cavity created has a time varying loss, together with a laser medium that has a relatively long upper state lifetime, it is possible for the cavity to operate in the regime of Q-switched modelocking (QSML). Here, a train of short pulses with the same duration, separated by the cavity round trip time is still generated, but this time the amplitudes are modulated by a giant pulse with a duration many times longer than the round trip time (see Fig 4.3). Typically, the modelocked repetition rate will be of the order megahertz, determined by the cavity length, whereas the Q-switched repetition rate will be in the kilohertz range, determined by the relaxation oscillation period of the laser medium. For some applications involving second harmonic generation or other frequency conversion, micro-fabrication or surgery, this Q-switched form can be useful as it provides greater peak pulse energy but still in a modelocked pulse train. It is the intention though to produce a stable, CW modelocked source and so an idea of the conditions that have to be fulfilled in order to avoid Q-switched operation will be useful.

Assuming a slow absorber and also that the absorber fully recovers in between each pulse, which is a reasonable assumption to make as the pulse separation will typically be several nanoseconds and the absorber recovery can quite easily be tens of picoseconds (for ultra high repetition rate lasers this condition may not necessarily be trivial), it can be shown that the mode-locked laser can be described

by the following coupled rate equations [102]:

$$T_R \frac{\mathrm{d}E_p}{\mathrm{d}t} = g - \gamma_c - q_p(E_p) \tag{4.25}$$

$$\frac{\mathrm{d}g}{\mathrm{d}t} = \frac{-g - g_0}{\tau_L} - \frac{E_p}{E_{SL}T_R}g \tag{4.26}$$

where τ_L is the upper state lifetime of the gain medium, E_p is the energy of a pulse in the cavity, E_{SL} is the saturation energy of the gain, and q_p is the round trip loss in average power. For stability, it is required that the relaxation oscillations are damped so that no large scale oscillations can grow into Q-switched behaviour. Linearising the differential equations around the average values of g and E_p it can be shown that the stability condition is [103]:

$$E_p \left| \frac{\mathrm{d}q_p}{\mathrm{d}E_p} \right|_{\overline{E_p}} < \frac{T_R}{\tau_L} + \frac{E_p}{E_{SL}} \tag{4.27}$$

where the bar denotes the average value of E_p. Physically, this can be understood as follows: If the pulse energy rises slightly from relaxation oscillations, the pulse energy will start to grow exponentially because of the stronger saturation of the absorber. This increased pulse energy however will also start to saturate the gain, and so the laser is stable against the relaxation oscillations (and hence Q-switching) if the gain saturation is strong enough to prevent this exponential growth in pulse energy.

This equality can be easily transformed into a combination of easily determinable experimental parameters if a series of common assumptions are made [102]. If it is first assumed that the modulation depth is small ($\ll$1), that the non-saturable losses are also small (effectively, the output coupler transmission), and that strong saturation of the absorber is present, q_p can be replaced with:

$$R(E_p) \approx 1 - \Delta R \frac{E_{SA}}{E_p} \tag{4.28}$$

where $R(E_p)$ is the non-linear reflectivity of the absorber, ΔR is the modulation depth and E_{SA} is the saturation energy of the absorber, which is related to the mode size on the absorber and so will depend on the specific geometry used. It is then assumed that operation is far above threshold so that the term involving τ_L in Eqn(4.27) can be neglected. The stability then depends only on the saturation

energy of the laser medium and Eqn(4.27) can be rewritten so that the criterion for stability against QSML is:

$$E_p^2 \gtrsim E_{SL} E_{SA} \Delta R \tag{4.29}$$

All the parameters in this equation, although dependent on the specific geometry of the cavity, are relatively easily determined experimentally. There is likely to be some difficulty in estimating the mode size both on the absorber and in the gain medium, but as the expression above relies heavily on assumptions and approximations that may become invalid in certain cases, a sensible estimate should give some idea of how close to the stability limit one is.

It has been seen that various systems do not necessarily correlate with this equality, especially ones involving ultra short pulses, and that there can be other effects that contribute to Q-switched formation, for this reason Eqn(4.29) should only be considered a very general rule of thumb for pulses in the picosecond range. What is clear though, is that although it may seem from §3.3 that a large modulation depth is favourable for short pulse generation, this will also have a detrimental effect on the stability of the system and so any increase in ΔR has to be balanced by a corresponding increase in pulse energy. Whether this is always possible will depend greatly on the geometry of the laser system used.

4.3 Semiconductor Saturable Absorber Mirrors (SESAMs)

Up to this point, saturable absorbers have been discussed as essentially 'black box' devices. The assumption has been that they exist, and have the properties desired of them, but very little has been said of how one might be realised in practice. The semiconductor saturable absorber mirror (SESAM) is now introduced as the saturable absorber that will be used in large part in this thesis to modelock a bounce geometry laser oscillator. As the name suggests, the device is based on absorption in a semiconductor material. In the vast majority of modern implementations, and in the devices used in this thesis, the absorbing region is integrated into a structure that also contains a highly reflecting mirror. Modelocking is then

relatively simple to implement as this monolithic structure simply replaces one of the highly reflecting cavity mirrors.

The SESAM has evolved enormously since its inception, so that now the growth procedures and mechanism are very well understood and they can be virtually tailor made over a wide range of design parameters to suit the particular application. They are very versatile and have been demonstrated in a vast array of different solid state and semiconductor laser schemes. They have been used in high average power systems at up to 80 W [104]; for ultra-short pulse generation where they have been used to generate 13 fs pulses direct from the cavity [105]; implemented in ultra-high pulse repetition rate systems up to 160 GHz [94]; in traditional solid state slab lasers with a variety of lasing species and host crystals [106, 107], in both diode and lamp pumped schemes, as well as in thin disc geometries [95]; in fibre lasers [89] and in all-semiconductor VCSEL's to produce ultra-small, compact systems [108].

4.3.1 SESAM device structure

A typical SESAM structure is shown in Fig 4.4. The absorption of the SESAM device comes from the use of a single, or small number, of quantum wells. This absorber-well is typically made out of InGaAs or AlGaAs depending on what wavelength range the laser will be operating in, and is sandwiched between half wavelength layers of GaAs. The concentrations of indium (In) and aluminium (Al) relative to the gallium (Ga) are the variables that enable the wavelength tuning. This well structure sits on top of a Bragg mirror suitably designed to give very high reflectance at the operation wavelength of the laser, and the whole structure is grown on a substrate, usually GaAs.

An anti-reflection coating is also usually added to the front surface to reduce the non-saturable insertion losses and provide another means of control over the saturation fluence. This is the most common structure these days and is known as an anti-resonant design. This design ensures that the standing wave electric field formed inside the structure has a minimum in amplitude at the surface of the device to minimise the likelihood of damage, and a local maximum at the location

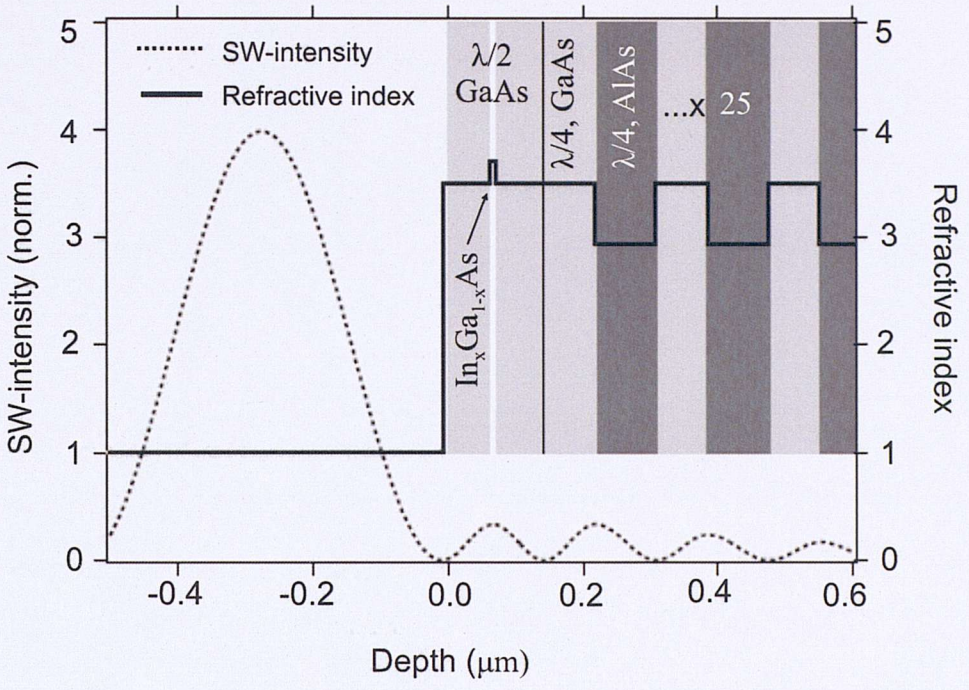


Fig 4.4. *Typical construction of an anti-resonant SESAM device. The quantum well sandwiched between $\lambda/4$ layers of GaAs is usually a few nanometres in width and this is on top of a $\lambda/4$ Bragg stack of GaAs and AlAs. This figure adapted from [109].*

of the quantum well to maximise the absorption. The device is designed in this monolithic way so that it is very simple to implement. As the whole package contains the absorber and a highly reflecting mirror it can be used simply by inserting it in place of one the cavity mirrors.

4.3.2 Action as a saturable absorber

The saturable absorption of the device arises because the absorber layers are isolated quantum structures. The density of states at the band edge does not follow the bulk properties of the material and sharp structure due to the exciton (electron and hole bound state) resonance can be seen as in Fig 4.5. The excitons absorb the incident light and the electrons and holes become free carriers again. These free carriers can then screen the remaining excitons so that they do not absorb and as this process continues, eventually any remaining excitons are completely

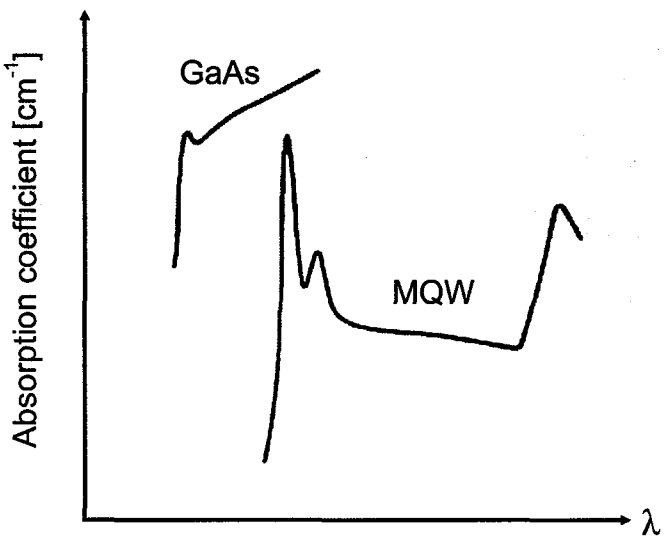


Fig 4.5. *Density of states for bulk GaAs and a multiple quantum well system (MQW) near the band edge. This figure adapted from [111].*

screened and no absorption takes place. As well as the position in wavelength of the resonance, the modulation depth of the absorber can be tuned via suitable choice of the well material, width, and potentially the number of wells used. This wide ranging variability means that it is now possible to produce SESAM devices with modulation depths from < 1 % up to as much as 45 % [110].

As has been seen, the recovery time of the absorber is also an important parameter to consider and contributes to determining the shortest pulse attainable from a system. The recovery time of the absorber relates to how quickly the free carriers created by the pulse can recombine to form excitons so that further absorption can take place. The recovery time typically shows a bi-temporal structure as shown in Fig 4.6. There is an initial fast recovery on the scale of $\sim$100 fs due to intraband thermalisation of the carriers. This is followed by a much slower (ps-ns) process of interband recombination. Pure SESAM structures have recovery times of many tens of nanoseconds, typical of bulk semiconductor materials, which is much too long for ultra-short pulse generation and was the chief concern in the early development of SESAM devices. In order to reduce the recovery time of the SESAM, the interband recombination process is targeted and artificial defects are introduced into the structure via techniques such as proton bombardment [113] or

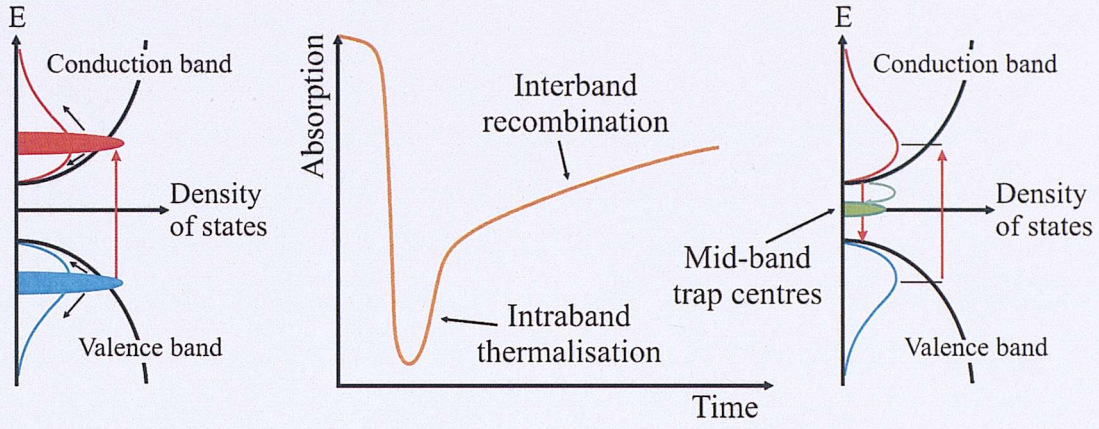


Fig 4.6. *The bi-temporal form of the absorber recovery time (centre) caused by fast intraband thermalisation (left) followed by slower interband recombination (right). This figure adapted from [112].*

ion implantation [109]. These sites act as recombination centres for the carriers and have resulted in commercial SESAM devices being available with recovery times of under 10 ps.

The bi-temporal form can also help with the modelocking process. The longer time scale results in a reduced saturation intensity for a part of the absorption, which helps to make the modelocking mechanism self-starting from intracavity noise; the fast time constant is useful for shaping sub-picosecond pulses.

4.4 Cavity design considerations for extension to modelocking

The necessary tools have now been obtained to start modifying a standard bounce geometry cavity for modelocking. In theory, replacing one of the cavity mirrors with the SESAM device should produce modelocking, providing there is sufficient intensity at the SESAM that a random noise spike can start to saturate the absorber. However, CW modelocking is also desired, and so Eqn(4.29) must also be satisfied. This inequality places more stringent conditions on the cavity and so it is anticipated that some care will be needed to achieve this. Eqn(4.29) contains the parameters that will be available in order to construct a functioning CWML

cavity. These are, the pulse energy, E_p, the saturation energy of the SESAM, E_{SA} and the modulation depth of the SESAM, ΔR.

The saturation energy of the gain, E_{SL}, is defined as the product of the mode size in the gain region and the saturation fluence of the gain ($F_S = h\nu/2\sigma$). This is then fixed by the fundamental design of the basic oscillator and gain medium, so any change to this would require a complete redesign of the bounce geometry. This is not practical and so the available design parameters are limited to E_p, E_{SL} and ΔR. These are often inter-related, but the design issues that could arise from trying to affect each one will now be covered briefly.

4.4.1 Varying the pulse energy, E_p

The intracavity pulse energy is calculated using the measured average output power of the laser together with the output coupler reflectivity, and the repetition rate of the cavity. Thus, for an otherwise fixed cavity, the pulse energy will vary, obviously, as the output power varies. The output power of the laser can be varied by changing the pump power, but this will affect the thermal loading on the crystal, leading to a different thermal lens strength. This altered lens power could affect the stability of the cavity, and require the cavity mirrors and any intracavity optics to be repositioned. For a given pump power and otherwise fixed cavity, the intracavity power can also be changed by varying the reflectivity of the output coupler. This will change the intracavity pulse energy but also affect the overall efficiency of the laser system, which has been shown to be optimal for $R_{OC} \approx 30\,\%$. High output coupler reflectivities ($R_{OC} > 80\,\%$) have also been seen to negatively affect the beam quality attainable from the bounce geometry due to extreme depletion of the gain region.

For a fixed average output power, the intracavity pulse energy can also be varied by altering the length of the cavity. In a modelocked system, as has been seen, the pulse repetition rate is equal to the inverse of the cavity round trip time. If the same *average* output power can be maintained while, for example, reducing the pulse repetition rate by increasing the cavity length, then the energy per pulse will be greater. The concern is then how best to alter the length of the cavity

whilst maintaining the fundamental function of the bounce amplifier. The cavity should also be kept to a sensible length so that it is relatively compact and not unwieldy. Significantly varying the length of a laser cavity and trying to maintain its performance is not a trivial task.

The question of pulse energy variability also raises a question over the desired performance of the laser itself. Is the design aim to achieve a high average power, with a relatively high repetition rate and low pulse energy; a high pulse energy, requiring a low repetition rate; ultra-high repetition rates with relatively modest pulse energies; or even high pulse energies and high repetition rates? The designated purpose of the final laser system will influence which parameters are most important, and thus determine the design path followed.

It should also be noted that the inequality Eqn(4.29) depends on the square of the pulse energy and so small changes to this parameter will have larger effects than similar changes to the other variables.

4.4.2 Varying the saturation energy of the absorber, E_{SA}

In a similar way to the saturation energy of the laser gain, E_{SA} is defined as the product of the mode area on the SESAM, and its saturation fluence. The saturation fluence of any commercial device is fixed by its particular design and so the only way E_{SA} can be influenced is by altering the mode size on the SESAM. The main issue with this is one of practical implementation. If the wish is to maintain the basic fundamental functioning of the bounce geometry, that is to say, the mode shape and size in the gain region, it is going to be necessary to greatly alter the cavity optics. A magnification system will be required which will add both length and complexity to the system. The extra length could also be useful in varying E_p, but the potential variability of the magnification factor is likely to be very discrete due to the discrete nature of lens focal lengths. Depending on resources available, it could also be difficult to vary the mode area on the SESAM by a small amount, whilst maintaining the cavity length and pulse energy.

Adding an intracavity magnification system will also increase the losses in the cavity and care will need to be taken to minimise the introduction of aberrations.

If the SESAM is to be used as one of the cavity end mirrors, the incident mode will have to be a plane wavefront as SESAM devices are grown on plane substrates. Adding multiple lenses and magnification to the system could easily add astigmatism or spherical aberration that could affect the stability of the cavity and the quality of the output beam.

Damage is also a concern when reducing the mode area on the SESAM. The device is a delicate structure and is not entirely passive, in the sense that it absorbs energy from the incident beam. This absorption could lead to heating and subsequent detuning of the SESAM, and other long term heat damage effects. As the situation also involves short pulses, the peak intensities on the surface could result in catastrophic ablation damage if the mode area is too small.

On a related note, it is also possible to oversaturate the SESAM so that the effective modulation depth is reduced. If the pulse intensity is too high, the SESAM will saturate almost instantly and not be able to perform it's pulse shortening function in the build up to modelocking.

4.4.3 Varying the modulation depth of the absorber, ΔR

As was seen in §4.2, the final pulse duration is inversely proportional to the modulation depth of the SESAM and so ΔR should be as large as possible. However, the dependence is relatively weak and a large ΔR has knock-on effects. Most commercial SESAMs are available with modulation depths of a few percent because a large proportion of solid state laser systems operate with output coupler losses of only a few percent. This way, the variable loss from the the SESAM is comparable to the normal cavity losses, and so the SESAM has a noticeable effect on the overall cavity dynamics. It is also quite difficult to engineer SESAM structures with modulation depths larger than $\sim 10\,\%$. In the case of the bounce geometry however, the normal output coupler losses are $\sim 70\,\%$. Thus, in order to get the saturable and non-saturable losses comparable, a balance will need to be struck betwen the output coupler reflectivity and modulation depth, which will have an impact on E_p as discussed above.

Growing these structures with large absorption coefficients also has an impact

on their other important properties. The general trend is that large ΔR SESAMs come with large non-saturable losses. In some solid state systems with otherwise low non-saturable losses, this addition could be significant and could make it difficult to reach laser threshold. With the bounce geometry this should be less of a problem as the gain is so high. What could be important is that the larger absorptions will lead to more significant heating effects and more easily to a damage threshold. The data for commercial devices usually show that high ΔR SESAMs have lower damage thresholds than their less absorbing counterparts.

The high ΔR SESAMs also tend to show lower saturation fluences, and so a change from one SESAM to another may also require a readjustment of the cavity to ensure sufficient saturation.

As has been seen, the recovery time of the SESAM is also an important parameter to consider. Most commercial devices available have recovery times of tens of picoseconds, which is more than short enough to stably modelock femtosecond pulses if the laser bandwidth allows. There is generally no variability available in this parameter.

These are the design issues that could arise during the construction of a modelocked bounce geometry cavity. It is hard to predict beforehand how a particular cavity will perform, and what effect certain changes will have on the performance. In this project, the modelocked cavity evolved over many iterations, each attempting to change only one of the possible parameters. The main initial aim was simply to produce a modelocked bounce geometry oscillator. Attaining a picosecond pulse train with a repetition rate of ~80 MHz, with an average output power of 10 W in a near diffraction limited beam would be considered an excellent result.

4.5 Evolution of the fundamental laser cavity to a CW ML laser oscillator

The main iterations of the bounce cavity that helped move towards modelocking will now be discussed. The asymmetric cavity described in §3.4.3 is used as the ba-

sis for all the modelocking work presented in this thesis. The commercial SESAM devices were obtained from BATOP and come soldered onto gold coated copper cylinders with 1" diameter, the same size as standard cavity optics. The initial SESAM chosen had $\Delta R = 3.1\,\%$ and non-saturable losses of 0.4 % which represented a compromise of maximum ΔR for short pulse durations and comparison to non-saturable cavity losses, low ΔR for avoiding QSML, and low non-saturable losses. Smaller values of ΔR might not be able to have sufficient influence on the cavity dynamics to cause modelocking, and the larger values always had large non-saturable losses, up to 3 % for $\Delta R = 5\,\%$. All the devices available had a stated recovery time of 10 ps which should be short enough to put us in the fast saturable absorber regime.

4.5.1 Compact cavity with no magnification

The most obvious first thing to try was to simply take the asymmetric bounce oscillator described in §3.4.3 and replace the highly reflecting back mirror, M1, with the SESAM. This produced the cavity shown in Fig 4.7 where a 40 W diode bar was brought to a line focus on a 1.1 at.% doped Nd:YVO_4 slab with 14° end faces. Under low pumping conditions the cavity is in the first stability zone (c.f §3.4.2, Fig 3.14b) and the mode on the SESAM is approximately collimated in the horizontal dimension. This results in a relatively large illuminated spot size ($\sim 400 \times 600\ \mu$m) on the SESAM and so no pulsed behaviour is produced due to the low fluence.

At higher pumping powers the cavity should enter the second stability zone (c.f §3.4.2, Fig 3.14c) where a waist is formed at the SESAM in the horizontal dimension. This should reduce the spot size and increase the fluence, potentially giving pulsed behaviour. Unfortunately, this cavity did not make the transition to the second stability zone under the available pump power. This is due to a better-than-average thermal contact between the crystal and the heatsink removing excess heat from the crystal more efficiently, and thus reducing the power of the induced thermal lens. If the thermal lens power is weaker than normal so that a waist cannot be formed in the short arm of the cavity, then the second stability

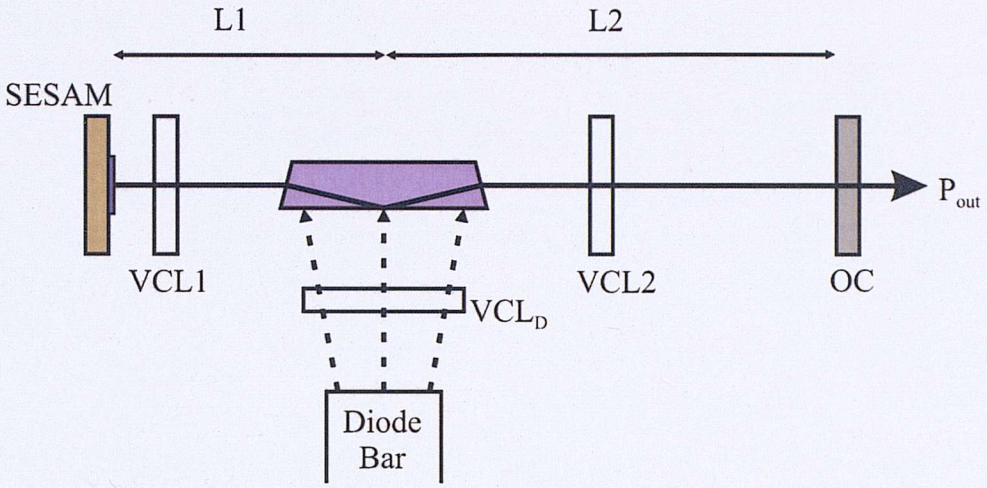


Fig 4.7. *A basic asymmetric bounce cavity with the plane back mirror replaced by a plane SESAM. VCL1,2 have f = 50 mm, VCL_D has f = 25 mm. L1 = 80 mm, L2 = 300 mm. OC is a plane output coupler whose reflectivity was varied*

zone will never be entered. Otherwise, the cavity operated normally up to 40 W of pump power, producing 18 W of output power in a near-diffraction limited TEM_{00} beam. No pulsed behaviour was visible even at these higher pump powers.

This cavity was initially constructed with an output coupler that had a reflectivity of 30 %, the same as would be used in a CW cavity. It should perhaps not be so surprising then that this first cavity did not modelock. The saturable losses are significantly lower than the non-saturable cavity losses (70 %), which will also result in low fluences at the SESAM that could not saturate its absorption. To counteract this, the cavity was also configured with output couplers that had $R = 50\,\%$, $70\,\%$, $80\,\%$ and $90\,\%$. In each of these cases, the maximum output power was reduced from the basic case, reaching 6.4 W for $R = 90\,\%$. The output beam was again near-diffraction limited TEM_{00} in all cases except $R = 90\,\%$. Here, the very strong depletion of the gain region due to the higher intracavity fluxes caused multimode structure to appear on the output. However, despite the higher fluences on the SESAM in these cases, no pulsed behaviour was seen with any of the output couplers.

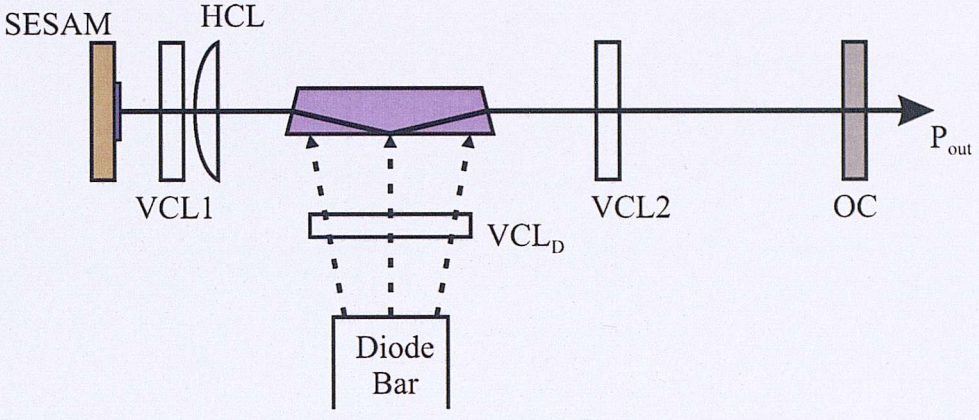


Fig 4.8. *Introduction of a HCL with focal length $f = 10$ cm into the short arm of the cavity forces the cavity into the second stability zone, with a waist formed at the SESAM in the horizontal.*

4.5.1.1 Forcing the second stability zone

To try and force the cavity into the second stability zone and create a smaller spot size on the SESAM, a HCL was introduced into the short arm of the cavity as illustrated in Fig 4.8. This acts in conjunction with the thermal lens to form a composite intracavity lens that is able to form a waist at the SESAM in the short arm of the cavity. In this configuration, it is expected that the cavity will transition to the second stability zone at very low pump powers, or possibly miss the first stability zone altogether. A plano-convex HCL with focal length $f = 100$ mm was chosen to approximately match the cavity arm length and was positioned close to the crystal with its flat face towards the crystal.

This cavity was seen to be in the second stability zone very soon after lasing threshold was reached and produced near-diffraction limited TEM_{00} output beams as before, though with slightly lower maximum output power. This configuration was tried with all the output couplers used before, but still only minor pulsed behaviour was visible at any available pump power. Occasional bursts of pulses lasting a second or so were seen at high pump powers with the high reflectivity output couplers.

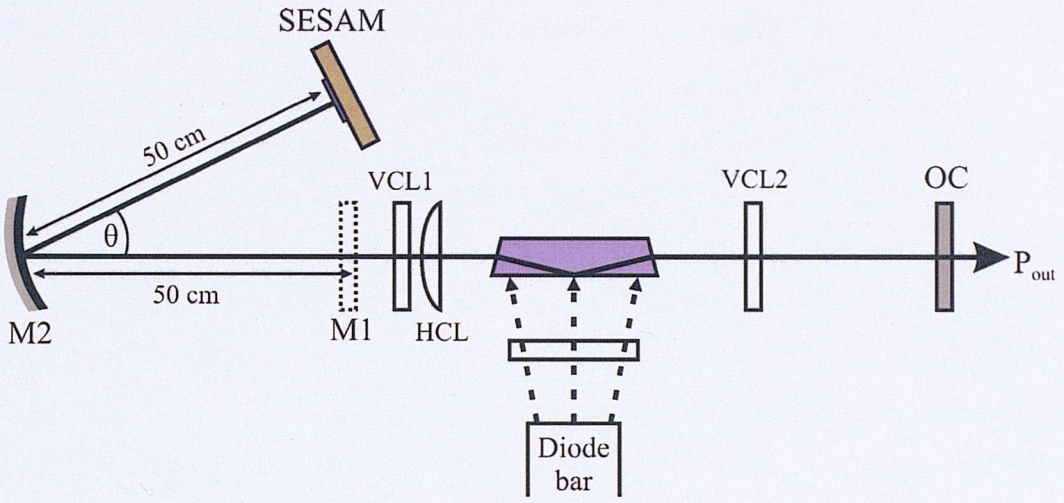


Fig 4.9. *An extended cavity for re-imaging the mode that would occur at M1 in the compact cavity. The configuration between M1 and the OC is identical to that in Fig4.8. The spherical mirror M2 has a radius of curvature $R_c = 50$ cm and the angle θ is $< 10°$ to minimise aberrations. The magnification factor between M1 and the SESAM is $m = 1$.*

4.5.2 Extended cavity with m=1

Having been unsuccessful with the basic cavity, the next attempt involved trying to increase the potential pulse energy, and hence fluence on the SESAM, by extending the length of the cavity. In order to maintain the mode shape in the bounce amplifier, this extension was to be achieved by imaging the position of M1 in the compact system. This would hopefully reproduce the beam waist of the compact system at the SESAM, thus retaining compact cavity performance, whilst adding length to the cavity to increase the possible pulse energy.

4.5.2.1 Single spherical mirror

To help keep the system relatively compact and simple, the cavity extension was initially done with a single spherical mirror M2, with a radius of curvature of 50 cm, positioned as indicated in Fig 4.9. A curved mirror with radius of curvature R_c acts as a lens with a focal length of $R_c/2$, and so M2 was located 50 cm from the position of the back mirror in the compact cavity. The SESAM was then positioned a further 50 cm from the curved mirror so that the object (M1) and

image (SESAM) are each a distance $2f$ from the lens, giving a magnification factor $m = 1$.

This cavity was more successful than the basic compact cavity. Stable QSML was seen with a strong Q-switched modulation. 2.9 W of output power was obtained with 20 W of pumping power using the $R = 90\,\%$ output coupler as in the compact cavity. The output power is lower in this case because the beam degradation that takes place due to the high intracavity power results in a loss of the pulsed behaviour. 2.9 W was the maximum output power that could be achieved whilst maintaining some form of pulsed output. The cavity was also configured with the $R = 80\,\%$ output coupler to try and improve the beam quality, but the pulsed behaviour became much more erratic and unstable. Bursts of QSML lasting up to a second would occur again but the laser would not operate in a stable, continuous pulsed state.

4.5.2.2 Dual spherical mirrors

Now that stable pulsed behaviour with a strong Q-switching modulation had been obtained, the propensity for Q-switching needed to be reduced in order to produce a CW pulse train. The next iteration was to extend the cavity further, with the aim of increasing the pulse energy so as to tip the QS inequality (Eqn(4.29)) in favour of CWML behaviour. This was achieved by the use of a further spherical mirror, M3, with $R_c = 25$ cm, positioned 75 cm from M2, as illustrated in Fig 4.10. The SESAM was then located 25 cm from M3 so that the intermediate image formed by M2 with $m = 1$, was further re-imaged by M3, again with $m = 1$. This should then reproduce the beam waist from the previous cavity, but add a further 50 cm to the length.

Once the intracavity lenses and the position of the SESAM had been optimised, this is the best performing cavity so far. The output beam was a stable train of CW modelocked pulses with no significant amplitude modulation apparent. The maximum average output power obtained was 16.7 W with 38 W of pump power using an $R = 50\,\%$ output coupler. The beam quality was TEM_{00} though with some slight structure, and is shown together with the pulse train in Fig 4.11. The peak amplitude variation of the pulses shown in the figure is mostly due to

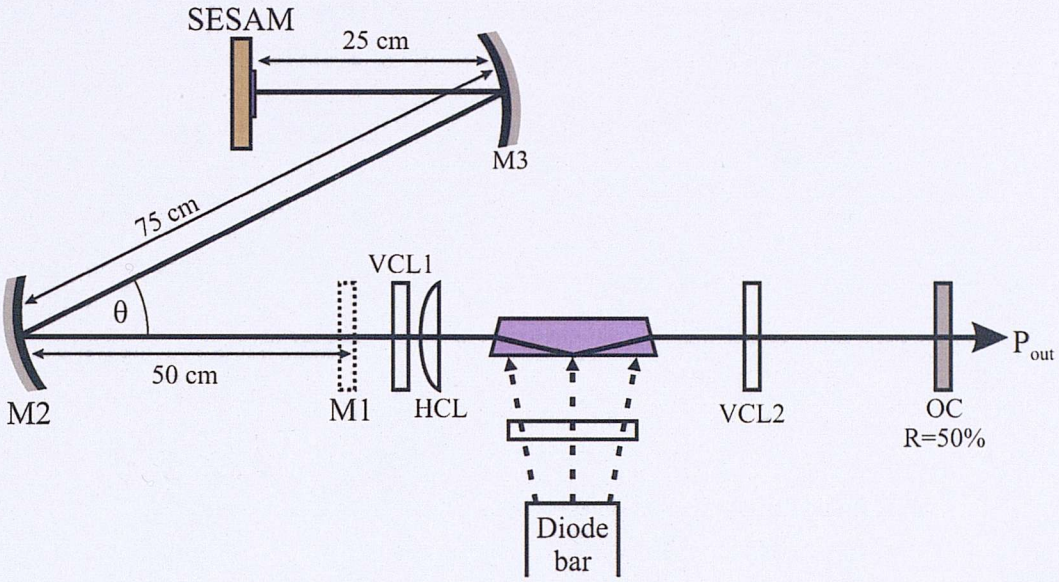


Fig 4.10. *Cavity using two spherical mirrors M2 and M3 to extend the length of the cavity. Mirror M2 has $R_c = 50$ cm, M3 has $R_c = 25$ cm and θ is again kept to $< 10°$. The configuration between M1 and the OC is identical to that in Fig 4.8.*

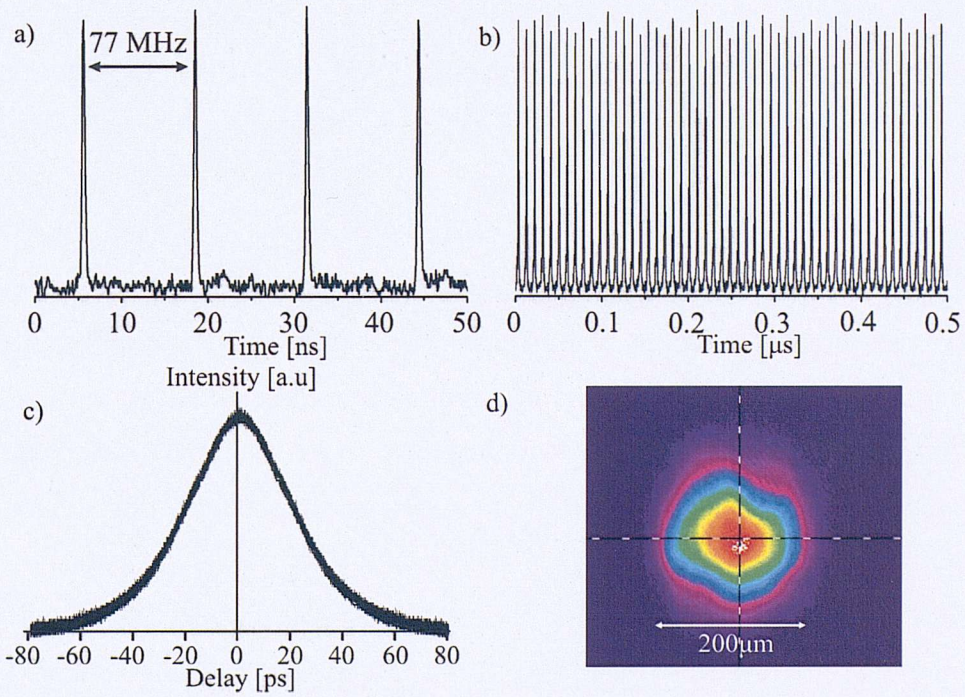


Fig 4.11. *The output modelocked pulse train on a nanosecond (a) and microsecond (b) timescale. The intensity autocorrelation of the output pulses (c). The spatial profile of the output beam (d).*

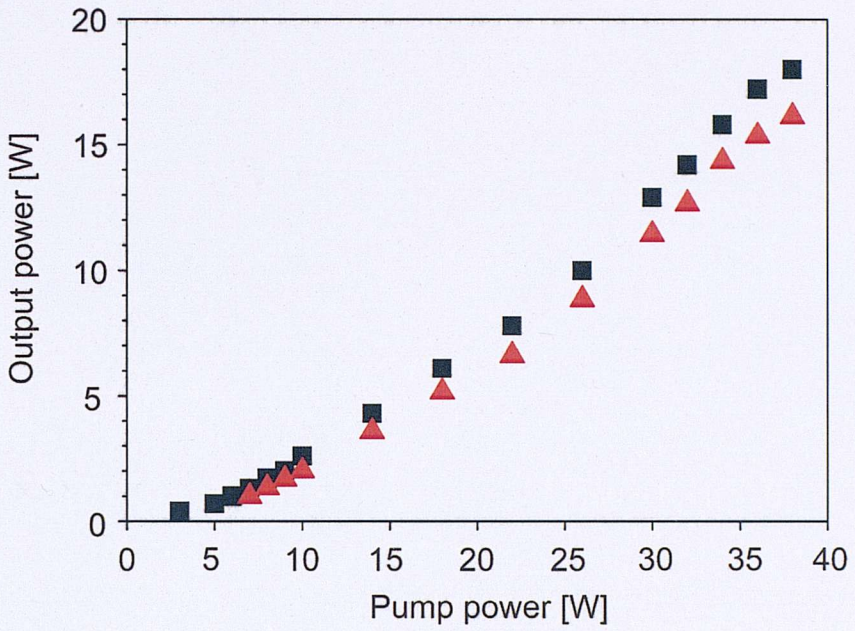


Fig 4.12. *A comparison of the output power of the modelocked cavity (red triangles) to a compact asymmetric cavity with the same output coupler reflectivity (black squares).*

aliasing on this timescale and the pulse-pulse variation in this case was $< 4\%$. The total cavity length was then ≈ 190 cm which gave a round trip time of 13 ns, and a pulse repetition rate of 77 MHz. The pulse train was analysed using the autocorrelator described in §2.5 and the pulses were found to have a FWHM of 30 ± 2 ps. It should be noted that this error is of purely experimental origin and there is likely to be at least as much uncertainty in the pulse duration derived from the assumptions inherent when extracting a value from the autocorrelation.

These output parameters represent a very good performance for the cavity. It was stated initially that a 10 W average power, picosecond pulse train with an 80 MHz repetition rate would be an excellent result, and this has been achieved here. The beam quality of the compact cavity has also been reproduced despite the extra complexity of the imaging optics. In fact, a comparison of the modelocked cavity to the compact asymmetric cavity shows how well the modelocked case is performing. A comparison of the power curves for the modelocked cavity and its base asymmetric cavity with an $R = 50\%$ output coupler is shown in Fig 4.12. Here it is seen that the power output from the modelocked cavity is only slightly below

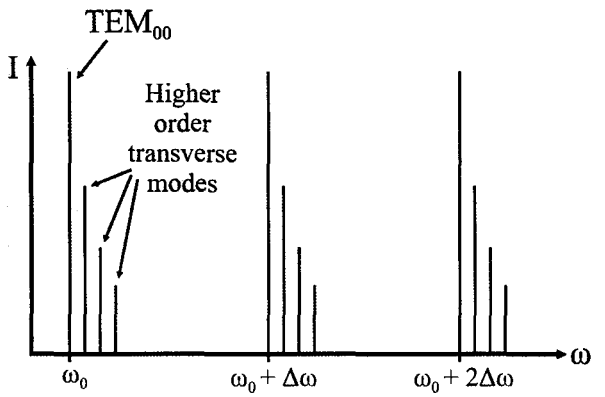


Fig 4.13. *Higher order transverse modes than the fundamental TEM_{00} oscillate on slightly different longitudinal modes.*

that of the compact, CW running cavity with an equivalent output coupler. This system was considered a significant result in the history of the bounce geometry and so was presented at an international laser conference (Europhoton '06), and accepted for publication in a peer reviewed journal [114].

While this is a good result, there are still one or two things that should be commented on. Although the pulses are of picosecond duration, they are still longer than could ideally be expected. The SESAM used has a recovery time of 10 ps and so based on the 250 GHz gain bandwidth of Nd:YVO_4, pulses of 2 ps should be achievable. That this is not the case suggests that the required fixed phase relationship between modes is not true across the full oscillating bandwidth. One possible cause of this is poor spatial quality of the propagating beam. Higher order transverse modes in a laser cavity will oscillate on slightly different longitudinal modes to the fundamental, lowest order transverse mode (TEM_{00}, Fig 4.13). If the cavity mode has some components of these higher order modes, there is no reason why they should be oscillating in phase with the fundamental modes. This could affect the range of the phase locking, resulting in a limited pulse duration.

Poor spatial quality could also have an effect at the SESAM. If the intensity profile of the spot on the SESAM is not uniform, the saturation of the beam will not be uniform. This could result in significant transverse structure which could affect the quality of the phase locking as just described. It is anticipated then, that it is important to have very good spatial quality at the SESAM. To check

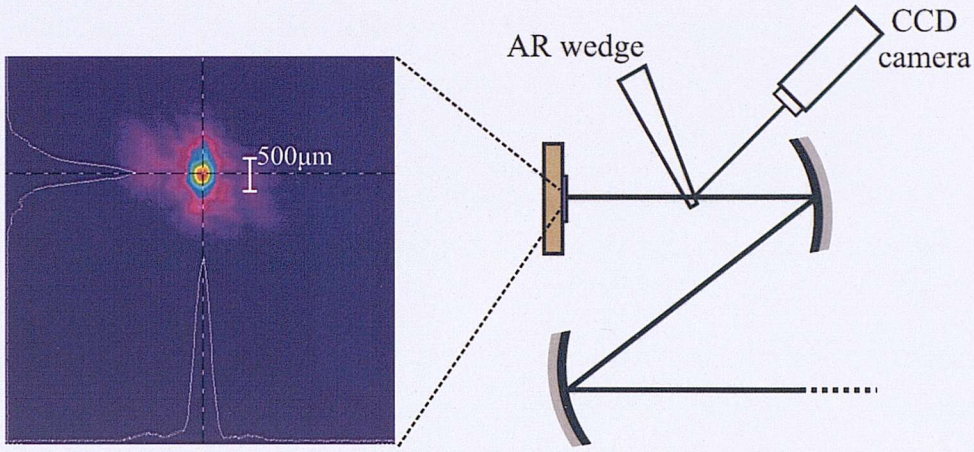


Fig 4.14. *Direct image of the mode formed on the SESAM using a wedge to image inside the cavity*

if this was the case, a wedge was inserted into the cavity between M3 and the SESAM to pick off a small fraction of the intracavity power and directly image the incident mode onto an IR camera. The visible mode is shown in Fig 4.14. Although the output beam appears to be of good quality (Fig 4.11) the mode at the SESAM is not a clean TEM_{00} form and exhibits higher order structure in both the horizontal and vertical dimensions.

This examination of the mode at the SESAM also gave insight into another of the comment-worthy performances of the cavity. It should be noted that the optimum performance reported above, made use of an output coupler with $R = 50\,\%$. This is in distinct contrast to the preceding cavities with $m = 1$ imaging, where the pulsed behavior was best with $R = 90\,\%$ and showed little or no pulsed behaviour with $R = 50\,\%$. The reasoning being that high intracavity intensities were needed to saturate the SESAM sufficiently. During optimisation of this cavity, output couplers with $R = 90\,\%$, $80\,\%$ and $70\,\%$ were tested. In some cases they could produce stable CW modelocking, but it was found that $R = 50\,\%$ could also produce this behaviour, at a higher output power. The performance of this system is thus superior and is the version reported.

Why could stable CW pulsed behaviour not be achieved with $R = 50\,\%$ in the previous $m = 1$ cavities? Whilst viewing the mode on the SESAM, it was noticed that the size of the mode was significantly smaller than expected. In the

base asymmetric cavity, the mode size at M1 was measured to be $\sim 400 \times 600\,\mu$m. In the extended $m = 1$ cavity, the mode size was seen to be $\sim 300 \times 500\,\mu$m. The mode size is thus smaller than expected and so the intensities could be high enough to saturate the SESAM sufficiently. Coupled with the potentially higher pulse energies from the longer cavity, this could explain why modelocking was achieved in this case.

The discrepancy between the measured and expected mode sizes is attributed to non-ideal imaging of the base cavity. The mirror spacings are determined by application of the lens equation ($\frac{1}{u} + \frac{1}{v} = \frac{1}{f}$) which is based on ideal geometrical optics. In reality this is not the case and Gaussian optics is more proper description of the propagation of a beam waist through a multi-lens system. This will result in the lens system not performing the transformation intended. This is likely to be compounded by the fact that the mode shape at the position of M1 in the extended cavity, is unlikely to be the same as the mode shape at M1 in the compact base cavity because the two cavities have different forms. This will be further exacerbated because the cavity mode behaves quite differently in the horizontal and vertical planes. The re-imaged horizontal waist may not be in the same position as the re-imaged vertical waist. There may then be no plane where the waist at M1 is re-imaged, and the mode shape at the SESAM, while being optimised for the particular cavity configuration, may not bear any relation to the mode shape that was at M1. The re-imaging principle that is used to extend the cavities should thus be viewed as a guide only.

A final note on this cavity concerns the long-term stability of its performance. During operation, it was noticed that the beam quality and the pulsed behaviour would deteriorate over time, but recover if the system was turned off and restarted later. This was found to be due to severe heating of the SESAM and its mount, which in turn was partially attributed to the cumulative absorption of the low intensity 'cloud' around the centre of the beam in Fig 4.14. Further improvements to this cavity were thus focused on improving the beam quality at the SESAM and effective cooling of the device and its mount.

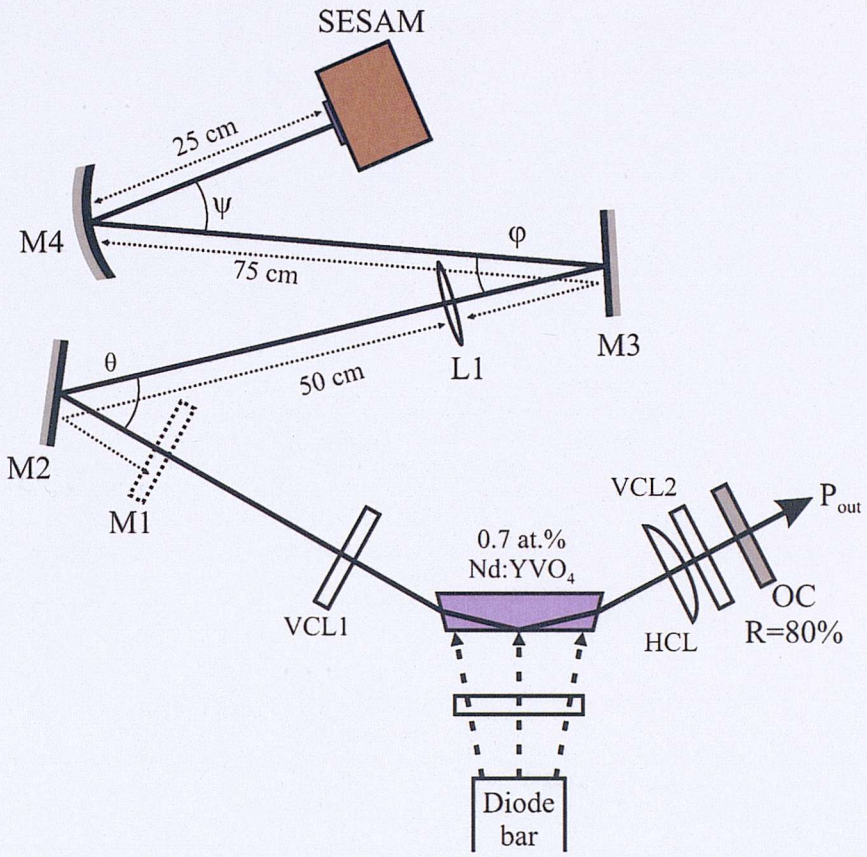


Fig 4.15. *Cavity with $m = 1/2$. Relay imaging is performed with lens L1, focal length f=50 cm, and spherical mirror M4, R_c=50 cm. The base cavity has the output coupler in the short arm and uses a 0.7 at.% doped Nd:YVO_4 crystal with 5° end faces. The optics between M1 and the OC remain the same distances from the centre of the crystal as in Fig 4.8. θ is $\approx 20°$, determined by the new crystal angle. ψ and φ are $< 10°$.*

4.5.3 Extended cavity with m=1/2

The next main iteration of the cavity that gave significant results is shown in Fig 4.15. This cavity produced stable CWML in an output beam with an average power of 6.1 W from 30 W of pump power. The pulses were measured using a manual autocorrelation and found to have a duration of 12±2 ps (Fig 4.16). The repetition rate was 81 MHz and the beam had a TEM_{00} spatial profile.

As can be seen from Fig 4.15, the cavity has accumulated several changes from the last system. Perhaps the most noticeable of these initially is a change of the laser crystal. This system uses a crystal with end faces angled at 5° to

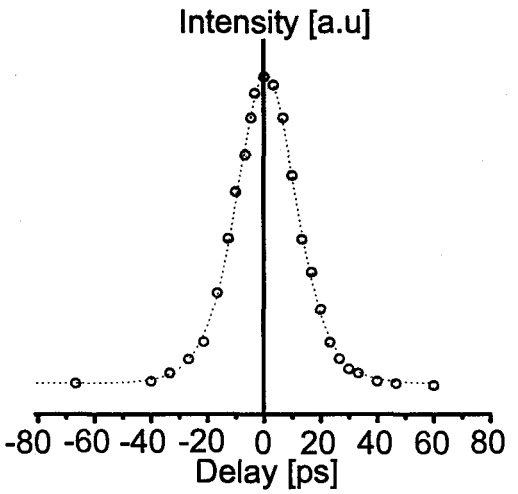


Fig 4.16. *Manual autocorrelation trace of the pulses from the cavity in Fig 4.15 The pulses are seen to have a duration of 12 ps.*

the pump face, compared to one with 14° in the previous system. This crystal is also 0.7 at.% doped Nd:YVO_4, compared to 1.1 at.% doped. This change was not intended to achieve anything specific but was instead forced by experimental circumstance. Another main addition is a cooling heatsink mount for the SESAM. This takes the form of a water cooled copper head that clamps the copper cylinder the SESAM is mounted on.

The further changes can be grouped roughly into two main categories: changes that aimed to improve the spatial quality of the mode on the SESAM; and changes that helped to keep the Q-switching inequality (Eqn(4.29)) balanced in favour of CW modelocking.

4.5.3.1 Improving the spatial quality

The first change was to try and improve the quality of the mode that was being re-imaged. In the compact cavity, forcing the second stability zone to produce a smaller spot on the SESAM might have been appropriate. When this spot is to be re-imaged however, the beam divergence in the horizontal and vertical planes are sufficiently different that it introduces too much astigmatism which propagates through the system, distorting the beam quality. To improve this, and still maintain operation in the second stability zone, the base cavity is essentially

'switched' around. Instead of M1 being in the short arm containing the HCL and the small beam waist, M1 is positioned in the long arm and the output coupler is placed in the short arm. This gives a more circular, approximately collimated beam at M1, with the divergence in the horizontal and vertical planes more closely matched. This results in the output from the cavity being highly divergent in the horizontal, but this can be compensated with a suitably positioned HCL outside the cavity.

The second change involved the realisisation that the re-imaging system used so far was not ideal. A better system is to use two lenses (L1, L2) separated by the sum of their focal lengths ($f_1 + f_2$), with L1 positioned a distance f_1 from M1, and the SESAM positioned a distance f_2 from L2. In this configuration, L1 takes the mode at M1 and produces the Fourier Transform at a distance f_1 on the image side, L2 then takes this Fourier Transform as its object, positioned at f_2, and also produces a Fourier Transform in the image plane at a distance f_2, the location of the SESAM. This multiple Fourier Transform, relay-imaging, completely reconstructs the mode shape present at M1 at the SESAM, and removes any problem arising from the difference between the horizontal and vertical planes. In this cavity, the relay-imaging is performed by the spherical mirror with $R_c = 50$ cm and a lens with focal length $f = 50$ cm.

The final adjustment to improve the spatial quality is to reduce the internal bounce angle in the amplifier. Normally, as discussed in §3.3.4, the bounce amplifier is configured to function with an angle $\theta_{int} \approx 7°$ between the pump face and the totally internally reflected propagating beam. This was previously determined to offer the best compromise of beam quality and high power. By reducing the internal bounce angle, the effective soft aperture of the gain seen by the propagating beam is narrowed. This aperturing effect forces the cavity mode towards TEM_{00}, improving the beam quality inside the cavity. The bounce angle used in this final system was $\theta_{int} \approx 3.6°$. The negative side effect of this change however, is that the mode overlap between the cavity mode and gain region is reduced, which will reduce the attainable output power. It was decided that a small drop in output power could be tolerated as this could be compensated for in an external amplifier.

4.5.3.2 Balancing the Q-switching inequality

Although not intended, the previous cavity design resulted in a reduction of the mode size between M1 in the base cavity, and the SESAM in the extended cavity. It is thought that this contributed to the production of modelocking by increasing the fluence on the SESAM. The mode size on M1 in the 'switched' base cavity that is now to be imaged, is larger than before (measured to be $\sim 600 \times 550\ \mu$m) and given that a lower output power is also expected with the smaller bounce angle, a reduction factor of $m = 1/2$ has been applied to the relay-imaging of the mode. This reduced mode size reduces the saturation fluence of the absorber, E_{SA}. The pulse energy, E_p, is also expected to be reduced however, because of the lower output power. Reducing the mode size thus helps to offset the effect of a lower E_p on the Q-switching inequality.

The reduction factor of $m = 1/2$ could easily be obtained using the two spherical mirrors from the previous system. The Fourier Transform, relay-imaging system now being used introduces a magnification factor of $m = \frac{f_2}{f_1}$ to the final image. The two mirrors with effective focal lengths of 12.5 and 25 cm could therefore easily be combined to give $m = 1/2$. However, appropriately spaced, the total cavity length is reduced to ~100 cm from ~ 190 cm of the previous system. The longer length of the cavity was seen to contribute positively to the production of modelocking, and a shorter cavity would also reduce the pulse energy even further than already anticipated. Wishing to keep the cavity length similar to the previous system to maintain the 80 MHz repetition rate, the relay imaging was performed with a lens of focal length 50 cm, and the spherical mirror with effective focal length 25 cm ($R_c = 50$ cm). The mode on the SESAM was subsequently measured to be $\sim 300 \times 220\ \mu$m.

As the output power from this system was reduced, the reflectivity of the output coupler had to be increased to provide sufficient pulse energy to both saturate the SESAM effectively and favour CWML in the Q-switching inequality. This of course reduced the output power and efficiency of the system. The $R = 80$ % output coupler was found to provide the best combination of beam quality, power and stable CWML operation, with $R = 90$ % once again displaying poor

beam quality and unstable modelocking, and $R = 70\%$ providing insufficient pulse energies to avoid QSML.

During the re-design of the system, the SESAM had to be replaced due to accumulated damage severely limiting its operation. In the intervening period, the SESAM vendor had increased the available range of modulation depths although the previous values were no longer available. The replacement device has $\Delta R = 5\,\%$ which should help to reduce the pulse duration.

Overall, this system is considered a good improvement over that in §4.5.2.2. The system as a whole was more robust and stable. CW modelocking could be maintained continuously over a number of hours with no degradation in the pulse train, output power or beam quality. The previous system would occasionally drift from its peak performance during prolonged use, with drops in output power and beam quality causing the modelocking to cease. Fine adjustment of the cavity was required to return to stable operation. This cavity displayed no such drift and would return to a stable, CWML state from turn on, with no fine adjustment required. The pulses were a factor of two and a half shorter than before, and although still not quite as short as the gain bandwidth could allow, were a marked improvement on the first system.

The output power was the most significant casualty of this system and the overall efficiency has dropped from 44 % in the initial modelocked cavity (very good for this type of picosecond system) to 20 % (just about average for a picosecond system) in the current form. This was due to two factors: the reduction in the bounce angle; and the increase in the output coupler reflectivity. The bounce angle was reduced to help improve the spatial quality of the beam by aperturing the cavity mode slightly, but this inevitably lead to a reduction in the overlap with the gain region. This then limited the available output power, which in turn necessitated an increase in the output coupler reflectivity to maintain sufficient saturation of the absorber. The two effects thus combined to give a rather significant drop in the overall system efficiency.

A reduction in output power and efficiency had been anticipated so this was no surprise, but the output of 6.1 W did then fall slightly short of the ideal perfor-

mance. The improvements achieved in beam quality, pulse duration and system stability however are considered significant enough that this fall in absolute power can be tolerated. If required, the extra power can be efficiently added by using a bounce geometry module as an external power amplifier with the modelocked cavity as a master oscillator.

4.6 Power scaling the modelocked system

As has been highlighted previously, one of the advantages of the bounce geometry is its potential for power scaling due to the high gain, spatial averaging effects, and simple pump delivery. An aim of this work was to investigate whether this power scaling potential could be applied to a modelocked system. As demonstrated, the bounce geometry has been successfully applied to a modelocked system, producing a relatively high output power with high efficiency. The question is then, can this output power be increased further, whilst maintaining the other performance parameters (beam quality, CW-ML, pulse duration)?

In principle, with all other things being equal, the output power and modelocked performance from a SESAM system can be scaled simply by scaling the mode area on the SESAM in proportion to the final output power. For example, if the pulse energy can be doubled by increased pumping, the fluence on the SESAM can be kept constant by doubling the mode area. This should then reproduce the modelocking conditions found in the lower power cavity. In practice, it is not so simple to keep all other things equal. The increased levels of pump power would produce more heating in the laser crystal and thus increase the strength of the thermal lens. This would alter the behaviour of the base cavity and the system would need redesigning around operation at high pump powers. Also, although the bounce geometry is very capable of mitigating adverse thermal effects, it nevertheless suffers under very high pumping conditions. This will still make it difficult to achieve the high beam quality needed for good modelocking performance.

Another aspect to consider is the efficiency of the system. Assuming that the performance of the modelocked system could be reproduced at higher pump powers, the overall efficiency may still be lower than could be achieved with an

external amplifier. The first modelocked system produced in §4.5.2.2 for example, had an overall optical-optical conversion efficiency of 44 %. This measure is somewhat worse in the final cavity in §4.5.3. If this performance could somehow be maintained by an effective reconfiguration of the cavity, it may be possible to achieve 44 % for the next 40 W of pump power. By contrast, the bounce geometry amplifier has been shown to operate extremely effectively as an external amplifier with optical-optical efficiencies of 50 %. Given that this is a relatively simple scheme to implement, it was decided that the best route to power scaling the modelocked system was to use an external amplifier.

4.6.1 Master Oscillator - Power Amplifier

This arrangement of an external, independent amplifier used to amplify another independent oscillator is generically termed a master oscillator - power amplifier (MOPA) configuration. MOPA configurations have been demonstrated as reliable schemes for power scaling laser systems. Previous demonstrations of such configurations have included a diode-pumped Nd:YAG system [115], an Nd:YAG MOPA with phase conjugate mirror [116], a combination of solid-state oscillator and fibre power amplifier [117, 118], as well as the bounce amplifier itself. For power scaling of bounce geometry laser systems, the MOPA configuration is attractive as the pump power may be distributed over multiple amplifier modules, which ensures that thermal lensing in each module is maintained at moderate levels.

The oscillator to be amplified was be the modelocked system described in §4.5.2.2 running with 10 W of output power. The power amplifier was simply a bounce amplifier module without cavity mirrors, consisting of a $25 \times 5 \times 2$ mm Nd:YVO_4 crystal, with 14° end faces and 1.1 at. % doping. This was pumped by an nLight diode bar rated up to 100 W of optical output power, temperature tuned so that its room temperature emission of 806.2 nm was shifted to the 808 nm absorption band of the crystal. This was again brought to a line focus on the crystal's front face by a vertical cylindrical lens of focal length 25 mm. The output from the oscillator was spatially matched to the gain region of the amplifier by two cylindrical lenses, one horizontal and one vertical. This MOPA arrangement

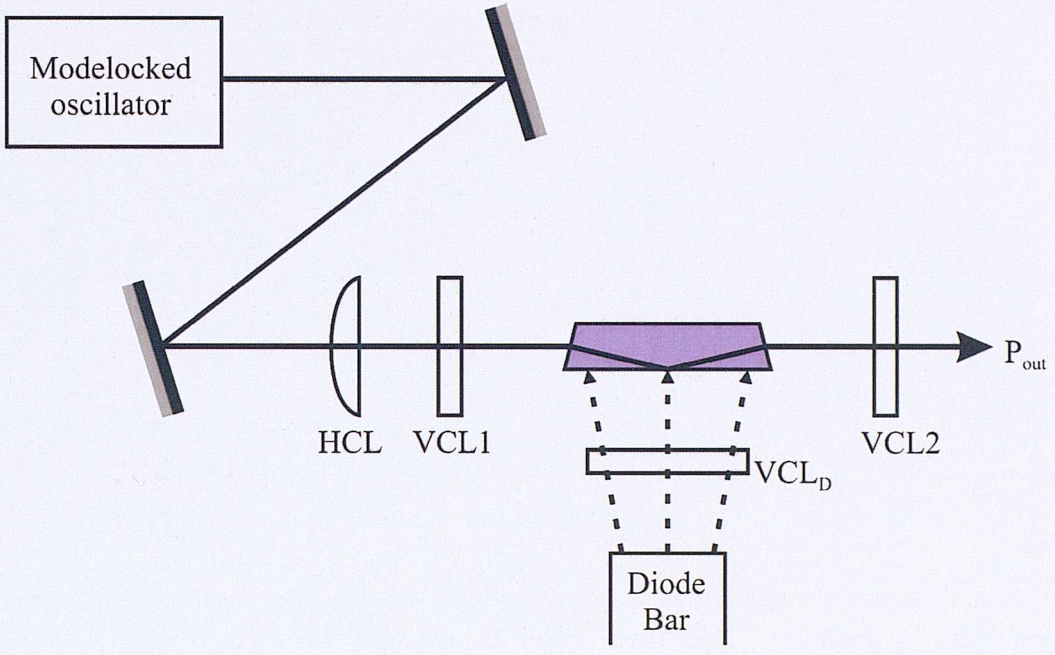


Fig 4.17. *Bounce geometry MOPA implementation. The HCL and VCL are used for mode matching the gain region in the amplifier. The amplifier crystal is 1.1 at. % doped Nd:YVO_4 with 14° end faces and pumped with a 100 W diode bar.*

is shown in Fig 4.17.

The output power of the MOPA plotted against the amplifier pump power is shown in Fig 4.18. A maximum output power of 60 W was achieved at an amplifier pump power of 100 W with no degradation of beam quality or pulse behaviour. This corresponds to a total optical-optical conversion of 50 % for the MOPA system. As expected, this is better than would be achieved by scaling the oscillator. The pulses are transmitted with no increase in their duration because the amplifier crystal is made of the same material as the oscillator crystal and so exhibits the same gain bandwidth. This is a significant increase in power of the modelocked source, and if so desired, it would be possible to add successive amplifier modules to push output power to 100 W and beyond.

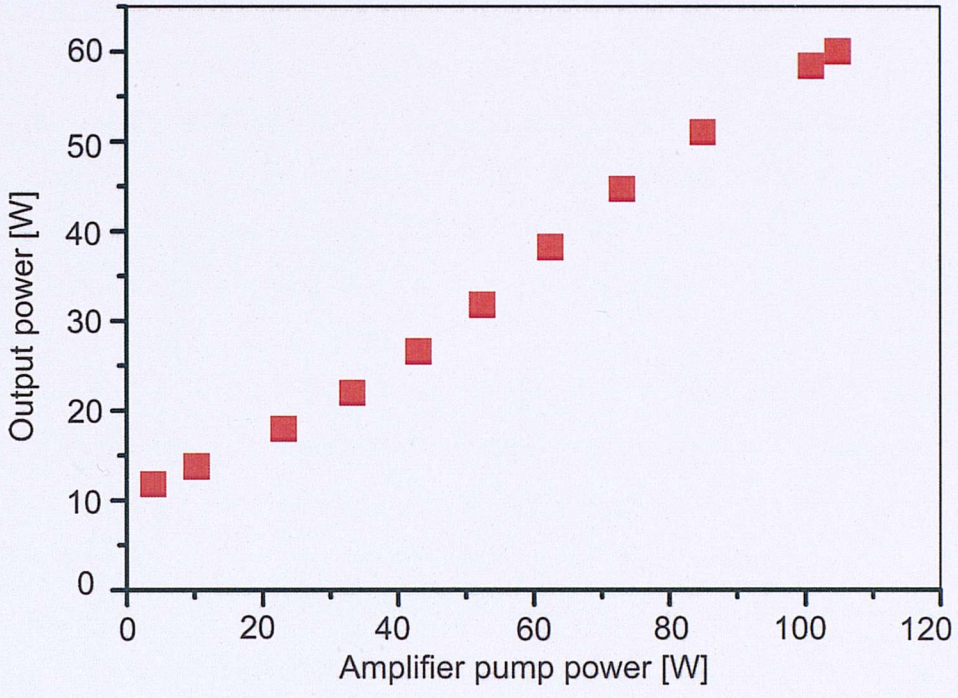


Fig 4.18. *Output power from the MOPA as a function of amplifier pump power. The maximum output power from an input of 10 W was 60 W.*

4.7 Conclusions

This chapter looked in more detail at saturable absorber modelocking, in particular the SESAM device. Picosecond modelocking was achieved for the first time in a bounce geometry oscillator and amplification up to the 60 W level was achieved by the use of a bounce amplifier MOPA system.

The action of a saturable absorber to produce modelocking was described by considering transmission operators for gain, loss and saturable absorber elements inside a cavity. The self-consistency requirement for propagating laser modes produced pulsed solutions with a $sech^2$ temporal form. A distinction was made between fast and slow saturable absorbers where the recovery time is shorter or longer than the pulse duration. The pulse stabilisation mechanism was seen to be qualitatively different in the slow case. An approximate inequality was shown that provides guidance when trying to avoid the Q-switching instability in a modelocked cavity. Cavity design considerations were discussed based on satisfying this inequality by making alterations to affect the pulse energy, mode area on the

SESAM and modulation depth of the absorber.

The SESAM device was introduced and its structure described, as well as its action as a saturable absorber. The multi-quantum well structure results in a sharp exitonic band edge with absorption at the design wavelength that can be saturated by carrier screening. The recovery time of the SESAM is influenced by intraband thermalisation and interband recombination of carriers, leading to a bi-temporal decay form.

The evolution of the compact asymmetric CW bounce oscillator into a modelocked source was outlined. Initial attempts were based on 1:1 re-imaging of the compact cavity to elongate the cavity and increase pulse energy. This resulted in the first production of a modelocked bounce geometry oscillator, with a 77 MHz, 30 ps pulse train of average power 16.7 W achieved. Alterations were made to this system which improved the beam quality at the SESAM device and reduced the incident mode size. The result was a modelocked oscillator that produced an 81 MHz pulse train of 12 ps pulses with an average power of 6.1 W. There was a drop in system efficiency from 44 % to 20 % as well as the drop in output power, and this was due to the reduction in the bounce angle and the increase in the output coupler reflectivity implemented in this system. These two changes enabled the reduction in pulse duration and improvement in output beam quality and so despite the loss of power, this was the best performing cavity.

Power scaling of the modelocked oscillator was discussed whereby the mode size on the SESAM is varied in proportion to the increase in pump power to maintain the saturation parameters of the cavity. Even if this were to have been done ideally using the final cavity as the parent, the overall system efficiency would still not be expected to be much above the 20 % achieved in this cavity. External amplification using a secondary bounce geometry module however, potentially allowed power increases with a much greater efficiency. A bounce geometry MOPA system was thus constructed with the modelocked oscillator as an input, and a modelocked average output power of 60 W was recorded with an amplifier efficiency of 50 %. This was achieved with no degradation in the beam quality or measured pulse duration, demonstrating that with sufficient pump power, this technique could potentially produce 100 W of average power in a picosecond pulse train, much

more efficiently and simply than directly scaling the oscillator.

Chapter 5

Quantum dot SESAM devices

5.1 Introduction

The SESAM devices used so far in this work have all been based on quantum well absorbers as described in chapter 4. It is also possible to construct SESAMs using quantum dots as the saturable absorber component and there has been extensive research into the growth of quantum dots. One of the groups that has been at the forefront of this research drive is a group from the same institution as the present author. They have been developing techniques for growing dots and have started to look at implementing them in SESAM structures. A collaboration was thus set up between the two groups whereby the quantum dot SESAM (QDSAM) devices could be tested for functionality in a bounce laser oscillator.

Initially, the concept of quantum dots is briefly developed, together with a comparison with the quantum well structures. The growth procedure is then outlined and the characteristics of the devices are highlighted. The first testing run is then covered, where some simple samples are used to produce pulsed behavior in a bounce geometry laser, similar to that used in chapter 4. The results of this test are then used to inform modification of the design of the QDSAM devices. A second set of devices is produced to a different design, and post-growth modification of the device properties is performed. These post-growth procedures are

outlined in brief before the second testing run is described, where improved pulsed behaviour is achieved from the QDSAMs in a bounce geometry oscillator.

5.2 Quantum dots

The term 'quantum dot' describes a system of electronic confinement which approaches a regime of quasi-zero dimensionality, leading to a discrete spectrum of well separated allowed energy states. If the symmetry of a bulk semiconductor crystal is disturbed by an interface with a different semiconductor, interesting and important electronic bandstructures can be engineered via the form of the interface and the choice of semiconductors. The quantum well is a very important example of such a system, where a thin layer of one semiconductor is deposited on a dissimilar bulk semiconductor host material, and the quantum well layer is then capped by another bulk region of the host material, forming what is known as the double heterostructure. A particularly useful double heterostructure is formed when the well material has a potential well for both electrons in the conduction band and holes in the valence band, and is known as the type I double heterostructure. Free carriers in this kind of system can be effectively confined in the potential well, and when the dimensions over which the carriers are confined is on the scale of several nanometres or less, the allowed energies and momenta of the carriers are described by the solutions to the one-dimensional Schrödinger equation for a finite square well potential.

The confinement of carriers and advances in crystal growth technology have allowed the realisation of high-quality, nanoscale structures. This is turn has led to significant efficiency improvements in the field of semiconductor optoelectronics. However, more than one degree of confinement is possible using the semiconductor heterostructure. The quantum wire confines carriers in two dimensions leaving only one degree of freedom, but a more intensively researched low-dimensional structure is the quantum dot, where the carriers in the dot are confined in all three dimensions. GaAs and InAs form a type I heterostructure and it is in this material system which forms the basis for the QDSAMs studied in this work.

Using QDs in SESAMs is a recent development and has numerous advantages

over other absorbing media such as quantum wells. The first demonstration of a QDSAM was in 2001 [119] and since then QDSAM structures have been implemented successfully in several systems [120–126], demonstrating their capabilities as passive mode-locking elements in the near infra-red. However, there is still a large amount of work to be done to realise the full potential of QDSAMs and so studies like this are an important step in the development of high performance systems.

5.2.1 Quantum dots vs Quantum wells

For use in SESAMs, quantum dots would ideally fulfill several criteria; firstly, be able to accurately target specific wavelengths to coincide with laser operation. Secondly, they should exhibit a fast recovery time for ultrashort pulse shaping and for use in high repetition rate systems. Thirdly, they should have sufficient absorption to function well as saturable absorbers. Quantum dots fulfill all these criteria, but then so do quantum wells. Quantum dots are interesting predominantly for the tunability they exhibit, and have a number of other useful properties.

The spectral characteristics of the dots can be modified post-growth using a simple rapid thermal annealing process. This will be outlined in more detail shortly, but the result is that the chemical composition, and hence electronic spectrum, of the dots can be altered, enabling tailoring of the dot spectra without the need to sacrifice high dot densities. This gives the possibility of producing devices of different performance characteristics from a single growth run. It also means that any deviation of the dot characteristics from the design parameters, due to irregularities in the growth procedure for example, can be corrected simply without the error causing wastage. There is also a large inhomogeneous broadening observed under certain annealing conditions which gives the potential for wide bandwidth absorption, suitable for femtosecond pulse generation. Additionally, and possibly most importantly for the international research drive, the tunability of quantum dots means that they are particularly suited for the important 1.3 μm telecommunications window, without the need for dilute nitride materials.

One of the main disadvantages of quantum dots is the reduced absorption

coefficients compared to quantum wells. As with quantum wells, the absorption is provided by excitonic confined states and the absorption coefficient is therefore related to the density of states. The density of states for the dot ensemble is governed by the volume dot density, and so quantum dots will always suffer from reduced absorption relative to quantum wells due to the lower coverage in the xy plane, which results in an effectively reduced density of states. The nature of dot growth limits the attainable dot density and thus the amount of absorption which can be achieved from a single layer. It is thus not possible to achieve densities sufficiently high to compete with the density of states of a quantum well material. To tackle this issue and achieve high modulation depths in quantum dot saturable absorbers, the simple solution is to use more dot layers. The three dimensional carrier confinement and large absorption cross section of the quantum confined dot shape does lower the saturation fluence as well. This makes dots more suitable to systems where low saturation fluences are critical, such as high repetition rate systems or solid state lasers with long upper state lifetimes.

Another possibility for increasing the absorption is to make use of excited state absorption. Previously, all work on quantum dot saturable absorbers has been concentrated on using the ground state of the dot system as the absorbing transition. The QDSAMs investigated in this work are the first in the world to make use of an excited state transition. The photoluminescence (PL) spectrum shown in Fig 5.1 illustrates the first four absorbing transitions in a simple quantum dot system at 12 K. At room temperature, this spectrum will shift and the position of the third excited state (X3) can be estimated as $\approx$1060 nm. The annealing process can then be used to tune this transition more precisely to the required position of 1064 nm. This figure also helps to show how a single quantum dot layer could in theory be used to give functional absorption at multiple wavelengths.

The significance of using this excited state transition is illustrated in Fig 5.2 which shows the calculated absorption coefficients for the the first three dot excitonic states, assuming the states are initially empty. This shows that the absorption coefficients for a single layer of dots is significantly increased for the excited state transitions, and so multiple layers could give the necessary absorption for effective QDSAM devices. This improvement arises because the higher lying ex-

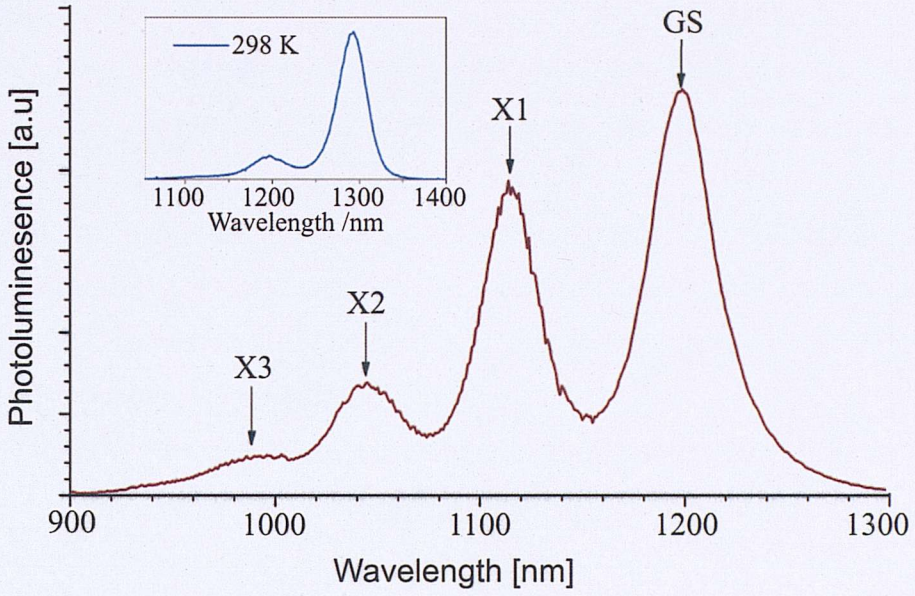


Fig 5.1. *Low temperature (12K) PL obtained from a quantum dot sample, showing the ladder of confined state transitions. Inset: Room temperature PL with only ground state and X1 states visible. The X3 transition, although not visible at room temperature, is predicted to occur at 1060 nm [127].*

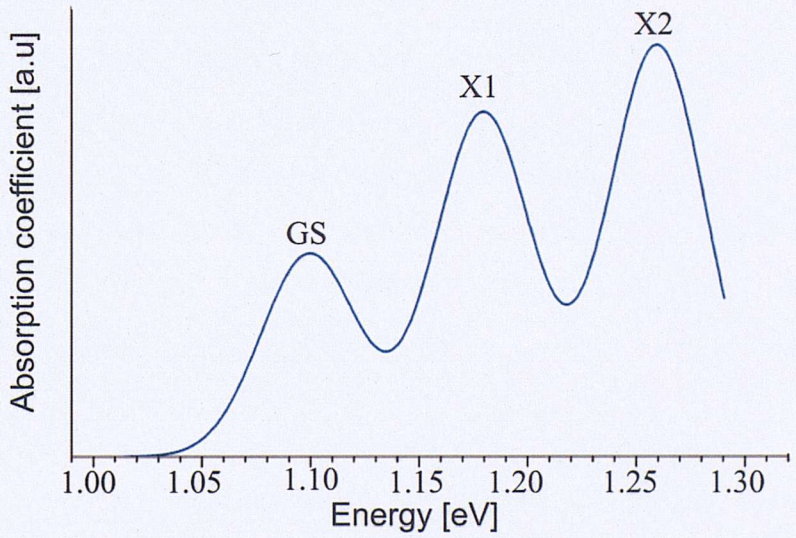


Fig 5.2. *Simulated absorption coefficients for the first three exitonic transitions in a quantum dot ensemble [127].*

cited states turn out to have an increased degeneracy to the lower lying states, and so the overall density of states is increased. Utilising this elevated absorption coefficient is an attractive feature of excited state quantum dots for SESAM applications, and the choice of dot state used as the absorptive transition provides a useful degree of flexibility.

Another potential benefit of using the excited state transition is that there are a greater number of decay pathways for the carriers. This offers the potential for faster absorption recovery dynamics than ground-state devices, which is suitable for ultrashort femtosecond pulse shaping.

Quantum dots then, can match quantum wells in the important parameters for effective saturable absorber action. The absorption coefficient can be competitive through the use of multiple layers and suitable transition choice, and the confinement of the dots leads to low values of saturation fluence. The dot states also exhibit sufficiently fast recovery times to be useful in ultrashort pulse shaping. The main draw of quantum dot devices however is the enhanced tunability of operating wavelength and the possibility for easy implementation in the important 1.3 μm telecommunications band.

5.2.2 Growth of quantum dots

Quantum dots are grown epitaxially by a process known as Stranski-Krastonow growth. The lattice constant of InAs is approximately 7 % larger than GaAs, and when InAs is deposited on to GaAs it is compressively strained. The first 1.6-2.0 monolayers of InAs are deposited as a highly-strained, layer known as the wetting layer. A critical thickness is reached whereupon it is energetically favourable for the material to organise into 3D island structures. This is to relieve the high strain, which has been accommodated by this elastic relaxation as opposed to dislocation in the crystal structure. This island formation allows for very high luminescence efficiency and very low defect density, even with large lattice mismatches as in the InAs/GaAs material system. The density of the dots formed can be controlled by the growth rate and the substrate temperature and the size of the dots is governed by the total InAs coverage for a given dot density. Figure 5.3 shows an atomic

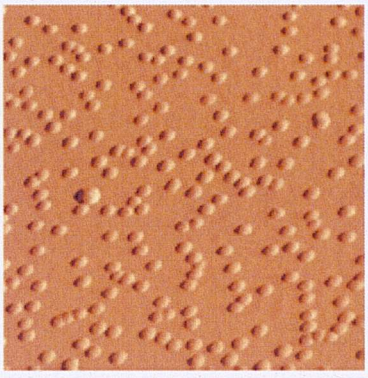


Fig 5.3. *A $1\mu m \times 1\mu m$ atomic force microscope image of uncapped InAs dots grown on GaAs [127]. The dots are typically a few nanometers in height.*

force microscope image of a typical distribution of uncapped dots with a density of approximately 1.6×10^{10} cm^{-2}. A single layer of dots can have a room temperature ground state transition ranging from < 1000 nm to around 1300 nm by controlling substrate temperature and InAs coverage. In order to reach 1300 nm the cap layer is modified. By capping the dots with an InGaAs alloy, with a lattice constant closer to the InAs dots, the strain is reduced allowing the formation of large indium rich dots. This method of capping is termed 'dots in a well' and has been successful in producing dots capable of emitting at long wavelengths [128].

In order to reach wavelengths longer than 1300 nm, two main routes are available. The first is to incorporate a dilute concentration of nitrogen into the crystal. The presence of nitrogen in the crystal reduces the bandgap of the material, but the process is not yet fully understood. The luminous efficiency and homogeneity of the quantum dots are reduced by the incorporation of nitrogen [129]. In addition, the small atomic radius and large electronegativity of N compared to As can lead to strain and compositional fluctuations during growth, and redistribution of the N is needed by post-growth annealing [130].

A different way of reaching long wavelengths is to use quantum dot bilayers, which is a precise and reproducible way to obtain ground state emission wavelengths as long as 1520 nm [131, 132]. If the separation between the multiple quantum dot layers is small, of the order of 10-40 nm, then the lower layer, known as the seed layer, can influence the electronic properties of the dots in the layer

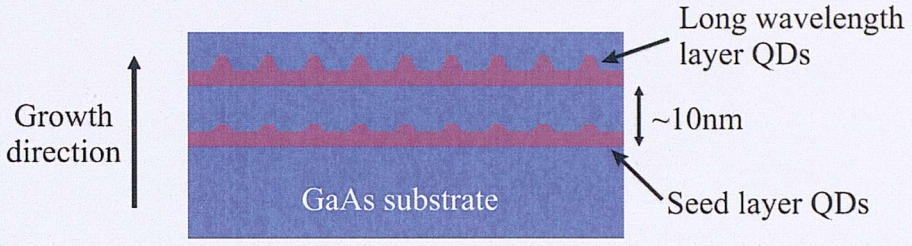


Fig 5.4. *Schematic view of a strain coupled quantum dot bilayer system with vertical alignment [127].*

above. The strained region around the seed layer dots extends through the spacer layer and affects the surface morphology of the surface on to which the second layer of dots is deposited. The dots of the second layer are seen to preferentially form directly above the dots beneath, due to a locally enlarged lattice constant at these points. Under the right growth conditions the dots in the layers are perfectly vertically aligned and the density of the upper layer is fixed by the lower layer [133, 134], shown schematically in Fig 5.4. The fixing of the density allows the substrate temperature to be changed without altering the dot density. By lowering the substrate temperature during the growth of the second layer it is therefore possible to form large, indium rich dots which produce long wavelength emission, without sacrificing a high areal density. The close proximity of the vertically aligned dots produces a strongly coupled system, where carriers in the seed layer can efficiently relax into the upper layer and radiatively recombine. In a well coupled bilayer, emission from the seed layer dots is almost completely extinguished and the emission spectrum is dominated by the upper layer.

5.2.2.1 Rapid Thermal Annealing

Precise independent control of dot densities and spectral characteristics during the growth procedure can be difficult. However, rapid thermal annealing (RTA) enables dot properties to be modified post-growth in order to tailor the dot emission and absorption without affecting the dot density. The effect of RTA on quantum dots has been studied in depth [135–140] and it has been found that thermally activated In/Ga interdiffusion leads to a blue-shift in the dot emission. This means that RTA can be used to modify the properties of quantum dots post-growth, thus

enhancing the tunability of the devices.

Rapid thermal annealing subjects the dots to very high temperatures for a controlled amount of time, with fast ramping and cooling to the anneal temperature. Typical temperatures for annealing QDs range from around $700 - 1000°C$. The rapid thermal annealer used to treat the QDSAMs being investigated in this experiment heats the samples using banks of high power UV lamps to irradiate a silica platter, on which the sample is placed. Argon gas is passed through the heating chamber of the annealer to create an inert atmosphere, and the surface of the sample is protected either with a GaAs proximity cap (essentially a piece of GaAs wafer placed directly on top of the exposed surface of the sample), or alternatively the surface is coated with a layer of deposited SiO_2. The purpose of these treatments is to minimise the desorption of arsenic from the sample which occurs at temperatures above 600°C and can leave the surface Ga rich [141, 142]. For the quantum dots used in this work, most of the annealing processes have been conducted using proximity capping due to the simplicity of this approach.

The collaborating group grew a set of dots with a ground state emission at 295 K of 1237 nm and then annealed them under a GaAs proximity cap for a range of temperatures between $750 - 900°C$ for a range of durations up to 40 s. The peak emission energy at 10 K for the annealed samples is shown in Fig 5.5. The magnitude of the blue-shift increased with the annealing temperature, as the thermal energy of the constituent atoms in the crystal rises and increases the rate of interdiffusion events. At 700°C no blue-shift occurred, and much longer anneal durations may be required to see an appreciable change in the ground state energy. The greatest blue-shift rates occurred at short anneal times, and although exact quantitative comparisons cannot be made, there was no significant reduction in the emission intensity of the annealed samples. This suggested that significant generation of defects in the dots as a result of the annealing did not take place.

For short anneal durations and at low anneal temperatures the emission FWHM of the samples was seen to increase. This is shown in Fig 5.6, which displays the low temperature ground state linewidth as a function of shift in ground state energy. The broadening of the spectrum could be very useful for QDSAMs designed for femtosecond pulse generation, enabling saturable absorption over wider

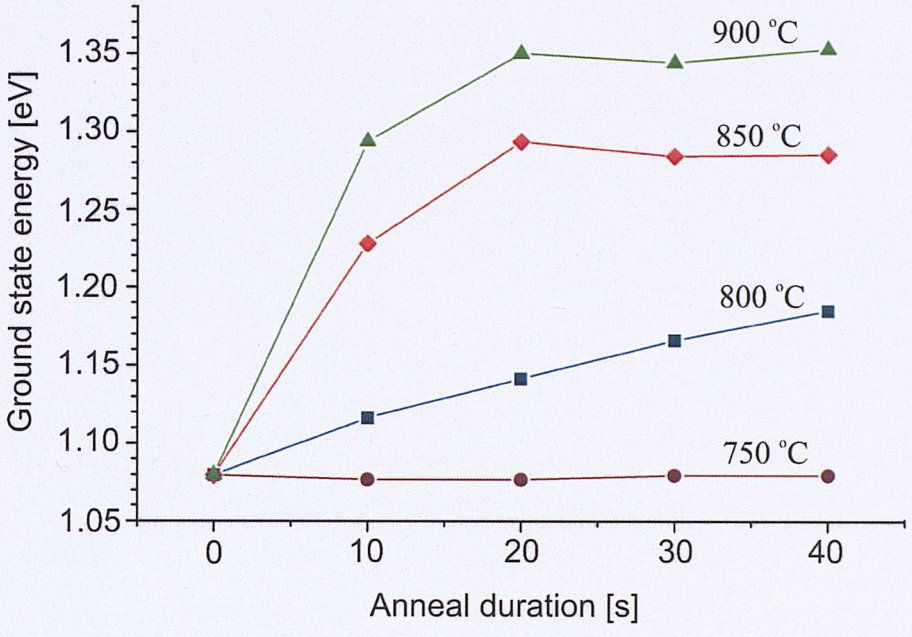


Fig 5.5. *The peak ground state emission energy at 10 K for the dot sample annealed for a range of temperatures and durations [127].*

bandwidths than as-grown dots.

5.3 Investigation of QDSAM devices

To create a functional quantum dot SESAM device, five dot layers were grown inside a low-finesse resonant micro-cavity, shown in Fig 5.7. The resonant design maximises the field strength in the cavity and ensures that the anti-nodes of the standing field pattern coincide with the location of the dot layers, thus maximising the absorbing power, and minimising the saturation fluence. The low-finesse cavity was formed by a 25 period AlAs/GaAs DBR designed for operation at 1064 nm, and the top surface of the structure. This design minimises the transmission (and hence non-saturable) losses and makes the device more flexible for post-growth modification. There are a number of different techniques for modifying the properties of the SESAM structure, all of which involve adding or subtracting material from the surface of the device. Forming the cavity from two DBRs would make alteration of the structure impossible and so any errors in the growth of the device could not be corrected, unlike with the low-finesse design. The nominal

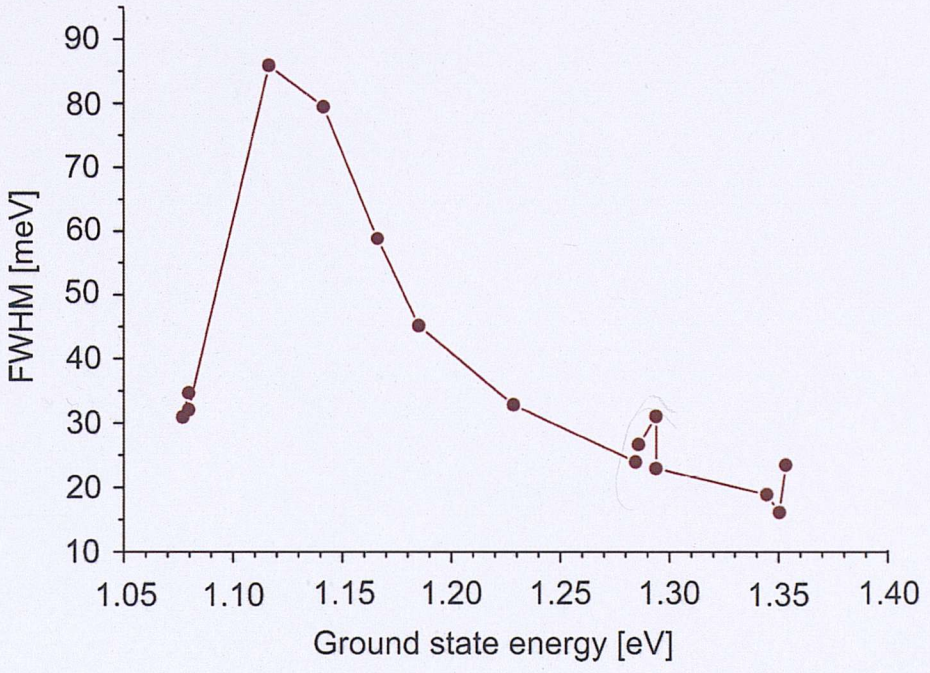


Fig 5.6. *The full width at half maximum of the ground state dot transition as a function of the ground state transition blueshift [127].*

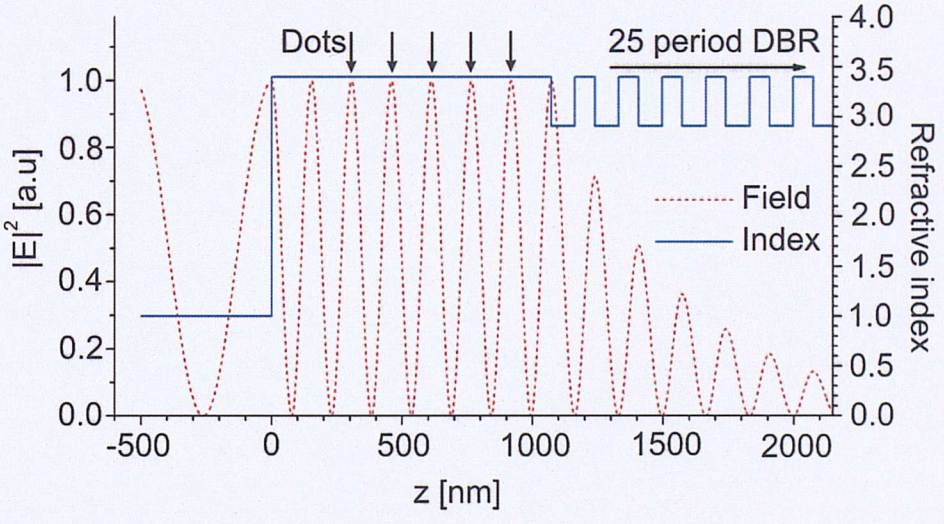


Fig 5.7. *The refractive index profile and calculated electric field structure at 1064nm for the low-finesse resonant QDSAM design [127].*

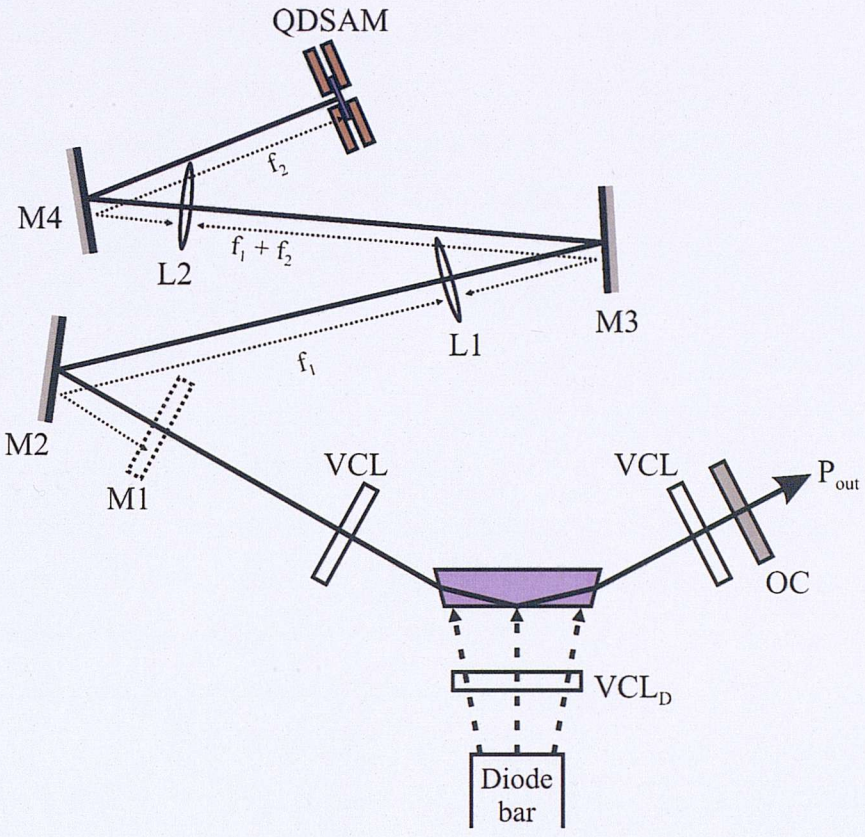


Fig 5.8. *The basis of the cavities for the QDSAM investigation. L1 and L2 are lenses with focal lengths f_1 and f_2 and these were changed to alter the magnification between M1 and the QDSAM.*

optical thickness of the cavity was $13\lambda/4$ and the dots were grown so that the laser wavelength of 1064 nm corresponded to the third excited state. Operating on the excited state transition makes use of the higher degeneracy of these states, increasing the absorption coefficient per layer and thus increasing the modulation depth of the device.

The QDSAMs were to be tested in a bounce geometry cavity similar to that described in Chapter 4, Fig 5.8. The saturation fluence of the QDSAMs is much lower than the commercial SESAMs used previously and so a lower pulse fluence may be required to obtain modelocking, so as not to oversaturate the devices. To achieve this, the same approach was used as in Chapter 4, whereby the pulse fluence is reduced by enlarging the mode size on the QDSAM. This again will be done through suitable choice of optics in the relay-imaging system. To start

with, a magnification factor of 2 was chosen to produce a large mode area, in a cavity of similar length to that in §4.5.3. Over the full range of pumping available, no modelocking was observed in this configuration, with only sporadic bursts of pulsed behaviour observed. The magnification factor of the relay-imaging system was gradually reduced step-by-step by varying L1 and L2 to try and increase the pulse fluence to the correct level. Magnification factors of 1.66, 1.2, 1, 0.83, 0.6 and 0.5 were tested, each time trying to keep the cavity length as similar as possible.

The quality of the pulsed behaviour gradually increased as the pulse fluence rose, until stable modelocking was achieved in the 0.6 and 0.5 systems. The output power levels of 1-2 W from ~20 W of pumping was slightly lower than those in the commercial SESAM systems, suggesting lower values of the pulse fluence at the QDSAM. Unfortunately, the shortest pulse duration measured in these two systems using the manual autocorrelator was 200±21 ps, which is significantly longer than that obtained with the quantum well-based commercial devices. The large error is due to the fact that the pulses were too long to completely fit into the scan range of the autocorrelator and so to enable a curve to be fit to the data, the base level of the scan had to be set manually (Fig 5.9). This was far from an ideal situation, but the pulses were so much longer than would be expected that something was clearly wrong with the functioning of the system anyway.

This poor performance was found to be due to defects in the growth of the QDSAMs. Errors in the MBE machine had resulted in an anomalously thick layer in the DBR structure, and slightly thinner layers than the design dictated. This resulted in a modified cavity length and a shift in the reflectivity spectrum. Transmission electron microscopy (TEM) measurements of the layer thicknesses are shown in Fig 5.10 together with the measured normal incidence reflectivity measurements of the sample. The reflectivity measurements showed that the QD-SAM resonance had shifted to ≈1045 nm, well away from the design of 1064 nm. This resulted in a modulation depth at 1064 nm of ≈ 0.7 %, which is too small to perform adequate pulse shaping in this system. Additionally, the spectrum also revealed that even on resonance, the maximum modulation depth of the five dot layer QDSAM would only have been 2 %, which may well also have been too little to produce short pulse modelocking.

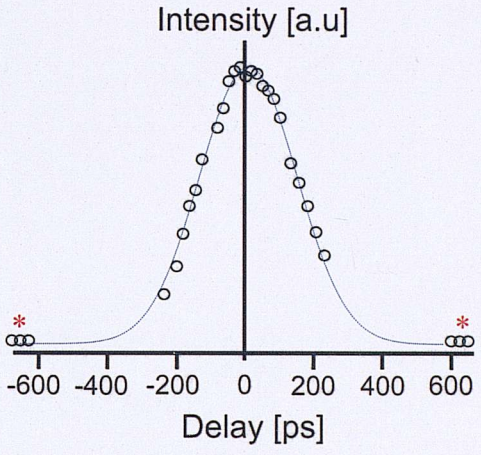


Fig 5.9. *Manual intensity autocorrelation of the pulses from the low modulation depth QDSAM. The pulse duration is too long to fit completely into the scan range of the autocorrelator and so the base level of the trace has to be artificially fixed (*). This introduces a large error in the measurement.*

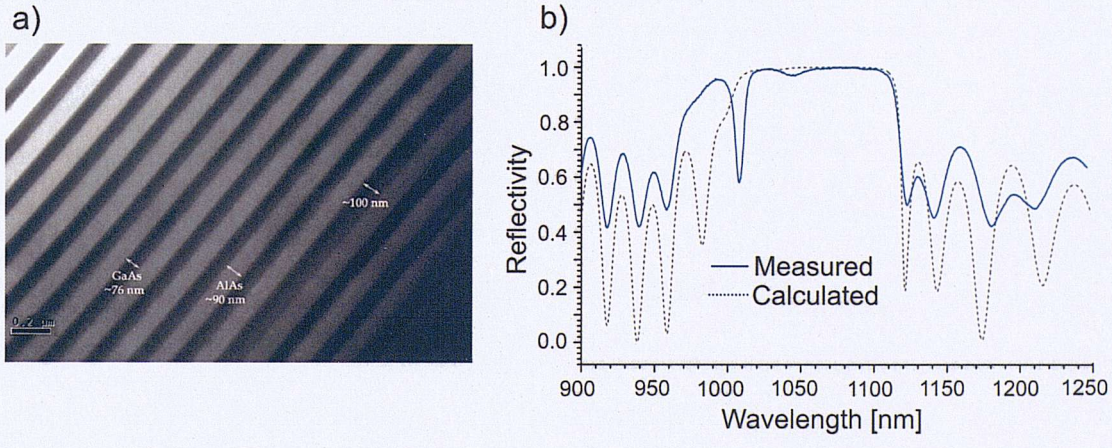


Fig 5.10. *a)TEM of the QDSAM showing an anomalously thick Ga layer; b)Normal incidence reflectivity of the QDSAM showing a shift in the absorption resonance to ≈1045 nm [127].*

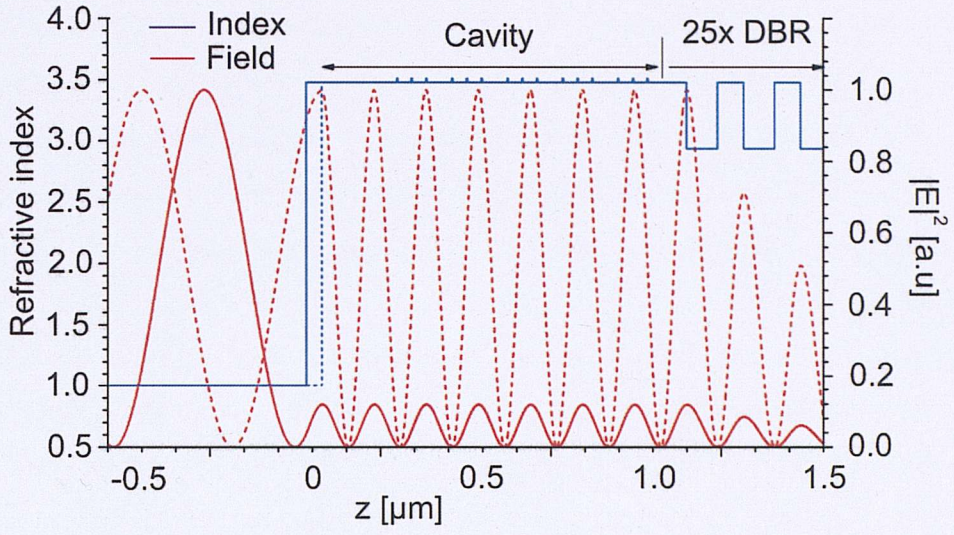


Fig 5.11. *The refractive index and square of the electric field calculated at 1064 nm across the cavity region for the nominal resonant, low-finesse QDSAM (dotted lines); and taking into account the properties of the 15 dot layers (solid lines) [127].*

5.4 QDSAMs with higher modulation depths

In order to test a QDSAM with a larger modulation depth, a sample containing fifteen dot layers was grown. The dot layers were positioned in groups of three layers, separated by 40 nm of GaAs and centred at the anti-nodes of the standing field in the same low-finesse resonant cavity as before. The dots were nominally identical to those contained in the previous device containing five layers. Assuming the thickness of the dot layers to be negligible, the cavity resonance coincides with the design wavelength of the DBR. In this case the standing wave field pattern for a resonant sample ends on an anti-node at the sample/air interface, as indicated by the dotted lines in Fig 5.11. However, the large number of layers in this structure means the dot layers cannot be neglected; their presence increases the effective cavity length and consequently detunes the cavity resonance away from the design wavelength of the structure. The solid lines in Fig 5.11 show the standing wave pattern inside the cavity region at λ_0, including the quantum dot layers. Now, the structure does not have an anti-node at the GaAs:air interface and the relative field strength inside the cavity is much reduced. In addition, because of the thickness

contribution from each dot layer the anti-nodes of the field at λ_0 inside the cavity are not perfectly aligned with the dot layers, which reduces the overall absorption compared to a structure where the dots are aligned exactly with the anti-nodes.

The reduction in the relative strength of the field inside the cavity (a ratio known as the enhancement factor), due to the presence of the quantum dots, lowers the modulation depth and raises the saturation fluence at λ_0 by a factor of $\sim$9 relative to the nominal design. In order to correct for this, the effective cavity length must be modified to tune the cavity through resonance at λ_0. The effectively elongated cavity region in these samples has shifted the cavity resonance to 1091 nm. This can be easily corrected by a simple process of chemical etching.

5.4.1 Chemical etching

In order to tune the cavity resonance through the design wavelength, the upper surface of the mirror was etched using a 2:1 solution of H_2O_2 and citric acid. This technique is attractive due to the simple processing requirements and nanometre precision possible using slow etch rates and is an alternative to other techniques for changing the effective cavity length, such as dielectric capping. Figure 5.12 shows normal incidence reflectivity for a range of etch durations, illustrating the shift in cavity resonance as the effective cavity length was reduced. A total of 70 nm was etched from the surface of the QDSAM to produce this range of resonance shift. There is a slight reduction in the depth of the reflectivity dip at the cavity resonance for successive etches due to the shorter anti-node spacing of the field in the cavity for shorter wavelengths. Consequently, the effective overlap of the dots and the field is slightly reduced as the resonance blue-shifts. This effect is also visible in Fig 5.11 where the anti-node spacing of the 1064 nm field was different to the dot spacing.

Another advantage of the etching process is that the reflectivity of the upper surface of the cavity remains unchanged. Consequently the enhancement factor on resonance is unity for a low-finesse, resonant cavity over a wide range of resonant wavelengths. The deposition of a lower index cap layer to modify the resonant wavelength however, reduces the enhancement factor on resonance by an amount

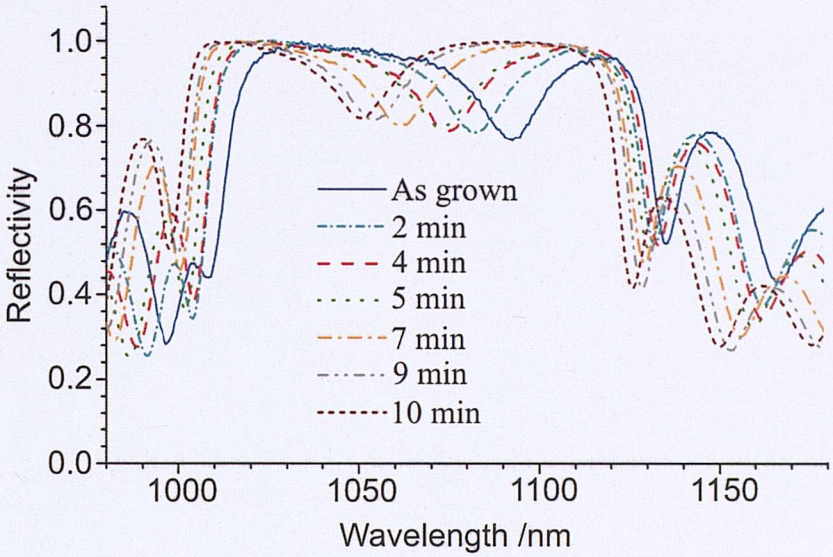


Fig 5.12. *The measured low intensity reflectivity of the QDSAM for a range of etch durations, demonstrating the shift of the resonance as the effective cavity length is reduced [127].*

dependent on the cap index and thickness, which in turn reduces the modulation depth and increases the saturation fluence.

The measured modulation depth and saturation fluence of the etched samples are shown in Fig 5.13 as a function of the detuning of the cavity resonance from the design wavelength. The sensitivity of ΔR to the etching process provides a useful method to tune the QDSAM, allowing optimisation of the modulation depth to best suit the particular laser system requirements. However, the change in saturation fluence with etching must also be taken into account and may require changes of the intracavity power or the spot size on the QDSAM to compensate.

5.5 Investigation of high modulation depth QD-SAM devices

The aim was to eventually test all of the etched samples to see if they acted as effective saturable absorbers, and to see if there was any variation in the pulsed behaviour for the range of modulation depths. Firstly though, the aim was to try to improve on the pulse duration obtained with the 5-dot layer samples. To do this,

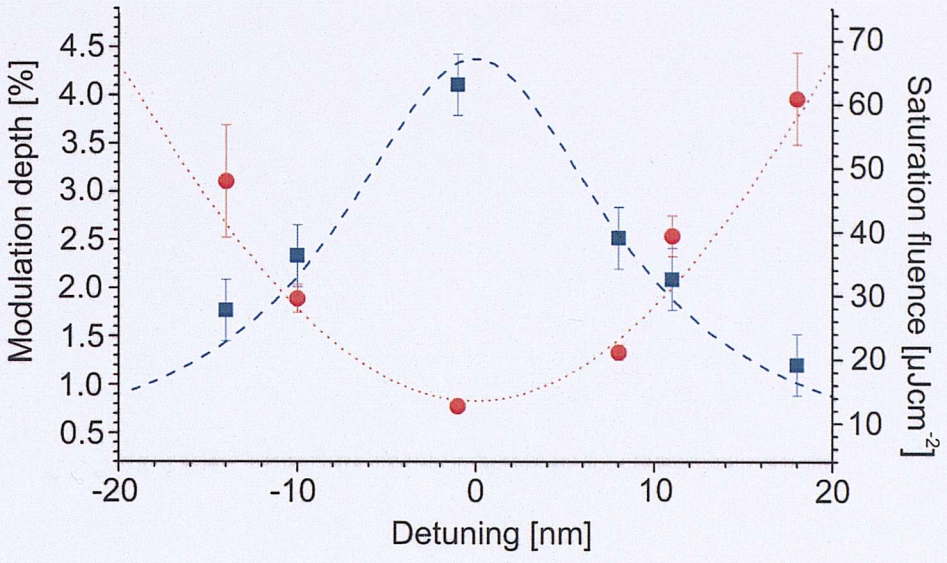


Fig 5.13. *Values for modulation depth (blue squares) and saturation fluence (red circles) obtained from intensity dependent reflectivity measurements against the detuning of the cavity resonance from the design wavelength [127].*

the QDSAM that had been etched so that its resonance now coincided with the operation wavelength of the laser was used. As can be seen in Fig 5.13, this sample had the largest modulation depth of approximately 4 %, and lowest saturation fluence of approximately 12 μJ cm^{-2} at 1064 nm. The modulation depth is thus comparable to that of the commercial quantum well based devices used in chapter 4 and significantly larger than the previous QDSAMs, which should help improve the pulse shaping dynamics in the cavity. The saturation fluence however was also significantly lower than the commercial devices and this will have implications on the suitable cavity design, where the intracavity pulse fluence may have to be reduced.

The QDSAM was tested in the same set of cavities described in §5.3, starting with the largest mode size on the QDSAM and reducing as necessary. Despite the low saturation fluence, it was again found that the optimal performance was achieved in the cavity which reduced the mode dimensions by a factor of two from those in the basic bounce cavity, albeit at a lower output power than achieved with the commercial devices. The minimum pulse duration obtained was 84±4 ps

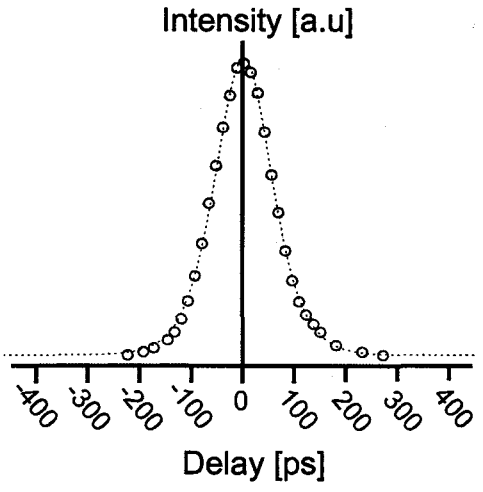


Fig 5.14. *Manual intensity autocorrelation of the shortest pulses achieved from the QDSAM devices. The pulses are determined to have a duration of 84±4 ps.*

with an average output power of 3.0 W from 25 W of pumping, in a 78 MHz, TEM_{00} beam. This is an improvement on the previous QDSAMs, although still not at the level that would be expected from this system. This could be due to a number of reasons: the pulse duration may be limited by the recovery time of the QDSAMs; the devices could be oversaturated, therefore not maximising the full modulation depth and restricting the pulse shaping.

The quantum dots should have a recovery time similar to that of the quantum wells, if not less. However, without actual tests of the carrier temporal dynamics it cannot be said for certain if this is the case. It is though, unlikely that the recovery time is so long as to give the significant pulse limiting seen here.

More likely is that the pulse fluence on the QDSAM is not at the right level to maximise use of the modulation depth. A simple test of this is to increase the pulse fluence by increasing the pump power of the system to see if any change is observed in the minimum pulse duration. The increased pump power may require some slight cavity modifications to maintain modelocking, but these changes should be small enough that they are insignificant to the overall laser performance and allow a fair comparison.

When the pump power was changed to increase the output power from 3.0 W to 5.7 W, the measured pulse duration increased from 84 ps to 145 ps. This is a

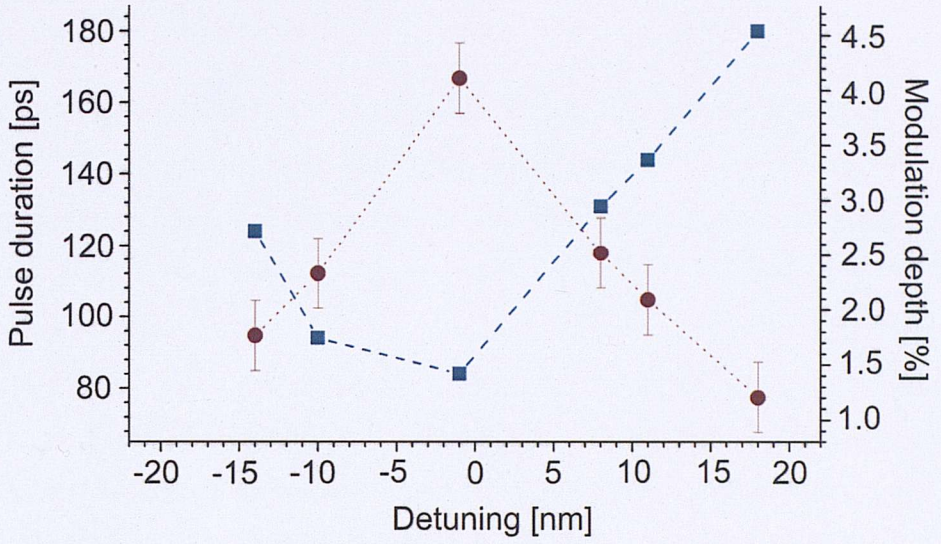


Fig 5.15. *The pulse duration of the laser (blue squares) for the QDSAMs with different detuning of the cavity resonance from 1064 nm, in good agreement with the modification to the modulation depth (red circles).*

significant degradation in performance and suggests that the device performance is very sensitive to the pulse fluence. However, no significant trend was seen if the pulse fluence is reduced, although the amount of reduction possible was limited by lasing threshold in this case.

Following this, the rest of the QDSAMs with varying modulation depths were tested. Again, each was tested in a variety of cavity configurations that varied the mode size on the QDSAM, to determine the minimum pulse duration from each. All the samples produced stable, self-starting modelocking, and again it was seen that the best performance, in terms of modelocking stability, output power, beam quality and pulse duration, was to be found in the 'factor of two' cavity. Each device was investigated over a range of pump powers, and the minimum attainable pulse durations for all the samples are plotted against the modulation depth in Fig 5.15. Here we see that, as expected, the shortest pulses are produced from the QDSAMs with the largest modulation depths. As well as neatly illustrating the tuning potential of the QDSAM devices, all of this work represents the first time modelocking has been achieved with excited state absorbing, quantum dot based SESAMs.

5.6 Conclusions

This chapter has looked at the implementation of SESAM devices based on quantum dots (QD), as opposed to the commercial standard of quantum wells (QW). More specifically, this work represents the first modelocking operation of QDSAMs that utilise excited state transitions in the QD confined states to provide the saturable absorption.

Initially, the concept of a quantum dot was introduced as a quantum system which is confined in all three spatial dimensions. This was then compared to the use of QWs in SESAM structures where it was illustrated that QDs have suitable properties for use in SESAMs, but also exhibit a number of advantages.

One of the main advantages was the ability to tune the electronic structure of the QD system post-growth. The electronic structure is determined by the size of the dots and their chemical composition. An initial layer of QDs may have an absorptive transition at 1000 nm, but several processes are available that allow modification of the chemical composition of the dots and their local environment. These can then allow the absorptive transition to be tuned to as high as 1500 nm. This covers the important telecomms band and also means that devices can be tailored to a particular laser system from a single growth sample. This tunability also means that any imperfections in the grown sample can be corrected easily.

One disadvantage that the QDs have is that they exhibit much lower absorption coefficients than their QW counterparts. This limits the modulation depths available from QD devices, which may need to be large in certain systems. This is compensated for by using multiple dot layers and making use of excited state absorptions which have higher absorption coefficients than the usual ground state transition.

The growth process of the QDs was outlined in brief, together with the post-growth modification technique of rapid thermal annealing, which also demonstrated an increase in the linewidth of the transitions, making the dots suitable for high bandwidth, short pulse operation. Following this introduction, a set of QDSAMs using 5 dot layers as the saturable absorber were tested in a bounce geometry oscillator and used to produce modelocked pulses of 200 ps duration. This

was much longer than expected, and the relatively poor performance is attributed to the low modulation depth of < 1 %, which itself is identified as being due to errors in the growth procedure.

A second set of QDSAMs were grown that used 15 dot layers to provide the saturable absorption. The presence of so many dot layers in the SESAM structure modified the internal field pattern from that calculated in the system modelling, where the optical properties of the thin dot layers are not taken into account. This resulted in a significant shift in the spectral properties of the real QDSAM devices from the modelled design. This was compensated for by the further post-growth technique of chemical etching which produced a set of QDSAMs with varying modulation depths at 1064 nm.

This set of QDSAMs were tested in the bounce geometry oscillator and it was found that the variation in modulation depth resulted in a variation in the minimum pulse duration. The shortest pulses of 84 ps were obtained when using the QDSAM with the highest modulation depth and the variation in pulse duration across the sample set was seen to be 96 ps. This pulse duration was still somewhat longer than obtained with the commercial QW-based SESAM devices (13 ps) and it was seen that the pulse duration from a given QDSAM was very sensitive to the incident pulse fluence. This suggested that the cavity was not optimally configured for the QDSAM parameters and more fine tuning of the illuminated mode size on the QDSAM is required. Despite the poorer than expected pulse durations, the work with the QDSAMs was the first time that excited-state quantum dot-based SESAM devices have been used to produce modelocked pulses and the work described led to the publication of two peer reviewed papers [42, 43].

Chapter 6

Non-linear mirror modelocking

6.1 Introduction

This chapter will introduce the second major modelocking mechanism to be used in this thesis. The non-linear mirror mechanism combines second harmonic and difference frequency generation in a non-linear optical crystal, together with a dichroic mirror, to produce an intensity dependent reflectivity. This intensity dependent reflectivity can then lead to modelocking as described in previous chapters. The non-linear conversion processes that give rise to the absorber effect are essentially instantaneous and so there is no physical process that limits the final pulse duration, as is the case with SESAM modelocking. This mechanism should therefore be able to support pulses limited only by the oscillating bandwidth of the laser. The non-linear processes are also parametric and so the final system should be much more robust against heating damage, unlike the SESAM systems which are susceptible to both high intensity ablation damage and long-term degradation due to heating.

This chapter will begin by giving a basic outline of the origin of non-linear optical effects. The non-linear polarisation of a media will be introduced together with the higher order susceptibilities and this will be shown to give rise to frequency conversion and mixing effects. Second harmonic and difference frequency genera-

tion will be highlighted in particular. A few potential non-linear optical media will be discussed and their relative benefits analysed. The concept of phase-matching for these non-linear processes and the methods for achieving it are outlined before going on to cover in more detail the non-linear mirror modelocking (NLM) technique. This then leads into an experimental study of NLM modelocking in the bounce geometry. Three non-linear optical media are utilised and new benchmarks for this type of system are achieved with respect to both output power and pulse duration.

6.2 Non-linear optics and the $\chi^{(2)}$ susceptibility

An ideal linear optical medium has an entirely linear response of its polarisation as a function of incident electric field:

$$P = \epsilon_0 \chi E \tag{6.1}$$

where ϵ_0 is the permittivity of free space and χ is the dielectric susceptibility of the medium. This can then be used as the source term in the electromagnetic wave equation which will describe the propagation of the wave in the medium:

$$\nabla^2 E - \frac{1}{c^2}\frac{\partial^2 E}{\partial t^2} = \mu_0 \frac{\partial^2 P}{\partial t^2} \tag{6.2}$$

where μ_0 is the permeability of free space. This is sufficient to describe propagation in most transparent optical materials, as long as intensity levels are low.

In general however, the polarisation is a non-linear tensorial relation of the form:

$$P = \epsilon_0 \{\chi^{(1)} E + \chi^{(2)} E^2 + \chi^{(3)} E^3 + \chi^{(4)} E^4 + \ldots\} \tag{6.3}$$

The expression now contains higher-order susceptibilities ($\chi^{(2)}, \chi^{(3)}$ etc.) that arise from anisotropy in the medium. The even order susceptibilities for example, are only present in non-centrosymmetric media where $P(-E) \neq -P(E)$. Now, when this expression is used as a source term in Eq(6.2) the resulting expression is called the non-linear wave equation (NLWE) and the terms involving powers of E result in the production of additional frequency components of the propagating field. Most ordinary media have zero or negligible high-order susceptibilities and

so these extra components do not manifest themselves under normal conditions. Certain special media however can have significant values of $\chi^{(2)}, \chi^{(3)}$ etc. and under sufficiently intense field conditions the magnitude of these components can be large. This leads to a material which exhibits a strongly non-linear response to the electric field. Depending on which order susceptibilities this highly non-linear medium presents, different frequency components and effects are seen. One of the most common, useful and simple effects in non-linear media, is second harmonic generation.

6.2.1 Second harmonic generation

Second harmonic generation (SHG) occurs in non-linear media with a strong $\chi^{(2)}$ susceptibility. Consider an electric field at frequency ω,

$$E = E_0 \cos \omega t \tag{6.4}$$

incident on such a material. According to Eqn(6.3) and Eqn(6.1), the resulting polarisation of the medium will be of the form:

$$P/\epsilon_0 = \chi^{(1)} E_0 \cos \omega t + \chi^{(2)} E_0^2 \cos^2 \omega t \tag{6.5}$$

$$= \chi^{(1)} E_0 \cos \omega t + \frac{1}{2}\chi^{(2)} E_0^2 (1 + \cos 2\omega t) \tag{6.6}$$

This then contains a component at the incident frequency ω, but also a component at 2ω, the second harmonic frequency. When this is used as a source term in Eqn(6.2), assuming monochromatic, linearly polarised plane waves, the resulting field is a superposition of two plane waves:

$$E(\omega, z, t) = \frac{1}{2}\{E_\omega(z) \exp i(\omega t - k_\omega z) + c.c.\} \tag{6.7}$$

$$E(2\omega, z, t) = \frac{1}{2}\{E_{2\omega}(z) \exp i(2\omega t - k_{2\omega} z) + c.c.\} \tag{6.8}$$

This is a field at the original incident frequency ω, and also a newly created field at 2ω. It is this new superposition of fields that then needs to be used in the NLWE. Using this, the NLWE can be split into two coupled equations at ω and 2ω which need to be solved simultaneously. If an additional assumption is made that $E_\omega(z) = const.$ then the equation need only be solved to see how $E(2\omega)$

evolves in the non-linear crystal. The assumption $E_\omega(z) = const.$ is valid in the regime of low conversion efficiency from $\omega \rightarrow 2\omega$ so that the 'pump' field at ω is undepleted over the length of the crystal.

The polarisation source term in the NLWE also needs to be modified now that two fields are present. The correct form is now:

$$\begin{aligned} P(2\omega, z, t)/\epsilon_0 =& \frac{1}{2}\{\chi^{(1)}_{2\omega} E_{2\omega}(z) \exp i(2\omega t - k_{2\omega} z) + c.c.\} \\ &+ \frac{1}{4}\{\chi^{(2)}_{\omega} E^2_{\omega} \exp 2i(\omega t - k_{\omega} z) + c.c. + DC\ term\} \end{aligned} \tag{6.9}$$

The first term corresponds to the linear response of the medium at 2ω. The second term corresponds to the non-linear response of the medium induced by the pump at ω. It is assumed for now that the 2ω field is too weak to excite any non-linear response in the medium. Using this in the NLWE and neglecting the DC term gives:

$$\begin{aligned} &\frac{\mathrm{d}^2 E_{2\omega}}{\mathrm{d}z^2} - 2ik_{2\omega}\frac{\mathrm{d}E_{2\omega}}{\mathrm{d}z}\exp(-ik_{2\omega}z) - k^2_{2\omega}E_{2\omega}\exp(-ik_{2\omega}z) \\ &\qquad + \frac{4\omega^2}{c^2}(1 + \chi^{(1)}_{2\omega})E_{2\omega}\exp(-ik_{2\omega}z) = \frac{-2\omega^2}{c^2}\chi^{(2)}_{\omega}E^2_{\omega}\exp(-2ik_{\omega}z) \end{aligned} \tag{6.10}$$

The third and fourth terms cancel by virtue of the fact that $1 + \chi^{(1)}_{2\omega} = n^2_{2\omega}$. The slowly varying envelope approximation is also used so that the first term can be neglected. This then finally results in a differential equation for the evolution of the 2ω field:

$$\frac{\mathrm{d}E_{2\omega}}{\mathrm{d}z} = \frac{-i\omega^2}{c^2 K_{2\omega}}\chi^{(2)}_{\omega}E^2_{\omega}\exp i\Delta k z \qquad \Delta k = k_{2\omega} - 2k_{\omega} \tag{6.11}$$

To calculate the total second harmonic intensity, integrate this expression over the crystal length, L:

$$E_{2\omega}(z = L) = \frac{-i\omega^2}{c^2 k_{2\omega}}\chi^{(2)}E^2_{\omega}\int_0^L \exp i\Delta k z\, \mathrm{d}z \tag{6.12}$$

then,

$$\begin{aligned} I_{2\omega}(z = L) &= \frac{1}{2}n_{2\omega}\epsilon_0 c|E_{2\omega}(z = L)|^2 \\ &= \frac{2\pi^2\left(\chi^{(2)}\right)^2}{\lambda^2 n^2_{\omega} n_{2\omega} c\epsilon_0} I^2_{\omega} L^2 \mathrm{sinc}^2\left(\frac{\Delta k L}{2}\right) \end{aligned} \tag{6.13}$$

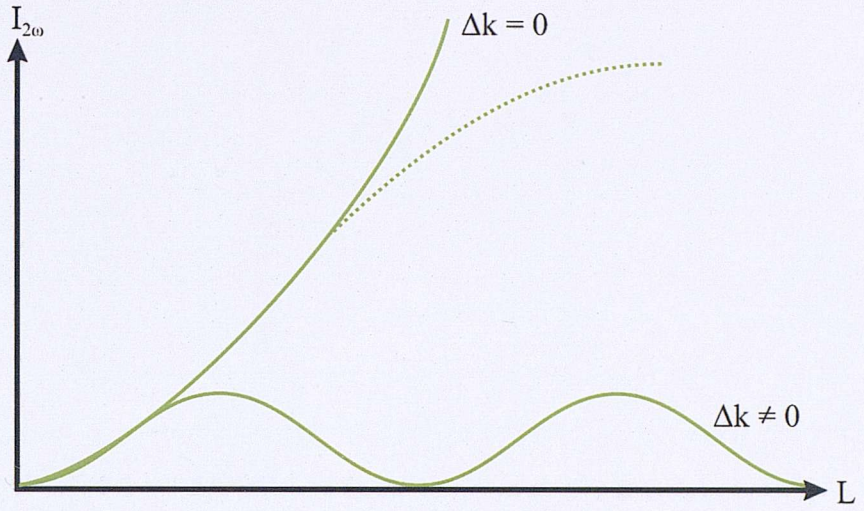


Fig 6.1. *Second harmonic growth in the non-linear crystal for* $\Delta k = 0$ *and* $\Delta k \neq 0$. *The dashed line represents the phase matched second harmonic growth for the more realistic case where pump depletion is significant i.e.* $E_\omega(z) \neq$ *constant.*

This is the form of the evolution of the 2ω field inside the crystal. Two important features of SHG are visible from this equation. Firstly, the efficiency of the conversion process from $\omega \rightarrow 2\omega$, given by $I_{2\omega}/I\omega$, is linearly proportional to the intensity of the fundamental wave. Secondly, the key parameter determining the SHG efficiency is Δk. For $\Delta k = 0$, the second harmonic intensity increases as L^2. For a non-zero Δk the intensity follows a sinc^2 function inside the crystal and never grows beyond a small value. This is illustrated in Fig 6.1. The key factor then in maximising the efficiency of the SHG is to ensure that the k-vectors of the fundamental and second harmonic fields are such that $\Delta k = 0$. This concept is known as *phase-matching* and turns out to be critical in all non-linear optical processes.

An alternative view of SHG is to consider the photon picture. Depicted in Fig 6.2, SHG occurs when two photons of frequency ω are absorbed simultaneously in a transition. The subsequent decay releases the energy in a single photon of frequency 2ω. The cross section of this process is small and so high numbers of photons (high intensities) are required to produce significant effects. Momentum conservation in this process then simply gives the phase matching condition

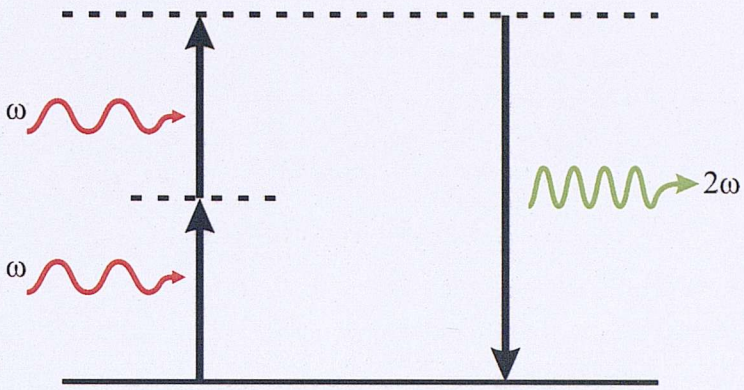


Fig 6.2. *The photon picture of SHG whereby two fundamental photons are absorbed in a single transition but the subsequent decay produces a single photon that has the combined energy of the two initial photons.*

required.

$$\hbar k_\omega + \hbar k_\omega = \hbar k_{2\omega} \Rightarrow 2k_\omega - k_{2\omega} = 0 \tag{6.14}$$

6.2.2 Difference frequency generation

Another non-linear process that arises from the $\chi^{(2)}$ susceptibility that will be important when discussing NLM is difference frequency generation. Consider two fields of frequencies ω_1 and ω_2 incident upon a $\chi^{(2)}$ media. The total field is given by $E_{tot} = E_1 \exp i\omega_1 t + E_2 \exp i\omega_2 t + c.c.$ where E_m are generally complex spatial amplitudes. As before, the non-linear polarisation term contains E^2, and in this case the total field has to be used so that the expression for the second order polarisation, $P_2 = \epsilon_0 \chi^{(2)} E_{tot}^2$, is:

$$\begin{aligned} P_2 \propto \quad & E_1^2 \exp i2\omega_1 t && \text{SHG} \\ & + E_2^2 \exp i2\omega_2 t && \text{SHG} \\ & + 2E_1 E_2 \exp i(\omega_1 + \omega_2)t && \text{SFG} \\ & + 2E_1 E_2^* \exp i(\omega_1 - \omega_2)t && \text{DFG} \\ & + const. && \text{DC terms} \end{aligned} \tag{6.15}$$

This polarisation then contains terms at the second harmonic frequencies of both input fields, as well as the sum frequency (SFG) $\omega_1 + \omega_2$ and difference frequency (DFG) $\omega_1 - \omega_2$. All of these fields will be generated in the crystal, but which one is

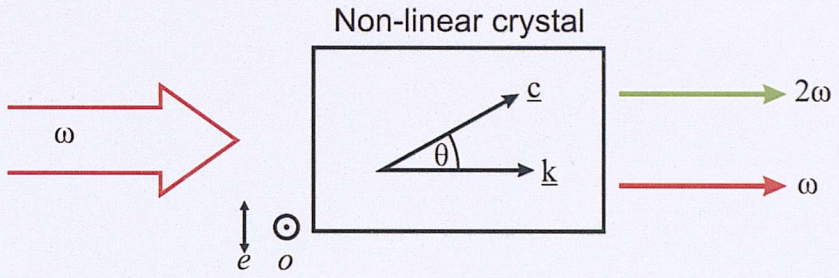


Fig 6.3. *General case of SHG in a birefringent non-linear crystal. An incoming field at a frequency ω with wave vector $\underline{k}$ at an angle θ to the crystallographic $c-axis$, is a mixture of o- and e-polarisation states. The different polarisation states will experience different refractive indices and can combine to generate a field at 2ω.*

to dominate is determined by the phase matching condition. In the case of DFG, the phase matching condition required is $k(\omega_3 = \omega_1 - \omega_2) = k(\omega_1) - k(\omega_2)$.

6.3 Phase matching considerations

In most cases, material dispersion in an isotropic medium means that $n_{2\omega} \neq n_\omega$ and therefore $k_{2\omega} \neq 2k_\omega$. This results in a finite value of Δk and so the efficiency of the non-linear process is low. In order to achieve the required phase-matching then, advantage is taken of the birefringence of many non-linear materials.

Consider a birefringent crystal with an input field that has a wave vector k, entering at an angle θ to the crystallographic axis c, Fig 6.3. In general, the incoming beam is composed of two polarisations, the ordinary (o-wave, perpendicular to the plane of c & k) and the extraordinary (e-wave, parallel to the plane of c & k) polarisations. The refractive index for the o-polarisation is independent of θ, whereas the refractive index for the e-polarisation depends on its principal value $\overline{n}_e$, n_o and the phase matching angle θ. For the case of a *negative uniaxial* crystal where $\overline{n}_e < n_o$, the extraordinary refractive index is given by:

$$n_e(\omega,\theta) = \left[\frac{\cos^2\theta}{n_o^2(\omega)} + \frac{\sin^2\theta}{\overline{n}_e^2(\omega)}\right]^{-1/2} \tag{6.16}$$

In the case of SHG, if the dispersion of the non-linear crystal is such that $\overline{n}_e(2\omega) \approx n_o(\omega)$, then the phase matching condition can be achieved by tuning the angle θ

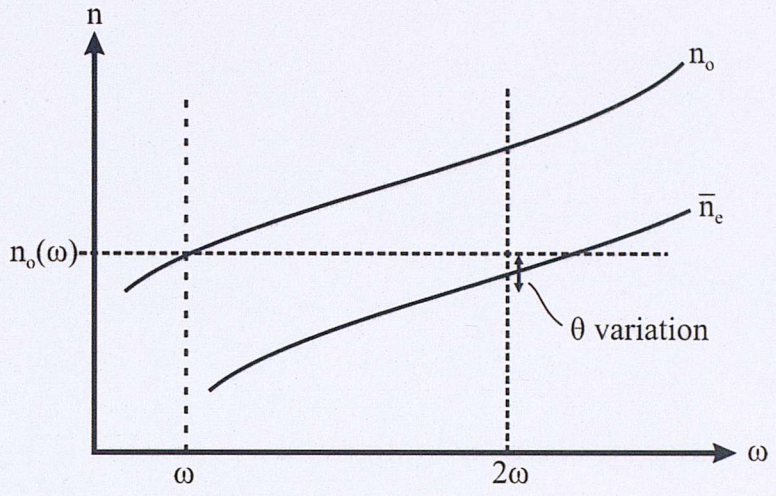
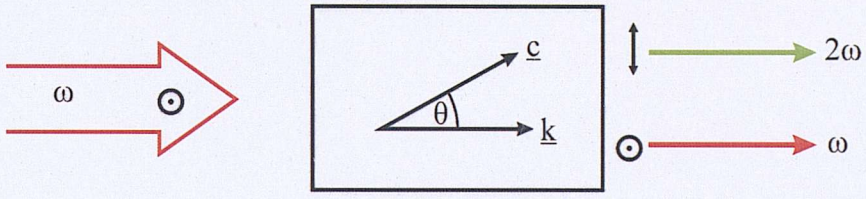


Fig 6.4. *Example refractive index curves for a negative uniaxial crystal. Angle tuning is used to ensure that* $n_e(2\omega) = n_o(\omega)$.



$$o_\omega + o_\omega \longrightarrow e_{2\omega}$$

Fig 6.5. *Polarisation states for type I phase matching. Two ordinary waves at the fundamental frequency combine to give a second harmonic wave with extraordinary polarisation.*

such that $n_e(2\omega, \theta) = n_o(\omega)$, Fig 6.4. The implication in this statement is that if the incident fundamental wave is an *o*-wave, then the resultant second harmonic wave is an *e*-wave. In fact, this situation is one of the two types of phase-matching, known as Type I and Type II.

6.3.1 Type I phase-matching

Again considering the simple case of SHG, Type I phase-matching in a negative uniaxial crystal is summarised in Fig 6.5. The input field at ω is a linearly polarised *o*-wave that sees a refractive index $n_o(\omega)$. The second harmonic field at 2ω is an *e*-wave and sees an angle dependent refractive index $n_e(2\omega, \theta)$. The phase matching

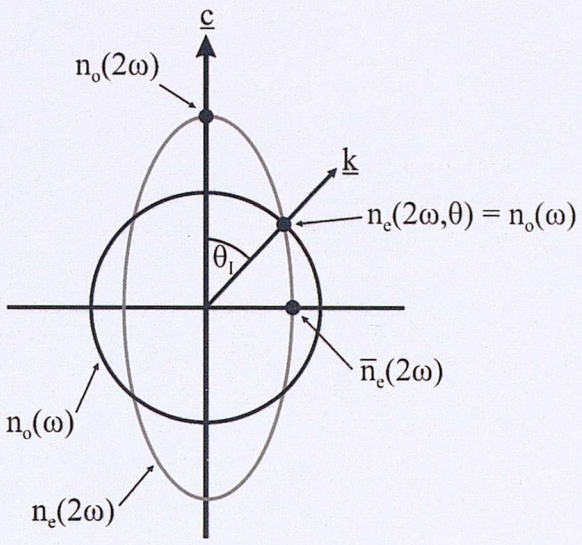


Fig 6.6. *Refractive index ellipsoids for type I phase-matching in a neagative uniaxial crystal. The phase-matching condition is satisfied when the two curves intersect at angle θ_I.*

condition $\Delta k_I = k_e(2\omega, \theta_I) - 2k_o(\omega) = 0$ is then satisfied if:

$$n_e(2\omega, \theta_I) = n_o(\omega) \tag{6.17}$$

In order to calculate θ_I, the refractive index ellipsoids for a birefringent crystal can be considered. Shown in Fig 6.6, the surfaces relate a propagation direction relative to the optic axis, to a refractive index. The curve for n_o is a circle as its value does not change with propagation direction. The curve for n_e is an ellipse because its value does change with propagation direction. The phase-matching condition is met when the two curves intersect at the angle θ_I, given by:

$$\sin^2\theta_I = \frac{\left(\frac{n_o(2\omega)}{n_o(\omega)}\right)^2 - 1}{\left(\frac{n_o(2\omega)}{\overline{n}_e(2\omega)}\right)^2 - 1} \tag{6.18}$$

From this picture it can be noted that this intersection will only happen if $\overline{n}_e(2\omega) < n_o(\omega)$, otherwise the ellipse for n_e lies wholly outside the circle for n_o. Thus, $\overline{n}_e(2\omega) < n_o(\omega) < n_o(2\omega)$, which shows that the crystal birefringence must be greater than the crystal dispersion.

$$n_o(2\omega) - \overline{n}_e(2\omega) > n_o(2\omega) - n_o(\omega) \tag{6.19}$$

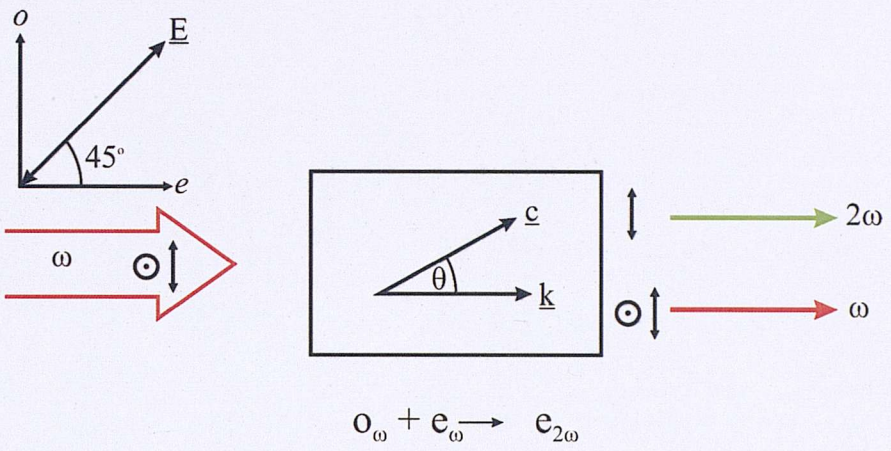


Fig 6.7. *Polarisation states for type II phase matching. With the pump beam polarised at 45° to the o and e axes, one ordinary wave and one extraordinary wave at the fundamental frequency combine to give a second harmonic wave with extraordinary polarisation.*

Type I phase-matching in a negative uniaxial crystal can also be summarised by:

$$o_\omega + o_\omega \Rightarrow e_{2\omega} \tag{6.20}$$

which says that two input waves at ω with o-polarisations can combine to give an e-polarisation wave at 2ω.

6.3.2 Type II phase-matching

The second type of phase-matching that is possible occurs when (again in a negative uniaxial crystal) an o-wave and an e-wave at ω combine to give an e-wave at 2ω.

$$o_\omega + e_\omega \Rightarrow e_{2\omega} \tag{6.21}$$

This is achieved by having the input field polarised at 45° to the $c-k$ plane, which excites both o and e-wave components (Fig6.7). The phase-matching condition is then given by:

$$\Delta k_{II} = k_e(2\omega, \theta_{II}) - [k_o(\omega) + k_e(\omega, \theta_{II})] \tag{6.22}$$

So that $\Delta k_{II} = 0$ for:

$$n_e(2\omega, \theta_{II}) = \frac{1}{2}[n_o(\omega) + n_e(\omega, \theta_{II})] \tag{6.23}$$

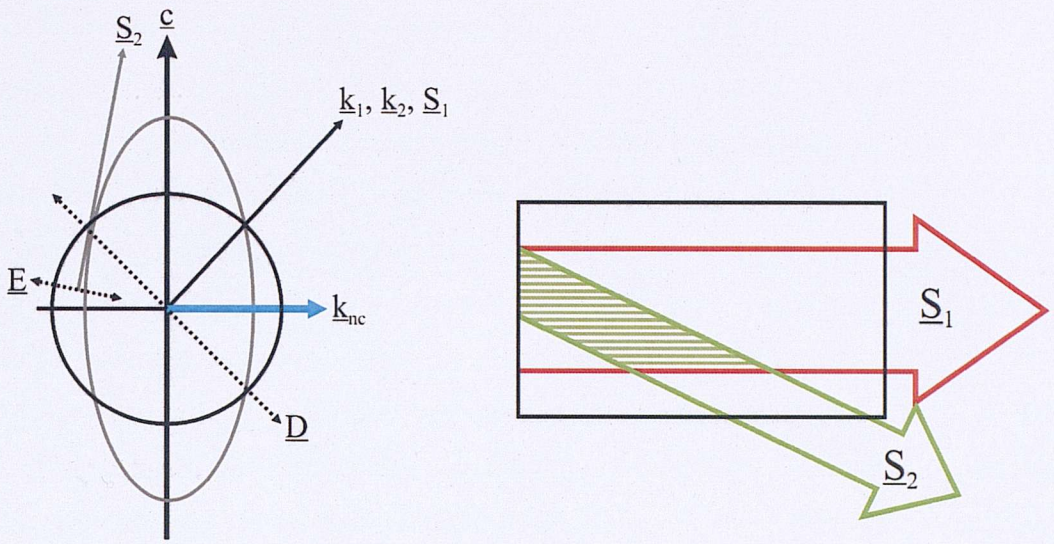


Fig 6.8. *The Poynting vectors are perpendicular to the refractive index ellipsoids and so in critical phase-matching, the fundamental and second harmonic beams walk-off from each other, even though they are still correctly phase-matched. In non-critical phase-matching, propagation is along k_{nc} so the beams do not walk-off.*

In general, type I phase-matching refers to situations where the input fields have the same polarisation, and type II to situations when they are orthogonal.

6.3.3 Non-critical phase matching

The discussion on phase-matching so far has been about what is known as *critical phase-matching*. That is, phase-matching is achieved by precise alignment of the non-linear crystal with respect to the input wave vector. There is an effect called *beam walk-off* however that can affect the phase-matching, even if the required conditions are satisfied. In a birefringent crystal, the Poynting vector is not necessarily in the same direction as the k-vectors. In fact, the Poynting vector is drawn as the tangent to the refractive index ellipsoid, at the point of intersection between the ellipsoid and the $\underline{\mathbf{D}}$ vector (which is perpendicular to $\underline{k}$), drawn through the origin (see construction in Fig 6.8). At the phase-matching angle then, the energy flow of the second harmonic wave is in a different direction to that of the fundamental wave. The two beams thus *walk-off* from each other, although still

satisfying the phase-matching criteria, which limits the interaction length in the crystal, and thus the total SHG possible.

This limitation could be overcome if the beams were to propagate at 90° to the optic axis. In this case, both refractive index curves are parallel and the Poynting vectors would point in the same direction. However at this angle of propagation, there is still a finite difference between $n_o(\omega)$ and $n_e(2\omega)$ and the phase-matching condition is not satisfied. This can be overcome in some crystals by using the temperature variability of the refractive index. The refractive index is typically temperature dependent, and the o and e-indices also show a differential variability with temperature. It is thus possible to achieve the phase-matching condition at an angle of 90° by carefully controlling the temperature of the non-linear crystal, typically to within 0.1°C. This method is known as *non-critical phase-matching* and potentially allows longer interaction lengths in the non-linear crystal to achieve higher conversion efficiencies.

6.3.4 Non-linear media

With the advancement of materials technology, there are now a large number of suitable non-linear materials available. The most appropriate for any particular circumstance will depend upon the specific requirements of the application. In general, a 'good' non-linear medium will have a high $\chi^{(m)}$, where the order of the non-linear susceptibility will vary depending on the intended application; be transparent at the wavelengths in use; phase-matchable by either type I, type II, critical or non-critical phase-matching; available in sizeable samples of optical quality; exhibit robust mechanical and chemical stability (some non-linear media are hygroscopic and have to be kept at a high temperature, others undergo phase changes at certain temperatures and can shear apart); and have a high damage threshold.

As well as these properties, some other figures-of-merit are used when discussing non-linear media. In SHG, the sensitivity to the phase-matching angle in critical phase-matching means that the angular spread of a non-collimated beam can result in varying phase-matching efficiency across its transverse profile. The

	LBO	KTP	BiBO	BBO	$KNbO_3$
$\chi^{(2)}$ [pm/V]	2.30	6.6	6.4	4.28	24.6
$\Delta\theta$ L [°cm]	1.79	1.82	0.07	0.03	0.028
ΔT L [°C cm]	3.2	24.0	2.17	51.0	0.29
PM Type	I	II	I	I	I

Table 1. *Summary of some key optical properties of non-linear crystals at 1064 nm*

acceptance angle $\Delta\theta$ is thus used to describe the change in angle over which the conversion efficiency has halved. Temperature sensitivity ΔT can also be important for long term system stability and these are usually quoted as length products. A summary of some popular non-linear materials for SHG at 1064 nm is shown in Table 1 .

6.4 The Non-linear mirror (NLM) modelocking technique

The basic setup for non-linear mirror modelocking is shown in Fig 6.9. A non-linear $\chi^{(2)}$ medium is introduced into the cavity and optimised to produce second harmonic radiation. A dichroic mirror at the end of the cavity has a high reflectivity $R_{2\omega}$ for the second harmonic radiation, but only introduces a partial reflectivity R_ω at the fundamental. The loss of this mirror acts as the output coupling for the laser fundamental ($T_\omega \approx 1 - R_\omega$). After reflection from the end mirror, on its way back through the non-linear crystal the second harmonic can be partially converted back into fundamental radiation by means of DFG, if the phasing is correct. To achieve the desired phase difference between the fundamental and second harmonic, dispersion in air can be used and controlled by the mirror-crystal displacement. Alternatively, some simple dispersive media such as a glass plate could also be used. This thus results in a greater overall loss for the fundamental at low SHG conversion efficiencies. The SHG conversion efficiency is determined by the intensity of the fundamental radiation (Eqn (6.13)) and so a

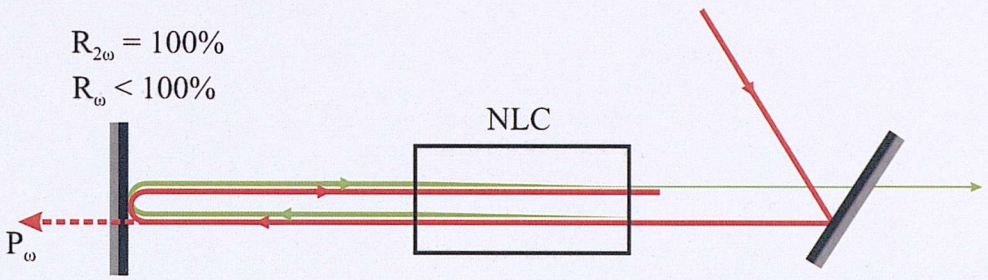


Fig 6.9. *The basic function of a non-linear mirror, consisting of a non-linear crystal (NLC) and a mirror with high reflectivity for the second harmonic but much lower reflectivity for the fundamental.*

short pulse will suffer greater attenuation in the low intensity wings, than at the high intensity centre. This creates a shuttering mechanism similar to that of the SESAM, and modelocking can be realised as described in previous chapters. This process was first put forward by Stankov [62] who gave a detailed analysis of the resulting reflectivity of the non-linear device [143].

Since the non-linear behaviour of the device is expected to be more pronounced for high conversion into the second harmonic, the depletion of the fundamental is significant and can not be neglected as in §6.2.1. The exact solutions for the amplitudes of the fundamental and harmonic waves are therefore needed. Additionally, the treatment assumes plane waves, perfect phase-matching ($\Delta k = 0$), and non-critical phase-matching so that the walk-off effect is avoided.

The real amplitudes of the fundamental and second harmonic are denoted by A_1 and A_2 and a new variable δ is introduced:

$$\delta = C(A_1^2 + A_2^2)^{\frac{1}{2}} z \tag{6.24}$$

where C is a constant which includes $\chi^{(2)}$, z is the distance traveled by the waves in the non-linear crystal, and the quantity in brackets is the total power flux. The normalised amplitudes for the fundamental F and second harmonic SH:

$$u = \frac{A_1}{(A_1^2 + A_2^2)^{\frac{1}{2}}} \tag{6.25a}$$

$$v = \frac{A_2}{(A_1^2 + A_2^2)^{\frac{1}{2}}} \tag{6.25b}$$

then obey the equations:

$$\frac{\mathrm{d}u}{\mathrm{d}\delta} = -uv \ \sin\Delta\phi \tag{6.26a}$$

$$\frac{\mathrm{d}v}{\mathrm{d}\delta} = u^2 \ \sin\Delta\phi \tag{6.26b}$$

where $\Delta\phi = 2\phi_\omega - \phi_{2\omega}$ is the initial phase difference between the two waves at the entrance to the crystal.

The solution to these equations are given by [144]:

$$v = \tanh(\delta + \delta_0) \tag{6.27a}$$

$$u = \mathrm{sech}(\delta + \delta_0) \tag{6.27b}$$

and these form the basis of the NLM mechanism. If the amplitude of the SH is initially zero, $A_2(0) = 0$, the constant $\delta_0 = 0$ and the second harmonic intensity increases with propagation distance in the crystal. This is the normal case of SHG and occurs when the incident light travels from right to left in Fig 6.9. If $A_1(0) \neq 0$; $A_2(0) \neq 0$ and the initial phase difference at the crystal boundary is $\pi/2$ then the second harmonic will be amplified first, $\delta_0 > 0$ and the fundamental wave may be completely converted into second harmonic. However, if $\Delta\phi = -\pi/2$ then the fundamental will be amplified first, $\delta_0 < 0$ and the second harmonic could be completely converted back into fundamental. This is the desired situation when the light is incident on the crystal from the left to the right in Fig 6.9 and the phase difference has been properly adjusted.

The analysis can be simplified by using relative intensities to calculate the non-linear reflectivity, and introducing the second harmonic power conversion efficiency η. The relative intensity of the fundamental is set to $A_1(0) = 1$ so that the normalised amplitudes of F and SH after the first (right to left) pass through the crystal are:

$$v = \sqrt{\eta} \tag{6.28a}$$

$$u = \sqrt{(1-\eta)} \tag{6.28b}$$

and δ is given by:

$$\delta = \mathrm{atanh}\,\sqrt{\eta} \tag{6.29}$$

If the power reflectivities for the dichroic mirror are R_ω and $R_{2\omega}$ then the amplitudes for F and SH as they enter the crystal on the second (left to right) pass are given by:

$$A_1' = u\sqrt{R_\omega} \tag{6.30a}$$

$$A_2' = v\sqrt{R_{2\omega}} \tag{6.30b}$$

So that the total power flux that enters the crystal after reflection by the dichroic mirror is $(A_1'^2 + A_2'^2)$, and the new δ is given by:

$$\delta' = C(A_1'^2 + A_2'^2)^{\frac{1}{2}} z = \delta(A_1'^2 + A_2'^2)^{\frac{1}{2}} \tag{6.31}$$

because $\delta = CA_1(0)z$ and $A_1(0) = 1$.

The new value of the normalised SH at the exit face of the non-linear crystal in the left to right direction is then given by:

$$v'' = \tanh(\delta - \delta_0) \tag{6.32}$$

The constant δ_0 is determined by the initial conditions at the entrance to the crystal in the left to right direction by:

$$\delta_0 = \operatorname{atanh}\left[\frac{A_2'}{(A_1'^2 + A_2'^2)^{\frac{1}{2}}}\right] \tag{6.33}$$

Then the normalised intensity of the fundamental wave emerging from the non-linear crystal is:

$$u''^2 \approx 1 - v''^2 \tag{6.34}$$

It is also noted that the scale for the reflected waves is decreased by a factor of $(A_1'^2 + A_2'^2)$ so that the intensity of the amplified fundamental represents the non-linear reflection coefficient R_{NL} so that:

$$R_{NL} = u''^2(A_1'^2 + A_2'^2) \tag{6.35}$$

Substituting Eqns(6.28)-(6.34) into Eqn(6.35), the final form of the overall non-linear reflectivity for the device is found to be:

$$R_{NL} = \rho \times \left\{1 - \tanh^2\left(\sqrt{\rho}\operatorname{atanh}\sqrt{\eta} - \operatorname{atanh}\sqrt{\frac{\eta R_{2\omega}}{\rho}}\right)\right\} \tag{6.36}$$

$$\rho = \eta R_{2\omega} + (1-\eta)R_\omega$$

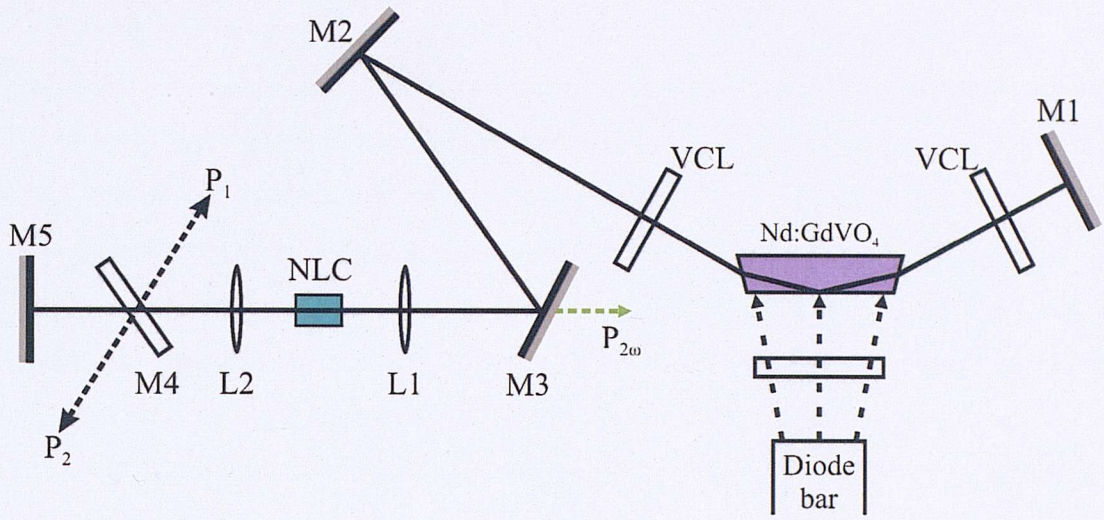


Fig 6.10. *A non-linear mirror modelocked bounce cavity. L1 and L2 form a telescope with unity magnification and an internal focus to enable efficient SHG from the non-linear crystal (NLC). M4 is a partially reflecting mirror at 1064 nm. M5 is dual coated for high reflectivity at 1064 nm and 532 nm. $P_{2\omega}$ is the residual second harmonic that remains after the DFG.*

The required non-linearity may not be immediately obvious, but arises from the intensity dependent form of the second harmonic conversion efficiency, η (Eqn(6.13)). The intensity dependent non-linearity is weaker than in the saturable absorber case and so the pulse shortening effect takes a longer time to build up. It is still sufficient however to induce the required shutter effect and has been used effectively to produce a modelocked source [145–156].

6.5 A NLM modelocked bounce geometry laser oscillator

In order to realise an NLM modelocked bounce geometry laser, the standard compact asymmetric cavity used previously was extended as in Fig 6.10. The crystal was a 1.1 at.% doped Nd:$GdVO_4$ with 5° angled end faces. This is different to the crystals used in all the earlier systems, which was an unfortunate situation but one again forced by the availabilty of laser crystals in the laboratory. The Nd:$GdVO_4$ has better thermal properties than the Nd:YVO_4 and so the strength

of the thermal lensing discussed in §3.2.5 can be reduced. The spectroscopic properties do not change significantly however, and so the Nd:YVO_4 systems can still be broadly used as a benchmark for performance. The approximately collimated long arm of the cavity was extended by the use of two folding mirrors, coated for high reflectivity at 1064 nm, to a simple telescope. The telescope consisted of two spherical lenses with focal lengths $f = 10$ cm positioned 20 cm apart so that they provided a total magnification of unity. The purpose of the telescope was to produce a small intracavity waist that could be used for efficient SHG. A non-linear crystal was thus located inside the telescope to coincide with the position of the focal region and take advantage of the higher intensities created to effect efficient SHG.

The back mirror of the NLM is required to have a very high reflectivity at the second harmonic wavelength but some arbitrary lower reflectivity for the fundamental. This would require a specially dual coated mirror and so for initial experiments the differential reflectivity was achieved by use of a dual coated mirror with nominal 100 % reflectivity at both 1064 and 532 nm (M5 Fig 6.10), in combination with a standard low reflectivity IR mirror positioned at an angle to the beam line, M4 Fig 6.10. Mirror M5 then provides the high reflectivity needed at 532 nm and M4 provides the loss at 1064 nm by coupling the fundamental radiation out of the cavity. This obviously creates two output beam paths, P_1 on the first right-left pass through M4, and P_2 on the second left-right pass. This would not be ideal for a real world application but allows the proof of principle of operation to be obtained, and fine tuning of the performance without requiring many specialist mirror coatings to be tested.

This arrangement allows the fundamental reflectivity of the NLM, R_ω, to be varied continuously by changing the angle of the mirror, M4. Standard dielectric mirrors are designed for operation at a designated angle of incidence, in this case 0°. However, the reflectivity is in fact angle dependent and at angles much greater than this, the reflectivity is reduced from its design value. This allows the IR output coupling strength to be varied continuously to achieve the optimum conditions for modelocking.

The actual angular dependence of the reflectivity is unknown and so the value

is determined empirically during operation. Considering the radiation incident on M4 from the right and the left in Fig 6.10, the ratio of the powers P_1 and P_2 is a function of the effective reflectivity, R_{eff}, of M4 as:

$$\frac{P_2}{P_1} = \frac{R_{eff}(1 - R_{eff})}{R_{eff}} = 1 - R_{eff} \tag{6.37}$$

The effective fundamental reflectivity of the NLM device is then given by;

$$R_\omega = (1 - R_{eff})^2 \tag{6.38}$$

and can be calculated by measuring the powers in the two output arms. In these initial experiments, M4 was a standard 50:50 IR beamsplitter, designed to have 50 % reflectivity at 1064 nm for an incident angle of 45°.

The non-linear crystal used could be a number of different materials, each with its own advantages and disadvantages. Three that were readily available and suitable were KTP, BiBO and LBO. Each of these were tried in the cavity with varying degrees of effectiveness and will be considered separately here.

6.5.1 NLM with type II phase matched KTP

The first crystal chosen was KTP ($KTiOPO_4$) because it has a large non-linearity and large acceptance angle (see Table 1). This should easily give a high conversion efficiency to the second harmonic. KTP is also a type II phase matched crystal so the incoming radiation has to be polarised at 45° to the o and e axis. The output from the bounce cavity is linearly polarised and so the rotation is achieved by the use of a $\lambda/2$ waveplate between M3 and L1 in Fig 6.10 to produce the correct orientation. This is determined by maximising the SHG from a single pass through the KTP.

Once the SHG has been optimised, the correct phasing between the fundamental and second harmonic for the DFG part of the process is achieved using dispersion in air. By varying the position of M5, a phase difference of $\Delta\phi = \pi/2$ can be obtained whereby the second harmonic lags behind the fundamental.The mechanism is particularly sensitive to this phase difference and so M5 is mounted on a micrometer controlled translation stage.

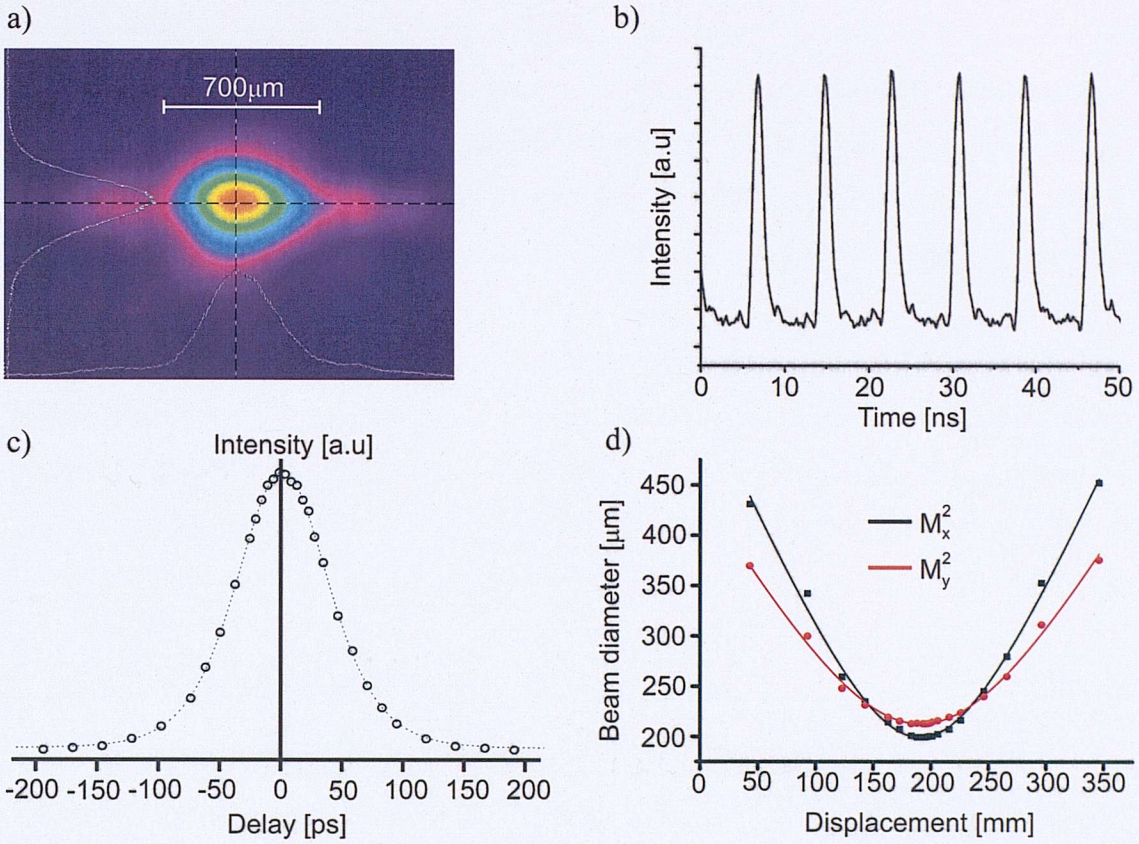


Fig 6.11. *Output beam quality (a), modelocked pulse train (b), intensity autocorrelation trace (c) and M^2 measurement (d) from the NLM modelocked oscillator with KTP. The pulses are seen to have a duration of 57 ps.*

Correct alignment is indicated by the production of a pulsed output. Preliminary to this, guidance is provided by monitoring the second harmonic power in the backwards direction, $P_{2\omega}$ Fig 6.10. This will be minimised when the DFG process is optimised and so provides a useful indicator of whether the correct phasing is being approached.

Once the correct delicate conditions have been met, the NLM system with KTP as a non-linear crystal produced a total of 11.3 W of average output power from 40 W of pumping, in a pulse train of 57±2 ps pulses at a repetition rate of 140 MHz. The pulse train, output beam quality, autocrrelation and M^2 measurement are shown in Fig 6.11. The beam was measured to have an M^2 of 1.5 in the horizontal and 1.2 in the vertical, which is favourably comparable to the standard asymmetric cavity. The output power of 11.3 W is the highest ever reported power

for a non-linear mirror modelocked system [145–156]. The effective fundamental reflectivity of the NLM was calculated to be $R_\omega \sim 70\,\%$ which is comparable to the reflectivity for the SESAM modelocked systems. This level of output coupling allows sufficient intracavity intensity to provide efficient SHG and a significant non-linearity, without compromisnig the overall efficiency of the system too much, or degrading the beam quality.

Although the output power is a record, the pulse duration is significantly longer than would be expected from this system. As mentioned previously, there is no physical timescale limiting the pulse duration and so bandwidth limited pulses of ~ 5 ps would be expected. It is supposed that this is due to the use of KTP as the non-linear element.

6.5.1.1 Dispersion problems with KTP

KTP is a type II phase matched material and so the propagating beam is composed equally of *o*- and *e*-waves. This is necessary for phase-matching in both the forward and backward directions. It also means however, that the two component polarisations will travel at different speeds in the KTP. In effect, this will spread out the pulse in time, thus limiting the pulse duration. Moreover, the laser crystal itself is birefringent and so further spreading will occur here too. KTP has a birefringence of $\Delta n = 0.0898$ and so for a crystal of length $L = 13$ mm the delay between the ordinary and extraordinary waves after a double pass is:

$$\Delta t = \frac{2L}{c_0}\delta n \approx 8ps \tag{6.39}$$

where c_0 is the speed of light in vacuum. The $GdVO_4$ laser crystal has a birefringence of $\Delta n = 0.22$ and so a double pass of a 20 mm crystal results in delay of $\Delta t \approx 30$ ps. The combination of the two crystals thus results in a total delay of $\sim$40 ps which is then the lower limit on the pulse duration.

In addition to this, the polarisation state of the beam will be distorted by double passage through the KTP and waveplate. The beam enters the KTP linearly polarised at 45° but because of the birefringence will emerge elliptically polarised. The return passage through the KTP and waveplate will not return the beam to a linear polarisation and the effect will be further amplified by passage

through the laser crystal. It is thus remarkable that the beam quality remains so good in spite of this, but then perhaps no surprise that the pulse duration is limited.

These polarising effects will be an issue with all type II phase-matching materials in this system, and so to avoid them, the switch to type I phase-matching was made.

6.5.2 NLM with type I phase matched BiBO

The crystal chosen for the type I phase-matching is BiBO (BiB_3O_6). It has a high $\chi^{(2)}$ like KTP but a lower acceptance angle which means the efficiency of the SHG could be compromised. The configuration of the cavity is essentially identical to that with KTP except that the waveplate is no longer needed. The output from the laser crystal is vertically polarised so all that is needed is for the ordinary axis of the BiBO to be aligned with this.

The alignment of the cavity is much more sensitive due to the small acceptance angle of BiBO, however, when correctly configured this system produced a train of modelocked pulses with a duration of 6±1 ps. This is the shortest pulse duration ever obtained by the non-linear mirror modelocking mechanism. The average power of the pulse train is 7.2 W from 33 W of pumping with a repetition rate of 144 MHz, which is the second highest output power ever recorded from the NLM technique. The beam quality, output pulse train and autocorrelation from the BiBO cavity are shown in Fig 6.12. This time, the M^2 values are greater than 2 in both the horizontal and vertical.

The long term stability of both the KTP and BiBO systems was limited, and continuous operation without adjusting the alignment could be achieved for a few minutes at a time, although the effect was more pronounced for BiBO. This is a very long time compared to the timescale of typical laser processes however, and so the dynamics of the NLM mechanism are not in question. This timescale suggests that more macroscopic properties of the system are affecting the performance.

One of the main problems seemed to be air turbulence created by moving objects, and also heating effects that resulted from the very high intra-cavity powers.

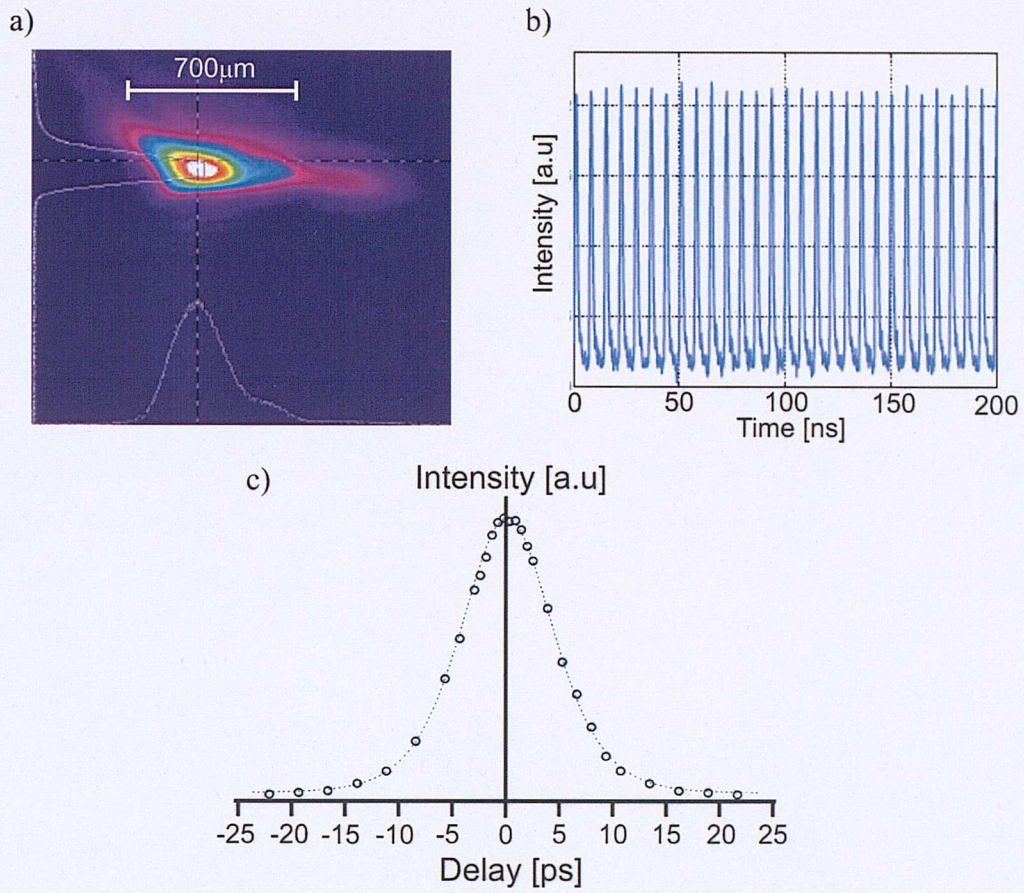


Fig 6.12. *Output beam quality (a), modelocked pulse train (b) and intensity autocorrelation trace (c) from the NLM modelocked oscillator with BiBO. The pulses are seen to have a duration of 6 ps.*

These lead to changes in air composition and so the dispersive phase difference between the fundamental and second harmonic may change. Additionally, all optical elements in the system introduce dispersion and 1 mm of BK7 glass produces a phase difference of about $13 \times 2\pi$ that also changes as the temperature varies. Finally, the thermal lensing effect within the system changes as its power fluctuates. The angle at which the beam enters the SHG crystal may thus vary, and due to the very small acceptance angle of BiBO, this changes the system's performance significantly.

These stability issues are reported in various works on the topic. In particular,[148] finds that temperature stability of the non-linear crystal is one of the key requirements for stable modelocking and quotes a temperature accuracy of about 0.1°C.

This accuracy is for LBO, which has a higher temperature sensitivity than KTP but a lower one than BiBO. This might in part explain the instabilities found with the systems, as the oven used to maintain the temperature of the non-linear crystal had only a very coarse control. Additionally, this explains why the BiBO system had a poorer stability than the KTP system.

6.6 Conclusions

This chapter has covered the technique of non-linear mirror (NLM) modelocking applied to a bounce geometry laser oscillator. Before the NLM mechanism could be described in detail, the concept of non-linear optics was introduced through the discussion of the $\chi^{(2)}$ non-linearity in the polarisation of the medium. When this was used as the source term in the wave equation it was shown to lead to several frequency mixing effects. Two of these effects that are important for the NLM mechanism are second harmonic generation (SHG), which is a degenerate form of three wave mixing, and difference frequency generation (DFG).

The concept of phase-matching was introduced, which is crucial for all forms of non-linear processes. In order for the correct phase relationship to exist between the different frequency components so that they mix efficiently, their wave vectors must be matched to a high degree of accuracy. However, due to material dispersion this is a very non-trivial condition to meet. To satisfy this criteria, advantage is taken of the birefringence of many non-linear materials. Using the refractive index variation between the ordinary and extraordinary axes enables the wave vectors to be matched. This gives rise to two types of phase-matching known as type I, where similar polarisation states are mixed, and type II where different polarisation states are mixed.

The NLM technique combines SHG, differential reflectivity between the fundamental and second harmonic waves, and subsequent DFG, to create a system that produces a non-linear loss. The initial SHG process is intensity dependent and so by introducing a greater loss for the un-converted radiation, the cavity preferentially retains high intensity radiation. This creates an effective shutter for propagating pulses, and modelocking is achieved by the same mechanism as for a

saturable absorber.

This technique was applied to a bounce geometry amplifier using two different non-linear materials. The first attempt used type I phase-matched KTP because it had a high non-linearity and large acceptance angle. This resulted in the highest average output power ever demonstrated from an NLM system. A pulse train of 140 MHz was produced with an average power of 11.3 W in a high quality spatial mode. The pulse duration in this system was measured to be 57 ps, which was much longer than the 5 ps that would be expected from transform limited pulses in the laser medium. The discrepancy was attributed to the time delay introduced when a pulse of mixed polarisations (required for type II phase-matching) passes through both a birefringent non-linear crystal, and a birefringent laser crystal. The potential spreading was calculated to be approximately 40 ps which then accounted for the long pulse duration.

To counteract this effect, a second non-linear crystal was used that used type I phase-matching. The crystal was BiBO which had a similar non-linearity to KTP but a much smaller acceptance angle and was more sensitive to temperature variations. This resulted in a system that had poorer beam quality, and exhibited more long term operational instability than the KTP system. However, stable operation was obtained and the BiBO system produced an output of 6 ps pulses with an average power of 7.2 W in a 144 MHz pulse train. This represents the shortest pulses ever obtained from an NLM system, as well as the second highest recorded average output power. Both of these results were presented at an international conference [44].

Chapter 7

Conclusions

7.1 Introduction

This final chapter presents a summary of the thesis followed by a brief overview of possible future work related to that presented here. This thesis has primarily been concerned with achieving modelocked performance using the bounce geometry laser oscillator, a laser amplifier configuration that exhibits a high gain, and gives considerable spatial averaging of the gain and thermal non-uniformities that occur in the laser cavity. This makes the system particularly suited to high power, high efficiency, high spatial quality operation. Following an introduction to the principles and implementation of modelocking, and a detailed account of the form and function of the bounce geometry laser amplifier, the three main results of this thesis were the successful production of a picosecond modelocked bounce geometry oscillator that was subsequently amplified to the 60 W level; the first demonstration of modelocking using excited-state quantum dot-based saturable absorbers; and the shortest pulses and highest power ever achieved from a non-linear mirror (NLM) modelocked laser system.

7.2 Thesis summary

The opening chapter of this thesis, Chapter 1, aimed to place the results and achievements of the thesis in context by introducing the concepts of solid-state lasers and pulse production methods. It started with a brief history of the solid-state laser, from the first demonstration of lasing in ruby, through to the modern day generation of femtosecond pulses in Ti:sapphire, and its importance in science and industry. The pumping methods and laser geometries available were mentioned briefly, before the first introduction to the bounce geometry amplifier. A discussion of pulsed sources followed, which included the varied applications to science and industry and an outline of the two types of pulsed behaviour, Q-switching and modelocking. This enabled the motivation for the thesis to be identified as an investigation into whether the many benefits of the bounce geometry amplifier could be applied to produce a high power, picosecond modelocked source.

Chapter 2 provided a more detailed study of modelocking and modelocked sources. It began with the frequency domain picture of modelocking, and showed that the coherent superposition of many longitudinal cavity modes leads to the production of a train of short, intense pulses that are separated in time by $^{2L}/_{c}$, where L is the length of the cavity. The time domain picture was then also introduced, where modelocking action is described by the effect of a shutter inside the cavity, which only allows the passage of a single propagating pulse, once every round trip. The two main categories of modelocking were then introduced as active and passive, which split modelocking mechanisms based on how the shutter action in the cavity is introduced. Active modelocking uses an external signal to drive the modulation, whereas passive modelocking uses the action of the propagating pulse on some non-linear optical property of a suitable material to affect the modulation. Passive modelocking is now the most prevalent category due to its general ease of implementation and ability to generate shorter pulses, and so the most common types: saturable absorber, Kerr lens, additive pulse and non-linear mirror modelocking, were then outlined in brief. The chapter finished with an explanation of how ultra-short pulses are measured using an autocorrelator, and a description of spinning mirror design that was used in this thesis.

Chapter 3 was all about the bounce geometry laser. It began by looking at thermo-optic effects in solid state media and how processes such as quantum defect heating, Auger upconversion, cross relaxation and excited state absorption all lead to a net deposition of heat in the laser crystal. It was then discussed how this heating leads to refractive index gradients in the crystal which effectively act as a lens in the cavity, whose strength varies with the applied pump power, affecting the cavity stability. The heating also leads to expansion of the crystal which generates strain in the crystal lattice and results in stress induced birefringence. These two effects both lead to degradation of laser performance at high pump powers and the bounce geometry is introduced as a means of combating them. The basic concept of the bounce is shown to be that by taking a total internal reflection off the pump face of the laser crystal, the very high inversion region close to the surface can be accessed, and the bounce path enables significant averaging of both the gain non-uniformity and the thermally induced lens aberrations. Detail was given on the specific crystal geometry and both the cooling and diode pumping mechanisms before two experimental bounce cavities were discussed. The first of these was a simple, compact, symmetric cavity which produced a spatially multi-mode output of 23 W when pumped with a 40 W diode, giving a total conversion efficiency of 57 %.There then followed a brief outline of the cavity stability theory of Magni in order to understand that to create a spatially single mode output (TEM_{00}), the simple symmetric cavity is made asymmetric. This asymmetric cavity was then detailed and shown to produce a maximum of 19 W in a TEM_{00} beam, with two distinct regions of stable operation visible in the total operating range, as predicted by the Magni theory.

Chapter 4 looked in more detail at saturable absorber modelocking, in particular an experimental system based on the semiconductor saturable absorber mirror (SESAM). To begin, the action of a saturable absorber to produce modelocking was described by considering transmission operators for gain, loss and saturable absorber elements inside a cavity. This enabled it to be shown that passive modelocking results in pulses with a $sech^2$ temporal form. The theory of Paschotta *et al* was highlighted, to arrive at an inequality that gave an approximation for the onset of Q-switching as opposed to modelocking when using saturable absorbers.

The SESAM device itself was then described, including both its internal structure, consisting of multiple quantum wells on top of a DBR, and the way in which the quantum wells act as a saturable absorber. There was then a brief discussion of how the Q-switching inequality could be used to guide cavity design, by varying the illuminated mode size on the SESAM, varying the cavity length, or changing the modulation depth of the absorber. This was then applied to the asymmetric bounce cavity previously described and the evolution of the cavity to a modelocked oscillator was detailed. The resultant oscillator produced 16.7 W average power, in a 77 MHz pulse train of 30±2 ps pulses. This was then used as the source for a master oscillator power amplifier (MOPA) configuration, and amplification to 60 W average power was achieved with an amplifier extraction efficiency of 50 %. A bounce geometry module was used as the amplifier in this case, and so the spatial quality was retained up to this high power level. The pulse duration of this system was longer than expected, with 2 ps being the theoretical minimum bandwidth limited duration. Further evolution of the cavity resulted in a system that produced an 81 MHz, 12±2 ps pulse train, albeit with a lower average power of 6.1 W.

Chapter 5 covered a collaborative project with the experimental solid state group at the same institution as the present author. They were developing techniques for growing quantum dots, and using these as the absorbing layers in SESAM devices. The testing of these devices to see if they functioned well as saturable absorbers formed part of the experimental work of this thesis. Initially, the concept of a quantum dot (QD) was introduced as being a system which is confined in all three spatial dimensions (*cf.* a quantum well where confinement is in one dimension only). When used as SESAM devices, this gave them some advantageous, and some disadvantageous properties compared to quantum wells, which are outlined. The growth process of the dots was then described, together with the post-growth technique of rapid thermal annealing (RTA) which enables the absorption wavelength of the dots to be tuned over a large range. A set of QD-based SESAMs (QDSAM) were then tested in a bounce geometry oscillator, and although modelocking was observed, the pulse durations of 200±21 ps were much longer than would be expected. This poor performance is attributed to the

very low modulation depth of the QDSAM devices, which is inherent in the QD design. In order to overcome this, a second set of QDSAMs was produced that had much larger modulation depths through the use of many QD layers. These samples were again tested in the bounce oscillator and it was found that the minimum achievable pulse duration varied over 96 ps, in line with the variation in the modulation depths of the devices. The minimum pulse duration of 84±4 ps was obtained using the QDSAM with the largest modulation depth. This duration was recognised as much longer than should be possible, and the difference is attributed to a non-ideal value of the pulse fluence on the QDSAMs, which are much more sensitive to this parameter than the well-based SESAMs. Despite this, this is the first time that this kind of QDSAM has been used to produce modelocked pulses.

Chapter 6 was the final experimental chapter and looked at a different method of modelocking than the SESAM-based work of the previous chapters. This chapter was concerned with the technique of non-linear mirror (NLM) modelocking which had briefly been introduced in Chapter 2. As a starting point, a brief overview was given of some relevant non-linear optics, starting with the non-linear susceptibility of a medium and showing how this leads to phenomena such as second harmonic generation (SHG) and difference frequency generation (DFG) under certain electric field conditions. The concept of phase matching for optimising the efficiency of non-linear processes was then introduced, together with four categorisations of such processes : type I, type II, critical and non-critical. Having covered the necessary background material, the construction of a non-linear mirror was then expounded in more detail, describing how a particular combination of SHG and DFG could produce a unit that exhibits an intensity dependent reflectivity. This is akin to a saturable absorber, and with the action of a saturable absorber as a suitable modelocking element already demonstrated, the NLM was then incorporated into a bounce geometry oscillator. Initially, NLM based on a non-linear crystal of KTP was used to produce a modelocked source, and this resulted in the highest average power ever recorded from an NLM system of 11.3 W. The output was a 140 MHz train of 57±2 ps pulses and it was again noted that this duration was much longer than expected. This is attributed to the fact that the type of phase-matching employed results in mixed polarisation states propagating

in the cavity, and the birefringence of the laser and non-linear crystals causes a time delay between the states which limits the minimum pulse duration. To overcome this problem, an alternative non-linear crystal was used which maintained a single polarisation state, and using this, a modelocked system was created that produced the shortest pulses ever recorded from an NLM system, with a duration of 6±1 ps. The average output power in this case was lower, at 7.2 W, but this still represented the second highest output power ever achieved from an NLM system.

7.3 Future work

This thesis has demonstrated the feasibility of using the bounce geometry laser as a high power modelocked source, however there is still much of interest that could be done to develop this potential further. There is still some refinement that needs to be done with some of the systems presented here, especially the QDSAM and NLM oscillators. The QDSAM system needs to be investigated to determine if the limited pulse duration is due to the QDSAM devices or the configuration of the laser cavity, and the long term stability of the NLM system also needs to be improved.

However, the most interesting possibilities take this work a little further. The most obvious is to expand the wavelength operating range of all the systems. The bounce geometry has been used previously to produce radiation at 1.3 μm by making use of a different atomic transition in Nd:YVO_4 and this could also be applied to the modelocked systems. Lasing at 1.3 μm and then also using this as a means for SHG (THG and FHG as well) allows different potential industrial applications to be targeted. The high peak powers produced in pulsed sources mean that the harmonic conversion efficiencies can be very high. There are QDSAM devices ready for use at 1.3 μm and in fact for many industrial applications sub-100 ps are all that is required, meaning the relatively poor performance of the QDSAM system in this thesis need not be too much of a concern. The NLM system should in principle also be easy to extend to function at 1.3 μm, although as with all the bounce geometry systems, the challenge is usually to suppress the extremely high gain at 1 μm enough that lasing at 1.3 μm may occur. Both the 1 μm and 1.3 μm

could then be used for supercontinuum generation in optical fibres.

Other wavelength conversion processes are also available. Intracavity SHG is possible which takes advantage of the high intracavity power to enable very efficient conversion and produce an output directly at harmonic wavelengths. It would also be possible to use non-linear processes such as stimulated Raman scattering (SRS) and stimulated Brillouin scattering (SBS) inside the cavity to produce frequency shifted outputs which would then allow harmonic conversion into the yellow for example.

Beyond wavelength diversification, the power scaling potential of the bounce is still to be exploited fully. While power scaling of the modelocked oscillator may not be the most economical means of reaching high power, multiple bounce amplifiers should enable picosecond pulse trains with average power at the 100 W level and beyond to be reached. The saturation energy of the gain in a typical bounce amplifier module is a few microjoules; an 80 MHz pulse train of 2 μJ pulses corresponds to an average power of 160 W and so this level should be reachable. This could even be readily increased by enlarging the gain region to increase the saturation energy of the gain. Pulses with an energy of 2 μJ and duration of 10 ps have a peak power of $\sim$180 kW; Q-switched systems in the bounce geometry lab have been demonstrated with peak powers of 1 MW and so the damage limits of optical components should be able to cope with these high power levels. Ultimately, the saturation energy of the gain will limit the power available directly from the oscillator as the pulse energies are much higher intracavity. Assuming the dimensions of the gain region are to be maintained at the size they are in this work, the oscillator could be scaled to $\sim$40 W, assuming the relevant modelocking conditions could still be met. Even this could be scaled further by increasing the size of the gain region to increase the saturation energy, but the efficiency of the oscillator is unlikely to change and it would remain an inefficient way to scale power. It would also be interesting to take the systems presented here and perform some kind of extracavity pulse-picking to reduce the repetition rate of the pulse train, and then amplify this to produce pulses with extremely high peak powers.

There may also be some benefit in a material study. Laser crystals made

of Nd:$GdVO_4$ like that used in the NLM work have been shown to have some advantageous properties. The thermal conductivity is much higher which means that crystal cooling is much more effective and the detrimental effects of thermal loading in the crystal are reduced. This is offset however by a reduced emission cross section which raises the lasing threshold. Recently, mixed vanadates of the form Nd:$Y_xGd_{1-x}O_4$ have been investigated which allow for tailoring of the physical and spectroscopic properties of the laser gain medium. These, along with highly doped ceramic materials may offer some improvement of the laser performance, although this is by no means restricted to modelocked systems.

7.4 Conclusions

The main goal of the work presented in this thesis was essentially to perform a feasibility study to assess the potential of the bounce geometry for application to high power modelocked sources. The bounce geometry has already been demonstrated to perform exceptionally well with respect to beam quality, output power and efficiency over a wide range of operating schemes (CW, Q-switched, adaptive, power amplifier), so could this be extended to include ultra-short pulse modelocked generation? Three main approaches were investigated: semiconductor saturable absorber modelocking (SESAM); quantum dot saturable absorber modelocking (QDSAM); and non-linear mirror modelocking (NLM).

The SESAM modelocking study resulted first in a 16.7 W average power oscillator that produced a 77 MHz modelocked pulse train of 30 ps pulses. This was then used as the master oscillator in a master oscillator power amplifier (MOPA) configuration using another bounce geometry module as the amplifier, to achieve 60 W of average power in a modelocked pulse train. This represented an amplifier extraction efficiency of 50 % with no degradation of beam quality or pulse train, and this result was presented at an international conference and in a peer reviewed journal. Although the efficiency of the oscillator is good for a laser of its type, high power operation would be best achieved by increasing the amount of amplification, either through stronger pumping or multiple amplifiers, rather than the considerable design effort that would be required to scale the oscillator much

beyond 20 W output. The effort would be best used to reduce the pulse duration, and this was achieved with the realisation of an 81 MHz, 6.1 W average power, 12 ps pulse train.

The QDSAM study looked to see if there was any advantage to using a new generation of quantum dot SESAM devices. Ultimately, the minimum pulse duration obtained with these was 84 ps, which is much longer than with the commercial devices, and at lower powers. The likelihood is that the QDSAMs are more sensitive to the cavity operating parameters and so further work could reduce this pulse duration and increase power. However, for many applications, sub-100 ps pulses are more than adequate and the operational stability of the QDSAMs could well justify their use. They are also likely to be better equipped for use at 1.3 μm, where standard SESAMs are difficult to come by, and the fast carrier dynamics should make them suitable for femtosecond pulse generation, although this could not be investigated with the materials available here. Despite the relatively poor performance of the system, the study was published in a peer reviewed journal and presented at an international conference.

The final study, of the oft neglected NLM modelocking scheme, promised shorter pulses than the SESAM systems and more robustness against damage. Initially, the best performance was a 140 MHz pulse train of 57 ps pulses with an average power of 11.3 W. This is the highest power ever recorded from this type of system and was presented at an international conference. The pulse duration was still quite long however, and the full potential of this system was not realised until the production of a 144 MHz pulse train of 6 ps pulses with an average power of 6.6 W. This is the shortest pulse duration ever obtained from this type of system. The downside to this however is that the modelocking mechanism is exceptionally alignment-sensitive, and so long term operating stability is a problem. The NLM scheme definitely offers potential for high power modelocked operation, but the issues with operating stability need to be addressed first.

Overall then, the bounce geometry certainly has potential for application in high power, modelocked operating schemes. The quantum dot-based SESAMs have still to prove their worth in picosecond systems and lag some way behind the commercially available quantum-well devices, although this is not really a surprise

for such a young and complex technology.

The SESAM and NLM mechanisms are very similar in terms of overall performance. At this timescale and for applications in industry there is not a great deal of difference between 12 ps and 6 ps and so both systems are similar in this respect; with further optimisation the SESAM system should be able to produce shorter pulses anyway. The main performance differentiators for industrial application are therefore efficiency and stability. At the shortest pulse durations, both systems had similar overall optical-optical conversion efficiencies ($\sim$ 25 %) although it seems very likely that this could be improved in both cases. There is a significant difference however in the ease of construction and operating stabilty between the two. The SESAM system requires careful thought during the cavity design process, but once constructed requires little further effort to produce modelocking and will then do so consistently for several hours. By contrast, the NLM system is slightly easier to design initially but requires much more iterative work and effort beyond this to optimise and produce modelocking. It is also yet to be demonstrated in a repeatedly stable system and would require a great deal of engineering before being useful in an industrial environment. The SESAM mechanism thus looks to be the most promising for long term investment, and in any case, the bounce geometry MOPA configuration is an exceptionally promising route for high power scaling.

References

[1] T. Maiman, "Stimulated optical radiation ion ruby," Nature **187**, 493 (1960).

[2] A. Javan, W. Bennett, and D. Herriott, "Population inversion and continuous optical maser oscillation in a gas discharge containing a He-Ne mixture," Phys. Rev. Lett. **6**, 106 (1961).

[3] D. Nelson and W. Boyle, "A continuously operating ruby optical maser," Appl. Opt. **1**, 181 (1962).

[4] R. Hellwarth, "Theory of the pulsation of fluorescent light from ruby," Phys. Rev. Lett. **6**, 9 (1961).

[5] F. McClung and R. Hellwarth, "Giant optical pulsations from ruby," J. Appl. Phys. **33**, 828 (1962).

[6] H. Mocker and R. Collins, "Mode competition and self-locking effects in a Q-switched ruby laser," Appl. Phys. Lett. **7**, 270 (1965).

[7] W. Gibbs and R. Whitcher, "Time-resolved beam structure of an active q-switched ruby laser," Appl. Opt. **6**, 1957 (1967).

[8] J. Geusic, H. Marcos, and L. Uitert, "Laser oscillations in Nd-doped yttrium aluminium, yttrium galium and gadolinium garnets," Appl. Phys. Lett. **4**, 182 (1964).

[9] M. Ross, "YAG laser operation by semiconductor laser pumping," Proc. IEEE **56**, 196 (1968).

[10] E. Snitzer, "Optical maser action of Nd^{3+} in a barium crown glass," Phys. Rev. Lett. **7**, 444 (1961).

[11] J. Endriz, M. Vakili, G. Browder, M. DeVito, J. Haden, G. Harnagel, W. Plano, M. Sakamoto, D. Welch, S. Willing, D. Worland, and H. Yao, "High power diode laser arrays," IEEE J. Quant. Elec. **28**, 952 (1992).

[12] T. Taira, A. Mukai, Y. Nozawa, and T. Kobayashi, "Single-mode oscillation of laser-diode-pumped oscillation Nd:YVO_4 microchip lasers," Opt. Lett. **16**, 1955 (1991).

[13] P. Lacovara, H. Choi, C. Wang, R. Aggarwal, and T. Fan, "Room-temperature diode-pumped Yb:YAG laser," Opt. Lett. **16**, 1089 (1991).

[14] J. der Au, S. Schaer, R. Paschotta, C. Honninger, and U. Keller, "High-power diode-pumped passively mode-locked Yb:YAG lasers," Opt. Lett. **24**, 1281 (1999).

[15] P. Peterson, A. Gavrielides, and M. Sharma, "Diode-pumped Tm:YAG solid-state lasers with indirect and direct manifold pumping," Appl. Phys. B **61**, 195 (1995).

[16] E. Honea, R. Beach, S. Sutton, J. Speth, S. Mitchell, J. Skidmore, M. Emanuel, and S. Payne, "115 W Tm:YAG diode-pumped solid-state laser," IEEE J. Quant. Elec. **33**, 1592 (1997).

[17] S. Konno, S. Fujikawa, and K. Yasui, "206 W continuous-wave TEM_{00} mode 1064 nm beam generation by a laser-diode-pumped Nd:YAG rod laser amplifier," Appl. Phys. Lett. **79**, 2696 (2001).

[18] S. Fujikawa, K. Furuta, and K. Yasui, "28% electrical-efficiency operation of a diode-side-pumped Nd:YAG rod laser," Opt. Lett. **26**, 602 (2001).

[19] M. Gong, C. Li, Q. Liu, G. Chen, W. Gong, and P. Yan, "200 W corner-pumped Yb:YAG slab laser," Appl. Phys. B **79**, 265 (2004).

[20] J. Kong, D. Tang, S. Ng, L. Zhaoa, L. Qinb, and X. Meng, "High-power diode-end-pumped CW Nd:$GdVO_4$ laser," Optics and Laser Technol. **37**, 51 (2005).

[21] S. Tidwell, J. Seamans, and M. Bowers, "Highly efficient 60 W TEM_00 cw diode-end-pumped Nd:YAG laser," Opt. Lett. **18**, 116 (1993).

[22] R. Zhou, E. Li, H. Li, P. Wang, and J. Yao, "Continuous-wave, 15.2 W diode-end-pumped Nd:YAG laser operating at 946 nm," Opt. Lett. **31**, 1869 (2006).

[23] A. Giesen, H. Huegel, A. Voss, K. Wittig, U. Brauch, and H. Opower, "Scalable concept for diode-pumped high-power solid-state lasers," Appl. Phys. B **58**, 365 (1994).

[24] A. Giesen and J. Speiser, "Fifteen years of work on thin-disk lasers: Results and scaling laws," IEEE J. Sel. Top. Quant. Elec. **13**, 598 (2007).

[25] J. Bernard and A. Alcock, "High-efficiency diode-pumped Nd:$YV0_4$ slab laser," Opt. Lett. **18**, 968 (1993).

[26] A. Minassian, B. Thompson, and M. Damzen, "Ultrahigh-efficiency TEM_{00} diode-side-pumped Nd:YVO_4 laser," Appl. Phys. B **76**, 341 (2003).

[27] A. Minassian, B. Thompson, G. Smith, and M. Damzen, "High-power scaling (>100 W) of a diode-pumped TEM_{00} Nd:$GdVO_4$ laser lystem," IEEE J. Sel. Top. in Quant. Electron. B **11**, 621 (2005).

[28] D. Sauder, "High power diode-pumped solid-state laser operation in the bounce amplifier geometry," Ph.D. thesis, Imperial College London (2008).

[29] T. Omatsu, T. Isogami, A. Minassian, and M. Damzen, ">100 kHz Q-switched operation in transversely diode-pumped ceramic Nd^{3+}:YAG laser in bounce geometry," Opt. Comms. **249**, 531 (2005).

[30] M. Trew, G. Crofts, M. Damzen, J. Hendricks, S. Mailis, D. Shepherd, A. Tropper, and R. Eason, "Multiwatt continuous-wave adaptive laser resonator," Opt. Lett. **25**, 1346 (2000).

[31] B. Thompson, A. Minassian, and M. Damzen, "Operation of a 33 W, continuous-wave, self-adaptive, solid-state laser oscillator," J. Opt. Soc. Am. B **20**, 857 (2003).

[32] V. Klimov, "Optical nonlinearities and ultrafast carrier dynamics in semiconductor nanocrystals," J. Phys. Chem. B **104**, 6112 (2000).

[33] P. Foggi, L. Bussotti, and F. Neuwahl, "Photophysical and photochemical applications of femtosecond time-resolved transient absorption spectroscopy," Int. J. Photoenergy **3**, 103 (2001).

[34] D. Piston, "Imaging living cells and tissues by two-photon excitation microscopy," Trends in Cell Biol. **9**, 66 (1999).

[35] "http://www.rp-photonics.com/fluorescence-microscopy.html," .

[36] S. Mangles, C. Murphy, Z. Najmudin, A. Thomas, J. Collier, A. Dangor, E. Divall, J. G. P.S. Foster and, C. Hooker, D. Jaroszynski, A. Langley, W. Mori, P. Norreys, F. Tsung, R. Viskup, B. Walton, and K. Krushelnick, "Monoenergetic beams of relativistic electrons from intense laser-plasma interactions," Nature **431**, 535 (2004).

[37] P. Gibbon and E. Forster, "Short-pulse laser-plasma interactions," Plas. Phys. Control. Fusion. **38**, 769 (1996).

[38] B. Klimt, "Picosecond lasers: the power of cold ablation," Optics and Laser Europe (2009).

[39] M. Yamashita, K. Yamane, and R. Morita, "Quasi-automatic phase-control technique for chirp compensation of pulses with over-one-octave bandwidth-generation of few- to mono-cycle optical pulses," IEEE J. Sel. Top. Quant. Elec. **12**, 213 (2006).

[40] D. J. Farrell and M. J. Damzen, "Passively modelocked Nd:YVO_4 laser in a bounce amplifier geometry," (Pisa, Italy, 2006).

[41] D. J. Farrell and M. J. Damzen, "High power scaling of a passively modelocked laser oscillator in a bounce geometry," Opt. Exp. **8**, 4781 (2007).

[42] M. P. Lumb, E. M. Clarke, D. J. Farrell, M. J. Damzen, and R. Murray, "Tailoring quantum dot saturable absorber mirrors for ultra-short pulse generation," Mater. Res. Soc. Symp. Proc. **1076**, K0904 (2008).

[43] M. P. Lumb, D. J. Farrell, E. M. Clarke, M. J. Damzen, and R. Murray, "Post-growth tailoring of quantum-dot saturable absorber mirrors by chemical etching," Appl. Phys. B. **94**, 393 (2009).

[44] G. Thomas, D. J. Farrell, A. Bauerle, and M. J. Damzen, "Non-linear mirror modelocking of a bounce amplifier laser," (Munich, Germany, 2009).

[45] D. Kopf, K. Weingarten, L. Brovelli, M. Kamp, and U. Keller, "Diode-pumped 100 fs passively modelocked Cr:LiSAF laser with an antiresonant Fabry-Perot saturable absorber," Opt. Lett. **19**, 2143 (1994).

[46] I. Sorokina, E. Sorokin, E. Wintner, A. Cassanho, H. Jenssen, and R. Szipocs, "14 fs pulse generation in Kerr-lens mode-locked prismless Cr:LiSGaF and Cr:LiSAF lasers: observation of pulse self-frequency shift," Opt. Lett. **22**, 1716 (1997).

[47] D. Spence, P. Kean, and W. Sibbett, "60 fs pulse generation from a self-mode-locked Ti:sapphire laser," Opt. Lett. **16**, 42 (1991).

[48] M. Asaki, C. Huang, D. Garvey, J. Zhou, H. Kapteyn, and M. Murnane, "Generation of 11 fs pulses from a self-modelocked Ti:sapphire laser," Opt. Lett. **18**, 977 (1993).

[49] E. Ippen, C. Shank, and A. Dienes, "Passive modelocking of the cw dye laser," Appl. Phys. Lett. **21**, 348 (1972).

[50] C. Shank and E. Ippen, "Sub-picosecond kilowatt pulses from a modelocked cw dye laser," Appl. Phys. Lett. **24**, 373 (1974).

[51] R. Fork, B. Greene, and C. Shank, "Generation of optical pulses shorter than 0.1 ps by colliding pulse modelocking," Appl. Phys. Lett. **38**, 617 (1981).

[52] Y. Silberberg, P. Smith, D. Eilenberger, D. Miller, A. Gossard, and W. Wiegmann, "Passive mode locking of a semiconductor diode laser," Opt. Lett. **9**, 507 (1984).

[53] A. Dienes, "Modelocked CW dye lasers," Opt. Quant. Elec. **6**, 99 (1974).

[54] R. Häring, R. Paschotta, A. Aschwanden, E. Gini, F. Morier-Genoud, and U. Keller, "High-power passively modelocked semiconductor lasers," IEEE J. Quant. Elec. **38**, 1268 (2002).

[55] S. Backus, C. D. III, M. Murnane, and H. Kapteyn, "High power ultrafast lasers," Rev. Sci. Intrum. **69**, 1207 (1998).

[56] C. Huang, M. Asaki, S. Backus, M. Murnane, H. Kapteyn, and H. Nathel, "17 fs pulses from a self-mode-locked Ti:sappire laser," Opt. Lett. **17**, 1289 (1992).

[57] C. Spielmann, P. Curley, T. Brabec, and F. Krausz, "Ultra-broadband femtosecond lasers," IEEE. J. Quant. Elec. **30**, 1100 (1994).

[58] L. Xu, G. Tempea, C. Spielmann, F. Krausz, A. Stingl, K. Ferencz, and S. Takano, "Continuous-wave modelocked Ti:Sapphire laser focusable to 5 $\times 10^{13}$ W/cm^2," Opt. Lett. **23**, 789 (1998).

[59] D. Huang, M. Ulman, L. Acioli, H. Haus, and J. Fujimoto, "Self-focusing-induced saturable loss for laser modelocking," Opt. Lett. **17**, 511 (1992).

[60] D. Sutter, G. Steinmeyer, L. Gallmann, N. Matuschek, F. Morier-Genoud, U. Keller, V. Scheuer, G. Angelow, and T. Tschudi, "Ultrabroadband pulses in the two-cycle regime by SESAM-assisted Kerr-lens modelocking of an all-solid-state Ti:sappire laser," OSA Trends in Optics and Photonics (TOPS) **26**, 358 (1999).

[61] U. Morgner, F. Kartner, S. Cho, Y. Chen, H. Haus, J. Fujimoto, E. Ippen, V. Scheuer, G. Angelow, and T. Tschudi, "Sub-two-cycle pulses from a Kerr-lens modelocked Ti:sapphire laser," Opt. Lett. **24**, 411 (1999).

[62] K. Stankov and J. Jethwa, "A new modelocking technique using a non-linear mirror," Opt. Comms. **66**, 41 (1988).

[63] M. Danailov, G. Cerullo, V. Magni, D. Segala, and S. D. Silvestri, "Nonlinear mirror mode locking of a cw Nd:YLF laser," Opt. Lett. **19**, 792 (1994).

[64] K. Stankov, V. Kubecek, and K. Hamal, "Mode locking of a Nd:$YAlO_3$ laser at 1.08 and 1.34 μm wavelengths using a single $LiIO_3$ crystal," IEEE J. Quant. Elec. **27**, 2135 (1991).

[65] C. ru Huo and Z. he Zhu, "The fluctuation model of a mode-locked laser using a mirror with intensity-dependent reflection coefficient," Opt. Comms. **79**, 328 (1990).

[66] P. Datta, Shivanand, S. Mukhopadhyay, A. Agnesi, and A. Lucca, "Picosecond pulse generation and its simulation in a non-linear optical mirror modelocked laser," Appl. Opt. **43**, 2347 (2004).

[67] J. Mark, L. Liu, K. Hall, H. Haus, and E. Ippen, "Femtosecond pulse generation in a laser with a nonlinear external resonator," Opt. Lett. **14**, 48 (1989).

[68] E. Ippen, H. Haus, and L. Y. Liu, "Additive pulse modelocking," J. Opt. Soc. Am. B **6**, 1736 (1989).

[69] L. Nelson, E. Ippen, and H. Haus, "Broadly tunable sub-500 fs pulses from an additive-pulse modelocked thulium-doped fiber ring laser," Appl. Phys. Lett. **67**, 19 (1995).

[70] J. Goodberlet, J. Jacobson, J. Fujimoto, P. Schulz, and T. Fan, "Self-starting additive-pulse mode-locked diode-pumped Nd:YAG," Opt. Lett. **15**, 504 (1990).

[71] Z. Yasa and N. Amer, "A rapid-scanning autocorrelation scheme for continuous monitoring of picosecond laser pulses," Opt. Comms **36**, 406 (1981).

[72] D. Riffea and A. Sabbah, "A compact rotating-mirror autocorrelator design for femtosecond and picosecond laser pulses," Rev. Sci. Inst. **69**, 3099 (1998).

[73] W. Koechner, *Solid State Laser Engineering* (Springer Verlag, 1999).

[74] T. Fan, "Scalable end-pumped diode-laser-pumped laser," Opt. Lett. **14**, 1057 (1989).

[75] M. Frede, D. Kracht, M. Engelbrecht, and C. Fallnich, "Compact high power end-pumped Nd:YAG laser," Opt. Las. Technol. **38**, 183 (2006).

[76] M. Frede, R. Wilhelm, and D. Kracht, "250 W end-pumped Nd:YAG laser with direct pumping into the upper laser level," Opt. Lett. **31**, 3618 (2006).

[77] D. Golla, "300 W CW diode-laser side-pumped Nd:YAG rod laser," Opt. Lett. **20**, 1148 (1995).

[78] S. Konno, S. Fujikawa, and K. Yasui, "80 W CW TEM_{00} 1064 nm beam generation by use of a laser-diode-side-pumped Nd:YAG rod laser," Appl. Phys. Lett. **70**, 2650 (1997).

[79] M. Damzen, M. Trew, E. Rosas, and G. Crofts, "Continuous wave Nd:YVO_4 grazing incidence laser with 22.5 W outpur power and 64 % conversion efficiency," Opt. Comms. **196**, 237 (2001).

[80] A. Minassian, B. Thompson, and M. Damzen, "High-power TEM_{00} grazing-incidence Nd:YVO_4 oscillators," Opt. Comms. **245**, 295 (2005).

[81] G. Smith and M. Damzen, "Quasi-CW diode-pumped self-starting adaptive laser with self Q-switched output," Opt. Exp. **15**, 6458 (2007).

[82] T. Omatsu, A. Minassian, and M. Damzen, "Passive Q-switching of a diode-side-pumped Nd-doped mixed gadolinium yttrium vanadate bounce laser," Appl. Phys. B **90**, 445 (2008).

[83] T. Omatsu, K. Nawata, D. Sauder, A. Minassian, and M. Damzen, "Over 40 W diffraction-limited Q-switched output from neodymium-doped YAG ceramic bounce amplifiers," Opt. Exp. **14**, 8198 (2006).

[84] S. Amarande and M. Damzen, "Measurement of the thermal lens of grazing-incidence diode-pumped Nd:YVO_4 laser amplifier," Opt. Comms. **265**, 306 (2006).

[85] V. Magni, "Resonators for solid-state lasers with large-volume fundamental mode and high alignment stability," Appl. Opt. **25**, 107 (1986).

[86] N. Metzger, C. Leburn, A. Lagatsky, C. Brown, S. Calvez, D. Burns, H. Sun, M. Dawson, M. L. Du, J. Harmand, and W. Sibbett, "Femtosecond pulse generation around 1500nm using a GaInNAsSb SESAM," Opt. Exp. **16**, 18739 (2008).

[87] J. Hopkins, G. Valentine, J. A. d. A. W. Sibbett and, F. Morier-Genoud, U. Keller, and A. Valster, "Efficient, low-noise, SESAM-based femtosecond Cr^{3+}:$LiSrAlF_6$ laser," Opt. Comms. **154**, 54 (1998).

[88] O. Okhotnikov, A. Grudinin, and M. Pessa, "Ultra-fast fibre laser systems based on SESAM technology: new horizons and applications," New. J. Phys. **6**, 177 (2004).

[89] O. Okhotnikov, T. Jouhti, J. Konttinen, S. Karirinne, and M. Pessa, "1.5 μm monolithic GaInNAs semiconductor saturable-absorber mode locking of an erbium fiber laser," Opt. Lett. **28**, 364 (2003).

[90] D. Burns, M. Hetterich, A. Ferguson, E. Bente, M. Dawson, J. Davies, and S. Bland, "High-average-power (¿20 W) Nd:YVO_4 lasers mode locked by strain-compensated saturable Bragg reflectors," J. Opt. Soc. Am. B **17**, 919 (2000).

[91] F. Brunner, T. Sudmeyer, E. Innerhofer, F. Morier-Genoud, R. Paschotta, V. Kisel, V. Shcherbitsky, N. Kuleshov, J. Gao, K. Contag, A. Giesen, and U. Keller, "240 fs pulses with 22 W average power from a mode-locked thin-disk Yb:$KY(WO_4)_2$ laser," Opt. Lett. **27**, 1162 (2002).

[92] T. Graf, A. Ferguson, E. Bente, D. Burns, and M. Dawson, "Multi-Watt Nd:YVO_4 laser, modelocked by a semiconductor saturable absorber mirror and side-pumped by a diode-laser bar," Opt. Comms. **159**, 84 (1999).

[93] V. Kolev, M. Lederer, B. Luther-Davies, and A. Rode, "Passive mode locking of a Nd:YVO_4 laser with an extra-long optical resonator," Opt. Lett. **28**, 1275 (2003).

[94] L. Krainer, R. Paschotta, S. Lecomte, M. Moser, K. J. Weingarten, and U. Keller, "Compact Nd:YVO_4 lasers with pulse reptition rates up to 160 GHz," IEEE J. Quant. Elec. **38**, 1331 (2002).

[95] V. Kisel, A. Troshin, V. Shcherbitsky, N. Kuleshov, V. Matrosov, T. Matrosova, M. Kupchenko, F. Brunner, R. Paschotta, F. Morier-Genoud, and U. Keller, "Femtosecond pulse generation with a diode pumped Yb^{3+}:YVO_4 laser," Opt. Lett. **30**, 1150 (2005).

[96] H. Haus, "Theory of modelocking with a fast saturable absorber," J. Appl. Phys. **46**, 3049 (1975).

[97] H. Haus, "Modelocking of laser," IEEE J. Sel. Top. Quant. Elec. **6**, 1173 (2000).

[98] D. Kuizenga and A. Siegman, "Modulator frequency detuning effects in the FM-modelocked laser," IEEE J. Quant. Elec. **QE-6**, 803 (1970).

[99] O. Svelto, *Principles of Lasers* (Springer, 1998).

[100] F. Kartner, J. A. der Au, , and U. Keller, "Modelocking with slow and fast saturable absorbers - what's the difference?" IEEE J. Sel. Top. Quant. Elec. **4**, 159 (1998).

[101] R. Paschotta and U. Keller, "Passive modelocking with slow saturable absorbers," Appl. Phys. B **73**, 653 (2001).

[102] C. Honninger, R. Paschotta, F. Morier-Genoud, M. Moser, and U. Keller, "Q-switching stability limits of continuous-wave passive mode locking," J. Opt. Soc. Am. B **16**, 46 (1999).

[103] F. Kartner, L. Brovelli, D. Kopf, M. Kamp, I. Calasso, and U. Keller, "Control of solid state laser dynamics by semiconductor devices," Opt. Eng. **34**, 2024 (1995).

[104] F. Brunner, E. Innerhofer, S. Marchese, T. Südmeyer, R. Paschotta, T. Usami, H. Ito, S. Kurimura, K. Kitamura, G. Arisholm, and U. Keller, "Powerful red-green-blue laser source pumped with a modelocked thin disc source," Opt. Lett. **29**, 1921 (2004).

[105] F. Kartner, I. Jung, and U. Keller, "Soliton modelocking with saturable absorbers," IEEE J. Sel. Top. Quant. Elec. **2**, 540 (1996).

[106] G. Paunescu, J. Hein, and R. Sauerbrey, "100 fs diode pumped Yb:KGW modelocked laser," Appl. Phys. B **79**, 555 (2004).

[107] A. Agnesi, A. Guandalini, A. Tomaselli, E. Sani, A. Toncelli, and M. Tonelli, "Diode pumped passively modelocked and passively stabilized Nd:BaY_2F_8," Opt. Lett. **29**, 1638 (2004).

[108] K. Jasim, Q. Zhang, A. Nurmikko, E. Ippen, A. Mooradian, G. Carey, and W. Ha, "Picosecond pulse generation from passively modelocked vertical cavity diode laser at up to 15 GHz pulse repetition rate," Elec. Lett. **40**, 34 (2004).

[109] M. Lederer, V. Kolev, B. Luther-Davies, H. H. Tan, and C. Jagadish, "Ion-implanted InGaAs single quantum well semiconductor saturable absorber mirrors for passive mode-locking," J. Phys D : Appl. Phys. **34**, 2455 (2004).

[110] "http://www.batop.de," .

[111] P. W. Smith, Y. Silberberg, and D. Miller, "Modelocking of semiconductor diode lasers using excitonic non-linearities," J. Opt. Soc. Am. B **2**, 1228 (1985).

[112] U. Keller, "Recent developments in compact ultrafast lasers," Nature **424**, 831 (2003).

[113] J. van den Ziel, W. Tsang, R. Logan, R. Mikulyak, and W. Augustyniak, "Subpicosecond pulses from a passively modelocked GaAs buried optical guide semiconductor lasers," Appl. Phys. Lett. **39**, 525 (1981).

[114] D. Farrell and M. Damzen, "High power scaling of a passively modelocked laser oscillator in a bounce geometry," Opt. Exp. **15**, 4781 (2004).

[115] M. Ostermeyer, P. Kappe, R. Menzel, and V. Wulfmeyer, "Diode-pumped nd:yag master oscillator power amplifier with high pulse energy, excellent beam quality, and frequency-stabilized master oscillator as a basis for a next-generation lidar system," Appl. Opt. **44**, 582 (2005).

[116] A. Brignon, J. Huignard, M. Garrett, and I. Mnushkina, "Nd:YAG master-oscillator power amplifier with a rhodium-doped $BaTiO_3$ self-pumped phase-conjugate mirror," Opt. Lett. **22**, 442 (1997).

[117] I. Zawischa, K. Plamann, C. Fallnich, H. Welling, H. Zellmer, and A. Tunnermann, "All-solid-state neodymium-based single-frequency master-oscillator fiber power-amplifier system emitting 5.5W of radiation at 1064 nm," Opt. Lett. **24**, 469 (1999).

[118] A. Liem, J. Limpert, H. Zellmer, and A. Tunnermann, "100 W single-frequency master-oscillator fiber power amplifier," Opt. Lett. **28**, 1537 (2003).

[119] A. Garnache, S. Hoogland, A. C. Tropper, J. M. Gerard, V. Thiery-Mieg, and J. S. Roberts, "Proceedings of CLEO/Europe-EQEC," in "Post-deadline Paper," (2001).

[120] E. U. Rafailov, S. J. Whitea, A. A. Lagatsky, A. Miller, W. Sibbett, D. A. Livshits, A. E. Zhukov, and V. M. Ustinov, "Fast quantum-dot saturable absorber for passive mode-locking of solid-state lasers," IEEE Photonics Technol. Lett. **16**, 2439 (2004).

[121] A. A. Lagatsky, E. U. Rafailov, W. Sibbett, D. A. Livshits, A. E. Zhukov, , and V. M. Ustinov, "Quantum-dot-based saturable absorber with p-n junction for mode-locking of solid-state lasers," IEEE Photonics Technol. Lett. **17**, 294 (2005).

[122] R. Herda, O. G. Okhotnikov, E. U. Rafailov, W. Sibbett, P. Crittenden, and A. Starodumov, "Semiconductor quantum-dot saturable absorber mode-locked fiber laser," IEEE Photonics Technol. Lett. **18**, 157 (2006).

[123] A. A. Lagatsky, F. M. Bain, C. T. A. Brown, W. Sibbett, D. A. Livshits, G. Erbert, and E. U. Rafailov, "Low-loss quantum-dot-based saturable absorber for efficient femtosecond pulse generation," Appl. Phys. Lett. **91**, 231111 (2007).

[124] C. Scurtescu, Z. Y. Zhang, J. Alcock, R. Fedosejevs, M. Blumin, I. Saveliev, S. Yang, H. Ruda, and Y. Y. Tsui, "Quantum dot saturable absorber for passive mode locking of Nd:YVO_4 lasers at 1064 nm," Appl. Phys. B **87**, 671 (2007).

[125] K. W. Su, H. C. Lai, A. Li, Y. F. Chen, , and K. E. Huang, "InAs/GaAs quantum-dot saturable absorber for a diode-pumped passively mode-locked Nd:YVO_4 laser at 1342 nm," Opt. Lett. **30**, 1482 (2005).

[126] D. J. H. C. Maas, A. R. Bellancourt, M. Hoffmann, B. Rudin, Y. Barbarin, M. Golling, T. Sudmeyer, and U. Keller, "Growth parameter optimization for fast quantum dot SESAMs," Opt. Express **16**, 18646 (2008).

[127] M. Lumb, "Quantum dot saturable absorber mirrors," Ph.D. thesis, Imperial College London (2009).

[128] E. C. L. Ru, A. J. Bennett, C. Roberts, and R. Murray, "Strain and electronic interactions in InAs/GaAs quantum dot multilayers for 1300 nm emission," J. Appl. Phys. **91**, 1365 (2002).

[129] M. Sopanen, H. P. Xin, and C. W. Tu, "Self-assembled GaInNAs quantum dots for 1.3 and 1.55 μm emission on GaAs," Appl. Phys. Lett. **76**, 994 (2000).

[130] Q. Gao, H. H. Tan, L. Fu, and C. Jagadish, "Effects of thermal stress on interdiffusion in InGaAsN/GaAs quantum dots," Appl. Phys. Lett. **84**, 4950 (2004).

[131] J. Tatebayashi, M. Nishioka, and Y. Arakawa, "Over 1.5 μm light emission from InAs quantum dots embedded in InGaAs strain-reducing layer grown by metalorganic chemical vapor deposition," Appl. Phys. Lett. **78**, 3469 (2001).

[132] E. Clarke, P. Spencer, E. Harbord, P. Howe, , and R. Murray, "Growth, optical properties and device characterisation of InAs/GaAs quantum dot bilayers," J. Phys.: Conf. Ser. **107**, 012003 (2008).

[133] E. C. L. Ru, P. Howe, T. S. Jones, and R. Murray, "Strain-engineered InAs/GaAs quantum dots for long-wavelength emission," Phys. Rev. B **67**, 165303 (2003).

[134] P. Howe, E. C. L. Ru, E. Clarke, B. Abbey, R. Murray, and T. S. Jones, "Competition between strain-induced and temperature-controlled nucleation of InAs/GaAs quantum dots," J. Appl. Phys. **95**, 2998 (2004).

[135] R. Leon, Y. Kim, C. Jagadish, M. Gal, J. Zou, and D. J. H. Cockayne, "Effects of interdiffusion on the luminescence of InGaAs/GaAs quantum dots," Appl. Phys. Lett. **69**, 1888 (1996).

[136] C. Lobo, R. Leon, S. Fafard, and P. G. Piva, "Intermixing induced changes in the radiative emission from III-V quantum dots," Appl. Phys. Lett. **72**, 2850 (1998).

[137] S. Malik, C. Roberts, R. Murray, and M. Pate, "Tuning self-assembled InAs quantum dots by rapid thermal annealing," Appl. Phys. Lett. **71**, 1987 (1997).

[138] S. Fafard and C. N. Allen, "Intermixing in quantum-dot ensembles with sharp adjustable shells," Appl. Phys. Lett. **75**, 2374 (1999).

[139] A. Babinski, J. Jasinski, R. Bozek, A. Szepielow, , and J. M. Baranowski, "Rapid thermal annealing of InAs/GaAs quantum dots under a GaAs proximity cap," Appl. Phys. Lett. **79**, 2576 (2001).

[140] Y. Kobayashi, "Control of photoluminescence wavelength from uniform InAs quantum dots by annealing," Applied surface science **244**, 88 (2005).

[141] J. R. Arthur, "Surface stoichiometry and structure of GaAs," Surface science **43**, 449 (1974).

[142] A. Y. Cho and J. R. Arthur, "Molecular beam epitaxy," Progress in Solid State Chemistry **10**, 157 (1975).

[143] K. Stankov, "A mirror with an intensity dependent reflection coefficient," Appl. Phys B **45**, 191 (1988).

[144] J. Armstrong, N. Bloembergen, J. Ducuing, and P. Pershan, "Interactions between light waves in a non-linear dielectric," Phys. Rev. **127**, 1918 (1962).

[145] A. Agnesi, G. Reali, and V. Kubecek, "Non-linear mirror operation of a diode pumped quasi-CW picosecond Nd:YAG laser," Appl. Phys. B **66**, 283 (1998).

[146] K. Stankov, "25 ps pulses from a Nd:YAG laser modelocked by a frequency doubling β-BaB_2O_4 crystal," Appl. Phys. Lett. **58**, 2203 (1991).

[147] A. Mani, P. Hollander, P. Thiry, and A. Peremans, "All-solid-state 12 ps actively passively mode-locked pulsed Nd:YAG laser using a nonlinear mirror," Appl. Phys. Lett **75**, 3066 (1999).

[148] G. Cerullo, M. Danailov, S. DeSilvestri, P. Laporta, V. Magni, D. Segala, and S. Taccheo, "A diode-pumped non-linear mirror modelocked Nd:YAG laser," Appl. Phys. Lett. **65**, 2392 (1994).

[149] K. Stankov, "Modelocking by a frequency-doubling crystal: generation of transform-limited ultrashort light pulses," Opt. Lett. **14**, 359 (1989).

[150] J. Lin, W. Yang, W. Hsieh, and K. Lin, "Low threshold and high power output of a diode-pumped non-linear mirror modelocked Nd:$GdVO_4$ laser," Opt. Exp. **13**, 6323 (2005).

[151] A. Agnesi, S. Dell'Acqua, and G. Reali, "Non-linear mirror modelocking of efficiently diode-pumped pulsed neodymium lasers," J. Opt. Soc. Am. B **16**, 1236 (1999).

[152] I. Buchvarov, S. Saltiel, and S. Gagarskii, "Non-linear doubling modelocking of feedback controlled pulsed Nd:YAG laser," Opt. Comms. **118**, 51 (1995).

[153] Y. Chen, S. Tsai, and S. Wang, "High power diode-pumped non-linear mirror modelocked Nd:YVO_4 laser with periodically-poled KTP," Appl. Phys. B **72**, 395 (2001).

[154] G. Petrov, V. Yakovlev, and N. Minkovski, "Broadband non-linear optical conversion of a high energy diode-pumped picosecond laser," Opt. Comms. **229**, 441 (2004).

[155] A. Agnesi, C. Pennacchio, G. Reali, and V. Kubecek, "High power diode-pumped picosecond Nd:YVO_4 laser," Opt. Lett. **22**, 1645 (1997).

[156] A. Ray, S. Das, S. Mukhopadhyay, and P. Datta, "Acoustooptic modulator stabilized low-threshold modelocked Nd:YVO_4 laser," Appl. Phys. Lett. **89**, 221119 (2006).